FACTORS INFLUENCING AVIATION VISIBILITY IN NEPAL

A THESIS SUBMITTED TO THE

CENTRAL DEPARTMENT OF PHYSICS,

INSTITUTE OF SCIENCE AND TECHNOLOGY

TRIBHUVAN UNIVERSITY

NEPAL

FOR THE AWARD OF

DOCTOR OF PHILOSOPHY

IN PHYSICS

BY

BHOGENDRA KATHAYAT

JANUARY 2024

FACTORS INFLUENCING AVIATION VISIBILITY IN NEPAL

A THESIS SUBMITTED TO THE

CENTRAL DEPARTMENT OF PHYSICS,

INSTITUTE OF SCIENCE AND TECHNOLOGY

TRIBHUVAN UNIVERSITY

NEPAL

FOR THE AWARD OF

DOCTOR OF PHILOSOPHY

IN PHYSICS

BY

BHOGENDRA KATHAYAT

JANUARY 2024

TRIBHUVAN UNIVERSITY

Institute of Science and Technology

DEAN'S OFFICE

Kirtipur, Kathmandu, Nepal

Reference No.:

Institute of Science & Technology
Dean's Office
Kirtipur 2045

EXAMINERS

The Title of Ph.D. Thesis: " Factors Influencing Aviation Visibility in Nepal "

Name of Candidate: Bhogendra Kathayat

Internal Examiner:

Prof. Dr. Sunil Adhikary
Tri-Chandra Multiple Campus
Tribhuvan University, NEPAL

External Examiners:

(1) Dr. Kundan Lal Shrestha
Kathmandu University
Dhulikhel, NEPAL

(2) Dr. Sachin Ghude
Indian Institute of Tropical Meteorology
Pune, INDIA

(3) Dr. Pawan Gupta
Earth Science at the Science and Technology Institute
NASA Marshall Space Flight Center, USA

16 August, 2024

(Dr. Surendra Kumar Gautam)
Asst. Dean

DECLARATION

Thesis entitled "**Factors influencing aviation visibility in Nepal**" which is being submitted to the Central Department of Physics, Institute of Science and Technology (IOST), Tribhuvan University, Nepal for the award of the degree of Doctor of Philosophy (Ph.D.), is a research work carried out by me under the supervision of Prof. Dr. Narayan Prasad Chapagain of Department of Physics, Amrit Campus, Tribhuvan University and co-supervised by Dr. Arnico Panday of Institute for Integrated Development Studies, Kathmandu.

This research is original and has not been submitted earlier in part or full in this or any other form to any university or institute, here or elsewhere, for the award of any degree.

Bhogendra Kathayat

RECOMMENDATION

This is to recommend that **Bhogendra Kathayat** has carried out research entitled **"Factors influencing aviation visibility in Nepal"** for the award of Doctor of Philosophy (Ph.D.) in **Physics** under our supervision. To our knowledge, this work has not been submitted for any other degree.

He has fulfilled all the requirements laid down by the Institute of Science and Technology (IOST), Tribhuvan University, Kirtipur for the submission of the thesis for the award of Ph.D. degree.

.....

Prof. Dr. Narayan Prasad Chapagain
Supervisor
(Professor)
Department of Physics, Amrit Campus
Tribhuvan University
Kirtipur, Kathmandu, Nepal

.....

Dr. Arnico Panday
Co-Supervisor
(Senior Research Fellow)
Institute for Integrated Development Studies
Mandikhatar, Kathmandu, Nepal

January 2024

TRIBHUVAN UNIVERSITY
CENTRAL DEPARTMENT OF PHYSICS
Kirtipur, Kathmandu, Nepal

☎ 4331054
www.tucdp.edu.np

Tribhuvan University Central Department of Physics Kirtipur

Ref. No.: (F.No .....) CDP ..... Date: .....

LETTER OF APPROVAL

20/02/2024

On the recommendation of Prof. Dr. **Narayan Prasad Chapagain** and Dr. **Arnico Panday**, this Ph.D. thesis submitted by **Bhogendra Kathayat,** entitled **"Factors influencing aviation visibility in Nepal"** is forwarded by Central Department Research Committee (CDRC) to the Dean, IOST, T.U..

OP Niraula

Dr. Om Prakash Niraula
Professor
Head
Central Department of Physics
Tribhuvan University
Kirtipur, Kathmandu, Nepal

ACKNOWLEDGEMENTS

I feel highly blessed to have come this far in this joyous journey of many years because of the contribution of many wonderful people, without which this would not have been possible. My most profound appreciation goes to my supervisors Prof. Dr. Narayan Prasad Chapagain and Dr. Arnico K. Panday. Sirs, you have gone far beyond my extreme hopes in providing me with the right mix of patience, motivation, trust, and mentoring—to maximize learning and pursue my potential. I will forever be grateful for your kind understanding of my situation—a profession airline pilot attempting to pursue graduate studies—and for providing me the required flexibility in time, if not it was unthinkable to navigate through the roller coaster of unexpected events during the last seven years. My special thanks to Dr. Binod Pokharel, Central Department of Meteorology, T.U.. Sir, you have been instrumental in honing my research ideas, and mentoring; you have always extended your helping hands whenever I needed. I owe my success in publications to you. My sincerest gratitude goes to Prof. Dr. Binil Aryal, dean of IOST for the motivation and support. At the Central Department of Physics, I would like to extend my special gratitude to Prof. Dr. Om Prakash Niraula, Head of the Department, for his support and motivation. I am highly thankful to the members of the Central Department Research Committee (CDRC) Prof. Dr. Narayan Adhikari, Prof. Dr. Raju Khanal, Prof. Dr. Iswar Koirala, and Prof. Dr. Balram Ghimire for actively reviewing my research progress and motivating. My sincerest gratitude to Prof. Dr. Ram Prasad Regmi for all the help during my studies. I would like to thank research mates, Dr. Usha Joshi, Prakash Man Shrestha, Dr. Drabindra Pandit, and Dr. Bashu Dev Ghimire for togetherness, mutual help, and comforting each other in moments of need during our graduate journey together. I am highly thankful to Dr. Maheswar Rupakheti, vice-chair, of IPCC WGI (Inter governmental Panel on Climate Change, Working group I) for his advice and for assigning me as a research assistant for SusKat-ABC (Sustainable Atmosphere for the Kathmandu Valley) atmospheric characterization campaign. It was indeed a lifetime opportunity to meet, work with, and get inspired by many pioneer scientists in the field of atmospheric science. Big thanks to Dr. Dipesh Rupakheti, Nanjing University, Dr. Khadak Mahata, and Dr. Shradda Dhungel, University of Delaware, USA for camaraderie in many field works and advice. I also cherish my friendship with Mr. Yash Raj Lamsal, Kathmandu University who helped me

through my programming struggles. I am very much thankful to the various sources of data used in this thesis: **I.** Government of Nepal (GoN), Department of Hydrology & Meteorology (DHM) **II.** Department of Environment (DoE), **III.** European Centre for Medium-Range Weather Forecasts (ECMWF), **IV.** National Climatic Data Center (NCDC), **V.** Aerosol Robotic Network (AERONET), Lumbini, and **VI.** Global Modeling and Assimilation Office (GMAO), Goddard Earth Sciences Data and Information Services Center (GES-DISC), USA.

From my workplace, Nepal Airlines Corporation, I want to thank Sr. Capt. Srawan Rijal, Sr. Capt. Rabindra Kumar Sherchan, Sr. Capt. Subash Rijal, Sr. Capt. Krishna Bikram Paudel Chhetri who helped and inspired me to pursue my dream. Unstinting motivation by Sr. Capt. Vijay Lama immensely helped me propel my journey; he considered my journey as his own and always pushed me. I wholeheartedly thank my batch mates Sr. Capt. Sanjay Paudel, Sr. Capt. Raman Ghimire and Sr. Capt. Mukesh Kumar Gupta (Etihad Airways) for the friendship, good company, support and motivation.

I feel very blessed to have my friends: Mr. Roshan Ghimire, Mr. Sukdev Regmi, and Mr. Tanka Mani Kharel, who unconditionally supported each of my endeavors, helped ease my work/study pressure, and brought fun. I would like to express my special appreciation and hugs to my wife Dr. Rekha Paudel for her unyielding support, for believing and encouraging me, and for enduring many personal sacrifices. Your support has been beyond measure! I cannot explain in words how your mere presence helped me overcome my career and academic struggles. I owe many vacation dues to my daughter Kaavya. You have always been a good child! I am equally thankful to my parents Krishna Kumari and Santosh Kathayat and my siblings: Ambika Kathayat Bimali, Ashok, and Suman Kathayat for their blessings, best wishes, and support. You have always trusted my dreams and felt proud of my achievements and dreams. I am highly thankful to my father-in-law Chandi Bahadur Paudel and brother-in-law Suman Paudel for their love and support throughout. Lastly, my sincerest gratitude goes to all my teachers from pre-school through university to my professional career.

……..

Bhogendra Kathayat

January 2024

शोध सार

पर्यावरण, मानव-स्वस्थ, पर्यटन जस्ता मानव-सरोकारका बिबिध विषयहरु का अतिरिक्त उड्डयन क्षेत्रमा पनि वायुमण्डलिय-पारदर्शिता (भिजिबिलिटी) ले गम्भीर प्रत्यक्ष/ परोक्ष असर गर्न सक्ने निचोड बिगतका अनेकन् बैज्ञानिक अन्वेषणहरूको रहेको छ। विमानस्थलहरूमा वायुमण्डलिय-पारदर्शिता निर्धारित दुरी भन्दा कम हुन गएमा वायुयान उडान र अवतरणमा असहजता उत्पन्न हुँदा उडान तालिका प्रभावित भै यात्रुहरु लाई असुविधा हुने, उड्डयन संचालन खर्च बढ्ने देखि हवाई दुर्घटना सम्म हुन सक्ने जोखिम रहन्छ । हाम्रो देश, नेपालको उड्डयन सु-संचालनमा एक मुख्य भूमिका खेल्ने बिषय ''वायुमण्डलिय-पारदर्शिता'' लाई प्रभाव पार्न सक्ने सम्भावित मूल अवयवहरुको पहिचान गर्ने, तिनीहरुसंगको सम्बन्धको प्रक्रियागत अध्यन गर्ने, वायुमण्डलिय पारदर्शिताको ऐतिहासिक अवस्था र त्यसले उडान क्षेत्रमा पारेको प्रभावहरूको बैज्ञानिक अन्वेषण गर्ने मूल उदेश्य रहेको यस शोधका लागि नेपालका दुई मुख्य अन्तर्राष्ट्रिय विमानस्थलहरु—त्रिभुवन अन्तर्राष्ट्रिय विमानस्थल, काठमाडौँ र भखरै स्तरोन्नति गरिएको गौतम बुद्ध अन्तर्राष्ट्रिय विमानस्थल, भैरहवामा मापन गरिएको चार दशक भन्दा लामो अवधि (ईश्वी सम्बत १९७६—२०२२) को जलवायू तथ्यांकको प्रयोग र विश्लेषण गरिएको छ । साथमा लामो अवधि सम्म जमिनमा मापन गरिएका बायु प्रदुषणका तथ्यांक, जमिनमा रही वायुमण्डलको मौसमी/ पर्यावरण सूचकाङ्कमा मापन गर्ने उपकरणहरु (रिमोट-सेंसिंग उपकरण) को प्रयोगबाट उपलब्ध तथ्यांक, पून-विश्लेषण गरि तयार पारिएका आँकडा (रि-एनालाइसिस्-डाटा) र भू-उपग्रहले संग्रह गरेका ऐतिहासिक तस्बिरहरुको बिस्तृत बैज्ञानिक अध्यन-विश्लेषण गरिएको छ । दुवै अध्ययन-स्थलमा मुख्यरुपमा तुवाँलो र हिउदें-हुस्सुका कारण वायुमण्डलिय-पारदर्शिता घट्ने गरेको यस अध्ययनले इंगित गरको छ । भैरहवा क्षेत्रमा अन्य मौसमको तुलना, मनसुनपछिको याम ((पोस्ट-मनसुन) (अक्टोबर, नोभेम्बर)) मा तुवाँलोले आकाश-ढाकिने-अवधि दर उच्च रहेको (१.४६% दिन प्रतिवर्ष) र हिउदें-हुस्सुले आकाश-ढाकिने-अवधि दर बढ्दो (१.०५% दिन प्रतिवर्ष) रहेको पाईएको छ । त्यसैगरी, ई. सं. १९७६—२००० को अवधिमा काठमाडौँ उपत्यकामा हिउँदे तुवाँलो तिब्र गति (२.३६% दिन प्रतिवर्ष) मा बढी तत्पश्चात उच्चतम बिन्दु आसपासमा रहेको र पछिल्लो अवधि (ई. सं. २०००—२०२२) काठमाडौँ विमानस्थलमा बाक्लो हुस्सुको आवृत्ति उल्लेखनीय रूपमा ह्रास (१.२८% दिन प्रतिवर्ष) भएको पाइयो । अध्यन गरिएका दुवै विमानस्थलहरू हरुको लामो समयको तथ्यांक विश्लेषण गर्दा, मूलतः बिबिध प्राकृतिक/ मानव सृजित बायु प्रदुषण उत्सर्जन श्रोतहरु बाट वायुमण्डलमा उत्सर्जन गरिएका अति सुक्ष्म बायु प्रदूषणका कण हरु (पीएम-२.५ (बायु गतिकिय ब्यास २.५ माइक्रो मिटर भन्दा कम भएका कण)) को वायुमण्डलमा एकाग्रता, तिनीहरु को प्रकार लगायतका बिबिध भौतिक तथा रासायनिक गुण हरुले वायुमण्डलको प्रकाशीय गुण र अन्त्यमा वायुमण्डलिय-पारदर्शिता निर्धारित हुने गरेको पाएको छौं । यसैगरि वायुमण्डलमा रहने जल बाष्प बढे संगै सल्फेट, नाइट्रेट, एमोनियम जस्ता जल बाष्प-संवेदनशील पीएम-२.५ समूह का प्रदूषणका सुक्ष्म कणहरुको आकार बढ्ने र अपवर्तक सूचकाङ्क (रिफ्र्याक्टिव इन्डेक्स) घट्ने साथै पीएम-२.५ समूहका प्रदूषणका बिशेष सुक्ष्म कणहरुको सामुहिक-ह्रास-प्रगुणता (मास एक्सटिङ्गसन इफिशियंशी) बढ्ने कारणले वायुमण्डलको प्रकाशीय गुणमा बदलाब हुदै वायुमण्डलिय-पारदर्शितामा उल्लेख्य ह्रास आउने गरेको तथ्य पनि हाम्रो शोधले इंगित गर्दछ । यसैगरि, बायुमण्डल-आर्द्रता कम भएको बखत (सापेक्षिक आर्द्रता $< ६०\%$) वायुमण्डलिय-पारदर्शिता

बिशेष गरि पीएम-२.५ को एकाग्रतामा निर्भर रहने र आर्द्रता बढे संगै पीएम-२.५ को एकाग्रता संगको सम्बन्ध कमजोर हुने र आर्द्रताको प्रभाव प्रमुख हुने तथ्य देखिएको छ। वायुमण्डलिय-पारदर्शिता र अति सुक्ष्म बायु प्रदूषणका कणहरुको एकाग्रता बीच विपरीतार्थक सम्बन्ध रहने र भैरहवा विमानस्थलमा ति दुई बीचको सहसम्बन्ध (को-रिलेशन) वर्षात याम (मनसुन (जून, जुलाई, अगस्त, सेप्टेम्बर)) मा उत्कृष्ट (पिअर्शन सहसम्बन्ध गुणक = —०.७४) रहेको पाइयो । यस्तै, काठमाडौँ उपत्यका माथिको आकाशको माथिल्लो सतह सम्म को मौसमी अवस्था बारेमा जानकारी लिन र मौसमी पूर्व-अनुमानमा मद्दतका लागि प्रत्येक बिहानी प्रक्षेपण गरिने बिबिध मौसमी विवरण मापन गर्ने उपकरण बोक्ने बेलुन (रेडियो-सन्ड) द्वारा मापन गरिएको लगभग तिन साल (ई. सं. २०१९—२०२२) को तथ्यांक को विश्लेषण गरि वायुमण्डलिय-सिमा-तह (बाउन्ड्री लेयर) पत्ता लगाउने बिबिध जटिल उपायहरु मध्ये तीनवटा तरिका हरुको निर्क्योल र प्रमाणिकरण गर्नु यस शोधको एक मुख्य उपलब्धि रहेको छ। बिहानीपख को काठमाडौँ उपत्यकाको बायुमण्डलीय-सिमा-तह सामान्यतः स्थिर प्रकृतिको रही बायु प्रदुषणका सुक्ष्म कणहरु लाई सिमा-तह भित्रै संकुचित राख्ने भएकोले बिहानी पखको वायुमण्डलिय-पारदर्शिता न्युन रहने गरेको पुष्टि हाम्रो उपरोक्त खोजले गरको छ। यसैगरि, काठमाडौँ उपत्यकामा बायुको गतिको घटबढ संगै बायु प्रदुषणका सुक्ष्म कणहरुको उपलब्धता/ एकाग्रतामा फरक पर्ने कारणले विमानस्थलको वायुमण्डलिय-पारदर्शिता फरक पर्न जाने साथै हिउँद महिनाहरूमा बिशेष गरि पूर्व दिशाबाट विमानस्थलको आकाशमा प्रवेश गर्ने प्रदुषित बायुका कारण विमानस्थलको वायुमण्डलिय-पारदर्शिता घट्ने गरेको पनि पाइयो । दुवै विमानस्थलहरू को वायुमण्डलिय-पारदर्शितामा बिगतका दशकहरुमा देखिएको सामयिक परिवर्तनको सम्बन्ध विशेषगरि बढ्दो बायु प्रदुषण, वायुमण्डलमा मौजुद जल बाष्प र हावाको गति जस्ता जलवायुमा आएका परिवर्तनसंग रहेको तथ्य हाम्रो शोधको निचोड रहेको छ । यस अलावा, हिउँद महिनाहरूमा दुवै विमानस्थलहरूको बिमान उडान-अवतरण सु-संचालनमा गम्भीर प्रभाव पार्ने हिउँदे-हुस्सु लाग्न शुरु-हुने र अन्त्य-हुन-सक्ने सम्भावित समय, र हुस्सुले आकाश ढाकि रहने सम्भावित अवधि पत्ता लगाएर उड्डयन क्षेत्र र मौसम पूर्व अनुमानमा सहयोगको प्रयास गरेका छौं। वायुमण्डलिय-पारदर्शिताको सामयिक परिवर्तनले दुवै विमानस्थलहरूमा कसरी असर गरिरहेको छ भन्ने प्रश्नको उत्तर खोज्ने प्रयास पनि यस शोधको रहेको छ। अन्त्यमा, घट्दो वायुमण्डलिय-पारदर्शिता र सो संग सम्बन्धित जोखिमहरुको न्यूनीकरणका हेतु बिबिध सुझाब पनि पेश गरेका छौं।

ABSTRACT

Visibility impairment in recent decades has become a serious challenge in the aviation sector of our region. This very issue has an adverse impact on comfort, air safety, and the overall aviation economy. Thus, quantification of the changes in atmospheric visibility and characterization of affecting factors at major airports is highly advantageous. Two major international airports in Nepal, Tribhuvan International Airport (TIA) at Kathmandu (KTM) and Gautam Buddha International Airport (GBIA) at Bhairahawa (BWA) were chosen as study sites. Over four decades of climatological data (1976–2022) supplemented with ground measurements, remote sensing data, reanalysis data, and satellite imagery were used. It was found that haze and fog are two major weather types reducing visibility in Nepal, both of which displayed a significant uptrend. At BWA, the fastest increase in haze is witnessed in the post-monsoon season (1.46% day/ year at 0.001 level of significance (α)); and winter fog is on the rise (1.05% day/ year, α = 0.001) too. A similar upward trend of winter haze frequency (2.36% day/year, α = 0.001) and fog frequency (0.46% day/year, at α = 0.05) in regime-I (1976–2000) in KTM was observed. Whereas, the trend of winter haze flattened to 0.36% day/year (at α = 0.05) and dense fog declined at the rate −1.28% per day per annum (at α = 0.01) in regime-II (2001–2022). By careful examination of all plausible climatological drivers of the change in KTM, strong evidence of decreasing humidity and increasing dew point depression after the year 2000 was found. A negative power function relationship between Aerosol Optical Depth (AOD) and visibility (VIS) at GBIA was seen. The relationship between PM2.5 and visibility (VIS) is similar. The best negative correlation between AOD and VIS occurred during monsoon ($r = -0.66$, $p < 0.001$) ($r = -0.74$, $p < 0.001$ between PM2.5 and VIS). The effect of aerosol water on VIS at GBIA was also seen, i.e., reduced airport visibility at increased RH. As a first effort to obtain sounding-based Planetary Boundary Layer Height (PBLH) climatology in Nepal, radiosonde measurements launched from a suburban site in KTM (November 2019–30 March 2022) were analyzed. It was observed that 91.20% of all early morning (0545 LT) soundings showed surface-based inversion, highlighting the existence of nocturnal Stable Boundary Layer (SBL) classification. Three different temperature-profile algorithms: Bulk Richardson method (RM) at a critical threshold (Ri_c) of 0.22, Gradient of potential temperature method (GM_θ) and Surface Based Temperature

inversion (SBI) method, were employed for estimating PBLH. Taking the SBI method as a benchmark method, we found that GM_θ yielded an almost unbiased estimate with a statistically significant coefficient (r = 0.99, p <0.001; R^2 = 0.99 and bias (ΔH) = -3.57 m); RM slightly overestimated (r = 0.83, p < 0.001; $R^2 = 0.65$ and ΔH = 15.0 m); whereas ERA5 reanalysis PBLH measurements grossly underestimated ($r = -0.22$, $R^2 = -0.55$ and $\Delta H = -100.94$ m) stable PBL tops. The strongest and deepest surface inversions during winter and pre-monsoon months (PBLH ~ 200 ± 115 m in April) and the weakest and shallowest stable boundary layer in the early morning of monsoon (PBLH ~ 30 ± 11 m in September) were found. In the valley, PM 2.5 is higher in dry (the highest in March: 100 ± 13 μg m^{-3}) and lower in the wet season (the lowest in August: 8.6 ± 1.2 μg m^{-3}). Whereas, airport visibility at TIA is the best in wet (the highest in June: 6.6 ± 0.3 km) and worst during the dry season (the lowest in January: 3.9 ± 0.2 km). A positive correlation between PBLH and PM2.5 (r = 0.35, p < 0.001), good anti-correlation between VIS and PM2.5 ($r = -0.59$, p < 0.001), and a poor-negative correlation between PBLH and VIS ($r = -0.16$, p < 0.001) were found. The impact of the optical properties of aerosols (specifically PM2.5) and their hygroscopic effect on visibility in TIA was also studied. A sharp decline in visibility with an increase in the PM2.5 extinction coefficient and mass extinction efficiency (MEE) was observed. An exponential growth of hygroscopic growth factor ($f(RH)$) and a subsequent decrease in visibility with increased RH was noticed. It was observed that increased wind speed tends to improve visibility at the airport. Deterioration of airport visibility by the wind with a speed of 1–2 m/s flowing from the northeast through the south direction in the winter season was also noticed. Further, some of the salient microclimatic properties of winter fog at both of the airports were studied, too. Visibility at both airport sites displayed a definitive declining trend that was found to be linked with changes in air pollution emission and different meteorological factors. These changes pose serious adverse impacts on the aviation sector amongst many others. For the sustainable improvement of visibility, regionally coordinated efforts on implementation of strict air pollution-mitigation-measures are required.

Keywords: *Air pollution, Aviation, Bhairahawa, Boundary layer height, Kathmandu, Meteorology, MK-Test, Radiosonde, Trend statistics, Visibility*

LIST OF ACRONYMS AND ABBREVIATIONS

A-SMGCS	:	Advanced Surface Movement Guidance, and Control System
AERONET	:	Aerosol Robotic Network
AIC	:	Accident Investigation Commission
AMS	:	American Meteorological Society
AOD	:	Aerosol Optical Depth
AQI	:	Air Quality Index
AQM	:	Air Quality Monitoring
ATC	:	Air Traffic Controller
BB	:	Biomass Burning
BC	:	Black Carbon
BWA	:	Bhairahawa
CAAN	:	Civil Aviation Authority Of Nepal
CALIPSO	:	Cloud-Aerosol Lidar And Infrared Pathfinder Satellite Observations
CAMS	:	Copernicus Atmosphere Monitoring Services
CAT	:	Category
CBL	:	Convective Boundary Layer
CCN	:	Cloud Condensation Nuclei
CFIT	:	Controlled Flight Into Terrain
CI	:	Confidence Interval
CO	:	Carbon Monoxide
COVID	:	Coronavirus Disease

CRB	:	Crop Residue Burning
CVA-AK	:	Ceiling and Visibility Analysis Alaska
CWV	:	Column Water Vapor Content
DEL	:	Delhi
DHM	:	Department Of Hydrology And Meteorology
DJF	:	December January February
EC	:	Elemental Carbon
ECMWF	:	European Centre for Medium-Range Weather Forecasts
ERA5	:	European Centre for Medium-Range Weather Forecasts (ECMWF) Reanalysis V5
FA	:	Free Atmosphere
FAA	:	Federal Aviation Authority
GBIA	:	Gautam Buddha International Airport
GEOS	:	Goddard Earth Observing System Model
GLDAS	:	Global Land Data Assimilation System
GM	:	Gradient of Potential Temperature Method
GMAO	:	Global Modeling and Assimilation Office
GOP	:	Gorakhpur
GVD	:	Good Visibility Days
HKH	:	Hindu Kush Himalayan
IATA	:	International Air Transport Association
ICIMOD	:	International Center for Integrated Mountain Development
IFR	:	Instrument Flight Rules

IGI	:	Indira Gandhi International Airport
IGP	:	Indo-Gangetic Plains
ILS	:	Instrument Landing System
IMC	:	Instrument Meteorological Condition
IMD	:	Indian Meteorological Department
IQR	:	Inter Quartile Range
JJAS	:	June July August September
KTM	:	Kathmandu
LAC	:	Light Absorbing Carbon
LKN	:	Lucknow
LT	:	Local Time
LWC	:	Liquid Water Content
MAE	:	Mean Absolute Error
MAM	:	March April May
MedAE	:	Median Absolute Error
MEE	:	Mass Extinction Efficiency
MERRA	:	Modern-Era Retrospective Analysis for Research and Applications
METAR	:	Meteorological Terminal Air Report
MH	:	Mixing Layer Height
MIT	:	Massachusetts Institute Of Technology
MK	:	Mann-Kendell
ML	:	Mixing Layer
MLH	:	Mixing Layer Height

MODIS	:	Moderate Resolution Imaging Spectroradiometer
NASA	:	National Aeronautics and Space Administration
NBL	:	Neutral Boundary Layer
NCDC	:	National Climate Data Center
NOAA	:	National Oceanic and Atmospheric Administration
NTSB	:	National Transportation Safety Board
OC	:	Organic Carbon
OLS	:	Ordinary Least Square
ON	:	October November
PBL	:	Planetary Boundary Layer
PBLH	:	Planetary Boundary Layer Height
PIA	:	Pakistan International Airlines
PM	:	Particulate Matter
POM	:	Particulate Organic Material
PTD	:	Potential Temperature Difference
PVD	:	Poor Visibility Days
RH	:	Relative Humidity
RL	:	Residual Layer
RM	:	Bulk Richardson Number Method
RMSE	:	Root Mean Squared Error
RNP	:	Required Navigation Performance
RS	:	Radio Sonde
RSS	:	Radiosonde Launch Site
SBI	:	Surface-Based Inversion

SBL	:	Stable Boundary Layer
SBLH	:	Stable Boundary Layer Height
SD	:	Standard Deviation
SOA	:	Secondary Organic Aerosols
SODAR	:	Sonic Detection and Ranging
SYNOP	:	Synoptic Observation
TIA	:	Tribhuvan International Airport
UHI	:	Urban Heat Island
UK	:	United Kingdom
UNEP	:	United Nations Environment Programme
UNESCO	:	United Nations Educational, Scientific and Cultural Organization
USAF	:	United States Air Force
UTC	:	Universal Time Coordinated
VC	:	Ventilation Coefficient
VFR	:	Visual Flight Rules
VIS	:	Visibility
VMC	:	Visual Meteorological Condition
VOR	:	Visual Omnidirectional Radio Range
WD	:	Wind Direction
WHO	:	World Health Organization
WMO	:	World Meteorological Organization
WRF-Chem	:	Weather Research and Forecasting Model Coupled with Chemistry

WRF-STEM	:	Weather Research and Forecasting Model Coupled with Sulfur Transport and Deposition Model
WS	:	Wind Speed

LIST OF SYMBOLS

%	:	Percentage
$\overline{(f_i(x))}$	:	Normalized Mass Distribution
$\langle T_v \rangle$	:	Average Virtual Temperature
yr^{-1}	:	Per Year
AOD_{340}	:	Aerosol Optical Depth at 340 Nano Meter
E_e	:	Mass Extinction Efficiency
$f_i\ (RH)$	:	RH Enhancement Factor
gfd_{pbwa}	:	General Fog Days at Bhairahawa
gfd_{pdel}	:	General Fog Days in Delhi
gfd_{pgop}	:	General Fog Days at Gorakhpur
gfd_{plkn}	:	General Fog Days at Lucknow
GM_θ	:	Gradient of Potential Temperature Method
km	:	Kilometer
NH_4^+	:	Ammonium
NO_3^-	:	Nitrate
Pom_h	:	Post-Monsoon Haze Day
Pom_p	:	Post-Monsoon Poor Visibility
Prm_h	:	Pre-Monsoon Haze Day
Prm_p	:	Pre-Monsoon Poor Visibility
Ri	:	Bulk Richardson Number
Ri_c	:	Critical Bulk Richardson Number

SBL_{tp}	:	Top of the Stable Boundary Layer
SO_4^{2-}	:	Sulfate
yr	:	Year
$\mu g\ m^{-3}$	:	Microgram Per Cubic Meter
$\sigma(r,\beta)_M$	:	Mie Scattering Function
$\sigma(r,\beta)_R$	:	Rayleigh Scattering Function
ΔH	:	Difference of Boundary Layer Height Estimates
°K (or, K)	:	Degree Kelvin
a.g.l.	:	Above Ground Level
Amsl	:	Above Mean Sea Level
$b_{ext,i}$	:	Extinction Coefficient Associated with *I*th Species
b_{abs}	:	Absorption Coefficient
b_{ag}	:	Absorption Coefficient By Gaseous Molecules
b_{ap}	:	Absorption Coefficient by Particles
b_{ext}	:	Extinction Coefficient
b_{scat}	:	Scattering Coefficient
b_{sg}	:	Scattering Coefficient by Gaseous Molecules
b_{sp}	:	Scattering Coefficient by Particles
$b_{sp}(RH)$	:	Scattering Coefficient at a given RH
℃	:	Degree Celsius
d	:	Molecule Diameter
D	:	Particle Diameter
D_g	:	Mass Mean Diameter

day yr^{-1}	:	Day Per Year
$d\Omega$	:	Increment of Solid Angle
E	:	Mass Extinction Efficiency
$f_i\,(x\ )$	:	Aerosol Mass Distribution of the *i*th Species
g	:	Acceleration due to Gravity
H_0	:	Null Hypothesis
H_1	:	Alternate Hypothesis
I_0	:	Actual Irradiance at Transmitter
I_r	:	Received Irradiance at the Receiver
K	:	Koschmieder Constant
m	:	Particle Mass Concentration
m	:	Meter
m/s	:	Meter Per Second
M_h	:	Monsoon Haze Day
m_i	:	Total Mass Concentration of *i*th Species
M_i	:	Mass of the *i*th Hygroscopic Species
M_p	:	Monsoon Poor Visibility
N	:	Number Of Molecules
n	:	Index of Refraction
n_i	:	Complex Refractive Index
$N_i(D)$	:	Aerosol Number Size Distribution of *i*th Species
nm	:	Nano Meter
NO_2	:	Nitrogen Dioxide

p	:	Air Pressure
PBLH	:	Planetary Boundary Layer Height
$PM10$	:	Particles having Aerodynamic Diameter of 10 Microns or Less
$PM2.5$	:	Particles having Aerodynamic Diameter of 2.5 Microns or Less
Q	:	Slope of Sen's Linear Fit Line
Q_e	:	Extinction Efficiency
r	:	Pearson's Correlation Coefficient
r	:	Position
R^2	:	Coefficient of Determination
RH	:	Relative Humidity
S	:	Mann-Kendall Statistics
$SBLH$	:	Stable Boundary Layer Height
T	:	Surface Air Temperature
T_d	:	Dew Point Temperature
T_{min}	:	Minimum Temperature
t_s	:	T-Statistics
T_{dep}	:	Dew Point Depression
$u\ and\ v$	:	Components of Wind Speed
u_*	:	Surface Friction Velocity
v	:	Visibility
VIS	:	Visibility
$V(S)$	:	Variance of MK Statistics

W_h	:	Winter Haze Day
W_p	:	Winter Poor Visibility
W_{pbwa}	:	Winter Poor Visibility at Bhairahawa
W_{pdel}	:	Winter Poor Visibility in Delhi
W_{pgop}	:	Winter Poor Visibility at Gorakhpur
W_{plkn}	:	Winter Poor Visibility at Lucknow
WS	:	Wind Speed
$X_i \; and \; X_j$	:	Time Series Observation of Variable of Interest X, in Chronological Order i and j
z	:	Planetary Boundary Layer Height
Z_{GM_θ}	:	Boundary Layer Height Estimates from $\boldsymbol{GM_\theta}$
Z_{MK}	:	Standardized MK-Test Statistics
Z_{RM}	:	Boundary Layer Height Estimates from RM
Z_{SBI}	:	Boundary Layer Height Estimates from The SBI Method
$z(Ri_c)$	:	Height (Above Ground Level) Corresponding To Critical Bulk Richardson Number
α	:	Level of Significance
α	:	Ångström Exponent
$\alpha_{i,d}$	:	Mass Scattering Coefficient
β	:	Angle of Scattering
$\hat{\beta}_1$	:	Estimate of β_1 Based On The Sample
β_0	:	Intercept
β_1	:	Slope
γ	:	Hygroscopicity Parameter

$\frac{\Delta\theta}{\Delta z}$	:	Potential Temperature Gradient
ε_i	:	Random Error
θ	:	Potential Temperature
θ_v	:	Virtual Potential Temperature
λ	:	Wavelength of Light
ρ	:	Particle Density
$\sigma(r,\beta)$	:	Volume Scattering Function
σ_g	:	Geometric Standard Deviation
τ	:	Aerosol Optical Depth
χ	:	Size Parameter

LIST OF TABLES

LIST OF FIGURES

Page No.

TABLE OF CONTENTS

CHAPTER 4

CHAPTER 1

INTRODUCTION

A byproduct of economic growth and urbanization, especially in the developing world, is the worsening of air quality because of various anthropogenic activities. Among many impacts of worsening air quality, obscuring the sky with a grey/brown haze layer is one of the major concerns, as it adversely affects human health, the tourism business, the aviation industry, etc. The clarity of a scene is usually evaluated in terms of atmospheric visibility, which is expressed as "the greatest distance at which an observer can see a black object against the horizon" (Middleton, 1952). Visibility is degraded by particulates and droplets suspended in the air whose concentration is governed by many factors including meteorology. Thus, assessment of particulate loading in the atmosphere and meteorological factors is vital for gaining deeper insight into the visibility of a place.

The unique topography and challenging weather conditions are preexisting and unavoidable challenges to the Nepalese aviation industry, which has gained a reputation for having bad air-safety records. The growth of population, urbanization, and industrialization in major cities of Nepal is rapid. Besides them, changing climatology may also have adverse consequences on airport visibility. Having deeper insight into visibility at major airports not only helps safer, more comfortable, and economic flight operations but also helps policymakers invest in proper airport facilities. Thus, this study focuses on the understanding of the status of atmospheric visibility, affecting factors and aviation implications mainly at two of the major international airports inside Nepal: Tribhuvan International Airport at Kathmandu and Gautam Buddha International Airport at Bhairahawa.

1.1 What is Atmospheric visibility?

American Meteorological Society (2023) defines meteorological visibility in its simplest form as the farthest horizontal distance in a given direction one can just see and identify—with the unaided eye—a prominent dark object against the sky and horizon (daytime) and a known light source that is moderately intense and preferably unfocused (nighttime). Horvath (1981) defines visibility as the farthest distance at which one can recognize the outlines of an ideally black target against the background

horizon. In practice, either a trained observer or an automatic weather station observes and reports visibility values. Visibility at a place is firstly determined around the whole horizon circle before it is resolved into a single value of prevailing visibility for visibility reporting. The traditional demand that visibility indicators be both detected and recognized has inherent problems. If the criterion for recognition were lifted, the visibility might be characterized as a subjective estimate of visual range since the more precisely defined idea of the visual range excludes reference to recognition. It can now be described in that way for the majority of practical reasons. While estimates of visibility during the day are subjective assessments of air contrast attenuation, estimates of visibility during the night are attempts to analyze something quite different, namely the attenuation of flux density. As a result, visibility data must be considered to be divided into those obtained by day and those by night.

1.2 Visibility impairment: A historical perspective

Although it seems a contemporary issue, visibility impairment induced by human activities has indeed occurred for as long as humans possess the ability to alter their surroundings. This began when humans first acquired the skill to create fire, nearly 790,000 years back, as suggested by analysis of flints at an archaeological site located near river Jordan (Alperson-Afil, 2008). A study by Sapart *et al.* (2012) analyzed ice core samples in the Netherlands and revealed a 2100-year-old chemical signature of methane in ice samples. They attributed the methane signature to then anthropogenic activities specifically metallurgy and large-scale agricultural activities. Emissions from worldwide metallurgical activities certainly contributed to the enhancement of ambient particulate concentration and subsequent visibility decline. More kilns, metal smelters, and the burning of fossil fuels had an ever-increasing impact on day-to-day living, including decreased visibility, as civilization and urbanization advanced. The industrial revolution, which began in Britain, in the mid-18th century, but quickly spread over Europe and the United States, marked the beginning of large-scale human influence on air quality. The worst recorded extended period of poor air quality and subsequent impaired visibility occurred in London in December 1952 (great smog of London) for five days resulting from a combined effect of industrial pollution and a high-pressure weather system (Martinez, 2019). Smog and fog brought London to a near standstill and resulted in many thousand deaths. Visibility at Heathrow Airport was reduced below 10 m for 48 h (Malm, 2016). This event marks a turning point in environmentalism

history as it grabbed the attention of the scientific community to consider visibility as a problem worthy enough for systemic investigation. Two decades later, Los Angeles in the United States caught attention for its reduced visibility because of emissions from road vehicle fleets (Tiao *et al.*, 1975). This led researchers to put effort into investigating ways to improve visual air quality by identifying the responsible factors of visibility impairment. Several such events of prolonged impaired visibility were documented in many other places in Europe and the United States.

The Industrial Revolution in China and the Asia-Pacific region began in the second half of the 20th century. This region's rapid economic growth from its industrial revolution contributed to the shift of global emissions from Europe and North America to Central, South, and East Asia (Igini, 2022). Other Asian countries, such as India and Pakistan also undergone a huge industrialization and urbanization, turning them into recent air pollution hotspots. Air quality and impaired visibility commensurate with urbanization and economic growth has become one of the major concerns of our country too.

1.3 Visibility as an indicator of air quality

Visibility degradation is an indicator of the pollution one can see or visual air quality (Hyslop, 2009; Yuan *et al.*, 2002). Numerous past papers (Chang *et al.*, 2009; Wang *et al.*, 2009) have well-established inverse relationship between aerosol concentration in the atmosphere and visibility. Therefore, changes in visibility can be equivalently used as indicators of air quality (Watson, 2002). For instance, Vajanapoom *et al.* (2001) estimated PM10 from visibility data in Bangkok. Based on such studies, some cities have even developed indexes for estimating PM levels from visibility data—one such example being, the city of Shasta in Canada (Shahzad, 2014) (**Table 1**).

Table 1: Air quality indexing and hourly average PM estimation from visual range (Shahzad, 2014)

Visibility (Miles)	Level of health concern	Hourly average PM levels ($\mu g/ m^3$)
>11	Good	0-38
6–10	Moderate	39-88
3–5	Unhealthy for sensitive groups	89-138
1.5–2.75	Unhealthy	139-350
1–1.25	Very unhealthy	351-526
<1	Hazardous	>526

1.4 Visibility as a commercial product

Many countries in the world heavily rely on the tourism business. Enjoying views of landscapes, mountains, sunrises, sunsets, etc. are some of the most popular activities for tourists, as are sightseeing flights. Thus, a reduction in visibility may adversely affect tourism and hence country's economy in many ways. Tourists may cancel, divert, or shorten their trip or decide not to return; Visibility degradation may also lower property prices and reduce investment in areas affected by poor visibility. Thus, visibility shall be considered not only as a meteorological phenomenon but also as an economic indicator and a commercial product.

1.5 Visibility in aviation

1.5.1 How significant is visibility in aviation?

Aircraft take-off and landings at the airport, aircraft flow management, ground movement of aircraft, and ground handling operations heavily rely on visibility. Importance is even higher for the aircraft operating the whole flight—from take-off to landing—under Visual Flight Rules (VFR)(**APPENDIX** A.1**)**, like small twin-otter airplanes flying in and out of dozens of remote airstrips in Nepal. VMC offers the ideal visual conditions in terms of flight safety, air-traffic flow management, cost, comfort, time, need for landing and navigation facilities at the airport, etc. The problem arises whenever the visibility gets lower than those specified for VMC—called Instrument Meteorological Condition (IMC) (**APPENDIX A.1**). In such conditions, aircraft can

take off and land only up until a certain visual threshold (determined by various factors, like landing and navigational facility at the airport, terrain, aircraft equipment and performance, pilot training, etc.) under Instrument-Flight rules (IFR) (**APPENDIX A.1**). Such condition brings more complexities to flight operation. Even though IFR operations can bring orderly progression of taking off and landing aircraft, it typically reduces the runway capacity and results in flight delays (Morisset & Odoni, 2011), results in less relaxed separation between air traffic, and demands extra workload to the Air Traffic Controllers (ATC) and pilots. Flight cancellations and diversions because of poor airport visibility result in substantial monetary losses in the form of lost time, fuel, and additional aircraft maintenance (Kulkarni *et al.*, 2019). In the worst-case scenario, reduced visibility may lead to serious aircraft accidents and incidents too. It has been identified as an important safety hazard in aviation contributing to several aircraft accidents and incidents (Gultepe *et al.*, 2015; Jenamani & Kumar, 2013; Regmi *et al.*, 2020).

Many aircraft incidents and accidents that happened in the past were contributed by poor visibility. For instance, a brand new Turkish Airlines aircraft met a runway excursion incident in Kathmandu airport on 4 March 2015 (Accident Investigation Commission (AIC), 2015). The accident aircraft, an Airbus A330 registered TC-JOC, was severely damaged beyond repair when it landed in dense fog with barely 200 meters of visibility. This prevented it from utilizing the active runway for four days, resulting in a significant loss of revenue and significant disruption to air travel.

Most of the aviation accidents in Nepal between 1952 and 2022 were caused by planes accidentally flying into the mountains hidden behind clouds (also termed CFIT (**APPENDIX A.2**) in aviation) (Dixit, 2022). According to the author, out of 818 total fatalities during the period 92% lost their lives in CFIT type accidents. Not only small turbo-props flying to remote airstrips in Nepal but also big jet aircraft with sophisticated instruments have experienced the fate of CFIT crashes. On 28 September 1992, Pakistan International Airlines (PIA) flight 268 operated by Airbus A300, impacted a steep cloud-covered hill side (~7300 ft), Bhattedanda, killing all 167 occupants (Ranter, 1992). That was the worst air crash that happened in the Nepalese sky and also in PIA's history.

Most of the investigation reports of fatal CFIT crashes point toward pilots failing to abide by VFR while flying in the mountains. Despite some inherent threats—e.g., turbulence because of strong convective activities, lightening, and hail of flying into the clouds—CFIT by flying inside the clouds occurs because of the pilot failing to see mountains behind. Eventually, visibility impairment by cloud plays the main role in such CFIT accidents.

Globally, CFIT is also one of the leading categories of aircraft accidents with the lowest survival ratio. One typical example is the crash of Garuda airlines flight GA 152 in Medan Polonia international airport on 26 September 1997 while approaching in low visibility conditions (less than 500m due to forest fire) (Ranter, 1997). The accident was nonsurvivable; all persons on board (234) perished. According to the National Transportation Safety Board (NTSB), statistics, visibility, and cloud ceiling alone have contributed to ~24% of general aviation accidents between 1989 and early 1997 (Kulesa, 2003).

1.5.2 How does visibility affect the pilot's visual perception?

There are several ways that visibility affects pilots' visual perception. When an aircraft flies inside a deep haze layer: Oblique visibility is—the "greatest distance at which a specified target can be perceived when viewed along a line of sight inclined to the horizontal" (American Meteorological Society (AMS), 2023) (**Figure 1**(a))—will reduce with increase in aircraft's height. Conversely, if the aircraft is flying above the same deep haze-layer, flying higher increases the oblique visibility (Meteorology, 2004). Similarly, if an aircraft is flying above a shallow fog layer (**Figure 1**(b)), the pilot may be able to see the airfield clearly below him/her. However, when the aircraft descends through the fog layer and attempts to align with the airfield for landing, the pilot may not be able to see the airfield; looking through the horizontal extent of fog, visibility becomes much poorer.

Pilots may experience many visual illusions while flying in low visibility conditions imposed by different weather conditions. For example, in an aircraft descending through shallow fog, pilots may perceive a false impression of having nose-high when they suddenly see bright approach lights; resulting correction may lead to dangerous situations.

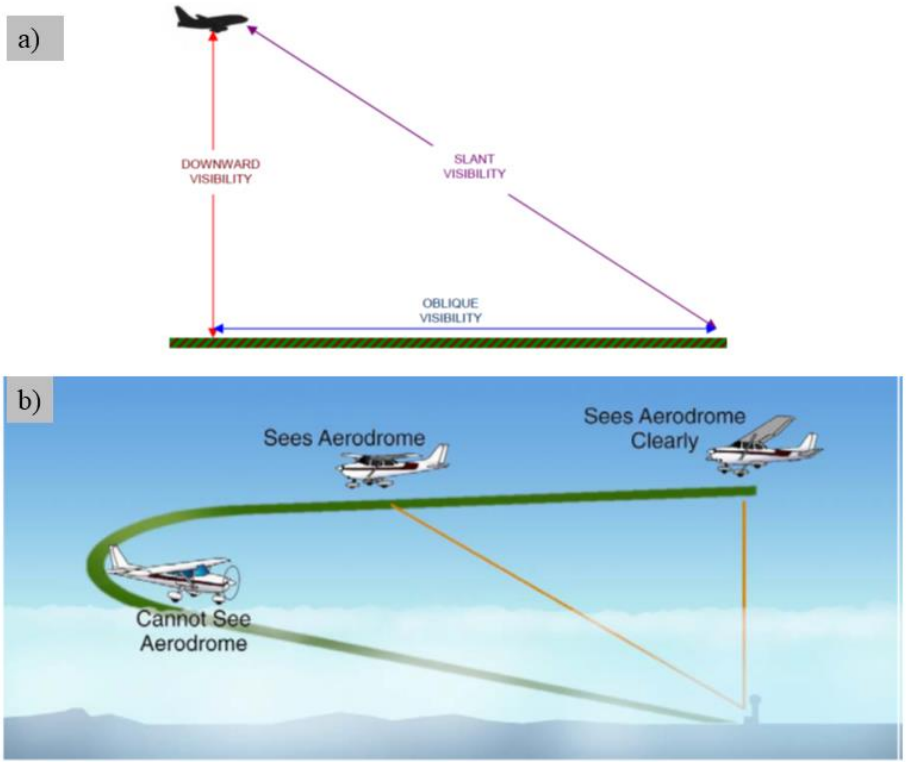

Figure 1: a) Different visibilities observed by a pilot in an aircraft, b) Seeing an aerodrome by a pilot in an aircraft through a shallow fog layer (Meteorology, 2004)

When the aircraft flies through a heavy rainstorm, the artificial horizon of the aircraft may move lower; the pilot may dive toward the ground if he/she believes in this illusion. If a pilot uses a cloud for a visual horizon, the pilot may probably level the aircraft to a datum other than the actual horizon. Similarly, heavy rain on the windscreen of a landing aircraft can impair the depth perception of the pilot because of the refraction of approach light by raindrops; the pilot perceives the runway to be further away.

1.6 Motivation

The main motivation for this study stems from the realization of the implications of atmospheric visibility in the aviation sector of our nation. Transportation to many inaccessible places in Nepal relies heavily upon air transport. Small turboprop aircraft, which fly to such places, have to fly through narrow mountain gorges at low altitudes. Low cloud ceilings and poor visibility add misery to such flying: risking lives, and property and ultimately tarnishing the country's aviation safety record. Pilots flying in such challenging flight routes of Nepal have scarce access to crucial information like en-route cloud ceiling and visibility conditions. Remote airports are poorly equipped, and weather-related information is limited to the vicinity of airports only.

Despite having capricious meteorological conditions and terrain like ours, the aviation industry in other parts of the globe can maintain a good safety record, e.g., Alaska region of the United States. Most of the credit goes to infrastructure, a well-developed research program, and proper dissemination of information including that of crucial cloud ceiling and visibility to end users (aviation personnel). With the product named Alaska (CVA-AK) Product Pilots can make vital go or no-go decisions, which is the key to air safety. Similarly, an algorithm created by a group of Massachusetts Institute of Technology (MIT) researchers combines data from web cameras placed by the Federal Aviation Authority (FAA) around Alaska to automatically assess visibility in a given area (Foye, 2019). Pilots and forecasters can exchange these visibility estimates in real-time online. To continue in the same direction is the primary driving force for our research. Though the development of a similar product requires a huge sum of funding, timing, and a huge team of experts, this research is motivated to lay some foundation stones for this very purpose. In addition, it is an area of atmospheric physics that has received little attention in Nepal and it is hoped that this research will set the foundation stone for future students to explore many interesting topics at the interface between meteorology, air quality, and optics in the Nepali atmosphere.

1.7 Physics of atmospheric visibility

Understanding the physics involved in atmospheric visibility is important since the perception of visibility by the human brain involves a complex interaction of light, object, atmosphere, human eye, and brain (Henry *et al.*, 2000; Mahadev & Henry, 1999). Our vision uses the contrast between the observed target and its background to detect the target edges. Consequently, our eyes work more efficiently under high contrast (Malm *et al.*, 1983). Each human observer has a unique threshold of contrast plus spatial visual frequency ("reception of structures per unit distance") (Shahzad, 2014), which brings about the difference in their visual observations from person to person. Such difference widens in the presence of atmospheric particulates and trace gases as the visible light coming from objects under observation disperses away from the observer (Ross *et al.*, 1997).

1.7.1 Interaction of visible light with the atmosphere

According to available literature (Zajonc, 1993), early mention of the interaction between light and atmosphere dates back to 569 B.C. Atmospheric processes such as

absorption and scattering by gaseous molecules and particles, which have a diameter close to the wavelength of light, are responsible for visibility impairment. The impairment is determined by the total amount of scattered light and the directional dependency of the scattering process. The image-forming light is weakened by scattering and absorption in each elementary segment of the sight path. Ambient light from all directions is also scattered toward the path segment to create air light, or equivalently, path radiance. Thus, by introducing noise (in the form of scattered light) into the signal, gas molecules and aerosols in the atmosphere lessen the contrast with the background. Hence, the observer's ability to view the target is diminished because the eye only receives a small amount of the real light reflected from the target.

A typical illustration of seeing a landscape feature is shown in **Figure 2**(a). It takes into account the sight path between observers to a far-off natural feature, specifically an ice-capped mountaintop, here. Light reflected from the mountaintop forms an image in the observer's eye whose characteristics are modified as it travels through the atmosphere. The image-forming information is scattered out of and absorbed within the sight path. When image-forming information is outcompeted by air light that reaches the observer's eye, the appearance of the image is degraded. In essence, atmospheric aerosols absorb or scatter visible light away from the sight path obscuring the contrast of the viewed target against the sky background (Watson, 2002). Seeing an object involves the following main factors: optical characteristics of illumination, viewed target, and intervening atmosphere as well as characteristics of the observer. The amount of ambient light lost through scattering and absorption inside any path segment is directly proportional to the light's intensity. A century ago (in 1924) Koschmieder presented one of the most practical explanations of the interaction between visible light and atmospheric constituents through his famous Koschmieder equation (**Eq.(1)**), which is still finding its application to explain the joint effect of light extinction and contrast on visibility.

$$VIS = {}^{K}/_{b_{ext}} \tag{1}$$

(Koschmieder, 1924)

Here, VIS and K refer to visibility and Koschmieder constants (= 3.912 at 2% visual contrast (Singh *et al.*, 2020), depending on eye health) respectively.

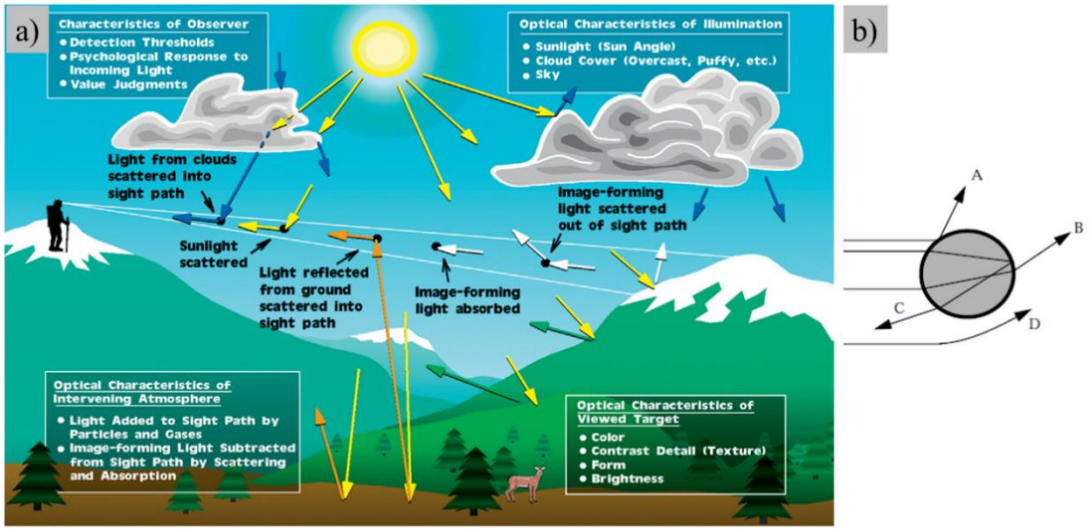

Figure 2: a) Important factors involved in seeing a scenic vista (Malm, 2016) **b)** Scattering of the radiation beam by an aerosol involving reflection (A), refraction (B), internal reflection (C), and diffraction (D) (Jacob, 1999)

The proportionality constant b_{ext} (km^{-1}), also called extinction or attenuation coefficient is "the fractional loss of light per unit distance along the light path" (Malm, 2016). It is solely a physical property of the atmosphere, i.e., a function of position (r) within the sight path and the sum of individual absorption and scattering coefficients by gaseous molecules and aerosols

$$b_{ext} = b_{scat} + b_{abs} = b_{sg} + b_{ag} + b_{sp} + b_{ap} \quad (2)$$

(Malm, 2016)

Where, b_{scat} and b_{abs} are scattering and absorption coefficients; b_{sg}, b_{ag}, represent scattering and absorption by gaseous molecules; and b_{sp}, b_{ap} represent likewise for the particles respectively.

The Koschmeider model assumes cloudless sky conditions and a homogenous distribution of aerosol in the atmosphere. After reviewing the Koschmieder model, Horvath (1971) concluded that this model is applicable (within a 10% error) under the following conditions:

- homogeneously illuminated atmosphere—otherwise up to 5% error may occur
- homogenously distributed aerosols—which make spatially constant extinction coefficients over a large distance, and

- ideally black target (zero reflectivity) is under observation—otherwise, errors up to 50% may occur.

Despite some limitations, this model (**Eq.(1)**) has been extensively used for airport visibility measurement, meteorological and environmental studies, etc. (Horvath, 1981). It can be used to calculate visibility from scattering or extinction coefficient measurements, and vice versa.

In between absorption and scattering light attenuation, the primary mechanism limiting visibility in the atmosphere is the scattering of solar light by aerosols (Jacob, 1999). In comparison, absorption plays very little role in visibility impairment. Light absorption in the atmosphere is dependent on the chemical composition of the atmosphere. The only gas that is typically present in the atmosphere and may absorb solar energy is NO_2 (b_{ag} = 330 Mm^{-1} at 0.55 μm). Compared to red, it absorbs more in the blue region of the spectrum, giving the sky a brownish or yellowish color. Among particles, Black Carbon (BC) and Elemental Carbon (EC) in the atmosphere absorb the most light (J. Wang & Martin, 2007). Normally, we ignore the contribution of absorption on visible light total attenuation; since, absorption bears only an overall share of 5–10% in rural settings (20–30% in urban settings due to EC) (Jacobson, 2002; White, 1990).

Since the light wavelets reflected or emitted from the viewed object are scattered in different directions, the scattering coefficient is defined as follows:

$$b_{scat} = \int_{4\Pi} \sigma(r,\beta)\, d\Omega \tag{3}$$

(Malm, 2016)

Where β is the angle of scattering and $d\Omega$ is an increment of solid angle. $\sigma(r,\beta)$, the volume scattering function, gives "the measure of the atmosphere's ability to scatter light in a given direction" (Malm, 2016). The sum of volume scattering by atmospheric particles (Mie scattering, $\sigma(r,\beta)_M$) and air molecules (Rayleigh scattering, $\sigma(r,\beta)_R$) gives the total volume scattering ($\sigma(r,\beta)$).

$$\sigma(r,\beta) = \sigma(r,\beta)_R + \sigma(r,\beta)_M \tag{4}$$

(Malm, 2016)

Rayleigh scattering represents the way that air molecules (ambient nitrogen and oxygen) scatter light. This elastic scattering process applies to spheres that are less than 10 times the wavelength of incident light radiation and is given by

$$\sigma(r,\beta)_R = \left(\frac{8\pi^4 d^6 N \left(\frac{n^2-1}{n^2+2}\right)^2}{\lambda^4} \right) (1 + \cos^2(\beta)) \quad (5)$$

(Malm, 2016)

Where d is molecule diameter, N is the number of molecules, β denotes the angle between incident and scattered radiation, and n is the index of refraction. While the amount of scattering at 90° is half of the amount scattered either forward or backward and polarized, the amount of scattering in both directions is equal and unpolarized.

Mie scattering, whose equations come from solving Maxwell's equation, describes scattering by particles with sizes almost equal to the wavelength of light. The solution, which yields $\sigma(r,\beta)_M$, depends on wavelength, particle size, and refractive index—a complex number whose imaginary component describes its absorption characteristics. The Mie scattering involves combinations of different phenomena: diffraction, refraction, phase shift, and absorption. All four of the aforementioned effects influence a particle's scattering efficiency as well as the direction of the redistribution of incident solar radiation.

It is more convenient to express the size dependency of particle scattering and absorption in terms of the extinction efficiency factor, which is the ratio of the effective to the actual cross-sectional area of a particle. Molecules and very small particles are very ineffective at scattering light. Particle size increases enhance the efficiency of light scattering until the size of the particles is about equal to the wavelength of the incident light. The single-particle extinction coefficient is

$$b_{ext} = (\pi D^2/4)\, Q_e\, (n_i, \chi, \lambda) \quad (6)$$

(Malm, 2016)

Where D and Q_e respectively denote the diameter of the particle and its extinction efficiency; n_i is complex refractive index; χ (=$\pi D/\lambda$) is size parameter. Since most of

the atmospheric monitoring programs measure particle mass concentration instead, equation (**Eq.(6)**) can be expressed in terms of extinction per unit mass or mass extinction efficiency $E\ (n\ ,\chi,\lambda\ )$ as:

$$b_{ext}\ =\ E\ (n\ ,\chi,\lambda\ )m \tag{7}$$

(Malm, 2016)

Where *m* represents particle mass concentration and $E\ (n\ ,\chi,\lambda\ )$ is:

$$E\ (n\ ,\chi,\lambda\ )\ =\ 3Q_e\ (n_i,\chi,\lambda\ )/2\rho D \tag{8}$$

(Malm, 2016)

In which, ρ represents particle density. Single or same-sized particles are represented by the aforementioned equations. Particles in the actual world are dispersed throughout a wide range of sizes and exhibit diverse physicochemical characteristics. Thus, the extinction coefficient associated with *i*th species particles expressed in terms of the number size distribution is

$$b_{ext,i}\ =\ \frac{\pi}{4}\int_0^\infty D^2\ Q_e\ (n_i,\chi)\ N_i(D)d(D) \tag{9}$$

(Malm, 2016)

Where $N_i(D)$ represents aerosol number-size-distribution of *i*th species. The coarse mode (diameter: 1–100 µm) has a greater aerosol mass than the fine mode (diameter: 0.1–1 µm), however the coarse mode's scattering cross section is less. Thus, most of the visibility impairment tends to be linked with fine particles. In terms of mass size distribution, we can write the extinction coefficient as

$$b_{ext,i}\ =\ \int_{-\infty}^\infty E_e\ \left(n_i\ ,\chi,\lambda\ \right)\ f_i\ (x\ )d(x) \tag{10}$$

(Malm, 2016)

where E_e refers to mass extinction efficiency; $f_i\ (x\ )$ is the aerosol-mass-distribution $\frac{dm}{dx}$ of the *i*th species; and x = $\ln\left[\frac{D}{D_\circ}\right]$.

Finally, total particle extinction associated with all particles is simply

$$b_{ext} = \sum_i \alpha_i m_i \tag{11}$$

(Malm, 2016)

where α_i is the integral mass extinction efficiency given by

$$\alpha_i = \int_0^\infty E_e\left(n_i, \chi, \lambda\right) \overline{f_i(x)} d(x) \tag{12}$$

(Malm, 2016)

in which, $\overline{f_i(x)}$ is normalized mass distribution; and $\overline{f_i} = \frac{f_i}{m_i}$ where m_i is the total mass concentration of *i*th species. A lognormal size distribution typically represents each of the size distribution modes as follows:

$$\overline{f_i}(\ln D) = \frac{1}{\sqrt{2\pi}\ln(\sigma_g)} \exp\left(-\frac{\left(\ln D - \ln D_g\right)^2}{2\left(\ln \sigma_g\right)^2}\right) \tag{13}$$

(Malm, 2016)

where D_g denotes the mass-mean-diameter and σ_g refers to geometric standard deviation. For all atmospheric particles, the minimum scattering angle is somewhere between 90º and 140º. This explains why visibility degradation is most noticeable in the early morning and late afternoon, and least noticeable in the afternoon (Malm, 2016).

1.7.2 How does meteorology affect visibility?

Apart from the significant contribution of atmospheric aerosols, such as sulfate and carbonaceous, to light extinction, meteorological parameters such as temperature (T), atmospheric pressure, precipitation, relative humidity (RH), wind speed and direction (WD), and temperature (T) can also have an impact on visibility. They may influence the sources and sinks of aerosols and trace gases in the earth's atmosphere, determining the total air pollution concentration (Deng *et al.*, 2011; Du *et al.*, 2013; Tsai *et al.*, 2007; Wen & Yeh, 2010). However, their net effect on visibility is quite complex because of the highly interrelated nature of these variables. Yet on complex topography, they can yield predictable outcomes, with impaired visibility found in cold air pools and other confined air masses near the surface. Our study focuses on the impact of some major

meteorological parameters only, namely, RH, WS, WD, and T (which is a proxy of planetary boundary layer (PBL) height). Thus, our introduction section is limited to only their implications on visibility.

1.7.2.1 Aerosol water

RH gives us a measure of ambient moisture. It has both direct and indirect effects on visibility. As a direct effect, when RH reaches saturation, visibility deteriorates because of the occurrence of special weather types, namely, fog, mist, cloud, and rain. On the other hand, an indirect effect of RH on visibility occurs via a change in aerosol's optical properties—which are largely affected by RH. This is what we refer to as the aerosol water effect on visibility. As the humidity increases, hygroscopic aerosols (e.g., SO_4^{2-}, NO_3^- , NH_4^+, sea salt, other inorganic components, and water-soluble organic compounds) progressively absorb ambient water (Engelhart *et al.*, 2011; Pilinis *et al.*, 1989). **Figure 3**(a) shows particle growth as a function of RH for ammonium sulfate ($(NH_4)_2SO_4$) and bisulfate (NH_4HSO_4). The ratio of the aerosol's diameter following water absorption to its dry aerosol's diameter is referred to as D/D_0, here. Normally, inorganic salts like them absorb and release water abruptly at an RH value called deliquescent or crystallization point. A sample of dry ammonium sulfate particles, for instance, will not absorb water until the relative humidity (RH) reaches approximately 80%. At this stage, it grows by a factor of about 1.5 on its own by absorbing more water; it then keeps growing as the relative humidity rises (**Figure 3**(a)). This process is reversible, i.e., if RH is reduced, the inorganic salt particle starts to shrink continuously until the crystallization point, when the particle spontaneously releases all absorbed water and returns to the crystallization state. However, because of contaminants in the aerosol mixture, once the particle absorbs water in ambient settings, it usually does not crystallize. As the RH drops, it will continue to lose water. The aerosol is said to be in a metastable state if the absorbed water is retained below the crystallization point (**Figure 3**(b)).

According to (Malm *et al.*, 1989) and (Gebhart & Malm, 1990) scattering coefficient at a given RH is

$$b_{sp}(RH) = b_{sp}(RH = 0)\ \frac{b_{sp}(RH)}{b_{sp}(RH = 0)} \tag{14}$$

(Malm, 2016)

Where $b_{sp}(RH = 0) = \alpha_{i,d} M_i$ and $f(RH) = \frac{b_{sp}(RH)}{b_{sp}(RH=0)} = \left(1 - \frac{RH}{100}\right)^{-\gamma}$ with γ the hygroscopicity parameter.

Thus,

$$b_{sp,i}(RH) = \alpha_{i,d} M_i \, f_i \, (RH) \tag{15}$$

(Malm, 2016)

Here $\alpha_{i,d}$ is mass scattering coefficient and M_i is dry mass of the *i*th hygroscopic species. $f_i \, (RH)$ is referred to as the RH enhancement factor (Tang *et al.*, 1981). It is calculated using Mie theory based on sampling-period-by-sampling-period.

The f (RH) curves for ammonium bisulfate with two distinct mass mean diameters ($D_g = 0.2 \; and \; 0.5$ µm) differ noticeably in **Figure 3**(b). The difference between them is nearly a factor of two at RH = 90%. This implies that "the same particle species will scatter twice as much light if its dry size distribution starts with a mass mean diameter of 0.2 µm rather than 0.5 µm"(Malm, 2016). This is because, in comparison to particles having a higher starting dry size, those with a smaller size distribution develop to a size more efficient in light scattering. Normally, the f (RH) (enhancement factor) of more acidic particles is higher than that of more neutralized particles.

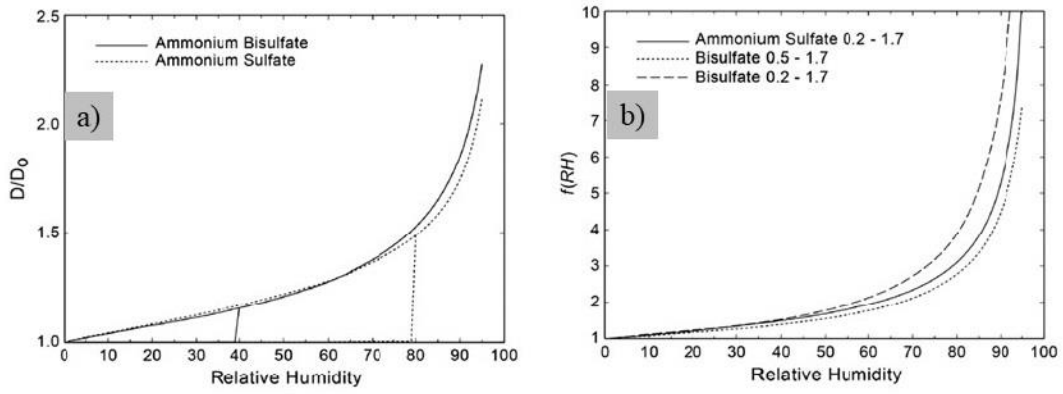

Figure 3: a) Metastable and deliquescent curves (D/D_0) for ammonium sulfate ($(NH_4)_2SO_4$) and ammonium bisulfate (NH_4HSO_4) **b)** Metastable f (RH) curves at two different size distributions**: (i)** $D_g = 0.2$ µm, $\sigma_g = 1.7$ (for both), **(ii)** $D_g = 0.5$ µm, $\sigma_g = 1.7$ (for bisulfate) (Malm, 2016)

By calculating the mass concentration of each species, one can determine the amount that aerosols' scattering and absorption of visible light contributes to extinction.

$$b_{ext} = \alpha_{AS}[(NH_4)_x SO_4]f_{AS}(RH) + \alpha_{AN}[NH_4 NO_3]f_{AN}(RH) + \alpha_{POM}[\mathrm{POM}]f_{POM}(RH) + \alpha_{soil}[\mathrm{Soil}] + \alpha_{sea\ salt}[\mathrm{Sea\ salt}]f_{sea\ salt}(RH) + \alpha_{CM}[\mathrm{CM}] + \alpha_{LAC}[\mathrm{LAC}] \quad (16)$$

(Malm, 2016)

This formula provides a good approximation of the extinction coefficient and assumes that the total scattering of ambient light is influenced by ammonium sulfate ($(\mathrm{NH_4})_x\,\mathrm{SO_4}$), ammonium nitrate ($\mathrm{NH_4\,NO_3}$), soil, sea salt, particulate organic material (POM), and coarse mass (CM). Light-absorbing carbon (LAC) contributes to the absorption. Each of them has a respective dry mass scattering (absorption for LAC) efficiency factor(α). The bracketed terms in the formula refer to the corresponding mass concentration ($\mathrm{m^{-3}}$). The growth factor (f (RH))—which is a function of RH—gives an estimate of the effect of water uptake by hygroscopic species.

1.7.2.2 Planetary boundary layer

Since planetary boundary layer height (PBLH) regulates the volume of air in the atmosphere available for the dispersion of all air pollutants (Kompalli *et al.*, 2014; Oleniacz *et al.*, 2016) and water vapor emitted at the earth's surface (Collaud Coen *et al.*, 2014), it is one of the most important meteorological parameters for air quality study and modeling. It has a notable effect on the accumulation and dissipation of air pollutants (Stull, 1988). Consequently, the determination of PBLH is pivotal for understanding air pollution and the visibility status of the atmosphere. Elucidating the link between PBLH, air pollution, and visibility is crucial for developing policies and strategies to address the anthropogenic factors contributing to the reduction in visibility. It is also essential for developing precise numerical weather/ air quality prediction models.

Significant mass, momentum, and energy transmission between the earth's surface and atmosphere is often contained in the lowest layer of the troposphere and evolves diurnally depending on radiation and energy balance (Aryee *et al.*, 2020). Large-scale turbulent airflows and exchanges between the earth's surface and atmosphere (Seidel *et*

al., 2010, 2012) are characteristics of this very layer, known as the PBL, which is directly impacted by the existence of the earth's surface (Seidel *et al.*, 2010, 2012). The PBLH is the height at which the earth's surface affects the flow and structure of the atmosphere. Strong parameter gradients, including aerosol concentration, are present near the top of the PBL structure.

PBLH exhibits a well-defined structure and distinct diurnal cycle (**Figure 4**) in fair-weather days. It is dependent upon topography, local and synoptic meteorological conditions, and both (Mues *et al.*, 2017). PBL structure is classified into stable boundary layer (SBL), convective boundary layer (CBL), and neutral boundary layer (NBL) based on their thermodynamic stability condition (Li *et al.*, 2015; Liu & Liang, 2010; Zhang *et al.*, 2018). When the sun is shining and warming the Earth's surface during the day, it is ideal to observe CBL. There is a strong mixing of convective turbulence and unstable stratification in CBL. CBL is kept apart from the free atmosphere above by the entrainment zone, a stable layer that stops pollutants from traveling vertically and reaching the free atmosphere. SBL—also called nocturnal boundary layer—is formed by inversion stratification accompanied by ground radiative cooling during the night and is capped by a residual layer (RL) that is separated from the ground and may contain pollutants from the evening before. Suppressed and sporadic turbulence, calm and stagnant air, and low mixing characterize SBL. On the other hand, NBL refers to a residual layer that is neutrally stratified and starts at the ground surface (Liu & Liang, 2010). This layer causes turbulence that is almost equal in strength in all directions (Sivaraman *et al.*, 2013).

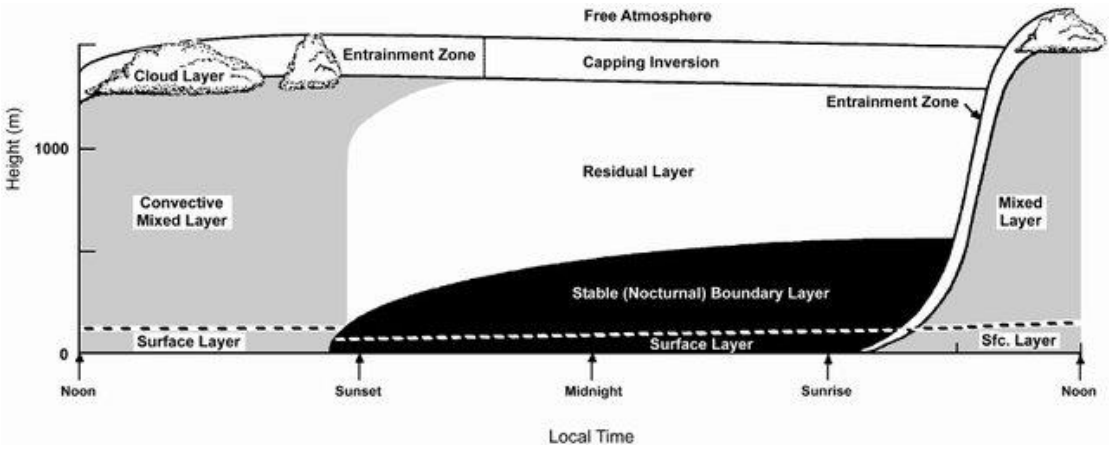

Figure 4: Diurnal cycle of the boundary layer during a clear convective day over land depicting three main sub-layers: Mixed, Residual, and Stable (Stull, 1988)

As buoyancy is almost negligible in these layers (Collaud Coen *et al.*, 2014; Li *et al.*, 2021), NBL examples are typically seen in cloudy situations with strong winds and little temperature difference between the earth's surface and air (Collaud Coen *et al.*, 2014). SBL and NBL usually form during the night and early morning. However, SBL and NBL may form at any time of the day under certain meteorological conditions (Stull, 1988; Zhang *et al.*, 2018). The diurnal evolution of PBL is less pronounced in cloudy and rainy conditions with a lower extent of this layer (Stull, 1988).

1.8 Measurement of visibility

Perception and appreciation of visibility are somewhat subjective to the observer's psychology; thus, visibility measuring techniques, scales, and units are different. All scales and units are assessed for their proximity to human perception and bear some limitations, which are difficult to omit wholly due to the involvement of complex and combined processes between human vision and the brain system (Henry *et al.*, 2000). Thus, visibility measurements by different techniques may yield values slightly different from those obtained from human observation. Some of the techniques for visibility measurements have been outlined in the subsections below.

1.8.1 Ground-based optical measurement

1.8.1.1 Transmissometers

A transmissometer measures the attenuation of visible light—transmitted from a transmitter and received by a transceiver—by forward scattering over a certain distance according to the following working principle.

$$b_{ext} = \frac{\ln\left(\frac{I_0}{I_r}\right)}{r} \tag{17}$$

(Horvath, 1981)

Where, b_{ext}, I_0, I_r and *'r'* are extinction coefficient, actual irradiance at the transmitter and received irradiance at the receiver, and distance respectively. Transmissometers are of two types—short-range and long-range—according to the distance between transmitters and receivers fixed on a metallic arm. They can provide visibility observation at lower intervals, unlike human observation. However, they are not capable of long-range measurements (over 50 km) (Watson, 2002) and are limited by

the use of lower-power light sources to avoid heating air in the vicinity (heated air has different optical properties than non-heated).

1.8.1.2 Nephelometer

It gives a measurement of the scattering coefficient (b_{scat}) in which, a sample of air is filled and heated before it is exposed to light radiation of known wavelength. The scattered light is measured at 90º to the incident light. Nephelometer finds its application while studying all size-spectrum of aerosols by using different sizes filters (Anderson & Ogren, 1998; Han *et al.*, 2009). Yet, it bears some structural design limitations that limit the instrument from measuring scattering beyond 170º. Furthermore, readings are prone to scattering properties bias because of the instrument being calibrated at a unique refractive index of a gas (Horvath & Kaller, 1994).

1.8.1.3 Teleradiometer

It measures the change in inherent contrast of the viewed object with background and perceived contrast at the radiometer by focusing a telescope coupled with a photodiode on the target (Malm *et al.*, 1981; Watson, 2002). Hence, the measurements of the Teleradiometer closely coincide with human observation. Telephotometer is an advanced form of this instrument (Horvath, 1981). The downside of these instruments is that they require more frequent calibration and maintenance to reduce signal attenuation.

1.8.1.4 Digital camera

Unlike costly visibility-measuring instruments mentioned in the above subsections, ordinary low-cost digital cameras can also estimate atmospheric visibility (Bäumer *et al.*, 2008; Duda & Hart, 1972). In this technique, visibility is estimated by computing the contrast of the viewed target with respect to its background employing advanced image processing techniques. In our country too, there are many digital IP cameras installed in various flight-critical locations across Nepal. Nonetheless, they have been only used for capturing real-time images/videos for monitoring the weather for aviation use.

1.8.2 Human eye observation

Human eye observation of surface visibility is the easiest and most common method. A well-trained human observer (e.g., trained meteorologist, Air Traffic Controller (ATC)) spots and identifies a most distant object—preferably a black target, to have better contrast with the background—across the horizon. In our real world, finding a perfectly black object is uncommon; thus, some common landscape targets such as mountains, trees, natural targets, buildings, etc., are used as targets in the daytime; while, in the nighttime, illuminated targets are used. The distance of the farthest spotted target is taken as the visibility in that direction. Accuracy is reduced under certain atmospheric conditions, e.g., target under the cloud, bright or dark cloud behind the target, target roofed by snow, etc. These atmospheric conditions alter the contrast of the spotted target against the horizon.

Different human observers may have different contrast thresholds, which gives rise to inconsistency among the readings by different observers. Thus, this method of visibility observation is a subjective approach, yet the most common method of observation because of the measurement ease and low cost. In our country too, trained human observers conduct routine estimates of airport visibility (half/one/three hours intervals) at the airports across Nepal.

Besides the aforementioned methods of estimating visibility, various other methods such as physical-chemical measurements (Bian, 2011; Jung *et al.*, 2009; Malm *et al.*, 1994) and visibility measurement from space (Hadjimitsis *et al.*, 2010; Shahzad, 2014) are used frequently elsewhere.

1.9 Objectives

The main objective of this study is to assess the role of various factors involved in the impairment of atmospheric visibility in selected major airports in Nepal, namely GBIA and TIA. Specific objectives are:

I. To quantify the temporal variation in visibility at selected major airports inside Nepal, namely GBIA and TIA, as well as some neighboring airports in the Indo-Gangetic Plains (IGP) region.

II. To evaluate the impact of atmospheric aerosol on visibility.

III. To evaluate the impact of meteorology on visibility and aerosol distribution.

IV. To assess the role of visibility change in aviation.

1.10 Significance of the study

As the upgraded GBIA airport and TIA are expected to be operating throughout the day and night, understanding visibility limitations serves to be a key planning ingredient for safe and efficient flight operations, as well as for decisions about investment in proper navigation equipment at the airports. Moreover, it will be a strategic starting point for designing policies as well as measures to address the anthropogenic origins of visibility decline.

1.11 Limitations

We conducted this research with the following limitations:

- Coarse time resolutions of climatological data and insufficient records of precipitation
- The upper limit of visibility recording in METAR for aviation use being 10 km only
- Investigating radiative impacts on the evolution of fog and visibility was limited by the lack of long-term records of solar radiation data
- Sites of air pollution measurements and climatological data sets are not collocated
- Single ascent time of radio soundings per day
- Data gap due to irregularity in radio soundings launched during the COVID-19 pandemic period.

1.12 Thesis organization

This dissertation consists of six chapters as the main body, followed by references and appendixes as follows:

i. Chapter 1 provides the background (historical/ theoretical) and objectives of the study.

ii. Chapter 2 includes a detailed review of the previous works of literature relevant to the study. This chapter aims to review advances in current knowledge on atmospheric visibility in global and local contexts. This section attempts to justify the objectives.

iii. Chapter 3 gives a detailed description of the study area, data, and methodologies used to meet the research goal.

iv. Chapter 4 includes results and discussions of our main findings commensurate with objectives.

v. Chapter 5 includes conclusions and recommendations, which highlight the main conclusions and possible extensions of the present work.

vi. Chapter 6 comprises a summary of the study.

CHAPTER 2

LITERATURE REVIEW

2.1 Factors affecting visibility

Horizontal visibility is one of the key elements in regular meteorological observation. In a pristine atmosphere, we can see up to a few hundreds of kilometers (Deng *et al.*, 2011). In contrast, bad meteorological conditions or heavy air pollution greatly limit the farthest distance we can see (Deng *et al.*, 2011; Zhao *et al.*, 2011). Thus, atmospheric visibility acts as an important indicator of atmospheric optics (Chen & Xie, 2013; Doyle & Dorling, 2002; Fu *et al.*, 2014; Sloane, 1982, 1984; Tsai, 2005).

Visibility reduction at a given place is a complex issue, as many factors can influence it. First, fine mass aerosols (PM2.5) in the atmosphere make a major contribution. Second, meteorological variables like RH, WS, and PBLH affect aerosols and trace gas concentration in the atmosphere thereby making a significant contribution. Due to their effects on surface type and aerosol deposition, other factors like urbanization, industry, human population, and vegetation cover also partially contribute to visibility loss (Diederen *et al.*, 1985).

2.1.1 Air pollution

Atmospheric aerosols have several important health and environmental impacts. They involve respiratory health risks (Maji *et al.*, 2018; Ratajczak *et al.*, 2021; Ray *et al.*, 2019; Xing *et al.*, 2016) and harm agriculture (Shrestha *et al.*, 2018). Through their dual roles as cloud formation nuclei and solar radiation scattering and absorption, they have a direct impact on the planet's climate. Additionally, they serve as the location for atmospheric condensed phase and surface chemistry (Jacob, 1999).

Although visibility is highly affected by prevailing meteorological conditions (e.g., rain, fog, mist, desert dust, etc.) and atmospheric circulation, it is mainly determined by the loading of atmospheric aerosols under clear sky conditions (Bäumer *et al.*, 2008; Davis, 1991; Doyle & Dorling, 2002; Malm, 1999; Singh & Dey, 2012; van Beelen & van Delden, 2012; Wang *et al.*, 2009). Our visual range would be about 300 km (Jacob, 1999) in the absence of aerosols in the atmosphere. As a result, it is reasonable to say that visibility across a region serves as a robust and trustworthy proxy for air pollution

(Founda *et al.*, 2016; Singh *et al.*, 2020). Reduced atmospheric visibility is caused by tiny particulate matter (PM), especially fine-mode PM, and water droplets suspended in the atmosphere, which scatter and absorb visible light spectrum (Che *et al.*, 2007; Chen & Xie, 2013; Doyle & Dorling, 2002; Fu *et al.*, 2014; Hu *et al.*, 2017; Luan *et al.*, 2018; Schichtel *et al.*, 2001; Sloane *et al.*, 1991). Seinfeld and Pandis (2016) claim that the main causes of reduced visibility are aerosol absorption and scattering by anthropogenic emissions.

How aerosols affect visibility is quite intricate. They rely on several physical and chemical characteristics of aerosols (Dayan & Levy, 2005; Sequeira & Lai, 1998), like, as concentration, size distribution, chemical composition, and hygroscopic growth factor by aerosol water (Pitchford *et al.*, 2007; Watson, 2002). Particle number-size distribution, followed by their refractive indices and shapes, is the most significant element in influencing light extinction by aerosol under dry ambient conditions (Charlson *et al.*, 1992; Covert *et al.*, 1972). The aerosol concentration is governed by the strength of the emission source and meteorology (Dayan & Levy, 2005; Sequeira & Lai, 1998; Sloane, 1983, 1984; Tsai *et al.*, 2007; Vautard *et al.*, 2009). Watson (2002) states that the extinction of light by air pollutants and its subsequent effects on visibility vary based on the abundance of air pollutants in the atmosphere and their mixing state. Sulfates, nitrates, organics, ammonium, and minerals primarily scatter light; in contrast, elemental carbon mainly absorbs visible light. Their relative contribution varies spatiotemporally depending on their sources and other atmospheric processes primarily reliant on meteorological differences (Hand *et al.*, 2019; Seinfeld & Pandis, 2016). The primary causes of the decline in visibility in different forms are the primary aerosols and precursors of secondary aerosols, such as ammonium, nitrate, sulfate, organic carbon, etc., released by different emission sources in the atmosphere (Hu *et al.*, 2017; Luan *et al.*, 2018; Quan *et al.*, 2011; Vautard *et al.*, 2009).

Some of the recent studies (e.g., Wang *et al.*, 2019) have stated that the association between air pollution concentration and visibility is negative linear at low ($PM2.5 < 50$ $\mu g/m^3$) and negative exponential with increasing pollution concentration levels. This quantitative relationship between them changes with variation in relative humidity (Fu *et al.*, 2016; Liu *et al.*, 2019). When both RH and air pollution concentration are low, visibility is mainly affected by the latter (Liu *et al.*, 2019; Wang *et al.*, 2019), i.e., when $RH < 60\%$, visibility is mainly affected by fine aerosol mass concentration. However,

the effect of RH becomes dominant at high RH (Rh > 60%) which is more prominent at low than high aerosol concentrations (Fu *et al.*, 2016; Liu *et al.*, 2019).

2.1.2 Meteorology

2.1.2.1 Aerosol water, wind, and ambient temperature

The role of RH in visibility is very important (Chen & Xie, 2013; Larson & Cass, 1989; Malm, 1999; Tang, 1996; Zhang *et al.*, 2010). As RH increases, hygroscopic aerosols uptake the ambient water via adsorption and absorption and grow in volume, size, and weight, eventually changing the overall particle composition. As a result, aerosols have an increased effective cross-section and a decreased refractive index. This is because water typically has a lower refractive index than common aerosol constituents (Harrison *et al.*, 2004) do. Therefore, as RH increases, the size distribution and mass concentration of aerosols in the atmosphere are drastically altered, changing the optical characteristics of the atmosphere and raising the extinction coefficient (Malm & Day, 2001; Randles, 2004). This, subsequently, results in visibility degradation (Chen & Xie, 2013; Deng *et al.*, 2016; Elias *et al.*, 2009; Liu *et al.*, 2012; Qu *et al.*, 2015; Zhang *et al.*, 2010).

With the same level of aerosol mass concentration, surface visibility worsens with higher RH (Malm & Day, 2001). Similarly, some studies (Eck *et al.*, 2008; Smirnov *et al.*, 2002) have suggested that an increase in aerosol optical depth (AOD) is also associated with an increase in total column water vapor content (CWV). During the severe haze episodes in Beijing in January 2013, a different study (Bi *et al.*, 2014) found a strong positive correlation between CWV and AOD, which they attributed to the formation of large accumulation mode particles by coagulation through condensation and gas-to-particle-conversion process. Jung *et al.* (2009) evaluated the contribution of aerosol water content to light extinction. They discovered that the increase of $(NH_4)_2SO_4$ and $NH_4\,NO_3$ was the main cause of the effect of aerosol water content on light extinction and visibility impairment in the Pearl River Delta region.

Similarly, high ambient temperature enhances the atmosphere's dispersion capability through mechanical and thermal turbulence (Du *et al.*, 2013), thereby improving visibility and air quality. On the contrary, the lower temperature does the opposite—a shallow mixing layer, disrupts circulation and vertical dispersion of air pollution (Ribeiro

et al., 2018). Moreover, temperature has a significant impact on the atmosphere's production of secondary organic aerosols (Singh *et al.*, 2017).

The wind carries horizontal transport of aerosols and trace gases from the source to the downwind region, affecting their concentration in both places. In other words, wind determines the origin, horizontal transport, and total concentration of air pollution (Founda *et al.*, 2016). It is the WS, which defines the horizontal transport rate. The windy condition leads to the cleaning effect of the atmosphere by replacing polluted air with cleaner air thereby improving visibility. However, visibility of the downwind region worsens because of the influx of air pollution from the source region, if the latter is polluted. This is not always the case; especially when strong wind blows over bare, arid, and semi-arid regions, the strong wind lifts large amounts of dust and sand from the bare surface to the earth's atmosphere obscuring the sky, e.g., during dust and sand storm in deserts (**Figure 5**). Thermally generated wind circulation (e.g., sea-land breeze, katabatic, anabatic wind) may influence local RH, temperature, and aerosol load at a site (Liu *et al.*, 2022; Tsai *et al.*, 2011).

Figure 5: Reduced Visibility by dust storm in Mitiga International Airport at Tripoli, Libya, Africa on March 19, 2022

2.1.2.2 Planetary boundary layer

Aerosols directly emitted from air pollution sources are typically trapped within the PBL, which results in high near-surface concentrations. Sun *et al.* (2013) noticed a

higher PM2.5 concentration at the bottom of a 325 m-tall tower in Beijing than at its top. Numerous studies (Boyouk *et al.*, 2010; Chou *et al.*, 2007; Mues *et al.*, 2017) have found an anti-correlation between the diurnal variation of air pollutants and PBLH. PM2.5 concentration at night was nearly twice the afternoon value in China as found by (Zhang & Cao, 2015, p. 2).

Interaction among aerosol, solar radiation, PBL structure, and prevailing meteorological conditions involve numerous complexities and uncertainties (Luan *et al.*, 2018). Black carbon (BC) aerosols can absorb solar radiation, change the vertical temperature profile, and stabilize the PBL structure, as per a study by Ding *et al.* (2016). By reducing solar radiation, aerosol enhancement in the atmosphere also tends to suppress PBL growth. The repressed structure of PBL therefore inhibits the diffusion of air pollution, leading to high levels of air pollution (Liu *et al.*, 2007; Quan *et al.*, 2013).

After analyzing more than four decades of data (1961–2003) in Southern Taiwan, Tsai (2005) reported the negative effect of low mixing layer height (MLH), slower WS, and high atmospheric pressure on visibility. In their study (urban Hong Kong, 1990–1992), Sequeira & Lai (1998) found that MLH is the most important meteorological variable affecting visibility. The local geography, weather, season, and time of day all have a significant impact on the PBL structure (Guo *et al.*, 2016; Zhang *et al.*, 2013). Because of such complexities, the accurate determination of PBLH is quite problematic (Seidel *et al.*, 2010) and no unique definition or criterion exists for doing so (Li *et al.*, 2021; Seibert *et al.*, 1998, 2000).

2.1.2.2.1 Estimating boundary layer height from radiosonde observation

Despite its great importance, we cannot directly measure PBLH. It is usually determined based on measured or modeled profiles of the atmospheric state (Beyrich & Leps, 2012). Because of its strong anti-interference capabilities and high detection accuracy, radiosondes (RS) are one such typical profile measuring device that is frequently used to calculate PBLH (e.g., Guo *et al.*, 2022; Holzworth, 1964; Seidel *et al.*, 2010, 2012). Some of the commonly used methods for the retrieval of PBLH are:

i. bulk Richardson's number (RM) (Aryee *et al.*, 2020; Collaud Coen *et al.*, 2014; Guo *et al.*, 2016),

ii. parcel method (PM) (Collaud Coen *et al.*, 2014; Li *et al.*, 2021),

iii. potential temperature gradient (GM_θ) (Aryee *et al.*, 2020; Guo *et al.*, 2016),

iv. relative humidity (RH) gradient (GM_{RH}) (Aryee *et al.*, 2020; Guo *et al.*, 2016),

v. the base of elevated temperature (T) inversion (Beyrich & Leps, 2012; Seidel *et al.*, 2010), and

vi. surface-based inversion (SBI) (Beyrich & Leps, 2012; Bradley *et al.*, 1993; Seidel *et al.*, 2010, 2012; Zhang *et al.*, 2021).

It is quite common for different methods to give a wide range of PBLH results (Beyrich & Leps, 2012; Seibert *et al.*, 2000; Seidel *et al.*, 2010). Therefore, a performance assessment of various algorithms is necessary to get a close estimate of PBLH (Krishnamurthy *et al.*, 2021).

2.2 Long-term trend: Use of visibility as a proxy to aerosol load

Due to many biases involved in observation procedures of visibility, many researchers have not agreed on its use as a viable atmospheric variable (Davis, 1991). While meteorological variables govern atmospheric visibility in an instant, a long-term trend in it is typically associated with the changes in the air pollution status of the place (Zhao *et al.*, 2011). Consequently, due to the fact that visibility observation has far longer records than direct measurements of air pollutants, there is growing interest in the use of visibility observation as a proxy to atmospheric aerosol load among scientific communities around the world (e.g., Zhao *et al*). In this line, many past studies—on a local, regional, or global scale—have used visibility observation to investigate spatio-temporal variation in the atmosphere's optical properties related to aerosol load and emission sources.

Globally, clear sky visibility over land decreased between 1973 and 2007, according to Wang *et al.* (2009). They ascribed it to global increases in aerosol emissions and the ensuing impacts on incident sun irradiance. Throughout the course of the investigation, they saw a significant drop in visibility over South America, Australia, Asia, and Africa. They also reported enhanced visibility, after the 1980s, in Europe, and attributed this to the effective implementation of air pollution-mitigation measures in Europe. Vautard *et al.* (2009) obtained similar findings in another study conducted in Europe,

which showed that the frequency of low-visibility days has significantly decreased since the 1980s and that this decline was both regionally and temporally linked with lower SO_2 emissions. Stjern *et al.* (2011) observed a notable increase in visibility (by 15 km) in previously highly industrialized areas of central Europe after a reduction in air pollution emissions from 1983 to 2008. In contrast, the previously clean area witnessed visibility raised only by 2.5 km. In numerous locations across the UK, Doyle and Dorling (2002) reported a noticeable improvement in visibility since the early 1970s; they attributed this to actions taken to mitigate air pollution. Likewise, since the early 1980s, the proportion of good days (days with visibility greater than 19 km) has nearly doubled in the Netherlands, according to Van Beelen & Van Delden (2012). These results for Europe are in line with the worldwide dimming/brightening period (Folini & Wild, 2011; Nabat *et al.*, 2013; Streets *et al.*, 2006), which is associated with a decrease or increase in surface solar radiation in Europe. In the past, several visibility studies were conducted in the USA and Canada when it was an important social issue, especially in the 1970s and 1980s. Miller *et al.* (1972) found a significant decline in summertime visibility at three non-urban airports in the USA. Similarly, Naegele and Sellers (1981) reported decreasing visibility in 18 cities in the USA from 1958 until 1972 and increasing from then until 1979. Malm (1999, p. 199) reported a declining summer visibility trend during 1940–1980 in the Southeast USA and attributed it to an increase in sulfur emissions. Studies in Canada (Inhaber, 1976; Munn, 1973) also report a substantial increase in summer haze at the airport stations of East Canada, from the mid-1950s to the early 1970s.

In contrast to the findings in Europe, a reduction in visibilities was reported by various similar studies conducted elsewhere in developing Asian countries (Che *et al.*, 2007; De *et al.*, 2001; Fu *et al.*, 2016; Ghim *et al.*, 2005; Hu *et al.*, 2017; Jaswal *et al.*, 2013; Singh & Dey, 2012; Wu *et al.*, 2012). Asia's nations, including China, India, and others, are dealing with severe air quality issues and the ensuing reduction in visibility as a result of their remarkably rapid economic expansion, rapid urbanization, expanding transportation networks, and steep rise in fossil fuel usage. In China, Wu *et al.* (2012) observed a declining visibility trend during the last 50 years and a strong association between AOD and horizontal surface visibility for the period 2000–2009.

Several past studies in India (Chandiramani *et al.*, 1975; De *et al.*, 2001; Mukherjee *et al.*, 1980; Padmanabhamurty, 1986) reported a considerable deteriorating visibility condition over a long period and identified atmospheric pollutants as a responsible factor. De *et al.* (2001) found that many Indian airports located in urban centers displayed a declining trend in surface visibility.

From 1961 to 2008, Jaswal (2013) examined a long-term trend (both temporal and spatial) in horizontal surface visibility at 279 stations throughout India. They reported overall declining visibility—annual morning poor visibility days (PVD, visibility < 4km) increased at the rate of 3.3% per decade while afternoon good visibility days (GVD, visibility > 10 km) declined significantly (−8.6% days per decade). Singh and Dey (2012) found a notable decline in visibility in Delhi, India, from 1980 to 2000, associated with aerosol load.

2.3 Winter fog

Fog—obscurity caused by the suspension of water droplets near the surface layer of the atmosphere—is a frequent occurrence during the night or early morning of the winter season. Atmospheric visibility is less than 1 km during fog events (World Meteorological Organization (WMO), 2023). Fog is described by Griffins *et al.* (1985) as suspended water droplets in the atmosphere at or near the surface of the earth within 10% of saturation. The opacity of the atmosphere and resultant visibility in foggy conditions is determined by the droplet concentration.

Fog, a very complex and interesting boundary layer phenomenon, occurrence, and persistence are dependent on numerous factors like meteorology, air pollution, land use, terrain, and topography (Gultepe *et al.*, 2007; Hunova *et al.*, 2020, 2021; Kim *et al.*, 2019; Safai *et al.*, 2019). Sometimes large-scale fog is driven by synoptic-scale circulation such as the passing of western disturbances like what happens during the formation of fog covering a very large area in the northern plains of South Asia, the Indo-Gangetic Plains (IGP).

The Cloud Condensation Nuclei (CCN) responsible for fog formation are aerosol particles released into the atmosphere by diverse sources of air pollution (Gultepe *et al.*,

2007). Some studies (such as Safai *et al.*, 2019) also reported having a mutually dependent two-way relationship between aerosol and fog, i.e., aerosol initially catalyzes the fog formation; however, fog droplets scavenge it when droplets grow in size.

Because of the high disruption potential of fog to general aviation, developing an intensity and duration-based fog microclimatic information system using long-term data is highly advantageous (Jenamani, 2012). This system benefits forecasters, air traffic controllers (ATC), airlines, and pilots by informing them about the vulnerability of airports under various fog conditions so that they can implement mitigation plans beforehand.

Using hourly visibility data collected at IGI for 25 years (1981–2005), Jenamani (2012) tried to build an intensity-based climatological fog information system for December and January. The author also computed consecutive duration and climatological timing of fog onset and dispersal for different fog intensities.

Various authors studied various aspects of winter fog occurrences over different places in India (Bhushan *et al.*, 2003; Singh *et al.*, 2007; Srivastava *et al.*, 2016), Nepal (Manandhar, 2006; Nakajima *et al.*, 1980; Shrestha *et al.*, 2018, 2023) and elsewhere (Hunova *et al.*, 2021; Liu *et al.*, 2012) using long-term weather data or satellite data. Because of the severity of the fog problem, most of the fog studies in our region focus on the occurrence of fog in cities and airports of IGP. Previous research (Saikawa *et al.*, 2019; Srivastava *et al.*, 2016; Syed *et al.*, 2012) has reported a significant rise in fog episodes in the area over time. Through the analysis of climatological data at Indira Gandhi International Airport (IGI) in New Delhi, India, Jenamani (2007) reported an alarming rise and persistence of fog at the airport. Another comprehensive study conducted by Ghude *et al.* (2017) at the same airport also supported it by finding that dense fog hours in the last three decades have doubled.

2.4 Visibility studies in Nepal

Rapid urbanization and population growth in big cities of Nepal, such as Kathmandu (the capital city), and Bhairahawa (the industrial city in the mid-western region) have already presented perceivable air quality and visibility problems. Kathmandu valley is usually blanketed with haze layers most of the time of year and the view of mountain ranges from the valley is obscured. Winter fog creates reduced visibility problems too.

Bhairahawa metropolis has witnessed an even worse fate in terms of visibility status. The aviation sector in both places has endured the adverse impact of worsening visibility over many years. Indeed, the degradation of visibility in Nepal is a multifaceted problem.

Despite the seriousness of the worsening visibility problem nationwide, dedicated visibility studies in Nepal are only a handful. Visibility has been regularly recorded in Kathmandu airport since 1969 (Larssen *et al.*, 1997). The first literature, we could trace back, on reduced visibility study in Nepal dates back to a winter fog study in Kathmandu (Nakajima *et al.*, 1980); in which, they investigated the mechanism of winter fog formation in the valley using photographs and meteorological data. Later in 1997, Sharma reported that fog covering the basin bottom often restricts visibility until 10 or 11 am in the valley. Winter fog in the valley increased and visibility decreased in recent decades, according to Larssen *et al.* (1997). The paper reported that the annual number of foggy mornings at the airport during November–February of 1969–1993 rose from 40 to 60; whereas, the number of days with visibility > 8 km at 11:00 am and noon in January dropped from 23 to just 1 and from 25 to 5 respectively, during the same period. The number of good visibility days at noon remained high from March through October. Visibility in November through February, starting early to mid-1980s, was declining with the largest decline taking place in December and January. They attribute the decrease in visibility at Kathmandu airport to an increased concentration of hygroscopic aerosols—including sulfate and organic aerosols—in the valley air. Sapkota (1996) and Kafle (1997) too known to have conducted a visibility study in Kathmandu; though, these works of literature are not available to us. Later in 2002, Sapkota (2002) investigated Kathmandu Valley's atmosphere by measuring the broadband light scattering coefficient as well as the extinction coefficient using Nephelometer and Telephotometer instruments. The author reported that the scattering coefficient in the valley displayed a distinct diurnal cycle especially in the winter season—with a morning high (~ 0900 LT) and late afternoon (~ 1600 LT) low, which was attributed to an increase in MLH (that allowed an increasing dilution of air pollutants) during daytime by strong solar insolation. Based on the spatial variation of the light extinction coefficient in the valley sector visibilities are lower towards the direction of highly populated areas, brick kilns, and heavy traffic (Sapkota, 2002). The

study also reported a declining visibility trend (1.58 km year^{-1}) in the valley by observing diurnal variation of average visibility for the years 1996, 1998, and 1999.

Moreover, we could find only one past literature (Shrestha *et al.*, 2018) examining visibility in winter at Bhairahawa—having a particular focus on fog occurrence. The paper investigated winter fog events across the southern plains of Nepal (namely, Nepalgunj, Bhairahawa, Simara, and Biratnagar airport) by analyzing historical climatological data spanning from 1980 to 2015 for November–February. They reported that average fog-day-frequency ranged between 24–56 days per year and fog hour ranged between 71–169 hr. They also observed declining winter visibility across the studied area. They also reported an increasing trend of fog parameters, viz., foggy/dense-foggy days, and foggy/dense-foggy hours, at 0.1 level of significance. About the IGP and the southern plains of Nepal, winter fog occurrences became a regular phenomenon in 1990, according to Manandhar (2006). In the Terai plains of Nepal, Baidya *et al.* (2008) observed a declining trend in the winter season's diurnal temperature range, which they linked to a rise in the frequency of fog episodes. On the other hand, Lumbini, a site near Bhairahawa airport, has witnessed a substantial volume of potentially relevant air pollution research in recent years. This comprises of identification of major air pollution sources (Islam *et al.*, 2021; Rupakheti *et al.*, 2018), their optical properties (Izhar *et al.*, 2021; Rupakheti *et al.*, 2018; Rupakheti, Kang, Rupakheti, *et al.*, 2018) and chemical characteristics (Tripathee *et al.*, 2017; Wan *et al.*, 2017), and temporal behavior (Rupakheti *et al.*, 2017).

2.5 Research gap

There are large holes in our understanding of visibility provided by earlier research and data. Past research leaves many questions not answered. Which weather type (e.g., fog, haze, mist, rain, etc.) is most responsible for reducing visibility at the airports? How is visibility changing in every season? What controls spatio-temporal variation of visibility? How may PM2.5 and AOD affect visibility? What is the role of PBLH on air pollution dilution and visibility? How do other meteorological variables—especially RH, and wind—affect local air pollution status and visibility? Is poor visibility a result of local air pollution sources or regional transport of air pollutants? How does winter fog behave, i.e., when does it form and dissipate, and how long does it last? How does changing visibility affect general aviation at these two major airports: TIA and GBIA?

Answering such questions requires a detailed analysis of a vast dataset, which forms the backbone of this thesis.

CHAPTER 3

MATERIALS AND METHODS

3.1 Background

This chapter provides a general description of the study area, various materials, and techniques used in this thesis work. It gives a detailed overview of different meteorological and air pollution data sets. Sources of data and corresponding analytical methods used for estimation of boundary layer height from radiosonde sounding in Kathmandu have been presented in detail, here, too. It also includes all other analytical methods and techniques used to meet the objectives.

3.2 Study area

Two of the international airports—Tribhuvan International Airport (TIA) at Kathmandu (KTM) and Gautam Buddha International Airport (GBIA) at Bhairahawa (BWA)—were chosen as the major sites. In addition, data from three neighboring airports situated in northern IGP, namely Gorakhpur (GOP), Lucknow (LKN), and Delhi (DEL) were gathered to gain a comparative understanding of visibility changes across the region. Geographic location details and some details of the used dataset are presented in **Figure 6** and **Table 2**.

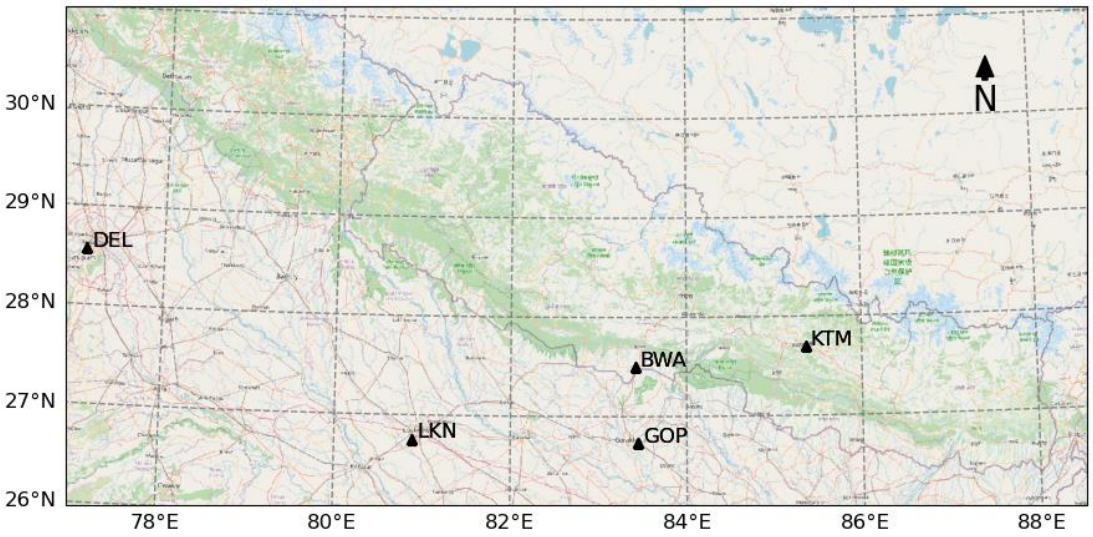

Figure 6: Geographical location of the study sites inside Nepal and India. Acronyms of site names and other details have been presented in **Table 2**

Table 2: Geographical information as well as additional climatological data details

NOAA Site ID.	Station	Location identifier	Country	Lat. (N)	Lon. (E)	Elev. (m)	Data availability
444380	Bhairahawa	BWA	Nepal	27° 30' 21.6"	83°24' 57.5994"	109.1	1977–2020
444540	Kathmandu	KTM	Nepal	27°41' 49.19"	85°21' 32.3994"	1338.1	1973–2020
423790	Gorakhpur	GOP	India	26°44' 22.95"	83°26' 58.9488"	78.94	1944–2020
423690	Lucknow	LKN	India	26°45' 38.14"	80°53' 21.6204"	124.96	1944–2020
421810	Delhi	DEL	India	28° 33' 59.4"	77°6' 11.1162"	236.82	1996–2020

NOAA station ID refers to the United States Air Force (USAF) unique catalog-station-number; Lat., Lon., Elev., m, N, and E stand for latitude, longitude, elevation, meters, North, and East respectively; Location Identifiers are the three-letter geocode given by the International Air Transport Association (IATA)

3.2.1 Kathmandu Valley

The bowl-shaped Kathmandu Valley is located in Nepal's mid-hills, between the Ganges lowlands to the south and the Tibetan plateau to the north (**Figure 7**). This valley is encircled by high mountains that range from 2000 to 2800 meters above mean sea level (amsl) with five mountain passes dipping down between 1500 and 1550 meters amsl (Panday & Prinn, 2009). The bowl-shaped topography of Kathmandu Valley makes it more vulnerable to air pollution by restricting airflow and ventilation of air pollution (Panday *et al.*, 2009; Panday & Prinn, 2009). There are four seasons in a year in Nepal's general meteorology, which is dominated by the Asian monsoon circulation (winter: Dec Jan Feb [DJF], pre-monsoon: Mar Apr May [MAM], monsoon: Jun Jul Aug Sep [JJAS], & post-monsoon: Oct Nov [ON]). In addition, large-scale synoptic features as well as mountain valley circulation (Panday *et al.*, 2009) influence the meteorology of Kathmandu Valley. Only during the monsoon season does the valley receive up to 90% of its yearly precipitation, which helps to maintain the valley's atmosphere comparatively clean through heavy convection and rain. Whereas, air pollution is a concern during the dry season and the rest of the months. The Kathmandu Valley's air pollution is mostly caused by changes in socioeconomic activity linked to air pollution emissions, such as exponentially increasing road traffic, and rapid urbanization.

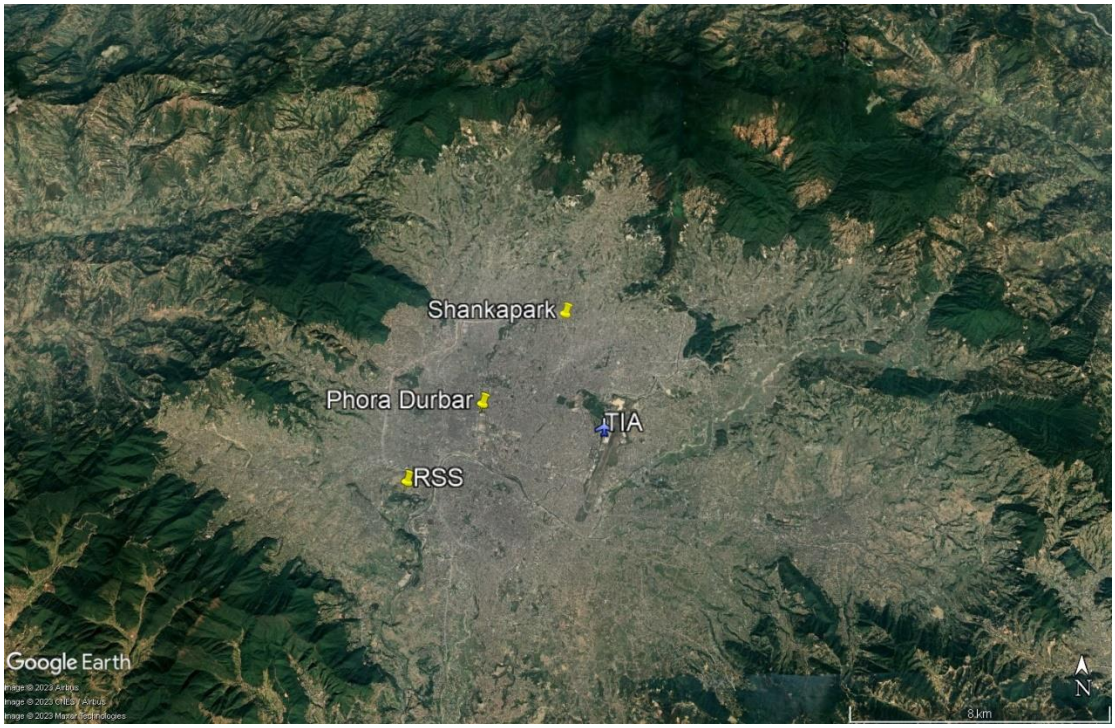

Figure 7: View of the Kathmandu Valley from above, showing locations of our sites: Tribhuvan International Airport (TIA), Phora Durbar, Shankapark, and Radiosonde Launch site (RSS) at Kirtipur (Google Earth Pro, 2023)

Research conducted in 2003 by Kitada and Regmi found that car emissions, which make up around 60% of all emissions in the valley, are the main source of CO. Similarly, air pollution in the valley displays a distinct diurnal pattern according to previous studies. Distinct peaks of CO levels in the morning and evening are attributed to emissions from rush hour traffic and cooking activities (Panday & Prinn, 2009). Brick kiln emissions are one of the major contributors to CO emissions in the valley.

3.2.2 Bhairahawa

In this dissertation, meteorological records of the GBIA—located approximately 3 km west of downtown BWA city—were used as one of the important datasets. Located ~265 km to the west of Kathmandu, the capital city of Nepal, BWA is a municipal city and serves as the administrative center of the Rupandehi district (**Figure 8**, **Table 2**). BWA is situated on the northern border of the Indo-Gangetic Plain (IGP), a vast region spanning over 2000 km in northern South Asia that includes much of Bangladesh, eastern Pakistan, northern and eastern Indian Territory, and the southern portion of Nepal. One of the UNESCO World Heritage sites, the birthplace of Lord Buddha, is situated about 14 km west of the airport.

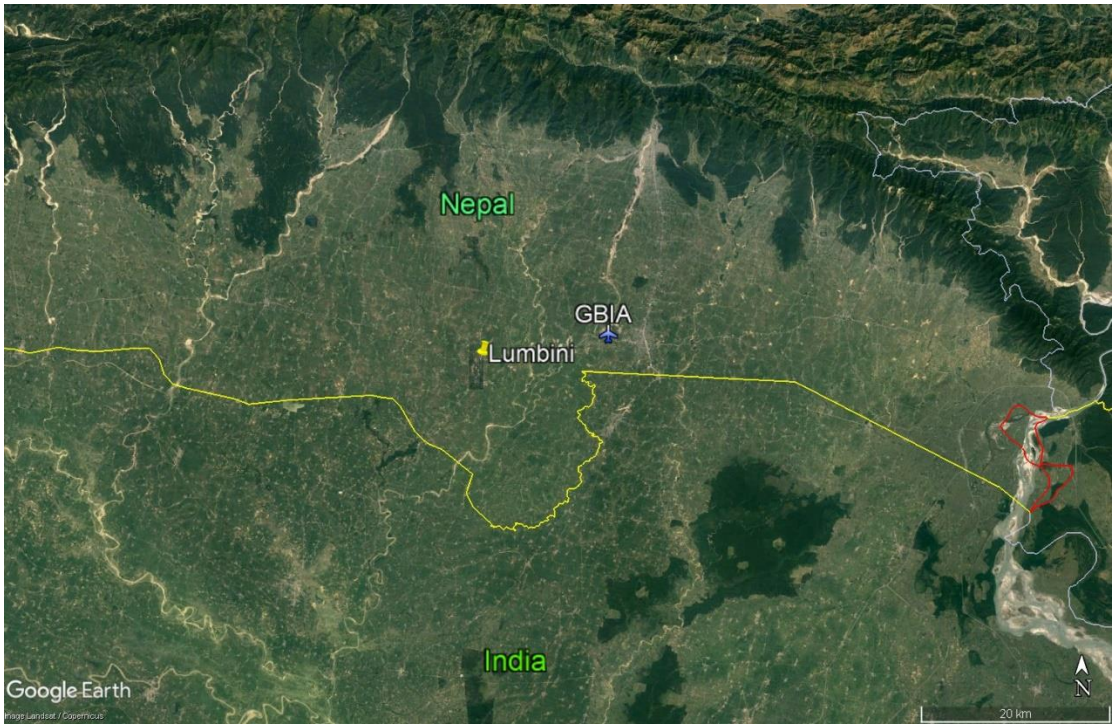

Figure 8: View of Gautam Buddha International Airport (GBIA) at Bhairahawa (BWA) from above, including AERONET and PM sites at Lumbini (PM and AERONET sites are very near to each other i.e., ~ 100 m apart). The yellow line marks the Indian-Nepal border (Google Earth Pro, 2023)

About 25 kilometers north of the city is the closest mountain foothill. The city is one of the larger industrial centers of Nepal. The Rupandehi district has a population of 11, 21,957, as per the results of the national census held in 2021 (National Statistics Office, 2021). The district's average annual growth rate between 2011 and 2021 was 2.4%. Near the city are numerous brick kilns, cement plants, pockets of villages, and a huge expanse of agricultural land. The Indian side of the area conjoining the city is densely populated; it contains agricultural fields and many industries too.

Through their study of wintertime air quality in Lumbini, Islam *et al.* (2021) identified a major source of PM2.5 OC as the burning of biomass (e.g., cow dung). Other contributors, in decreasing order, are plastic/garbage burning, vehicle emissions, coal combustion, and different types of Secondary Organic Aerosols (SOA). Rupakheti *et al.* (2017) also noted that during the study period (April–June 2013), average 24-hour PM2.5 and PM10 concentrations routinely surpassed WHO recommendations, putting the region's public health in danger. The authors attributed that to the burning of agricultural residue, local forest fires, and weather conducive to the transportation of air pollution to Lumbini. They also reported that more than half of Black Carbon (BC) concentrations were contributed by fossil fuel burning. They identified that the Ganges

Valley's upwind region was the primary source of carbon monoxide (CO) through simulation employing the WRF-STEM model.

The IGP is now a region of local, regional, and international concern due to its status as a hotspot for air pollution (Ramanathan *et al.*, 2007; UNEP *et al.*, 2014; World Health Organization (WHO), 2016). Emissions from automobiles, industries, thermal power plants, biomass, and fossil fuels used in agriculture, burning crop residue, and forest fires are the primary causes of air pollution in the IGP and its surrounding areas (Rupakheti *et al.*, 2017). Western disturbances, or a sequence of alternating low- and high-pressure systems moving eastward, have an impact on the IGP region during the dry season. These disturbances provide the perfect environment for pollutants to accumulate within the boundary layer over several days, resulting in severe haze and fog (Gautam *et al.*, 2007; Hameed *et al.*, 2000).

Air pollution in this region is not limited to the area surrounding the emission source; it can be transported to a reasonably long distance away from the emission source and across the national boundary. Thus, to compare the findings of this study for BWA with other neighboring stations on the Indian side of the IGP region, we have used visibility records from airports at Gorakhpur, Lucknow, and New Delhi (Delhi). GOP, LKN, and DEL are located about 50 km south, 266 km southwest, and 632 km northwest of BWA respectively (**Figure 6** and **Table 2**).

3.3 Data

To meet the objectives, various datasets ranging from in-situ measurements, remote sensing, and reanalysis to satellites were used. Historical climatological data from both sites for the quantification of the trend of various parameters, e.g., annual, and seasonal trends were used. Various factors affecting visibility were also explored; their link with visibility was determined using this meteorological data covering certain times in conjunction with data on air pollution. Reanalysis data of air pollution and precipitation were also used to cater to the data gap in Bhairahawa. In Kathmandu, vertical profile data of different meteorological parameters by radio soundings (RS) were obtained and the boundary layer height was computed from the profile dataset.

3.3.1 Meteorological data

Department of Hydrology and Meteorology (DHM) in Nepal and the Indian Meteorological Department (IMD) in India routinely record and transmit weather observation at most of the major airports inside their territories—including the study sites—as a part of the Meteorological Terminal Air Report (METAR) or Surface Synoptic Observation (SYNOP). METAR is optimized for aviation use, whereas, SYNOP is intended for encoding detailed weather information of interest to synoptic analysis. The former is typically issued every hour/half-hour at the airports and the latter is issued every 3 hours at selected stations. Given the choice, METAR reports are preferred over SYNOP for scientific research due to their high sampling density and hourly/half-hourly transmission. National Climate Data Center (NCDC) in the USA stores such data and distributes quality-controlled data as a global hourly database (https://www.ncei.noaa.gov/maps/hourly/) under the data exchange protocol of the World Meteorological Organization (World Meteorological Organization (WMO), 1996). Such climatological data spanning more than four decades for most of the airport sites were collected through the global hourly-public-data-archive. The majority of records in BWA are SYNOP-type records; however, those in the rest of the study sites are of METAR type in general. BWA dataset contains daytime-only observations at 0000, 0300, 0600, 0900, and 1200 UTC. While, older recordings at KTM have coarse time resolution ranging from one to three hours, recordings since December 15, 2015, are further improved to every half-hourly resolution.

Precipitation values in the decoded data set were scarce and thus were disregarded and replaced with a reanalysis data product—ERA5 (European Centre for Medium-Range Weather Forecasts (ECMWF) Reanalysis v5). Hourly precipitation records since 1981 were collected from a public domain (https://cds.climate.copernicus.eu/) (**Table 3**).

3.3.2 Air pollution data

3.3.2.1 AERONET

Aerosol composition and their optical properties shall remain similar in two sites that share common geographical and meteorological features on a regional scale, but located some distances apart. In line with this, it was assumed that aerosol optical properties measured at Lumbini could well represent that at BWA despite the 14 km distance between them.

Table 3: Details of precipitation and air pollution data at Bhairahawa and vicinity

Station	parameter	Instrument/ Data Source	Lat. (N)	Lon. (E)	Elev. (m)	Data period
Bhairahawa	Precipitation	ERA-5 Reanalysis	27°30'21.6"	83°24'57.60"	109.1	1981–2020
Lumbini	AOD	CIMEL Sun-photometer/ NASA-AERONET	27°29'24"	83°16'48"	110.0	2012–2018
PM2.5 site at BWA	PM2.5	GRIMM EDM 180/ Department of Environment and ICIMOD	27°29'22.3"	83° 16' 44.7"	110.0	April–Dec 2019
Bhairahawa area	PM2.5	MERRA-2 Reanalysis	bounding box (82° 14' 25.8" E, 26° 30' 57.6" N, 84° 57' 54.36" E, 28° 3' 14.76" N), spatial resolution (0.5 ° × 0.625 °)			Jan 1980 –Feb 2020

For a better understanding of the aerosol impact on visibility at BWA, AOD time-series (level 1.5, version 3, cloud screened, and quality-controlled data) were collected for 2012–2018 from the nearest available NASA Aerosol Robotic Network (AERONET) site of Lumbini that is available through public archive: http://aeronet.gsfc.nasa.gov/. The NASA AERONET collaboration offers globally distributed observation on spectral AOD, precipitable water in diverse aerosol regimes as well as inversion products. The sunphotometer measures direct sun irradiance and sky radiance in a total of 9-spectral channels (340, 380, 440, 500, 675, 870, 940, 1020, and 1640 nm) to determine optical properties (e.g., scattering and transmission) of the atmosphere (Giles *et al.*, 2019). However, spectral channel 940 nm is not used for AOD measurement.

3.3.2.2 Mass concentration of fine and coarse particulate matter

An in-situ measurement of PM2.5 at the nearest available location to BWA airport was also used (**Table 3**). The Government of Nepal in collaboration with the Department of Environment, and the International Center for Integrated Mountain Development (ICIMOD) manages the site and the public domain (https://opendatanepal.com/dataset/realtime-air-quality-datasets) provides measured data. To gain a better understanding of the interplay among visibility, PBLH, and air pollution status over the Kathmandu valley, routinely measured hourly-average PM2.5 time-series of a nearby location—the US State Department Station at Phora Durbar (located 4.22 km west of TIA) (**Table 4**), Kathmandu—were gathered from a centralized data system maintained by AirNow (www.airnow.gov). In partnership with

various other agencies, AirNow offers quality-controlled data from US diplomatic missions around the world openly accessible to the public. A standardized instrument, MetOne BAM 1020, which uses the beta ray attenuation method for the measurement, records PM2.5 at the station. Since PM10 and PM2.5 stations were not collocated, simultaneous in-situ measurements of particulate concentration (both PM 2.5 and PM10) from a site (Shankapark, **Table 4** and **Figure 7**) situated about 4.15 km northwest of TIA were used while finding extinction coefficient, mass extinction efficiency, and hygroscopic growth factor at TIA.

3.3.2.3 PM2.5 reanalysis data (MERRA-2)

Monthly average PM2.5 reanalysis-time-series (Jan 1980–Feb 2020) with a bounding box centered at BWA were collected from Modern-Era Retrospective analysis for Research and Applications version 2 (MERRA-2)—a NASA public domain (Global Modeling and Assimilation Office (GMAO), 2015, https://giovanni.gsfc.nasa.gov/giovanni). NASA atmospheric reanalysis product MERRA-2 replaced MERRA reanalysis and began in 1980 (Rienecker *et al.*, 2011). Using more recent microwave sounders, hyperspectral infrared radiance instruments, and other data types, this makes use of an enhanced version of the Goddard Earth Observing System Model, version 5 (GEOS-5, version 5.12.4) data-assimilation system (Bosilovich *et al.*, 2015). A detailed overview of MERRA-2 is available in (Gelaro *et al.*, 2017). Buchard *et al.* (2017) provide a detailed description of aerosol measurement techniques in MERRA-2.

Table 4: Details of radio sounding and air pollution data in Kathmandu

Station	Measured parameter	Instrument/Data Source	Lat. (N)	Lon. (E)	Elev. (m)	Data period
RSS launch site	Vertical profiles of T, RH, Pressure, etc.	Department of Hydrology and Meteorology	27° 40' 54.426"	85° 17' 22.5888"	1311	Nov 2019–March 2022
Phora Durbar	PM2.5	MetOne BAM 1020/ AirNow/ US embassy	27° 42' 20.16"	85° 18' 51.1194"	1301	2017–Mar 2022
Shankapark	PM2.5 &PM10	GRIMM EDM 180/ Department of Environment	27° 44' 4.452"	85° 20' 33.273"	1337	2019 – 2020

There is a notable difference in AOD values between NASA's pre-Earth Observing System (EOS) period (1980–1999) and post-EOS period (post-2000) due to difference in data coverage—despite best efforts to harmonize the observing systems with rigorous quality control (Randles et al., 2017; Yao et al., 2021).

3.3.3 Boundary layer height

3.3.3.1 Radio soundings data

Up to around 32 km in height, routine Radiosonde (RS) measurements offer a fine-resolution vertical profile of temperature (T), pressure (P), RH, WS, and WD. Because of their high operational cost, RS are generally launched only once or twice a day at 00:00 and/or 12:00 UTC from most of the RS launch stations around the world (Seibert *et al.*, 2000).

Department of Hydrology and Meteorology, Nepal launches routine RS soundings every early morning at 0000 UTC (0545 LT) from a site (marked by the name "RSS" in **Figure 7**) (**Table 4**) located inside the premises of Tribhuvan University at Kirtipur, Kathmandu (~6.76 km southwest of TIA). Near the launch site, there are a few university buildings and an agricultural scene in a suburban area with minimal traffic. The time resolution of the RS measurement is one second, which corresponds to approximately a constant height resolution of 6 to 12 m. The strict nationwide lockdown brought on by the COVID-19 pandemic, which began on March 24 and lasted on July 21, 2020, had an impact on DHM's RS launch. Thus, sounding data were only available for every alternate day from 24 March 2020 to 1 April and missing up until 20 November 2020. Measurements were not regular even afterward, with many missing days between two successive launches until 6 June 2021. Thus, there were only 460 days of data out of a total of 880 days of the study period.

3.3.3.2 Reanalysis data

Worldwide continental blended high-resolution PBLH dataset (https://zenodo.org/records/6498004#. Ysc1JezMJB0) covering the years 2017 to 2021 with a 3-hour resolution in space and time and a 0.25º resolution were collected. The dataset was created using a machine-learning technique. The boundary layer height estimated from radiosonde measurements served as the learning target for the machine-learning method,

which was configured using parameters provided by the NASA Global Land Data Assimilation System (GLDAS) and the ERA5 reanalysis as inputs. Once the model is trained, it is then used to predict PBLH in other grids across the globe with ERA5 and GLDAS input parameters: lower tropospheric stability, surface wind speed, and standard deviation of orography (extracted from ERA 5 reanalysis), latent and sensible heat flux, transpiration, evapotranspiration, downward long and short wave radiation, precipitation rate, near-surface pressure (extracted from GLDAS).

3.4 Methodology

As an initial step, a vast climatological dataset was processed rigorously with the help of programming languages: python and R. A classification scheme for various weather types was also customized, and the trend analysis was carried out using widely used statistical tools in our field. Then, the influence of optical properties and the hygroscopic effect of ambient aerosol on visibility were investigated. The applicability of different well-established techniques of finding boundary layer height was verified from radio-sounding data, and later validation of their performance was performed. Lastly, further implications of aerosol and meteorology on visibility were investigated; regression equations for visibility forecast in TIA were developed and validated. The onset and consecutive duration of winter fog and their implication for aviation were also studied in both of the sites. **Figure 9** illustrates the overall flowchart of the adopted methodology with major research inputs and outputs; succeeding subsections describe them in detail.

3.4.1 Meteorological data processing

Firstly, the entire encoded meteorological data were decoded in compliance with the decode procedures mentioned in the corresponding decoding manual (NCDC, 2010). Here, all the records where the variable of prime interest—visibility— was missing were omitted. Among many, only those weather types that affect visibility (e.g., haze, rain, fog, and mist) were decoded from the "present weather" feature of the dataset. These records do not have direct measurements of RH, one of the important meteorological variables of the study.

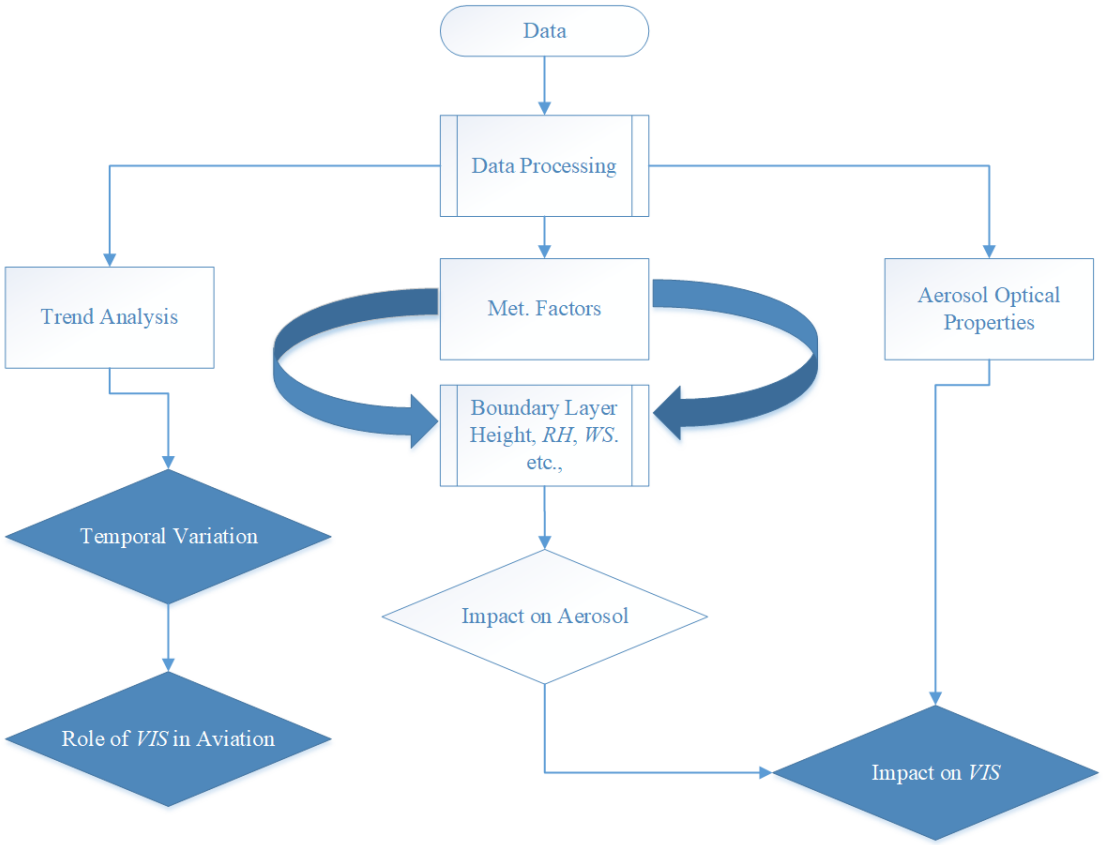

Figure 9: Schematic representation of entire methods used in this research with major inputs and outputs

With the help of the following formulas from other studies (Chang *et al.*, 2009; Chen *et al.*, 2012), RH time series were computed utilizing the available variables: surface air temperature (T (°C)) and dew point temperature (T_d (°C)) from the METAR/ SYNOP dataset

$$RH \approx 100\left(\frac{112 - 0.1T + T_d}{112 + 0.9\,T}\right)^8 \tag{18}$$

(Chang *et al.*, 2009)

3.4.2 Weather-types

Earlier studies have classified prevailing weather according to different thresholds of RH, precipitation, and visibility. However, there have been some overlapping conditions while transitioning from one to another condition. The following classification scheme has been followed in this thesis:

I. Poor-visibility event: visibility ≤ 5 km (Hu *et al.*, 2017) and precipitation = 0

II. Haze: visibility ≤ 5 km (Vautard *et al.*, 2009), RH ≤ 90% (Wu, 2006), and precipitation = 0 (Du *et al.*, 2013)
III. Mist: 1 km < visibility ≤ 2 km (Quan *et al.*, 2011; Vautard *et al.*, 2009), RH ≥ 90% (D. Wu, 2006), and precipitation = 0
IV. General-fog: visibility ≤ 1 km (Jenamani, 2012; Shrestha *et al.*, 2018; Vautard *et al.*, 2009), RH ≥ 90% (D. Wu, 2006), and precipitation = 0
V. Dense-fog: visibility ≤ 200 m (Shrestha *et al.*, 2018), RH ≥ 90%, and precipitation = 0
VI. Rain: precipitation > 0
VII. Normal: Other than all above

Meteorological data frequency was non-uniform across the study period—having fewer records in earlier than recent years. Thus, the use of percentage occurrence was opted over frequency, as done in some of the past pieces of literature (Hu *et al.*, 2017). Since BWA consisted of daytime observation only, the occurrence frequency refers to the daytime occurrence percentage.

Hourly occurrence frequency of each weather type at BWA was computed to identify and quantify their respective contribution over the study period. For this, firstly the time resolution of NCDC and ERA5 datasets were matched (approximated) to a common 3-hourly resolution. For analytical purposes, assumptions were made that a weather type observed in a particular recording persists from 1.5 h before to 1.5 h after the observation time. Lastly, the hourly occurrence frequency of a weather type was defined as the ratio of its total occurrence hours to the total occurrence hours of all-weather types combined.

3.4.3 Trend analysis

The annual occurrence frequency of any weather type defined in sub-section 3.4.2 for a considered temporal scale (e.g., season, year) is the percentage of total reported visibility observation in that year which fits respective criteria.

In the IGP region, widespread winter fog normally lasts from November to February. In this thesis, the terms ‘general fog’ and ‘fog’ were used interchangeably. As mentioned above, because of the coarse three-hourly time resolution of our data at BWA, it was assumed that if we observe a fog event in one observation, it could have persisted from 1.5 h before to after the observation timestamp. The occurrence frequency of fog/

dense fog is a percentage of total days (hours) in Nov–Feb that witness fog/ dense fog. Wintertime meteorological conditions in IGP offer one of the most favorable conditions for poor quality and poor visibility. To gain a comparative understanding of long-term change in visibility among northern IGP airports, all station's time series were resampled to match with that of BWA, i.e., daytime observation from 0000 to 1200 UTC.

3.4.3.1 Statistical tests

To investigate trend values of different meteorological variables from the decadal time series that we have, some of the widely used statistical tests, namely, the Mann-Kendell Test (MK Test) and Sen's Slope Estimator (Sen's Slope) were chosen. The interface to these tests is provided by the pyMannKendall package in Python (Hussain & Mahmud, 2019). The first test detects the trend and the second quantifies it. To compare their trend results with the well-known linear regression method, the Ordinary Least Square (OLS) regression test was employed from the Statsmodels Python package (Seabold & Perktold, 2010). The former two tests are effective tools for estimating the trend results from large time series with many missing values, errors, and outliers (Mann, 1945; Sen, 1968). Thus, to cater especially to the inhomogeneity in the large dataset with a lot of missing values, these tools were opted for—like many other researchers in the past (Kahya & Kalayci, 2004; Shrestha *et al.*, 2018; Tabari & Marofi, 2011; Van Belle & Hughes, 1984; Yue & Wang, 2004).

3.4.3.1.1 Mann- Kendall Test

MK Test is a well-established non-parametric tool for testing randomness against the trend in hydrological or climatological time series (Yue & Wang, 2004). According to this approach, the variable of interest has no linear trend over time (H_0), whereas the alternate hypothesis (H_1) holds that there is a linear trend. The following formulas provide the Mann-Kendall Statistics (S), its variance ($VAR(S)$), and, lastly, the standardized test statistics (Z_{MK}) (Ahmad *et al.*, 2015; Shrestha *et al.*, 2018).

$$S = \sum_{i=1}^{n-1} \sum_{j=i+1}^{n} sig\left(X_j - X_i\right) \tag{19}$$

$$sig(X_j - X_i) = \begin{cases} +1 \; if(X_j - X_i) > 0 \\ 0 \; if(X_j - X_i) = 0 \\ -1 \; if(X_j - X_i) < 0 \end{cases} \quad (20)$$

$$VAR(S) = \frac{1}{18}\left[n(n-1)(2n+5) - \sum_{p=1}^{q} tp\,(t_p - 1)(2t_p + 5)\right] \quad (21)$$

$$Z_{MK} = \begin{cases} \dfrac{S-1}{\sqrt{VAR(S)}} & if\ S > 0 \\ 0 \quad if\ S = 0 \\ \dfrac{S+1}{\sqrt{VAR(S)}} & if\ S < 0 \end{cases} \quad (22)$$

Here, n indicates the duration of observation, t_p indicates the number of ties corresponding to the pth value, and q indicates numerous tied values. X_i and X_j are time series observations of variables of interest X, in chronological order. Positive value of Z_{MK} stand for upward trend, negative means declining and zero value indicates not having any trend. If $|Z_{MK}| > Z_{1-\alpha/2}$ or p-value < significance level (α), H_0 is rejected. The critical value of $Z_{1-\alpha/2}$ (at $\alpha = 0.05$) is 1.96 from the standard normal table.

3.4.3.1.2 Sen's Slope estimator

This non-parametric test considers a linear equation of trend line as:

$$f(t) = Qt + B \quad (23)$$

(Sen, 1968)

Here, t is *the* variable of interest; Q is the slope and B represents the intercept; and ith value pair's slope in the distribution is given by:

$$Q_i = \frac{x_j - x_k}{j - k} \quad (24)$$

(Sen, 1968)

Where, x_j and x_k are observation at time j and k in chronological order.

The median value of all Q_i, which is the necessary Sen's slope estimator, is as follows:

$$Q = \begin{cases} Q_{\frac{N+1}{2}} \ when, & N\ is\ odd \\ \frac{1}{2}\left(Q_{(N)/2} + Q_{(N+2)/2}\right) when, & N\ is\ even \end{cases} \quad (25)$$

(Sen, 1968)

Here, Q assumes zero, negative, or positive values representing no, decreasing, and increasing trends over time respectively.

3.4.3.1.3 Ordinary least squares (OLS) regression

OLS, a parametric test, is the most common and powerful statistical method when it comes to estimating trends in time-series data (Hess *et al.*, 2001). Nevertheless, there are some prerequisites, like, non-autocorrelation, normality, and homoscedasticity of residuals before applying this method (Helsel & Hirsch, 1992). This method looks for a linear trend by analyzing the following relationship between the time *t* and the variable of interest *X*:

$$X_i = \beta_0 + \beta_1\, t_i \, + \varepsilon_i \quad (26)$$

Where, X_i corresponding to time t_i with $1 \leq \ i \ \leq n$, and n as the length of time series; β_0, β_1 and ε_i represent intercept, slope, and random error, respectively. The errors are considered independent and identically distributed.

For a given value of *t*, the fitted line gives the corresponding predicted value of *X;* it minimizes the sum of squared error (difference between predicted and observed values in y-direction). Thus, the intercept and slope of the regression line are:

$$\hat{\beta}_0 = \hat{X} - \beta_1 \hat{t} \quad (27)$$

And,

$$\hat{\beta}_1 = \frac{\sum_{i=1}^{n}(t_i - \hat{t})(X_i - \hat{X})}{\sum_{i=1}^{n}(t_i - \hat{t})} \quad (28)$$

Where, $\hat{X}$ and $\hat{t}$ denote expected values of response and predictor variable respectively.

Similarly, the following equation gives the standard error or the regression line's slope.

$$se(\hat{\beta}_1) = \sqrt{\frac{\sum_{i=1}^{n}(X_i - \hat{\beta}_0 - \hat{\beta}_1\, t_i)^{\,2}}{(n-2)\sum_{i=1}^{n}(\,t_i - \hat{t})^{\,2}}} \quad (29)$$

This model tests a null hypothesis.H_0: $\beta_1 = 0$ using t-statistics (t_s) with n-2 degree of freedom.

$$t_s = \frac{\hat{\beta}_1}{se(\hat{\beta}_1)} \tag{30}$$

If $t_s >$ critical value of two-tail t-distribution at a level significance level (α) or, p-*value* $< \alpha$, or, $0 \notin (\hat{\beta}_1 \pm t^*_{[\alpha,n-2]}\, se(\hat{\beta}_1))$, H_0 is rejected; where, $t^*_{[\alpha,n-2]}$ represents t^*multiplier at the significance level (α) and n-2 degree of freedom.

3.4.4 Relationship between air pollution, aerosol water, and visibility

Firstly, Ångström exponent (AE) (α) between two spectral channels: 340 and 1020 nm were computed using the below-given formula as used by previous works of literature (Kumar *et al.*, 2020; Liu *et al.*, 2012):

$$AE = -\frac{\log(^{AOD_{340}}/_{AOD_{1020}})}{\log(^{340}/_{1020})} \tag{31}$$

(Kumar *et al.*, 2020)

Afterward, to compute AOD at 550 nm—the wavelength in the visible spectrum that is most sensitive to human vision—from AOD at 500 nm the following formula (Nabat *et al.*, 2013) was used:

$$AOD_{550} = AOD_{500} \left(\frac{550}{500}\right)^{-\alpha} \tag{32}$$

(Kumar *et al.*, 2020)

AOD—a measure of the attenuation of sunlight (photon) while passing through a vertical/ slant atmospheric column—is a vertical entity. Contrarily, visibility is horizontal. Nevertheless, many previous studies (e.g., Bäumer *et al.*, 2008; Founda *et al.*, 2016) have attempted to explore the relationship between them.

From the definition of AOD (τ),

$$\tau = \int_0^{z_i} b_{ext}\, dz \tag{33}$$

(Bäumer *et al.*, 2008)

Where, z represents mixing layer height. Similar to the previous researchers (e.g., Bäumer *et al.*, 2008; Founda *et al.*, 2016), it was also assumed that the mixing layer (specified by height z_i) traps all the aerosols in the atmosphere above a site and the extinction of light is uniform across it.

Combining equation **(33)** with the working formula of visibility, i.e., Koschmieder relation given by equation (1) yields the required functional relationship between visibility (VIS*)* and AOD (τ) as

$$VIS = 3.912\, z_i\, \tau^{-1} \tag{34}$$

(Bäumer *et al.*, 2008)

Additionally, an effort was made to look into how RH and AOD together affect visibility. The feedback among visibility, RH, and PM 2.5 was also looked upon.

3.4.5 Estimation of boundary layer height

It is not possible to measure the mixing layer height (MH/MLH) or, more accurately, PBLH using conventional meteorological methods. According to Seibert *et al.* (2000), the metric in question lacks specificity and presents challenges in both definition and estimation. Radiosoundings are one of the most common data sources for the operational evaluation of MH. Sounding data are taken only once or twice daily at most of the stations at specified synoptic times (0000 UTC, 1200 UTC). The horizontal displacement of sonde can reach up to 200 km. To neglect the effect of horizontal displacement of RS and avoid confusion with free tropospheric features for the top of PBLH different researchers have limited the highest PBLH estimates to slightly different heights. For instance, Seidel *et al.* (2010) and, Wang and Wang (2014) used 4 km; Collaud Coen *et al.* (2014) used 3.5 km (corresponding to ~12 minutes of balloon ascent); Beyrich *et al.* (2012) used 3 km as the highest limit of PBLH. In line with this, analysis of RS profiles was limited up to 3 km into the atmosphere. PBLH estimates exceeding 3 km were also omitted. In line with the findings of Li *et al.* (2021), any RS readings that had a nearby height difference of more than 200 meters were eliminated to increase the accuracy of the results. Since RS data used in this study acquired the PBL profile in the early morning (0545 LT) only, vital boundary layer profile information was lacking for the rest of the day, especially, the convective mixing layer at noon.

3.4.5.1 Boundary layer classification

At first, boundary layer types that may have existed during the radiosonde launch were identified by examining the RS profile. PBL structure is classified, according to its thermodynamic properties as mentioned in sub-section 1.7.2.2., by evaluating the difference in potential temperature (PTD) between different sample points of an RS profile (Li *et al.*, 2021; Liu & Liang, 2010; Zhang *et al.*, 2018) such that

PTD_{5-2} > 0.1 K & PTD_{3-1} > 0 ⇒ SBL (H. Li *et al.*, 2021)

PTD_{5-2} < - 0.1 K ⇒ CBL (H. Li *et al.*, 2021)

Rest ⇒ NBL (H. Li *et al.*, 2021)

In the RS profile data, the PTD between the third and first sample points is denoted by PTD_{3-1} and the PTD between the fifth and second sample points from the earth's surface by PTD_{5-2}.

3.4.5.2 Boundary layer estimates

Because of various complexities, the accurate determination of PBLH is quite problematic (Seibert *et al.*, 1998; Seidel *et al.*, 2010; Stull, 1988) and no unique definition or criterion exists for doing so (e.g., Li *et al.*, 2021; Seibert *et al.*, 1998, 2000). Different methods use different algorithms to estimate PBLH from the profiles directly measured by RS or profile of parameters deduced from RS profile data. The right choice of approach relies on several variables, including the boundary layer type and time of day. It is quite common for different methods to yield a wide range of PBLH estimates (Beyrich & Leps, 2012; Seibert *et al.*, 2000; Seidel *et al.*, 2010). Therefore, a performance assessment of various algorithms is necessary to get a close estimate of PBLH (Krishnamurthy *et al.*, 2021). We can anticipate the presence of surface-based inversion, a definite sign of SBL, in most of the situations because the RS data was obtained from the early morning launch. Thus, the following three widely accepted *T*-profile-based methods were used.

3.4.5.2.1 Bulk Richardson's number method (RM)

The dimensionless ratio of turbulence creation by wind shear to turbulence suppression by buoyancy is known as the bulk Richardson number (Ri) (Seidel *et al.*, 2010, 2012). This method of estimating PBLH was originally proposed by (Vogelezang & Holtslag,

1996) and is believed to be applicable for both stable (Zhang *et al.*, 2021) and convective boundary layers. This method is independent of the vertical resolution of soundings. The bulk Richardson number (Ri) is given by

$$Ri\ (z)\ =\ \frac{(g/\langle T_v\rangle)(\ \theta_{vz}-\ \theta_{vs})(z-z_s)}{(u_z-\ u_s)^2+\ (\ v_z-\ v_s)^2\ +(bu_*^2)} \tag{35}$$

(Wallace & Hobbs, 2006)

Where *s* is the surface of the radiosonde launch, θ_v is the virtual potential temperature, $\langle T_v\rangle$ is the average virtual temperature across the layer Δz, u and v are components of wind speed, b is a constant, and u_* is the surface friction velocity. Finally, z is the height. From the RS data u_* is not known. Thus, $b=0$ is set, neglecting the effect of surface friction as is done in the work of Seidel *et al.* (2012) and Vogelezang & Holtslag (1996).

The primary PBLH metric is the lowest level (z) at which interpolated (Ri) crosses a critical value (Ri_c). Different literatures have proposed different values of Ri_c, typically between 0.2 and 1.0. Higher values can also be found in some works (Seibert *et al.*, 1998; Stull, 1988). According to the study by Stull (1988), the choice of Ri_c depend on the characteristics of the data being analyzed (e.g., the vertical resolution, measured vs. modeled profile, etc.). Collaud Coen *et al.* (2014), however, found that the estimate of PBLH is mostly unaffected by the precise threshold value. In this study, two different critical values 0.22 for unstable (convective) and 0.33 for stable conditions respectively, have been used, similar to the previous works (e.g., Collaud Coen *et al.*, 2014; Jeričević & Grisogono, 2006; Szintai, 2010).

Firstly, Ri profile were computed from the vertical profile of θ_v, u, and v; setting $b=0$ and estimate $z(Ri_c)$ by scanning the Ri profile upward from the surface. If the boundary layer were CBL or NBL, the first level with $Ri \geq Ri_c$ were identified. A linear interpolation between this layer and the adjacent upper level was carried out. The average height of these two consecutive layers provides the required estimate of (Ri_c), i.e., the PBLH.

During night, Ri at the ground level might be greater than Ri_c because of a stable θ profile, which introduces complexities in detecting PBL by this method (Collaud Coen *et al.*, 2014). For SBL cases, the profile of Ri is just opposite to that of convective

cases—the highest near the ground. Thus, to find the PBLH, this method was improvised by finding a first level at which $Ri \leq Ri_c$. Like in CBL/NBL cases, the average height of this layer and a layer just above it gives the required PBLH estimate. Low-level cloud—even when exists during the particular sounding—has not been considered in the analysis. This method was used for estimating PBLH from all sounding profiles irrespective of their classification.

3.4.5.2.2 Gradient of potential temperature method (GM_θ)

Profile of the potential temperature (θ) (in Kelvin, K) indicates static stability of the atmosphere and significantly affects the diffusion of air pollutants (Wang & Wang, 2014). It is one of the basic atmospheric parameters and is given by

$$\theta(z) = T(z).\left(\frac{p_s}{p(z)}\right)^{0.285} \tag{36}$$

(Wallace & Hobbs, 2006)

Where z is the geometric height, T is the air temperature (in K), p is the air pressure (in hPa), and index "s" indicates the surface value.

When there is convection, the highest vertical gradient in potential temperature signals a change in temperature from the less stable layer below to the more stable layer above. It is defined as the average height of that layer between subsequent RS data points where the potential temperature gradient $\left(\frac{\Delta\theta}{\Delta z}\right)$ attains its maxima. It gives the estimate of PBLH and is one of the most common operational methods.

Nonetheless, there is a transition between a stable surface layer and a neutral residual layer in the atmosphere when surface-based inversion occurs. In such a case, the top of the SBL (SBL_{tp}) also gives the estimate of PBLH that can be detected by vanishing θ gradient $\left(\frac{\Delta\theta}{\Delta z} = 0\right)$ (Collaud Coen *et al.*, 2014).

Thus, from the gradient of potential temperature $\left(\frac{\Delta\theta}{\Delta z}\right)$ profile, the first height in the profile at which $\left(\frac{\Delta\theta}{\Delta z} \leq 0\right)$ have been checked. The average height between this level and the adjacent level above it provides the required estimate of PBLH, in our case, stable boundary layer height (SBLH).

3.4.5.2.3 Surface-based inversion method (SBI)

A surface-based temperature inversion, when exists in RS measurement, is an obvious indicator of a stable boundary layer (SBL). Collaud Coen *et al.* (2014) reported that the residual layer (RL) height is retrieved by humidity and wind turbulence profiles; hence, the only way to determine the nocturnal steady boundary layer (SBL) height from the RS profile is through the vertical profile of temperature (T). In SBL cases, the top of the inversion layer (SBI_{tp}) marks the PBLH—more specifically, SBLH (Bradley *et al.*, 1993; Li *et al.*, 2021; Seidel *et al.*, 2010, 2012; Zhang *et al.*, 2021). Where, SBI_{tp} is the height of the surface-based temperature inversion layer after which T starts to decrease with the height, i.e., $\frac{\Delta T}{\Delta z} = 0$.

According to the study (Stull, 1988), turbulence decreasing from the surface upwards nearly ceases at SBI_{tp}. Whenever embedded isothermal layers occur, they have been considered as part of the overall inversion.

3.4.5.3 Inter-comparison and validation

Different techniques estimate PBLH differently since they employ different algorithms and PBL does not have a well-defined textbook structure. Inter-comparison and validation of different estimate techniques—T-profile methods—were performed on early morning PBLH at Kathmandu, on a set of 417 days of vertical profile data. Later, the performance assessment and validation were extended for ERA5 reanalysis PBLH on a set of 365 days of data. Surface-based temperature inversion was detected in 91.2 percent of the sounding profiles. Seidel *et al.* (2010) also firmly advocated the use of only the SBI method whenever surface-based temperature inversion exists in the soundings. Hence, the *SBI* method was picked as the reference method for the validation purpose because of its reliability and wider application while computing PBLH from SBL (or, SBLH). This comparison to the reference method allows us to estimate the reliability of the other methods.

While performing inter-comparison of the estimates yielded from different estimation techniques, various statistical metrics, such as Pearson's correlation coefficient (r) at 99% confidence interval, bias, mean absolute error (MAE), and root mean square error (RMSE) (**APPENDIX B**) were employed.

3.4.6 Influence of optical properties and hygroscopic effect of aerosol on visibility

The key to comprehending PM's impact on visibility in urban areas is to understand its optical properties, which are dependent on both ambient relative humidity and other intrinsic PM characteristics (Kotchenruther et al., 1999; Markowicz *et al.*, 2003). These properties are specific to certain atmospheric conditions (Cheng *et al.*, 2017). Therefore, knowing how RH and PM characteristics affect its optical properties is very helpful in getting accurate estimates for visibility impairment (Malm *et al.*, 1996; Pitchford *et al.*, 2007) and direct radiative forcing of ambient aerosols (Carrico *et al.*, 1998, 2000; Randles, 2004). Thus, we may better understand the impact of aerosols on visibility impairment by utilizing the extinction coefficient (b_{ext}), mass extinction efficiency (MEE), and extinction hygroscopicity (f (RH)) of PM2.5.

3.4.6.1 Extinction coefficient of PM2.5

The total extinction coefficient (b_{ext}, 550 nm) (Mm^{-1}) of PM2.5 in KTM were computed from the particulate mass concentration time series (PM2.5 & PM10) recorded at Shankapark (**Table 4**). As with earlier studies (e.g., Cheng *et al.*, 2017; Shin *et al.*, 2022), a modified Koschmieder formula was used for this, as follows

$$b_{ext}(PM_{2.5}) = \frac{3912}{VIS} - 0.6(PM_{10} - PM_{2.5}) - 10 - 0.33(NO_2) \quad (37)$$

(Cheng *et al.*, 2017)

The first term represents the overall extinction coefficient, which is derived from visibility (km) using the Koschmieder formula. The second term denotes the coarse particle extinction contribution, with PM2.5 and PM10 measurements expressed in $\mu g/m^3$. Likewise, the third term represents light extinction contribution by Rayleigh scattering of air molecules and the last term corresponds to absorption by ambient NO_2 molecules (ppb). Because of the unavailability of the NO_2 dataset in TIA matching the study period, its contribution was omitted as is done in previous works (e.g., Shin *et al.*, 2022).

3.4.6.2 PM2.5 Mass Extinction Efficiency (MEE) and Growth Factor

One important metric for calculating the light extinction intensity per unit mass concentration in the atmosphere is the mass extinction efficiency (MEE) of PM2.5 (Shin *et al.*, 2022). Cheng *et al.* (2017) state that the mass extinction efficiency and hygroscopic

growth factor (*f*(RH)) of PM2.5 are related to the ambient extinction coefficient in addition to the absolute values of mass concentration and relative humidity. The chemical composition and size distribution of PM2.5 predominantly influence these quantities, i.e., MEE and *f* (RH). The light extinction by ambient particulates is primarily related to hygroscopic deliquesce (Ding & Liu, 2014; Zhao *et al.*, 2019), while MEE is proportional to RH due to the enhancement of water absorption capability of aerosols (Hyslop, 2009; Liu *et al.*, 2011).

PM2.5 MEE (m^2/g) was estimated by dividing fine mass concentration (PM2.5) from its extinction coefficient—obtained from (**Eq. (37)**)—as:

$$MEE = \frac{b_{ext}(PM_{2.5})}{PM_{2.5}} \tag{38}$$

(Cheng *et al.*, 2017)

Similarly, the hourly average *f* (RH) of PM2.5 was calculated as the ratio of the extinction coefficient of PM2.5 at ambient RH ($b_{ext(wet)}(PM_{2.5})$) to that at dry conditions ($b_{ext(dry)}(PM_{2.5})$).

$$f(RH) = \frac{b_{ext(wet)}(PM_{2.5})}{b_{ext(dry)}(PM_{2.5})} \tag{39}$$

(Malm, 2016)

Here, $b_{ext(wet)}(PM_{2.5})$ is given by **Eq. (37)** while the $b_{ext(dry)}(PM_{2.5})$ is obtained by applying RH corrections to the former as previously done in the work of Hassoon *et al.* (2018). Following are the equations converting ambient to dry extinction coefficient:

$$b_{ext(dry)}(PM_{2.5}) = \frac{b_{ext(wet)}(PM_{2.5})}{0.85} \qquad RH \leq 30\% \tag{40}$$

(Hassoon et al., 2018)

$$b_{ext(dry)}(PM_{2.5}) = \frac{b_{ext(wet)}(PM_{2.5})}{0.05(RH - 30) + 0.85} \qquad 30 < RH \leq 40\% \tag{41}$$

(Hassoon et al., 2018)

$$b_{ext(dry)}(PM_{2.5}) = \frac{b_{ext(wet)}(PM_{2.5})}{0.05(RH - 40) + 0.90} \qquad 40 < RH \leq 50\% \tag{42}$$

(Hassoon et al., 2018)

$$b_{ext(dry)}(PM_{2.5}) = \frac{b_{ext(wet)}(PM_{2.5})}{0.05(RH - 50) + 0.95} \qquad 50 < RH \leq 60\% \qquad (43)$$

(Hassoon et al., 2018)

$$b_{ext(dry)}(PM_{2.5}) = \frac{b_{ext(wet)}(PM_{2.5})}{0.05(RH - 60) + 1.00} \qquad 60 < RH \leq 70\% \qquad (44)$$

(Hassoon et al., 2018)

$$b_{ext(dry)}(PM_{2.5}) = \frac{b_{ext(wet)}(PM_{2.5})}{0.03(RH - 70) + 1.05} \qquad 70 < RH \leq 75\% \qquad (45)$$

(Hassoon et al., 2018)

$$b_{ext(dry)}(PM_{2.5}) = \frac{b_{ext(wet)}(PM_{2.5})}{0.04(RH - 75) + 1.20} \qquad 75 < RH \leq 80\% \qquad (46)$$

(Hassoon et al., 2018)

$$b_{ext(dry)}(PM_{2.5}) = \frac{b_{ext(wet)}(PM_{2.5})}{0.05(RH - 80) + 1.40} \qquad 80 < RH \leq 85\% \qquad (47)$$

(Hassoon et al., 2018)

$$b_{ext(dry)}(PM_{2.5}) = \frac{b_{ext(wet)}(PM_{2.5})}{0.29(RH - 85) + 1.65} \qquad 85 < RH \leq 90\% \qquad (48)$$

(Hassoon et al., 2018)

Additionally, in line with earlier studies (Cheng *et al.*, 2017; Liu *et al.*, 2008; Zhang *et al.*, 2015), the relationship between f (RH) and RH was fit to an empirical convex function that characterizes the monotonic rise of f (RH) with RH (**Eq.(49)**).

$$f(RH) = a_0 + a_1\left(1 - {}^{1}/_{RH}\right)^{-1} + a_2\left(1 - {}^{1}/_{RH}\right)^{-2} \qquad (49)$$

(Deng *et al.*, 2016)

Where, the parameters a_0, $a_1$and a_2 were derived from the fitting of the curve.

3.4.7 Microclimatic properties of winter-fog

Because of its high damage potential to aviation, developing intensity-cum-duration based fog's micro-climatic information from multiyear data is highly advantageous (Jenamani, 2012). Various users like Air Traffic Controllers (ATC), pilots, airlines, and forecasters may benefit from such systems giving information about the persistence of fog, favorable time of formation and dissipation of fog, etc. They can understand the vulnerability of airports to different fog conditions and implement prior mitigation-measures, e.g., CAT- I/II/III ILS for runways (**APPENDIX A**), training ATCs and pilots, planning winter schedules, etc. In this research, the wintertime onset, dispersal timing, and consecutive duration of fog at KTM and BWA airports were investigated.

Depending on the coarse and uneven time resolution of the dataset, it was assumed that if a fog event were detected in a record, it would have persisted from half of the period (time resolution) before and after the timestamp of observation. For example, if the fog were observed in a half-hourly observation, it would have persisted from 15 min before to 15 min after the observation time. Consecutive duration of fog represents the cumulative period for a fog event of a given intensity. According to the previous assumption, an isolated fog observation could last for a period equal to or less than the time resolution of data during that period. On that basis, if we observe another same-intensity fog, then consecutive duration is the cumulative duration lasting less than double the time resolution, and so on. Its occurrence frequency (percentage) is the percentage of the total number of days with a given consecutive duration to a total of all fog days.

A fog observed in a record could have started any time before. When the same intensity fog is observed in the next record, the onset of the fog should be the first instance when it was recorded. Similarly, if a fog event were recorded earlier but not in the successive measurement, it could have dispersed anytime in between. The ratio of the number of fog onsets and dispersals during the study period to the total number of onsets and dispersals during the entire study period is their occurrence frequency.

CHAPTER 4

RESULTS AND DISCUSSION

4.1 Atmospheric visibility at BWA

4.1.1 Reduced visibility by different weather types

The occurrence frequency of different weather types, according to different visibility thresholds, at BWA from 1981 to 2020 has been shown in **Figure 10**. Among all, haze occupies the highest percentage (26.7 ± 0.3%) of the entire duration; fog accounts for (7.9 ± 0.2%), followed by rain (7.2 ± 0.2%) and mist (3.9 ± 0.1%) (**Figure 10**(**a**)). This indicates that besides the rain—a result of many complex regional and local processes—BWA is prone to frequent occurrences of haze, fog, and mist in decreasing order. These weather types result in impaired visibility at the airport.

Figure 10 (b & **c)** shows season-wise-annual-occurrence-frequencies of haze and fog at BWA.

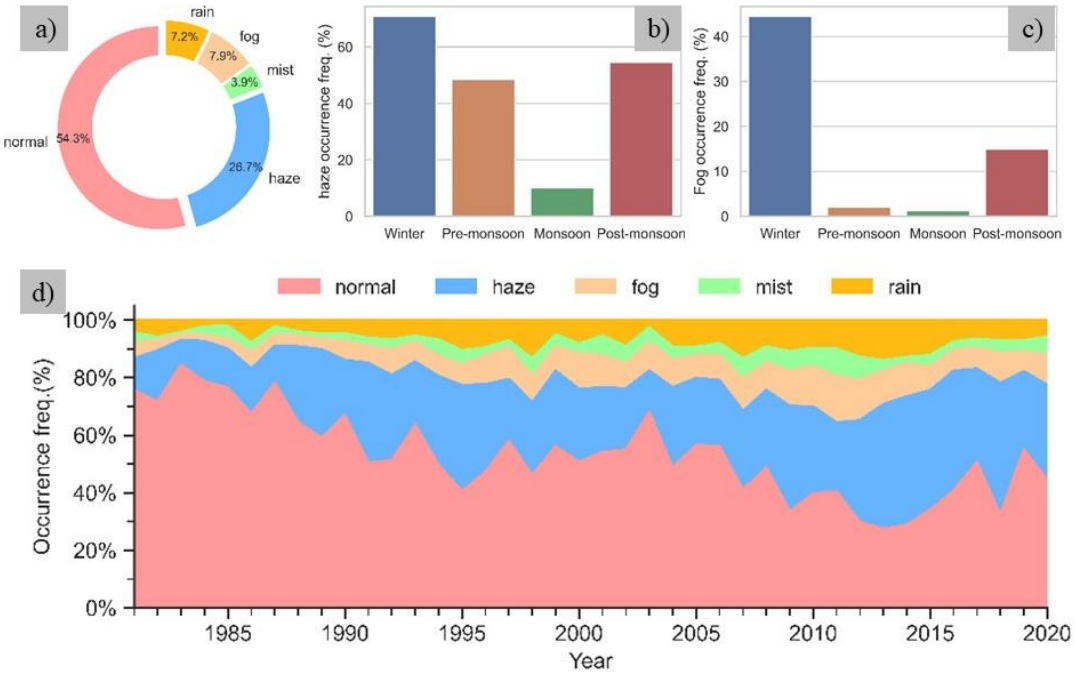

Figure 10: Occurrence of reduced visibility by different weather types at BWA (1981–2020): Hourly frequency (**a**), annual occurrence frequency (**d**); Occurrences of haze (**b**) and fog (**c**) in different seasons (Kathayat *et al.*, 2023)

Haze is most common throughout the winter, then during the post-, pre-, and monsoon seasons. Fog occurs primarily in the winter and occasionally in the post-monsoon. Trend results (**Table 5** and **Figure 10**(**d**)) of different weather types affecting the airport's visibility reveal a marked increase in the occurrence of fog (0.215% yr^{-1}) and haze (0.556% yr^{-1}) over four decades. Meanwhile, the occurrence of clear visibility (normal) conditions declined notably ($-0.931\%\ yr^{-1}$). Hence, fog and haze have been singled out as the two main visibility-reducing weather types because of their occurrence frequency, trend, and aviation implications. The detailed discussions in succeeding sub-sections also cover the discussions on the results of this subsection.

4.1.2 The trend of poor-visibility events, haze, and winter fog

Figure 11 shows the trend of poor-visibility-events **(a–d)** and haze (**e–h**) in different seasons at BWA and **Table 6** includes corresponding results using the statistical tools, described above. The highest frequency of poor-visibility-events was observed in winter, which reached ~100% since 2007 with an overall trend of 1.02% yr^{-1} (α = 0.001). In the early years pre-monsoon, the occurrence of poor-visibility-event was quite rare and increased sharply towards the middle of the data period. Poor-visibility-events at BWA in pre-monsoon displayed a marked upward trend of 0.84% yr^{-1} (α = 0.001) and little but significant positive trend in the monsoon season (0.42% yr^{-1}, α = 0.001) either. Poor visibility occurrence were the lowest (median = 13%) and varied the least (standard deviation (σ) = 8%) among the rest of the seasons, indicating persistently better seasonal visibility. On the contrary, the steepest upward trend (1.57 % yr^{-1}, α = 0.001) and largest variation (σ = 19.8%) was seen in post-monsoon season. A positive trend (0.94% yr^{-1}, α = 0.001) in interannual variability of poor-visibility-events was also observed. Similarly, across all seasons, the winter season in BWA witnessed the largest number of haze days (70.8%) (

Figure 10(**b**)) with the second highest annual trend (0.75 % day yr^{-1}, α = 0.001) (**Figure 11** (e–h) & **Table 6**). An alarming positive trend (1.46% day yr^{-1}) is found in the post-monsoon season. The pre-monsoon season also witnessed increased haze days (trend = 1.09 day yr^{-1} at α = 0.001) with a rise of ~80% over the last 44 years. While haze scarcely occurs during monsoon (**Figure 10**(**b**)); though, its annual trend is the smallest (trend = 0.31 day yr^{-1} at α = 0.05). Similarly, winter fog days have witnessed a notable rise over the years in BWA (**Figure 12**).

Table 5: Trend results of annual occurrence frequency (%) of different weather types affecting visibility at BWA airport (1981–2020)**.** Bold-faced values are statistically significant values at a defined significance level (α) (Kathayat et al., 2023)

		Mann-Kendall		**Sen's slope**		**OLS regression**			
		Z_{MK}	p –value	Trend Q (% yr^{-1})	[CI] %	Trend $\hat{\beta}_1$ (% yr^{-1})	[95% CI] %	t_s	p -value>$\|t\|$
Weather-type	Haze	4.41*	1.0×10^{-5}	0.57*	[0.213, 0.926]	0.57* ± 0.09	[0.374, 0.759]	5.97	0.000
	Mist	3.13†	1.7×10^{-3}	0.08†	[0.031, 0.138]	0.08 † ± 0.02	[0.033, 0.131]	3.41	0.002
	Fog	4.60*	4.18×10^{-6}	0.22*	[0.064, 0.354]	0.20* ± 0.03	[0.127, 0.263]	5.80	0.000
	Rain	3.76*	1.7×10^{-4}	0.18*	[0.027, 0.322]	0.16* ± 0.04	[0.082, 0.234]	4.20	0.000
	Normal	−5.34*	8.9×10^{-8}	−0.94*	[−1.351, −0.462]	−0.90* ± 0.11	[−1.118, −0.673]	−8.15	0.000

* 0.001, † 0.05, ** 0.1 - level of significance; *ns* non-significant

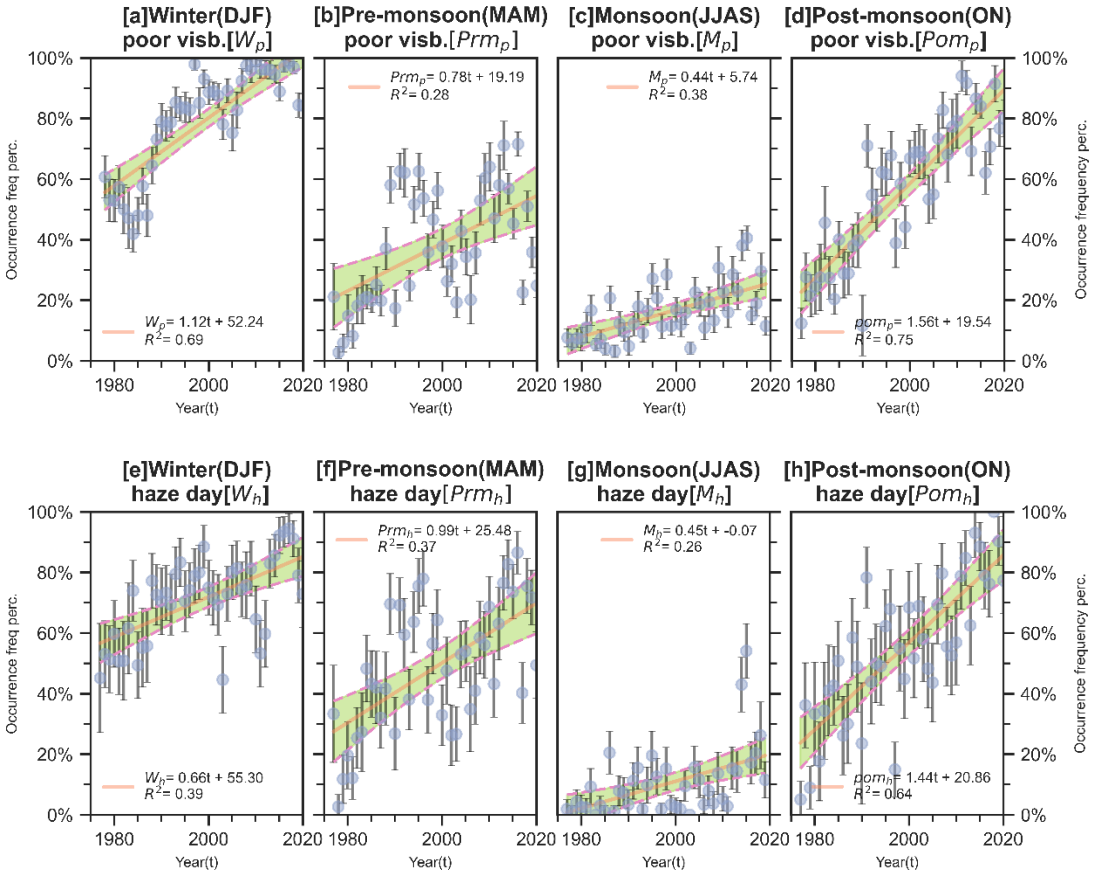

Figure 11: Time evolution of occurrence of poor-visibility events (a–d) and haze (e–h) in different seasons at BWA from 1977 to 2020. Here, the error bar means a 95% confidence interval; solid lines represent fitted linear regression lines (OLS) and dashed lines are boundary lines corresponding to their 95% confidence interval; and R^2 represent goodness of linear fit (Kathayat *et al.*, 2023)

Other fog parameters, namely, fog hours, dense fog days, and hours, also displayed some uptrend during the same period. Air pollution begins to build up significantly over the IGP atmosphere early in the post-monsoon season, giving the atmosphere an opalescent appearance and reduced visibility—what we call haze.

It occurs mainly because of the suspension of aerosols coming from the agro-residue burning after rice crop harvest in large swathe of the region (Khanal *et al.*, 2022; Saikawa *et al.*, 2019) besides other regular emission sources. This intensifies in winter (Dey & Di Girolamo, 2010).

Some additional emission sources are active, especially in the dry season only; these include burning fossil fuel (especially in urban areas) and wood (especially in rural areas) for residential heating in winter which is very common in IGP (Kedia *et al.*, 2014; Ramachandran *et al.*, 2015), and operation of brick kilns. From a meteorological

viewpoint, winter months in the BWA region are characterized by slower wind, adequate moisture content (RH) in the atmosphere (**Table 7**), and frequent low-level temperature inversion resulting in a shallow PBL suppressing buoyant vertical transport of pollutants (Tare *et al.*, 2006) which eventually induces and intensifies haze. The slower wind too results in reduced horizontal dispersion of air pollution. A recent study (Islam *et al.*, 2021) at Lumbini reported that a significant proportion (20 ± 6%) of total PM2.5 composition is composed of secondary inorganic ions (e.g., SO_4^{2-},NO_3^- , NH_4^+). Under sufficiently high levels of aerosol water (>60%) in the BWA atmosphere, which is mostly observed during winter months (**Table 7**), the optical properties of such hygroscopic secondary aerosols are altered resulting in enhanced extinction efficiency that is manifested as haze with reduced visibility.

Winter haze and fog are strongly coupled systems over IGP. A sufficient amount of ambient moisture, cloud condensation nuclei (CCN) onto which moisture can condense, and a temperature below the dew point are the essential components for the development of fog (Gultepe *et al.*, 2007). Winter season in BWA fulfills these prerequisites. Similar to the rest of the IGP, radiation fog forms over the BWA due to cooling near-surface air under stable, stagnant clear skies (Syed *et al.*, 2012). Many earlier literary works have pointed out that Western disturbances and synoptic-scale processes provide the prerequisites for large-scale radiation fog production across IGP quickly (Saikawa *et al.*, 2019). The low-pressure system first introduces moisture into the boundary layer during the western disturbances. The low-pressure system is then replaced by the high-pressure system, which has slow wind, surface radiative cooling, and temperature inversion (Pasricha *et al.*, 2003). According to Jenamani (2007), apart from ambient moisture introduced by western disturbances, moisture originating from winter crop irrigation of large areas of agricultural fields in Punjab, Haryana, and Uttar Pradesh, India could contribute to the widespread winter fog in northern IGP. Irrigation of winter crops in large agricultural fields in and around the BWA region introduces some more moisture over the BWA atmosphere. The worst seasonal visibility condition occurs in the form of haze and fog during winter at BWA because of the synergetic effect of the highest air pollution level and meteorological conditions—low temperature, temperature inversion, high RH, and slow wind.

Table 6: Trend results of different weather types at BWA (1977–2021) using three different statistical techniques. Trends represent linear fit between variables of interest and years. Boldface values are statistically significant trend values at a given significance level (α) (Kathayat *et al.*, 2023)

		Mann-Kendall		**Sen's slope**		**OLS regression**			
		Z_{MK}	p –value	Trend Q (% yr^{-1})	**[CI]** %	Trend ($\hat{\beta}_1$)(% yr^{-1})	**[95% CI]** %	t_s	$p-$ value $>\|t\|$
Occurrence frequency of poor-visibility events (%)	Winter	5.90*	3.71×10^{-9}	**1.02***	[0.582, 1.481] *	**1.1*** ± 0.1	[0.886, 1.355]	9.66	0.000
	Pre-monsoon	3.57*	4×10^{-4}	**0.84***	[0.079, 1.576] *	**0.8*** ± 0.2	[0.396, 1.173]	4.08	0.000
	Monsoon	4.19*	2.83×10^{-5}	**0.42***	[0.108, 0.780] *	**0.45*** ± 0.09	[0.264, 0.626]	4.97	0.000
	Post-monsoon	6.50*	7.85×10^{-11}	**1.57***	[1.069,2.076] *	**1.6*** ± 0.1	[1.277, 1.839]	11.18	0.000
	Annual	5.74*	9.27×10^{-9}	**0.94***	[0.524, 1.273] *	**0.9*** ± 0.1	[0.699, 1.094]	9.17	0.000
Occurrence frequency of haze days (%)	Winter	4.58*	4.6×10^{-6}	**0.75***	[0.218, 1.137]	**0.7***± 0.1	[0.416, 0.927]	5.31	0.000
	Pre-monsoon	4.02*	5.92×10^{-5}	**1.09***	[0.274,1.795] *	**0.9***±0.4	[0.584,1.388]	4.95	0.000
	Monsoon	3.71†	2.11×10^{-4}	**0.31**†	[0.021, 0.668]	**0. 4**†± 0.1	[0.209, 0.682]	3.80	0.000
	Post-monsoon	5.96*	2.56×10^{-9}	**1.46***	[0.806,2.106]	**1.4*** ±0.2	[1.103,1.778]	8.618	0.000
Occurrence frequency of fog parameters (%)	fog days	4.95*	7.58×10^{-7}	**1.05***	[0.518,1.577] *	**1.1*** ± 0.2	[0.809,1.311]	8.52	0.000
	dense fog days	5.37*	7.84×10^{-8}	**0.51***	[0.253, 0.776] *	**0.5*** ± 0.1	[0.354,0.645]	6.91	0.000
	fog hour	4.62*	3.80×10^{-6}	**0.55***	[0.229, 0.862] *	**0.5*** ± 0.1	[0.363,0.677]	6.67	0.000
	dense-fog hour	4.06*	5.00×10^{-5}	**0.20***	[0.054, 0.387] *	**0.20***± 0.08	[0.112,0.287]	4.61	0.000

* 0.001, † 0.05 - level of significance

Table 7: Monthly averages of selected meteorological variables in BWA airport from 2013 to 2018. Bold-faced values represent the highest and the lowest monthly averages

Met parameter	Jan	Feb	Mar	Apr	May	Jun	Jul	Aug	Sep	Oct	Nov	Dec
Visibility (km)	**1.9** ± 0.2	2.7 ± 0.1	4.5 ± 0.2	5.3 ± 0.1	6.1 ± 0.1	6.3 ± 0.1	**7.3 ± 0.2**	6.9 ± 0.2	6.3 ± 0.2	4.8 ± 0.2	3.3 ± 0.2	2.1 ± 0.1
Temperature (℃)	**14.7 ± 0.4**	20.2 ± 0.4	25.4 ± 0.5	30.2 ± 0.5	31.8 ± 0.3	**31.9 ± 0.3**	30.5 ± 0.3	30.6 ± 0.3	30.3 ± 0.3	27.9 ± 0.4	23.4 ± 0.4	17.8 ± 0.4
Relative Humidity (%)	**83 ±1**	71.0 ± 1.5	57.5 ± 1.6	**47.1 ± 1.7**	56.1 ± 1.3	68.3 ± 1.2	78.6 ± 1.0	79.6 ± 1.0	78.1 ± 1.0	74.1 ± 1.4	67.8 ± 1.7	77.3 ± 1.4
Wind Speed (m/s)	2.3 ± 0.2	2.4 ± 0.1	3.5 ± 0.2	**4.8 ± 0.3**	4.2 ± 0.2	3.4 ± 0.2	3.8 ± 0.3	3.0 ± 0.1	3.1 ± 0.2	2.6 ± 0.4	**2.0 ± 0.1**	2.2 ± 0.2

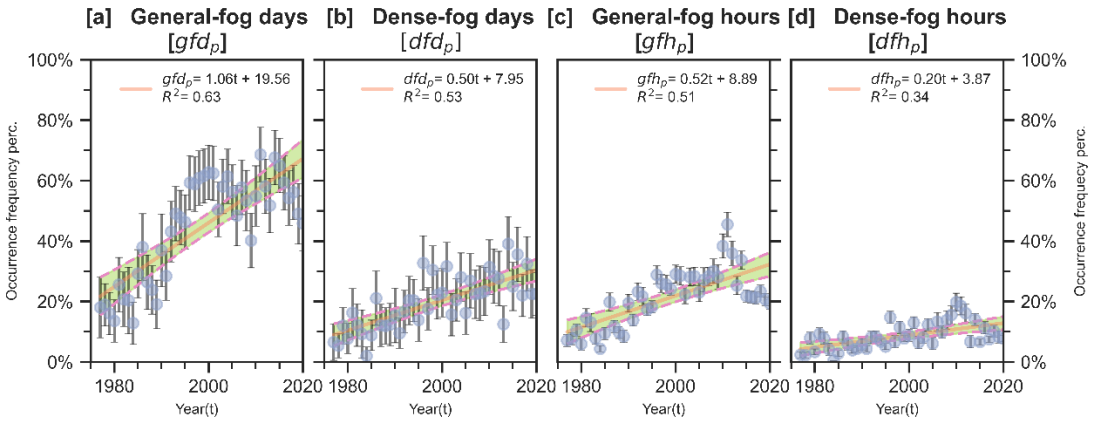

Figure 12: Time evolution of occurrence frequency of different fog parameters at BWA for the period 1977–2020: **(a)** fog days, **(b)** dense fog days, **(c)** fog hours, and (**d**) dense fog hours. Here, the error bar means a 95% confidence interval; solid lines represent fitted linear regression lines (OLS) and dashed lines are boundary lines corresponding to their 95% confidence interval; and R^2 represent goodness of linear fit (Kathayat *et al.*, 2023)

At BWA, Jan is the coldest and most moist month of the year (**Table 7**) which causes winter- haze and fog to peak in intensity and duration impairing visibility to the yearly lowest. As the winter months advance from January to February, a sharp rise in temperature causes the PBLH to rise, improving the vertical dispersion of CCN aerosols. In addition, an increase in dew-point depression and reduction of ambient moisture (**Table 7**) slightly weakens winter haze and fog occurrences leading to visibility improvement.

The temporal trend in fine mass concentration (PM2.5) was investigated to explain the observed seasonal trend in visibility. **Figure 13** illustrates the interannual change in average PM2.5 during Jan 1980–Feb 2021. A sudden jump in MEERA-2 reanalysis PM2.5 values is seen between NASA's pre-EOS period (1980–1999) and post-EOS period (after the year 2000). Possible causes could range from significant changes in emissions/ policy implementation, and algorithm changes used for data assimilation, to data assimilation changes. Several previous literatures (e.g., Buchard *et al.*, 2017; Randles *et al.*, 2017; Yao *et al.*, 2021) have also pointed this out as one of the major caveats of the MEERA-2 dataset that occurred specifically due to the difference in data coverage (availability of observational data) before and after the assimilation of EOS. MEERA-2 reanalysis product incorporates observational data into model simulations. Any changes in the availability, quality, or types of observational data being assimilated into the model can cause noticeable shifts in the reanalysis outputs as observed in

Figure 13. According to Rienecker *et al*. (2011), this reanalysis product is quite sensitive to observing system changes, dealing with which is the most pressing challenge for the next generation of reanalysis. Despite some deficiencies, many previous studies (e.g., Buchard *et al.*, 2017; Randles *et al.*, 2017; Yao *et al.*, 2021) have demonstrated that this aerosol assimilation system exhibits considerable skill in simulating numerous observable properties of aerosol and is hence reliable to use. In light of this caveat of the MEERA-2 dataset, we only considered data from the year 2000 to 2021 while calculating the trend of PM2.5 to avoid the bias discussed above.

Since the IGP region has become undeniably one of the major global air pollution hotspots, the increased air pollution in the region shall result from a gamut of anthropogenic activities associated with rapid population growth, urbanization, and industrialization as agreed by scientific communities. There is an increase in RH ($0.36\%\ \mathrm{yr}^{-1}\ at\ \alpha = 0.001$) and a slight decline in wind speed (-0.009 m/s yr^{-1} at α = 0.1) at BWA during the same period (**Table 8**). Irrigation areas in BWA have expanded manifold (MoF, 2020) in the last few decades possibly resulting in an observed increase in wintertime RH. As for why persistent and extensive fog has become more common in IGP in recent decades, scientists cannot agree on a single explanation (Saikawa *et al.*, 2019). This study suggests that the increasing trend of fog intensity and frequency at BWA and northern IGP regions may result from increased air pollution, RH, and the slowing down of wind. A body of literature has reported an increasing frequency of fog elsewhere in IGP (e.g., Ghude *et al.*, 2017; Jenamani, 2007; Mohan & Payra, 2014; Shrestha *et al.*, 2018; Syed *et al.*, 2012). This fact also agrees with the general perception of residents of Terai regions about the main climatic variation during winter "fog occurs more frequently and is denser" and "cold spells are getting more intense" (Smadja *et al.*, 2015). The increasing trend of poor visibility in winter is, hence, the result of an increase in fog and haze frequency as discussed earlier. It was observed that the surface warming effect of aerosols at BWA that daily minimum temperature (T_{min}) has increased over the last four decades ($\mathrm{trend} = 0.020°\mathrm{C}\ \mathrm{yr}^{-1}$)similar to other studies at BWA (Baidya *et al.*, 2008; Shrestha *et al.*, 2017; Shrestha *et al.*, 2018). Among the rest, the absorbing aerosols (BC in particular) trap solar energy in the daytime and heat the atmosphere eventually warming the earth's surface. This atmospheric heating counteracts the loss of long-wave solar insolation at night. Thus, increased occurrence of winter haze and fog at BWA may contribute to surface warming as indicated by an

increase in T_{min}. Ramachandran and Rupakheti (2022) also reported a notable positive trend in wintertime Biomass Burning (BB) aerosol type at Kanpur city (located ~313 km southwest of BWA). A body of literature (Jaswal *et al.*, 2013; Kaskaoutis *et al.*, 2012; Saikawa *et al.*, 2019; Sarkar *et al.*, 2006; Srivastava *et al.*, 2012) also suggests increasing winter haze elsewhere in IGP commensurate with increased air pollution.

In pre-monsoon season, visibility deterioration takes place in the form of haze resulting from the accumulation of aerosols from different regular and season-specific sources. One such season-specific source in IGP is wind-blown-desert-dust originating as far from the Thar Desert (Dey & Di Girolamo, 2010; Gautam *et al.*, 2009; Hegde *et al.*, 2007; Ram *et al.*, 2010). Pandithurai *et al.* (2008) reported the influence of such desert dust on visibility over IGP. From a meteorological standpoint, the atmosphere over BWA turns drier, warmer, windier, and more turbulent in pre-monsoon (**Table 7**); PBL elevates slightly higher due to the atmosphere getting warmer. Dispersion of air pollution may occur horizontally and vertically over a large area. The level of aerosol water in the atmosphere is usually below the deliquescent/crystallization point indicating negligible impact of light extinction by hygroscopic aerosol species. These conditions contribute to improved visibility than in the winter season despite having higher levels of seasonal air pollution.

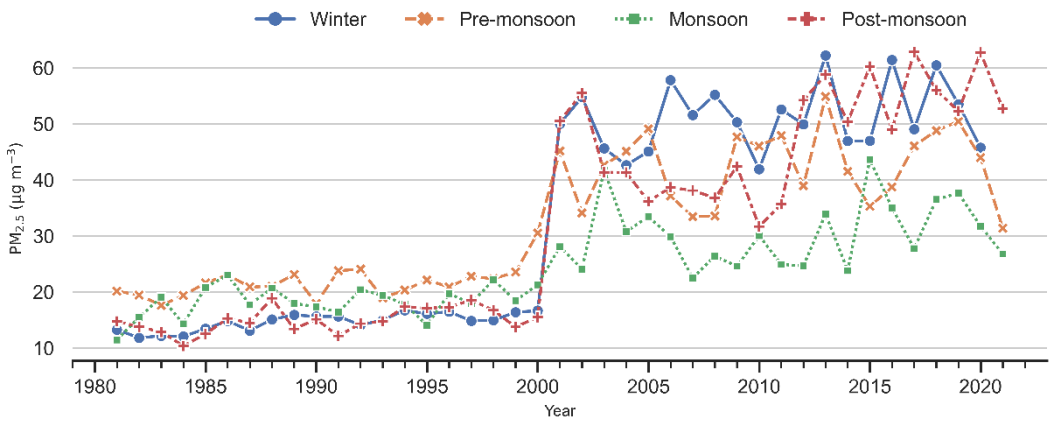

Figure 13: Interannual variation of average PM2.5 in a bounding box centered at BWA (MERRA-2 Model M2TMNXAER v5.12.4; Spatial Coverage: 82.2405ºE, 26.516ºN, 84.9651ºE, 28.0541ºN; Temporal coverage: Jan 1980–Feb 2021; Spatial resolution: 0.5º × 0.625º, Temporal resolution: 1 Month) (Global Modeling and Assimilation Office (GMAO), 2015)

Table 8: Trend results of PM2.5 (2000–2020) and different meteorological variables at BWA (1977–2020) using three different statistical techniques. Trends represent linear fit between variables of interest and years. Boldface values are statistically significant trend values at a given significance level (α) (Kathayat *et al.*, 2023)

		Mann - Kendall		**Sen's slope**		**OLS regression**			
		Z_{MK}	p –value	Trend (Q) (yr^{-1})	[CI]	Trend ($\hat{\beta}_1$) (yr^{-1})	[95% CI]	t_s	p -value>$\|t\|$
PM2.5 ($\mu g\ m^{-3}$)	Winter	0.55	0.58	0.17	[−0.80, 1.29]	0.22 ± 0.2	[−0.270, 0.717]	0.95	0.354
	Pre-monsoon	0.51	0.61	0.13	[−1.21, 1.33]	0.08± 0.24	[−0.419, 0.594]	0.36	0.722
	Monsoon	0.94	0.35	0.18	[−0.81, 1.08]	0.19± 0.22	[−0.268, 0.644]	0.86	0.399
	Post-monsoon	1.97†	0.04	**0.92†**	[−0.81, 2.16]	**0.88†**± 0.3	[0.247, 1.502]	2.92	0.009
RH (%)	Winter	4.16*	3.22×10^{-5}	**0.36***	[0.084, 0.646]	**0.38*** ± 0.07	[0.230, 0.523]	5.20	0.000
	Pre-monsoon	2.28†	2.28×10^{-2}	**0.15†**	[−0.093, 0.441]	**0.2**** ± 0.1	[−0.025, 0.365]	1.76	0.086
	Monsoon	0.65ns	5.03×10^{-1}	0.029ns	[−0.107, 0.179]	0.30ns± 0.04	[−0.053, 0.112]	0.73	0.471
	Post-monsoon	1.22ns	2.20×10^{-1}	0.062ns	[−0.132, 0.291]	0.08ns± 0.06	[−0.046, 0.199]	1.258	0.215
WS (m/s)	Winter	−1.7**	8.74×10^{-2}	**−0.009****	[−0.032, 0.009]	**−0.010**** ± 0.006	[−0.023, 0.001]	−1.78	0.082
	Pre-monsoon	−1.2ns	2.28×10^{-1}	−0.009ns	[−0.034, 0.016]	−0.012ns± 0.007	[−0.023, 0.007]	−1.12	0.268
	Monsoon	−0.63ns	5.30×10^{-1}	−0.004ns	[−0.013, 0.006]	−0.003ns± 0.005	[−0.014, 0.008]	−0.59	0.556
	Post-monsoon	−1.18ns	2.31×10^{-1}	−0.006ns	[−0.015, 0.003]	−0.006ns± 0.005	[−0.017, 0.005]	−1.14	0.261
T_{min} (℃)	Winter	2.41†	1.57×10^{-2}	**0.020†**	[0.004, 0.036]	**0.019† ± 0**.008	[0.003, 0.035]	2.40	0.021
	Pre-monsoon	1.62ns	1.05×10^{-1}	0.016ns	[−0.004, 0.034]	**0.018†± 0**.008	[0.001, 0.34]	2.15	0.038
	Monsoon	3.27†	1.06×10^{-3}	**0.016†**	[0.007, 0.223]	**0.014†± 0**.004	[0.008, 0.022]	4.16	0.000
	Post-monsoon	4.13†	3.53×10^{-5}	**0.032†**	[0.019, 0.046]	**0.030†± 0**.008	[0.014, 0.047]	3.75	0.001

* 0.001, † 0.05, **0.1 -level of significance; ns: non-significant

Based on the analysis and literature, the increasing trend of hazy days and overall poor-visibility events at BWA in the pre-monsoon season is attributed to a combination of worsening seasonal air pollution and enhancement of aerosol water (**Table 8**).

South Asian summer monsoon brings the seasonal highest rainfall from June through September in the BWA region resulting in scavenging of air pollutants through processes like rainout (capturing of aerosols inside the cloud as CCN) or washout (capture of aerosols and gaseous pollutants by falling raindrops below the cloud). The amount of rainfall peaks in July and gradually declines. Certain major air-pollution sources like brick kilns shut down during this season; power cuts are less frequent because of more hydroelectric generation leading to lesser emission from fossil-fuel generators. The major meteorological change while advancing from pre-monsoon to monsoon season is the rain. Because of efficient rain-scavenging and decreased emissions, air pollution is lower during the monsoon, which ultimately results in the best seasonal VIS. Because of higher surface temperature, the boundary layer height is elevated making more room for available particulates and gaseous pollutants to disperse vertically. Higher-speed wind also helps disperse the pollutants across large areas horizontally. These help pollutants get uniformly mixed in the atmosphere. Dey and Girolamo (2010) also suggested that monsoon-visibility impairment occurs by the extinction of solar radiation by cloud and rain droplets or by aerosols during the occasional haze, which occurs during monsoon break.

As the post-monsoon season progresses visibility gradually declines (**Table 7**) with the increase in air pollution in the atmosphere, fall in rainfall, temperature, and slowing down of wind at BWA. Brick kilns, a major air pollution source, started operating across IGP after the cessation of the rainy season. Paddy residue burning after rice harvest occurs across large agricultural areas situated in the upwind region of IGP such as northern Pakistan, and north Indian states (Punjab and Haryana) (Jethva *et al.*, 2019; Kulkarni *et al.*, 2020). Air pollutants thus produced build-up and transported to downwind sites giving a hazy appearance to the atmosphere. Kulkarni *et al.* (2020) also reported the effect of such paddy residue burning in Delhi's atmosphere. After a thorough analysis of the Lumbini atmosphere during the post-monsoon, it was found that a considerable portion (about 40% of the total Organic Carbon) came from Biomass Burning (BB) (Wan *et al.*, 2017). This finding validated the impact of burning agro-residues in IGP on the aerosol concentration of BWA in the region. Together with a fall

in temperature, the boundary layer shrinks, restricting vertical transport of air pollution. Slower wind in this season shall not be strong enough to disperse air pollution over a larger area in a short time. Active scavenging of air pollution is lacking in this season since there is little to no rain. Thus, with the advancement of the season, air pollution intensifies, and VIS declines. Steep rise in inter-annual air pollution (PM2.5) (0.92 $\mu g\, m^{-3}\ yr^{-1}$) (**Table 8**) shall result in the all-season highest trend of haze (1.46 $\%\, yr^{-1}$ at $\alpha = 0.001$) and poor visibility events (1.57 $\%\, yr^{-1}$ at $\alpha = 0.001$) at BWA.

Although, this is beyond the scope of this thesis, the observed abrupt drop in poor visibility since pre-monsoon of 2020 may be attributed to lesser air pollution emissions due to COVID-19, which started in March 2020.

4.1.3 Comparison of the trend of winter-poor-visibility and fog among northern IGP airports

Temporal variation of the occurrence of poor-visibility-events across selected northern IGP airports reveals that BWA experienced major visibility impairment quite later than GOP, LKN, and DEL (**Figure 13**(a–d) & **Table 9**). The minimum frequencies of poor visibility events are yet very high in GOP (91.5 ± 2% in 2019), LKN (79.6 ± 2% in 2005) and DEL (94.7 ± 1% in 1998). Poor visibility in the winter season already peaked before the study period and exhibits lesser variation. Thus, its trend in the study period is small—none for LKN, only 0.01 $\%\ yr^{-1}$ (α = 0.001) for GOP and 0.06 $\%\ yr^{-1}$ (α = 0.01). In contrast, BWA witnessed a gradual visibility impairment with a significant upward trend of 1.02 $\%\ yr^{-1}$ (α = 0.001). However, each airport station witnessed an obvious rise in the number of foggy days in winter (**Figure 14**(e–h) & **Table 9**); the steepest trend occurred in DEL (1.29% day yr^{-1} at α = 0.001), followed by BWA (1.19% day yr^{-1} at α = 0.001), LKN (0.93% day yr^{-1} at α = 0.05), and GOP (0.62% day yr^{-1} at α = 0.05).

During winter, all of the airports involved in the comparative study share similar meteorological features.

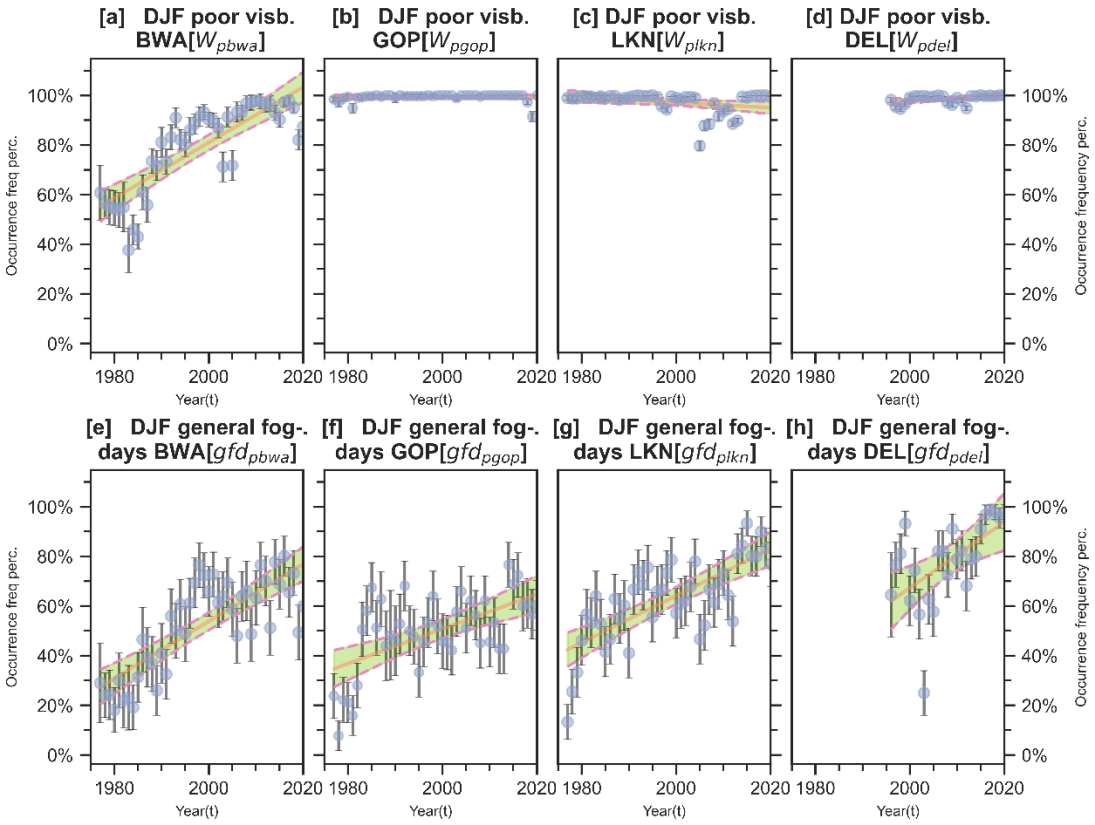

Figure 14: Trend of poor-visibility events (a–d) and foggy days (e–h) in winter at BWA, GOP, LKN, and DEL airports from 1977 to 2020. Here, the error bar means a 95% confidence interval; solid lines represent fitted linear regression lines (OLS) and dashed lines are boundary lines corresponding to their 95% confidence interval; and R^2 represent goodness of liner fit (Kathayat *et al.*, 2023)

The only feature that distinguishes BWA from the rest is the level of local air pollution and proximity to major emission sources in the IGP upwind sector. BWA is comparatively a smaller city inside Nepal with a lesser industrial setup and population, even from the beginning of the study period, suggesting lesser local air pollution emission and better visibility conditions initially. The city and its immediate neighborhood witnessed rapid industrialization and urbanization lately, which resulted in air pollution-emission manifold in recent decades degrading winter visibility. However, the rest of the neighboring megacities of northern IGP: DEL, LKN, and GOP witnessed the worst winter visibility from the beginning because of having higher local air pollution emissions.

Table 9: Trend results of winter-poor-visibility-events and winter fog across BWA, GOP, LKN, and DEL airports of northern IGP (1977–2020). Boldface values are statistically significant trend values at a given significance level (α) (Kathayat *et al.*, 2023)

	Site	Data period	Mann - Kendall		Sen's slope	
			Z_{MK}	p-value	Trend (Q) (% yr^{-1})	**[CI]**(%)
Occurrence frequency of poor visibility events (%)	BWA	1977–2020	5.98*	2.27×10^{-9}	**1.02***	[0.523, 1.506]
	GOP	1977–2020	3.72	1.97×10^{-4}	**0.01***	[0.000, 0.020]
	LKN	1977–2020	−0.58	0.563	0.00	[−0.061, 0.010]
	DEL	1996–2020	2.85**	4.34×10^{-3}	**0.06****	[0.005, 0.210]
Occurrence frequency of fog -days (%)	BWA	1977–2020	5.44*	5.28×10^{-8}	**1.19***	[0.573, 1.723]
	GOP	1977–2020	3.07	2.17×10^{-3}	**0.62**	[0.261, 0.979]
	LKN	1977–2020	5.20	1.99×10^{-7}	**0.93**	[0.630, 1.212]
	DEL	1996–2020	3.32*	8.95×10^{-4}	**1.29****	[0.000, 2.798]

* 0.001 level of significance, ** 0.01 level of significance

4.1.4 Relationship between air pollution and visibility

Daily averages of visibility (VIS) and AOD ($\boldsymbol{\tau}$) for each day of the year aggregated for 2013–2018 have been shown in **Figure 15**(a). It shows that the daily average AOD in winter gradually increased and peaked in February (0.80 ± 0.02). Unlike the empirical relation between AOD and visibility (Equation (34)), visibility was better in February (2.7 ± 0.2 km) than in January (1.9 ± 0.2 km) and December (2.1 ± 0.1 km) at BWA (**Table 7**), despite higher AOD values. Seasonal association between AOD and VIS was weak ($r = -0.36$, $p < 0.001$) in winter. Aerosol loading in the BWA atmosphere starts increasing concurrent with improvement in VIS as the pre-monsoon season advances; both of them peak in May ($\tau = 0.75 \pm 0.01$ & VIS = 6.1 ± 0.1 km).In this season, AOD and VIS display an inverse association; however, the correlation is weaker ($r = -0.23$, $p < 0.001$). A marked improvement in VIS and plunge in AOD occurs with the onset of south Asian monsoon ($r = -0.66$, $p < 0.001$); the seasonal highest VIS (7.4 ± 0.2 km) and lowest AOD (0.21 ± 0.01) was observed in July. Towards the end of monsoon season, AOD is found to rise and VIS starts to decline gradually again. A sharp enhancement in AOD and gradual reduction of VIS occurs over post-monsoon months ($r = -0.42$, $p < 0.001$).

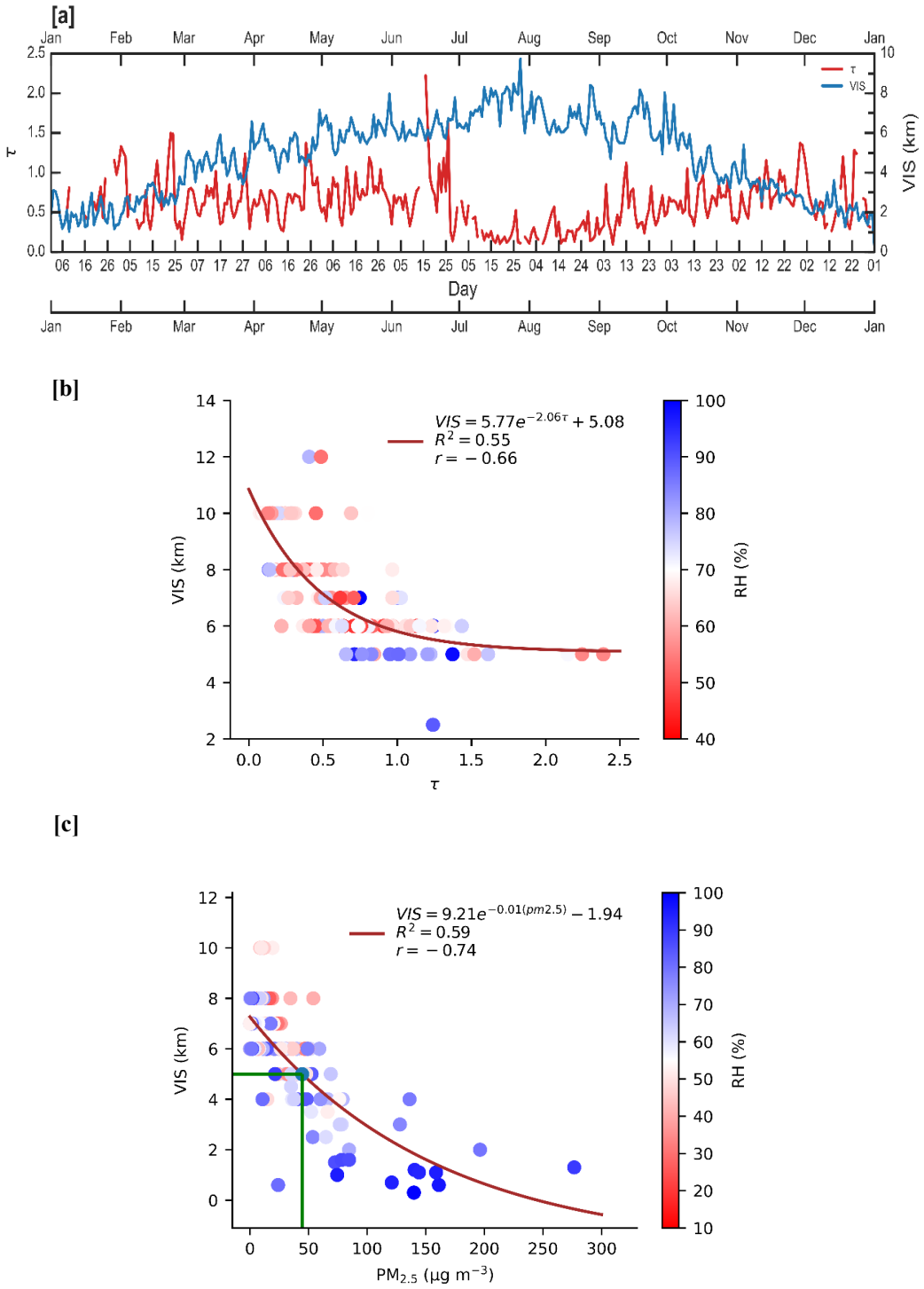

Figure 15: **(a)** Daily average visibility at BWA Vs. AOD ($\boldsymbol{\tau}$, at $\boldsymbol{\lambda}$ = 550 nm) at Lumbini site, from 2013 to 2018 **(b)** Visibility (VIS) at BWA as a function of AOD ($\boldsymbol{\tau}$) at Lumbini during the monsoon of 2013–2018, **(c)** Visibility (VIS) at BWA as a function of PM2.5 during April–December 2019. Points in plots (b) and (c) are color-coded for RH (Kathayat et al., 2023)

Figure 15(b) is a graphical representation of the association of VIS with AOD and relative humidity (RH) for 2013–2018 in which, the best-fit curve (brown line) complies with the above empirical relation (Eq. (34)). The fitted curve has the goodness

of fit (R^2) (**APPENDIX B**) of ~0.55, indicating that during monsoon season 55% of the variability in VIS can be explained by the variability of AOD alone. Here, the effect of aerosol water (RH) on VIS can be seen; the higher the aerosol water (RH) level, the lesser the VIS. Below 60% of RH, its influence on VIS is negligible at BWA; concentration of aerosol (AOD) governs VIS. In contrast, aerosol water (RH) governs VIS when RH > 60%.

A similar negative power-function relationship between in-situ PM2.5 measurements and VIS at BWA, with a better anti-correlation ($r = -0.74$, $p < 0.001$) (**Figure 15(c)**) was witnessed. For RH < ~50%, BWA witness generally a good VIS condition; lower VIS occurs when fine mass concentration (PM2.5) is high in the BWA atmosphere. When RH increases beyond this, VIS tends to worsen with higher PM2.5. A threshold VIS for aviation use (VIS = 5 km) corresponds to PM2.5 ~48 μgm^{-3}.

According to studies by Sharma *et al.* (2014) and Rupakheti *et al.* (2018), the BWA region's AOD is maximum during the winter. The low correlation between air pollution and VIS ($r = -0.36$) between AOD and VIS, however, raises the possibility that the VIS drop cannot be entirely explained by aerosol loading in the atmosphere.

The observed weaker relationship between air pollution and visibility in pre-monsoon ($r = -0.23$ between AOD and VIS) suggests that besides aerosols, meteorology also plays a key role in pre-monsoon visibility. Yet in the pre-monsoon season, most of the atmospheric aerosols are trapped within a relatively thin mixing layer making aerosol-columnar-distribution non-uniform. This shall explain, to some extent, the poor anti-correlation between AOD and VIS—as the equation relating them (**Eq. (34)**) assumes aerosol's uniform distribution. The strongest anti-correlation between them during the monsoon season implies that the amount of atmospheric aerosols during this time of year significantly influences VIS. The monsoon season is distinguished by greater scavenging, advection, and vertical mixing of air pollution due to its higher annual rainfall, hotter atmosphere, and quicker wind (**Table 7**). These meteorological conditions shall explain why there is the best anti-correlation between VIS and PM2.5/AOD. Based on in-situ measurements Baumer *et al.* (2008) detected a similar power function relationship between AOD and VIS in south-west Germany. Similarly, Lin *et al.* (2011) reported a good anti-correlation ($r = \sim -0.75$) and exponential relationship between AOD and VIS over 200 locations across Asia. Having a generally

humid atmosphere during monsoon (RH > 60%), we observed evidence of the hygroscopic effect of aerosols on visibility.

4.1.5 Implication to Aviation in Nepal

The occurrence of poor visibility in various forms holds numerous serious implications for the air transport system at BWA. Widespread and persistent winter fog and regional haze in the rest of the season impose major challenges in flight operations at Bhairahawa Airport. In **Figure 16**(a), a significant decline in the airport's visibility condition when aircraft are able to land using Visual Flight Rules (VFR) (**APPENDIX A**) was seen. It also shows an increase in the fraction of time when the airport shall operate in Instrument Flight Rules (IFR) (**APPENDIX A**) and airport closure time solely due to visibility. Currently, available navigation systems that aid aircraft's landing at BWA—Visual Omnidirectional Radio Range (VOR) (**APPENDIX A**) and Required Navigation Performance (RNP) (**APPENDIX A**)—enable aircraft landing up until hazy conditions; but, they are unable to guide aircraft to make a safe landing at the airport in foggy condition, let alone the dense fog—due to their precision on guiding capability. Closure of airport operations in low-visibility conditions causes inconvenience and financial burden to all stakeholders especially when BWA has started international operations. TIA at KTM and GBIA are highly unlikely to serve as alternate airports to each other in winter when poor visibility is the major challenge to both international airports (**Figure 16(b)**, **Table A.2**). Thus, one of the major motives for upgrading BWA to an international airport is yet to materialize under currently operating navigational and guidance facilities. However, BWA airport has already installed a precision landing guidance system (CAT -I Instrument Landing System (ILS) (**Table A.1**) (CAAN, 2022) and waiting for operational permission from the Indian authority. Once it starts operating, the airport will be able to operate even in foggy conditions. GBIA was expected to serve as the nearest suitable alternate international airport to the major international airport TIA. One of the primary investment objectives for GBIA airport's international upgrade would be justified if the airport made additional investments in upgrading to a higher category ILS (CAT – II/III) and in an Advanced Surface Movement Guidance and Control System (A-SMGCS). This would enable the airport to operate effectively in extremely low visibility conditions, such as dense fog.

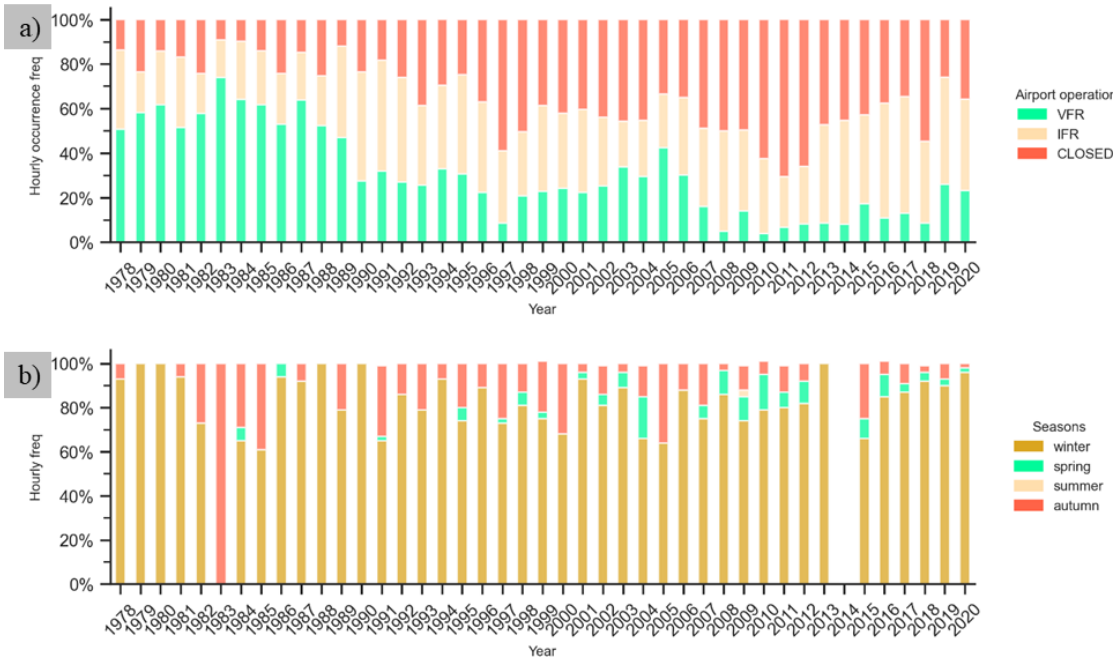

Figure 16: (a) Hourly occurrences of BWA airport flight conditions (1978–2020): VFR and IFR. Their definition has been given in **A PPENDIX (b)** Interannual hourly frequency when BWA and KTM airport cannot serve as each other's alternate (Kathayat et al., 2023)

4.2 Atmospheric visibility at Kathmandu

4.2.1 Estimates of boundary layer heights

Firstly, existing boundary layer types were confirmed based on the thermodynamic properties of the atmosphere during the launch of RS instruments. Overall, the occurrence of SBL, NBL, and CBL account for 91.20%, 7.03%, and 1.54%, respectively, suggesting that SBL dominates in Kathmandu valley during detection time (0545 LT), i.e. early morning irrespective of the season of a year. This finding indicates that for the majority of the RS observation, the atmosphere of the valley is stable. This finding can be attributed to the diurnal cycle of solar radiation. The formation of SBL is facilitated by low heat flux caused by long-wave radiation cooling of the earth's surface at night (Nieuwstadt, 1984; Poulos *et al.*, 2002; Stull, 1988). Radiative cooling in the Kathmandu Valley basin is further aided by cold katabatic wind flowing downslope from the valley rim (Panday & Prinn, 2009). Occasional cases of NBL were observed in the radiosonde observations when there were overcast conditions in the valley.

The vertical structure of the atmosphere has been studied through the RS profile. **Figure 17** shows a typical demarcation of different atmospheric layers according to their thermodynamic property on 14 Jan 2020.

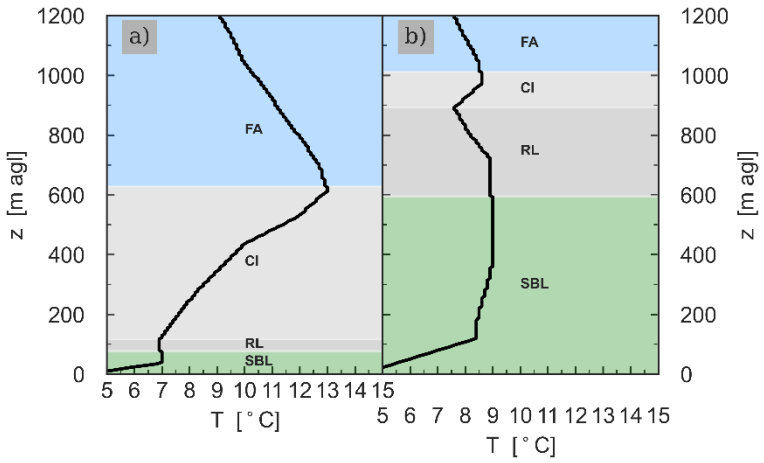

Figure 17: Vertical profile of ambient temperature (T) and structure of PBLH—represented by different colored layers— as detected by radio soundings profile at 0000 UTC (05:45 LT) on 14 Jan **(a)** and 15 Jan **(b)** 2020 in Kathmandu. Where, z, SBL, RL, CI, and FA stand for height (a.g.l.), Stable Boundary layer, Residual Mixed Layer, Capping Inversion Layer, and Free Atmosphere, respectively. Different layers have been determined according to the temperature inversion method.

The top of Surface-Based Inversion (SBI) (SBI_{tp}) was observed at a height of 77 m and a thin (40 m) residual layer (RL) was noticed on the top of the SBL. While there was a thick, (511.5 m) capping inversion layer (CI) with its top at 628.5 m. Surface-based inversion occurs when solar radiation from the earth's surface surpasses that of the incoming radiation from space. The thickness of this inversion increases gradually as the surrounding atmosphere cools. Thus, the lower the surface temperature, the deeper the inversion layer is (Bradley *et al.*, 1992). Due to the subsidence above, synoptic factors such as a clear sky, anticyclonic conditions, and low wind speed are typically linked to the deepest SBI and elevated inversions (Busch *et al.*, 1982). Using continuous Ceilometer measurement (Mar 2013–Feb 2014) of MLH at Bode, Kathmandu Valley, Mues *et al.* (2017) reported a median MLH of 150 m in the winter mornings.

The findings of this study on winter morning PBLH are consistent with the observations. Panday *et al.* (2009) reported that the thickness of the valley's cold air pool reaches the height of mountain passes at approximately the same height as the average SBLH that was obtained in winter.

Figure 18 shows the SBL heights (early morning PBLH) deduced by each T-profile method from soundings of 0000 UTC performed in Kathmandu on 14 January 2020. Generally, all methods detect the SBL height with very little variation in height estimates. PBLH estimates by *RM, GM_θ and SBI* is 77 m, 74 m, and 77 m, respectively indicating having a very shallow boundary layer. The SBL top was marked by a sharp gradient in vertical profiles of potential temperature gradient $\left(\frac{\Delta\theta}{\Delta z}\right)$ (**Figure 18(b)**) and temperature (T) (**Figure 18**(c)), indicating a sudden change in atmospheric properties between the SBL and the nocturnal residual layer (RL). The vertical profile of wind speed (**Figure 18**(c)) also shows of having light wind conditions (~ 0.5 m/s) during that morning. Firstly, all SBL heights were estimated by the SBI method, and all CBL/NBL heights by using the RM method as done in previous studies. SBL heights ranged between ~16.0 m to ~768.5 m a.g.l.; NBL heights ranged between ~1.5 m to ~146.5 m; and CBL heights ranged between ~2.5 m to ~14. 5 m.

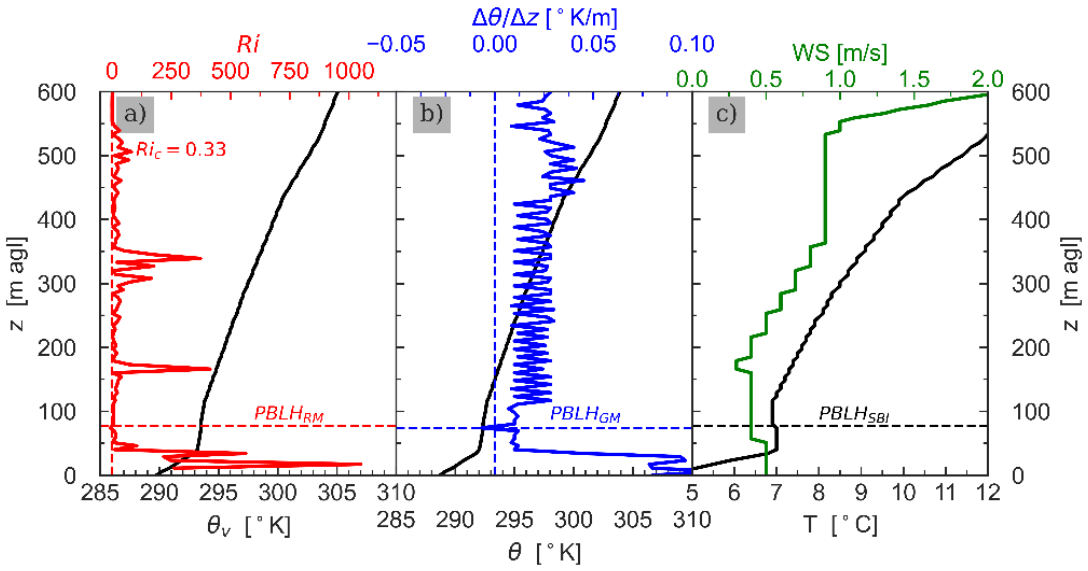

Figure 18: Detection of the SBL from RS T-profiles of 0000 UTC in Kathmandu on 14 January 2020 determined by Bulk Richardson number method (RM) **(a)**, Gradient of potential temperature method ($\mathbf{GM_\theta}$) **(b)** and Surface-based inversion method (SBI) **(c)**, where z, $\boldsymbol{\theta_v}$, $\boldsymbol{Ri}$, $\boldsymbol{Ri_c}$, $\boldsymbol{\theta}$, $\frac{\boldsymbol{\Delta\theta}}{\boldsymbol{\Delta z}}$, T & WS stand for height above ground level, virtual potential temperature, Bulk Richardson number, Critical Bulk Richardson number, Potential temperature, Potential temperature gradient, Ambient temperature, and wind speed respectively

This indicates that convective conditions are very weak during the early mornings. PBLH from all sounding profiles was separately estimated by all three *T*-profile methods. PBLH estimates obtained by using SBI methods on real-time RS measurement ($PBLH_{SBI}$) in the early morning at Kathmandu were very much scattered in between 12.5 m and 768.5 m with a large standard deviation (SD) of 160.43 m and an interquartile range (IQR) of 71.5 m. Similarly, the Bulk Richardson Number technique (RM) yielded PBLH between 1.5 m and 768.5 m with SD of 147.94 m and IQR of 82.5 m., PBLH detected up by RM was typically indicated by a shift in wind direction, a decrease in wind speed, or both. PBLH estimates by GM_θ ranged between surface level (0 m) and 1997.0 m with IQR of 71 m and SD of 174.27 m. It was found that PBLH estimates obtained by GM_θ were zero only when the thermodynamic condition of the atmosphere was either convective or neutral. The variation in PBLH obtained from various techniques can be ascribed to disparities in the boundary layer height parameters, which serve as the foundation for the study.

4.2.2 Inter-comparison and validation

PBLH from different T-profile methods were estimated out of the same RS data for the whole study period. The GM_θ method gave the closest estimates (near to unbiased) of PBLH to SBI with very small bias (-3.57 m), both coefficients of determination (R^2) with the 1:1 line and regression slopes ~ 1 (**Figure 19** [(a) & (c)], **Table 10**). The interquartile range (IQR) of the difference in PBLH (ΔH) is 0.5 m only. All other error metrics (**APPENDIX B**) are the lowest too (MedAE = 3.0 m, MAE = 4.75 m, and RMSE = 15.49 m). Similarly, RM also shows a good agreement with the results of SBI, having a bias of -14.28 m, RMSE ~89 m, and IQR of the difference in PBLH (ΔH) ~ 32.0 m. RM versus SBI has a regression slope of ~ 0.83 and a coefficient of determination (R^2) ~ 0.65 with their regression fit (**Figure 19** [(a) & (b)], **Table 10**). This method slightly underestimates PBLH by SBI. Reanalysis data could only be compared on a reduced data set (328 cases) because of reanalysis data availability. Since the reanalysis of PBLH uses an entirely different algorithm and detection methods, its comparison with the RS-SBI method revealed large variations.

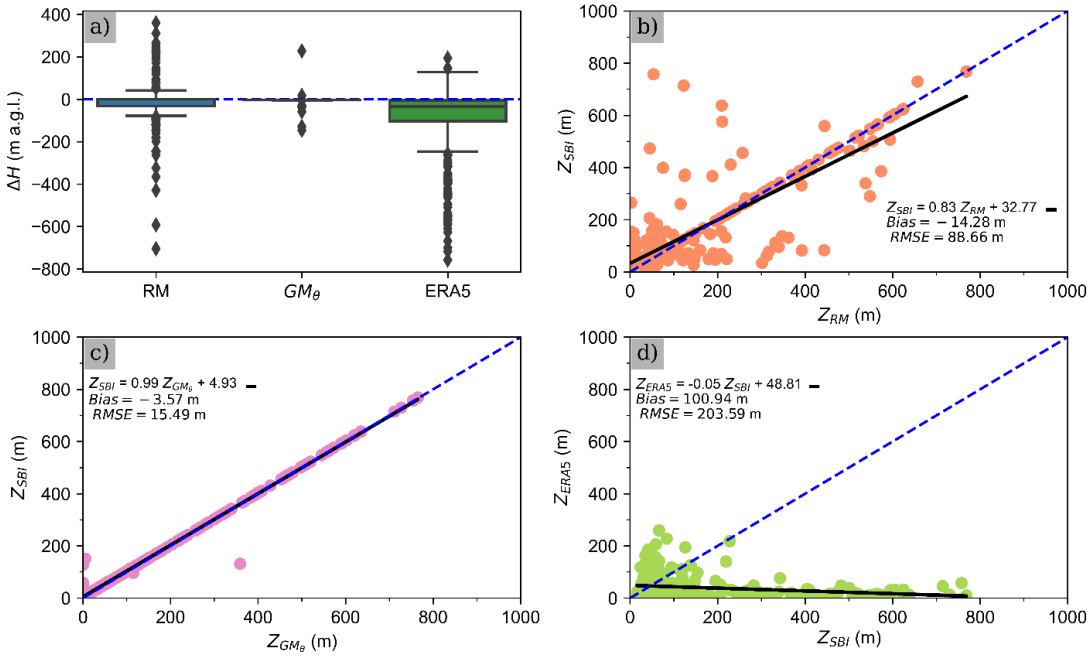

Figure 19: (a) Box plots of difference in PBLH estimates ($\Delta \boldsymbol{H}$) detected by two T-profile methods, i.e., RM and $\mathbf{GM_\theta}$, using radio soundings profiles (Nov 2019–Mar 2022) and ERA5 reanalysis data (Nov 2019–Dec 2021) w.r.t. PBLH from SBI method at 0545 LT in Kathmandu; (b–d) their respective Scatter plots. Here, $\boldsymbol{Z_{GM_\theta}}$, $\boldsymbol{Z_{RM}}$ and $\boldsymbol{Z_{SBI}}$, represent PBLH by $\boldsymbol{GM_\theta}$, RM and SBI methods respectively; $\boldsymbol{Z_{ERA5}}$ represents PBLH from ERA5 reanalysis data

Table 10: Linear regression metrics for performance assessment of early morning (0545 LT) PBLH from radiosoundings data (Nov 2019–Mar 2022) detected by two T-profile techniques, i.e. RM and GM_θ, and ERA5 reanalysis PBLH data—w.r.t. reference method (SBI) for inter-comparison, in Kathmandu. Where, r, R^2, MedAE, MAE and RMSE denote Pearson's correlation coefficient, coefficient of determination, median absolute error, mean absolute error, and root mean square error between the PBLH estimates from two different methods; and N denotes a total number of considered data pairs. Details of the regression metrics have been given in APPENDIX B

Methods	r	R^2	Bias (m)	MedAE (m)	MAE (m)	RMSE (m)	N
RM / SBI	0.83*	0.65	−14.28	15.0	42.09	88.66	417
GM_θ / SBI	0.99*	0.99	−3.57	3.0	4.75	15.49	417
ERA5/ SBI	−0.22*	−0.55	−100.94	44.4	118.981	203.59	328

* 0.001 - level of significance

With respect to SBI-PBLH estimates, reanalysis PBLH has a slope of -0.05, correlation coefficient (r) of -0.22, large bias (-100.94 m), and a very high RMSE (203.59 m). Their goodness of fit (R^2) is -0.55, suggesting that they cannot be linearly related. IQR of difference in PBLH (ΔH) (**Figure 19**(a)) and the rest of the error metrics is the highest of all comparisons. This comparison of $PBLH_{ERA5}$ to the reference $PBLH_{SBI}$ suggests that PBLH from reanalysis data have a strong negative bias i.e. $PBLH_{ERA5}$ under-estimates PBL height during early morning in Kathmandu. This behavior is not only limited to a season; it is observed throughout the year. PBLH yields produced from RM are generally higher than those retrieved from other methods under the SBL classification, according to a comparison of PBLH yields obtained from other approaches. In China, H. Li *et al.*(2021) also reported similar results while comparing PBLH estimates from different methods for SBL cases using RS measurements (Jan–Dec 2019) of 0000 UTC at nine sites across China.

Under SBL classifications, SBI and GM_θ are more effective than RM, however, results from RM are quite consistent and reliable. The conclusion of this study also agrees with Aryee *et al.* (2020)'s findings, which show that GM_θ is better performing than RM and other approaches, including SBL situations. A body of literature (e.g., Li *et al.*, 2021; Seidel *et al.*, 2012) negated the use of RM to estimate PBLH from SBL classifications since turbulence is weak in surface-level inversion. RM finds its wider application in CBL cases. Unlike many studies, reliable estimates of PBLH by RM were obtained in SBL cases, which became possible by reversing the use of critical Richardson's

number (Ri_c) while estimating PBLH as mentioned in the methodology section (3.4.5.2.1). Based on the performance assessment, GM_θ and SBI method are recommended as primary methods for estimating PBLH from SBL classification, while RM might be used, either. With the preceding optimization statement, it was decided to use $PBLH_{SBI}$ as the representative PBLH, if SBL was observed in the particular day sounding profile. Likewise, $PBLH_{RM}$ were selected for CBL or NBL classifications.

4.2.3 Effect of boundary layer on air pollution dispersion and visibility

Figure 20 and **Table 11** show the seasonal variation of PBLH, ventilation coefficient (VC), PM2.5, and some key meteorological parameters in Kathmandu at 0545 LT measured between Nov 2019 and Mar 2022. The highest early morning average PBLH (206.28 ± 115.81 m) was observed in the pre-monsoon month of April, gradually falling as the season advances to monsoon season. The lowest value (34.52 ± 10.77 m) was observed in September, it again starts rising and gains another secondary peak (205.27 ± 51.43 m) in December. Interestingly, early morning PBLH in winter months (DJF) is generally higher than during summer months (JJAS).

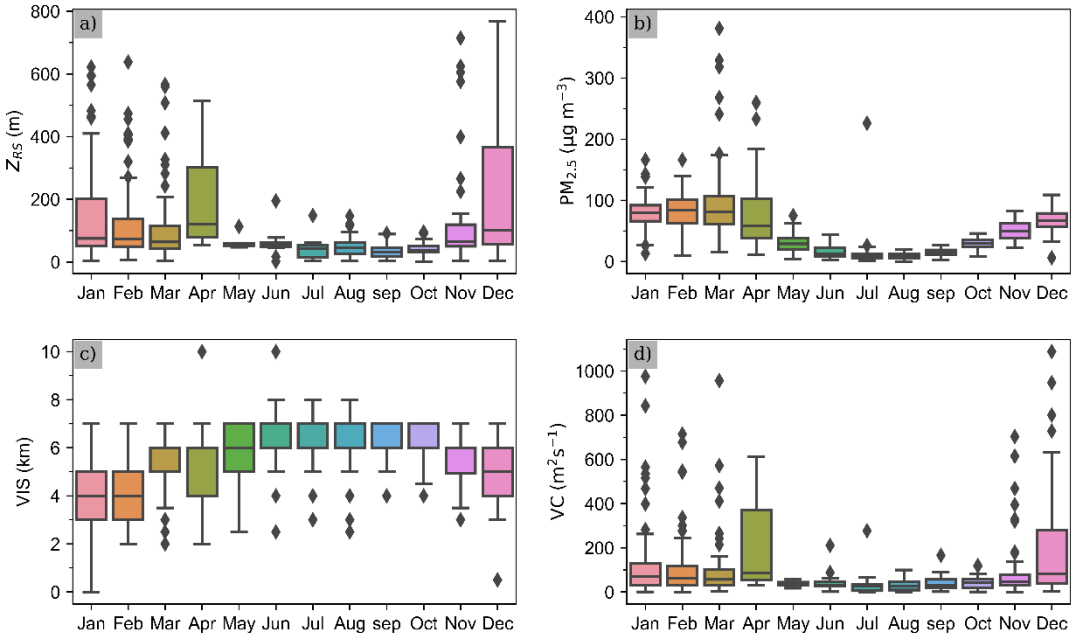

Figure 20: Box plots of seasonal variation of (**a & d**) PBLH (Z_{RS}) and Ventilation Coefficient (VC) from radiosonde soundings profile **(b)** PM2.5 and **(c)** Visibility (VIS) in Kathmandu at 0545 LT from Nov 2019 to Mar 2022

Table 11: Monthly average values of different parameters, namely, PBLH and VC (Ventilation Coefficient) in Kathmandu, PM2.5 at Phora Durbar, and visibility, temperature, relative humidity, and wind speed in Tribhuvan International Airport (TIA) in Kathmandu at 0545 LT from Nov 2019 to Mar 2022. The bold-faced values are the highest and lowest monthly averages

Parameter	Jan	Feb	Mar	Apr	May	Jun	Jul	Aug	Sep	Oct	Nov	Dec
PBLH (m)	160 ± 44	140± 36	110± 32	**200± 115**	60± 16	60± 14	40± 10	50± 14	**30± 10**	42± 8	120± 40	210± 51
VC ($m^2\ s^{-1}$)	140± 51	120± 40	110± 39	**200± 135**	40± 10	40± 17	**30± 18**	30± 11	40± 16	44± 11	100± 37	190± 58
PM2.5 ($\mu g\ m^{-3}$)	89± 8	82± 6	**100± 13**	80± 15	30± 4	16± 3	13± 7	**8± 1**	15± 2	29± 2	51± 3	68± 4
Visibility (km)	**3.9± 0.2**	4.3± 0.3	5.0± 0.2	5.2± 0.4	5.9± 0.3	**6.6± 0.3**	6.0± 0.3	6.4± 0.3	6.5± 0.2	6.1± 0.2	5.4± 0.2	4.9± 0.2
Temperature (°C)	**5.1± 0.4**	6.6± 0.5	11.1± 0.5	12.6± 0.6	16.8± 0.6	**20.4± 0.3**	21.0± 0.2	21.0± 0.2	20.2± 0.3	16.6± 0.7	9.8± 0.5	5.4± 0.5
Relative Humidity (%)	96.5± 0.6	94.8± 0.7	89± 1	**86± 3**	93± 2	96± 1	98.0± 0.6	98.0± 0.7	**97.5± 0.6**	96.3± 0.7	96.9± 0.5	96.9± 0.5
Wind Speed (m/s)	1.7± 0.3	1.5± 0.2	1.6± 0.2	1.7± 0.2	1.8± 0.4	1.5± 0.2	1.7± 0.6	1.6± 0.2	1.8± 0.3	**1.4± 0.2**	1.4± 0.1	**1.9± 0.6**

Typically, sunrise in Kathmandu varies between ~0500 and ~0700 LT: 0500–0630 LT in pre-monsoon, 0500–0600 LT in monsoon, 0510–0550 LT in post-monsoon and 0630–0700 LT in winter season (Mues *et al.*, 2017). The variations in early morning PBLH estimations between seasons are in line with the seasonal variations in soil heat capacity and surface air temperature (**Table 11**). Because of the late sunrise and enhanced cooling of the earth's surface in the winter season, a strong surface inversion layer forms over the Kathmandu Valley overnight through the early morning. As a result, in winter, heights that correspond to the top of the surface inversion layer—that is, early morning PBLH, as identified by RS in this instance—are often higher than in other seasons. However, daytime PBLH shall follow the opposite suit, with higher PBLH in warmer summer months than winter months since daytime PBLH corresponds to the CBL type.

Shrestha *et al.*(2015b) reported MLH of 80 m at 0500–0600 LT at a central location of valley basin, Sanothimi, Bhaktapur on 12 March 2013 (pre-monsoon) by using monostatic flat array Doppler SODAR (Sonic Detection and Ranging) data. Similarly, Shrestha *et al.* (2015a) found an early morning MLH of ~520 m during their SODAR measurement campaign from 11 to 24 June 2013 at a western low-mountain pass of Kathmandu Valley, Aindanda. Contrary to this result, MLH obtained by Ceilometer measurements at Bode, Kathmandu valley, Mues *et al.* (2017) reported a higher nighttime/ early-morning MLH in monsoon and post-monsoon rather than pre-monsoon and winter seasons. The highest deviations of these results (PBLH < 60 m) from theirs (median MLH = 220–370 m) occur in monsoon season. They attributed their findings to the higher seasonal average temperatures in monsoon and post-monsoon seasons. Since early morning is mostly characterized by a stable boundary layer, higher PBLH was expected when the average seasonal temperature is low—commensurate with the findings. Rather, the observed opposite seasonal variation of early-morning RS-PBLH and ceilometer MLH at two different measuring sites located within Kathmandu Valley shall be attributed to different techniques employed for their respective measurement. Mues *et al.* (2017) used a gradient-based algorithm in which attenuated-back-scatter profiles of the laser beam transmitted from the ceilometer are looked for gradient minima that mark the aerosol layers top (Münkel, 2007). They assumed that aerosol concentration is nearly uniform vertically across ML and higher than above, (Steyn *et al.*, 1999). In that respect, the lowest seasonal early-morning-

MLH in winter as reported by Mues *et al.* (2017), and the highest PBLH as observed by us have the same physical meaning. According to the algorithm used in this study, the higher the PBLH the stronger the SBL that suppresses the vertical mixing of aerosols. Thus lowest MLH (as reported in (Mues *et al.*, 2017)) is equivalent to the highest PBLH (reported in this study) and vice-versa.

The peak level of monthly average PM2.5 ($97.77 \pm 13.31\ \mu g\ m^{-3}$ in March) was witnessed during premonsoon, which fell to its lowest point ($8.65 \pm 1.20\ \mu g\ m^{-3}$, in August) during the summer monsoon period. It again rises and reaches a higher level during winter. As a result, compared to the wet season (monsoon), the fine mass concentration (PM2.5) level is higher during the dry season (winter, pre/post-monsoon). Likewise, seasonal visibility is worse in winter and best during monsoon at TIA. The best (6.59 ± 0.27 km) visibility condition was witnessed in June and the worst (3.90 ± 0.24 km) in January.

To describe the vertical transport of pollutants in Kathmandu, it was attempted to establish the correlation between PM2.5, PBLH, and VIS in the early morning. A weak correlation between PBLH and PM2.5 ($r = 0.35$, $p < 0.001$) and a similar weak correlation of PBLH with VIS ($r = -0.16$, $p < 0.001$) (**Table 12**) were found.

VIS and PM2.5, however, have a strong anti-correlation ($r = -0.59$, $p < 0.001$). It was attempted to examine the relationship between visibility and PBLH under different RHs since a higher level of aerosol water could have favored corresponding enhanced extinction by hygroscopic aerosol species that need higher PBLH for better vertical transportation to have better visibility. However, variation in early morning RH is very small around the year.

Analyzing PBLH, PM2.5, and VIS relationships independently during fog-haze mixed events and haze occurrences in Beijing (Jan 2014–Mar 2015), Luan and colleagues (2018) observed that there was a negative exponential association ($R^2 = 0.80$) between PM 2.5 and VIS. They also observed an inverse linear correlation between PM2.5 and PBLH in the case of haze events, and a negative exponential relation in the case of fog-haze mixed events.

Table 12: Results of Pearson's correlation coefficient among fine particulate mass (PM 2.5), planetary boundary layer height (PBLH), and ventilation coefficient (VC) from radio-sounding profiles, and early morning (0545 LT) visibility (VIS) at TIA in Kathmandu.

PBLH vs. PM2.5	PM2.5 vs. VIS	PBLH vs. VIS	VC vs. VIS
$r = 0.35, p < 0.001$	$r = -0.59, p < 0.001$	$r = -0.16, p < 0.001$	$r = -0.13, p < 0.001$

They also found a positive linear correlation between PBLH and VIS (R^2 = 0.35 (for haze events) and 0.56 (for fog-haze mixed events)). In contrast, Lou *et al.* (2019) in China also noticed a positive correlation between PM2.5 and PBLH in SBL cases utilizing four years of L-band radiosonde data (2014–2017).

Apart from PBLH, WS also plays a role in regulating the amount of air pollution. WS determines the horizontal diffusion capabilities of pollutants whereas PBLH governs the vertical diffusion. The combined effect of these two entities (PBLH * WS) yields a ventilation coefficient (VC). This is frequently used as an index to assess how well the atmosphere can disperse air pollution. The ventilation coefficient (VC) was the highest ($200 \pm 135\ m^2\ s^{-1}$) in April and the lowest ($30 \pm 18\ m^2\ s^{-1}$) in July.

4.2.4 Relationship between air pollution, meteorology, and visibility

Figure 21 shows a typical monthly snapshot view of variation of visibility, other related meteorological parameters (RH, WS), and PM2.5 in Kathmandu. In general, the diurnal variation of visibility is concurrent with the temperature variation (T); as the day progresses, surface temperature rises and peaks at about 3–4 pm when net solar flux is maximum and visibility follows suit. It is also evident that higher WS, low RH, and low PM concentration are typically linked to greater VIS. Due to rain on 16 and 17 Jan, high RH was observed, lower peak visibility than other days, and lesser diurnal variation in VIS. These two days witnessed fog, mist, and haze limiting visibility at the airport. Visibility less than 1 km is associated with the occurrence of winter fog over the airport.

From **Figure 22**(a), it was seen that high RH is strongly correlated with low visibility. As RH increases, the occurrence of good visibility (VIS ≥ 10 km) drops and that of poor visibility (VIS ≤ 5 km) rises. When RH is greater than 70%, the occurrence frequency of poor visibility category (1 <VIS ≤ 2 km) increases.

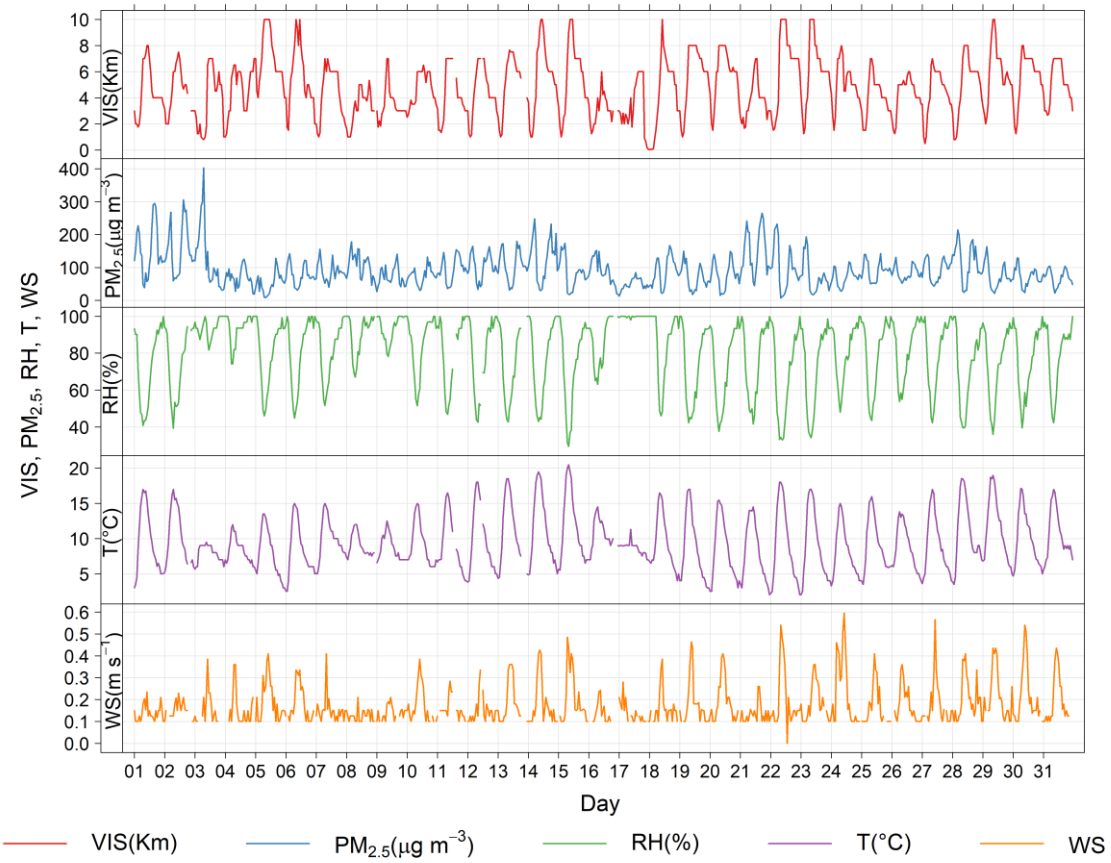

Figure 21: Time series of visibility (VIS), PM2.5, RH, Temperature (T), and wind speed (WS) in TIA for January 2020

The occurrence of the poorest visibility category (VIS ≤ 1 km) increases sharply when RH exceeds 90%, which should probably be because of rain, mist, and fog and partly by the aerosol effect on ambient aerosols in the Kathmandu atmosphere. The frequency distribution of RH at TIA reveals the airport having a high level of moisture (> 90%) for the highest period (~28% of the time) (**Figure 22**(a)). The valley witnessed a dry atmosphere (RH < 40%) for only ~7% of the period. The results of this study are consistent with many previous works (e.g., Malm & Day, 2001; Sequeira & Lai, 1998; Zhang *et al.*, 2010) which showed visibility reduction under high RH.

Analyzing the relationship between visibility and wind—a factor that defines air pollution transport—is necessary in order to comprehend variations in visibility at a given location. TIA witnessed a higher occurrence of very low visibility (VIS ≤ 1 km) in calm wind conditions (WS < ~1 m/s) (**Figure 22**(b)). These conditions generally correspond to winter fog, heavy rain, or extreme haze.

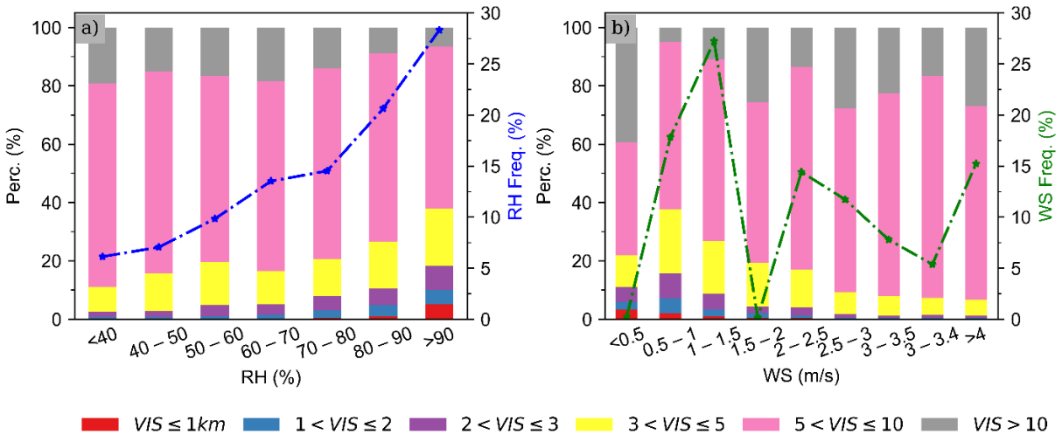

Figure 22: Occurrence frequency of visibility (VIS) at TIA, Kathmandu, in relation to RH (**a**) and WS (**b**) for 1973–2020

A high occurrence (~38%) of good visibility conditions (VIS ≥ 10 km) was observed under calm wind conditions, which correspond to very little air pollution in the valley's atmosphere. With slight speeding up of wind (0.5 < WS ≤ 1 m/s), the occurrence frequency of good visibility sharply declines to less than ~5%. This suggests that a slow transport of aerosols originating from local emission sources near the airport shall occur towards the airport, which disperse away quite slowly from the airport leading to impaired visibility at the airport. Further faster wind (WS > 1.5 m/s) causes moderately good (5 < VIS ≤ 10 km) to good visibility occurrence to rise and poor visibility occurrence to drop. There is very little (~ 10%) chance of poor visibility (VIS ≤ 5 km) when the wind is blowing faster than 2.5 m/s. This indicates that the faster the wind, the better the horizontal dispersion of air pollutants in the valley. It was also found that TIA witnesses the highest frequency of wind in the speed range of 1–1.5 m/s (~ 27.5%) (**Figure 22**(b)).

Figure 23 presents the distribution of visibility in TIA in relation to wind direction and -speed in different seasons. These bivariate polar plots enable particulate source apportionment and provide an efficient graphical representation of emission sources with wind speed and direction. KTM exhibits distinct dominant wind direction from the western quadrant in all seasons. The fastest and slowest wind occurs in pre and post –monsoon, respectively. A very little dependence of wind direction on visibility was found in all seasons except for the winter—when the slow easterly wind (1–2 m/s); more specifically from Northeast to south is seen to cause poor visibility at TIA.

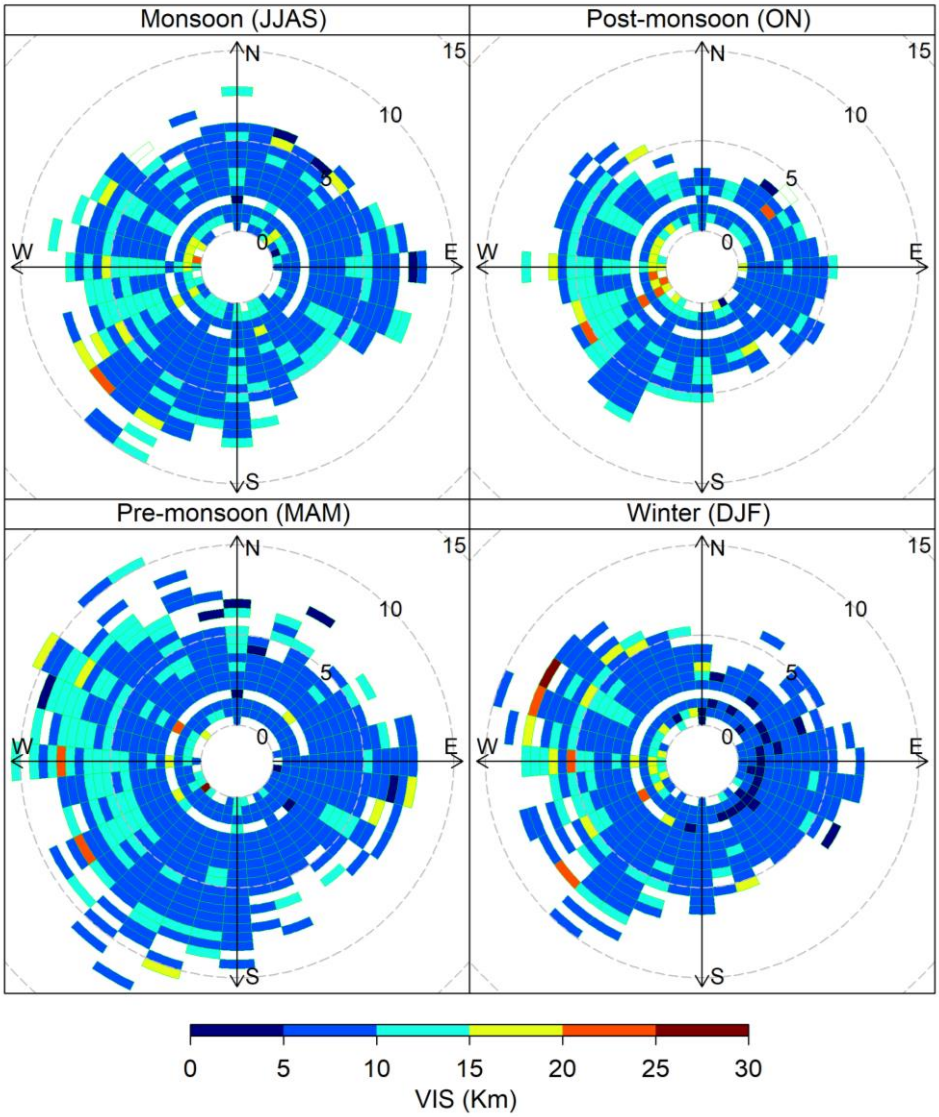

Figure 23: Seasonal visibility (VIS) distribution at TIA, KTM relative to wind speed and direction (1973–2020)

The precise reason for this directional dependence, particularly in winter needs extensive investigation of the location of emission sources, which is beyond the scope of the study. Kathmandu Valley has a distinct geographical behavior.

4.2.4.1 Influence of optical properties and hygroscopic effect of aerosol on visibility

4.2.4.1.1 Extinction coefficient of PM2.5

Figure 24(a) presents the relationship between ambient extinction coefficient and visibility at TIA. It was found that the average extinction coefficient of PM2.5 and VIS at TIA was 621 ± 4 Mm^{-1} and 6.91 ± 0.02 km respectively. Here, a sharp decrease in VIS with an increase in b_{ext} was seen; they exhibit a power-function relationship. Additionally, a notable rise in the extinction coefficient was noticed because of the particles' hygroscopic growth, which is not depicted in this figure. These results point to having a high atmospheric aerosol load in the area. Then, a power law function relating these two parameters was fitted. The fitted model is highly consistent with the observed/computed VIS-b_{ext} relationship (R^2 = 0.91). The link between b_{ext} and PM2.5 is shown in **Figure 24(b)**, where the mass extinction efficiency of PM2.5 (6.45 m2/g) is indicated by the slope of the regression line.

4.2.4.1.2 Mass extinction efficiency and hygroscopic growth factor

The PM2.5 MEE, in the current study, ranged from 5.93 to 116.19 m^2/g (**Figure 25 (a)**). The observed MEE values are quite large and much scattered when compared with the results from other works conducted elsewhere (e.g., Cheng *et al.*, 2017; Shin *et al.*, 2022).

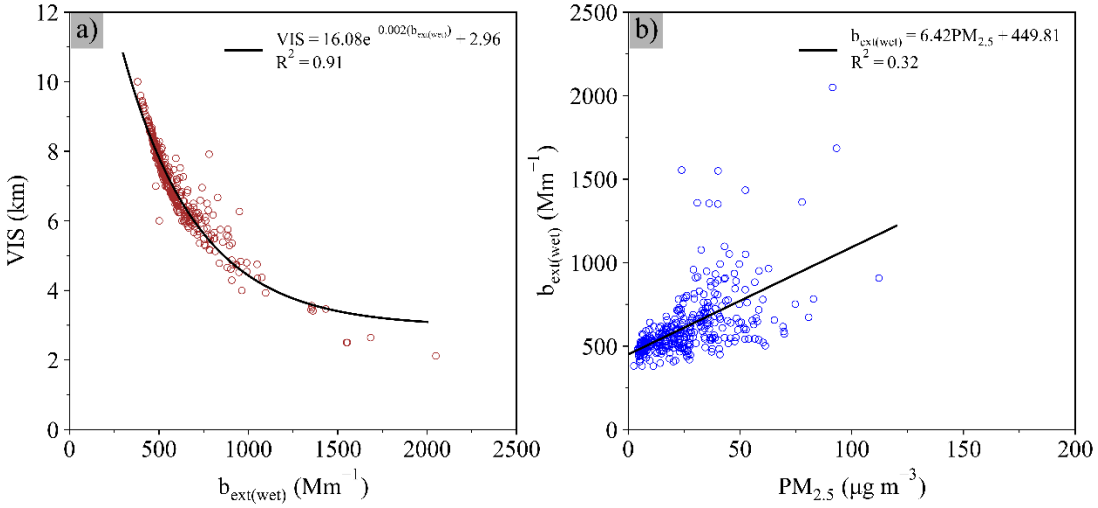

Figure 24: Relationship between: **(a)** visibility (VIS) and wet extinction coefficient (b_{ext}) of PM2.5 and **(b)** wet extinction coefficient (b_{ext}) of PM2.5 and PM2.5—in TIA, Kathmandu for Jan–Dec 2020

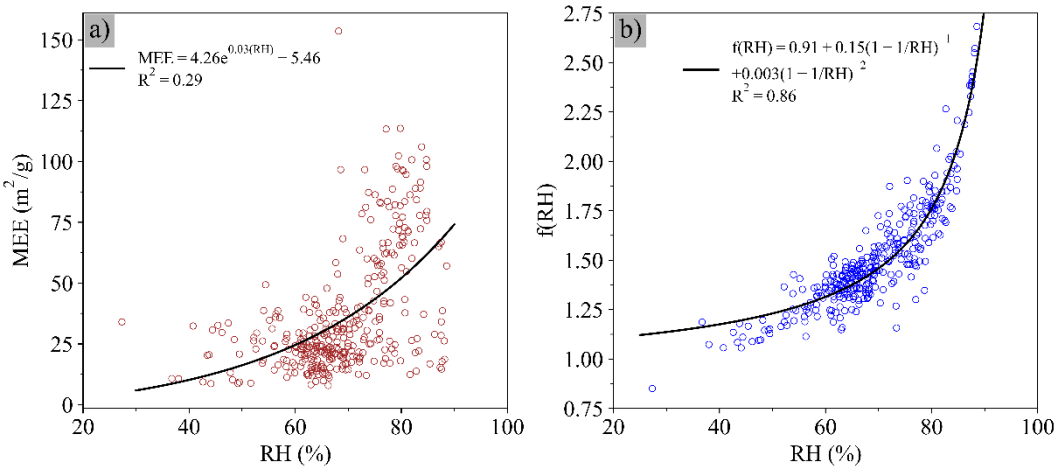

Figure 25: The relationship between **(a)** daily average mass extinction efficiency (MEE) and relative humidity (RH), and **(b)** daily averages of hygroscopic growth factor f (RH) and RH—at TIA, Kathmandu in 2020. Here, R^2 represents the coefficient of determination of fitted curves

The relative mass ratio between the three primary PM2.5 constituents—organic, inorganic, and crustal—had the greatest impact on the MEE values (Pitchford *et al.*, 2007). Prior studies (Cheng *et al.*, 2017), for example, showed that the corresponding MEE value increased with the mass percentage of secondary inorganic and carbonaceous species in PM2.5. The higher value of MEE in TIA can be attributed to this reason. The goodness of fit of the PM2.5 MEE-RH relationship curve is quite small (R^2 = 0.29). Similarly, regression results of the hygroscopic growth factor were presented in **Figure 25 (b).** The hygroscopicity of PM2.5 is often measured using a value of *f* (RH) when RH = 80% (Cheng *et al.*, 2017; Liu *et al.*, 2008; Pan *et al.*, 2009). It was found that *f* (RH = 80%) in TIA is ~1.52 falls in similar ranges of other previous studies (Cheng *et al.*, 2017). The main contributors to hygroscopicity in PM2.5 are the concentrations of hydrophilic species such as sea salt, ammonium, sulfate, and nitrate. This differs slightly from the factors that affect MEE. Although some water-soluble organic carbon has some hygroscopicity, the hygroscopic effect of carbonaceous species is thought to be much weaker than that of inorganic ions. The regression equation in **Figure 25(b)** is very much able to model the relationship between *f* (RH) and RH, with a high R^2 value (0.86). Hygroscopic growth, thus, has a significant influence on the VIS-PM relationship.

4.2.5 Visibility regression model development and validation

Visibility forecasting is extremely difficult for both numerical and statistical models because it involves numerous intricate processes related to radiation, droplet microphysics, aerosol chemistry, surface conditions, and turbulences (Chmielecki & Raftery, 2011; Doran *et al.*, 1999; Gultepe *et al.*, 2007; Herman & Schumacher, 2016; Smith *et al.*, 2002). Nevertheless, after examining the effects of numerous environmental and meteorological variables on atmospheric visibility at TIA, a numerical model was created for visibility forecasting.

In order to have a more profound understanding of the various elements that influence visibility, a Pearson correlation analysis between visual information, air pollutants (PM2.5), and meteorological variables (T, WS, and RH) (**Figure 26**) was performed. A positive correlation between T and VIS ($r = 0.62$, $p < 0.001$); a negative correlation between RH and VIS ($r = -0.39$, $p < 0.001$), and PM2.5 and VIS ($r = -0.65$, $p < 0.001$); and a very small positive correlation between WS and VIS ($r = 0.04$, $p < 0.001$) were seen. The strongest anti-correlation found between PM2.5 and VIS suggests that atmospheric air pollution is the primary determinant of visibility. Air pollutants in the atmosphere increase air light in the sight path thus obscuring visibility through attenuation of light.

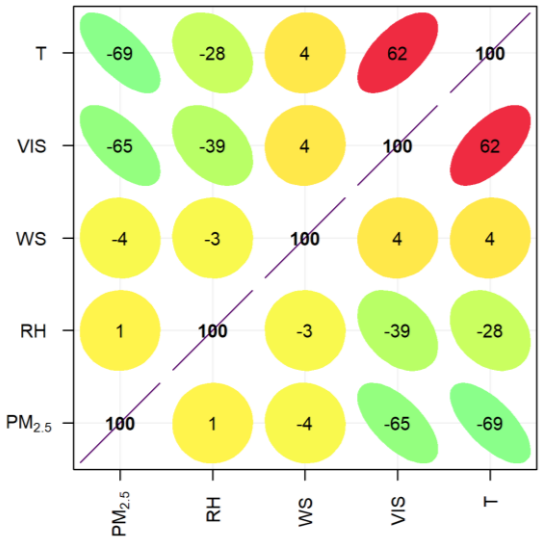

Figure 26: Correlation matrix showing the relationship between different meteorological variables measured in Tribhuvan International Airport (TIA) and fine mass concentration (PM2.5 (μg/m^3)) measured at US Embassy, Phora Durbar, Kathmandu, in the year 2020. Where T, VIS, WS, and RH denote ambient temperature (ºC), atmospheric visibility (km), wind speed (m/s), and relative humidity (%)

While ambient temperature (T) governs the diurnal cycle of boundary layer height (BLH) in the atmosphere. The increased temperature destroys static stability and elevates BLH, making more room available for air pollutants to mix vertically which brings about the VIS improvement. Whereas, the impact of RH on VIS is rather a complex phenomenon. It varies with the level of ambient pollution. With the increase in RH, hygroscopic aerosols greatly increase PM concentration and light extinction capability that eventually impairs VIS. Likewise, increased wind speed promotes horizontal diffusion of pollutants reducing the pollution concentration near the surface resulting in improved VIS.

To examine the relationships between VIS and two of the major factors (PM2.5 and RH) affecting it, scatter plots and fitted regression functions of their hourly averages for one year (2020) have been visualized (**Figure 27**). Here, RH was classified into four ranges: RH ≤ 60%, 60% < RH ≤ 80%, 80% < RH ≤ 90%, and RH > 90 %. We observe that as PM2.5 concentration rises in each RH range, VIS drops exponentially. Thus, a functional relationship between the two can be reasonably presumed, i.e.:

$$\text{VIS} = f(PM_{2.5}) \tag{50}$$

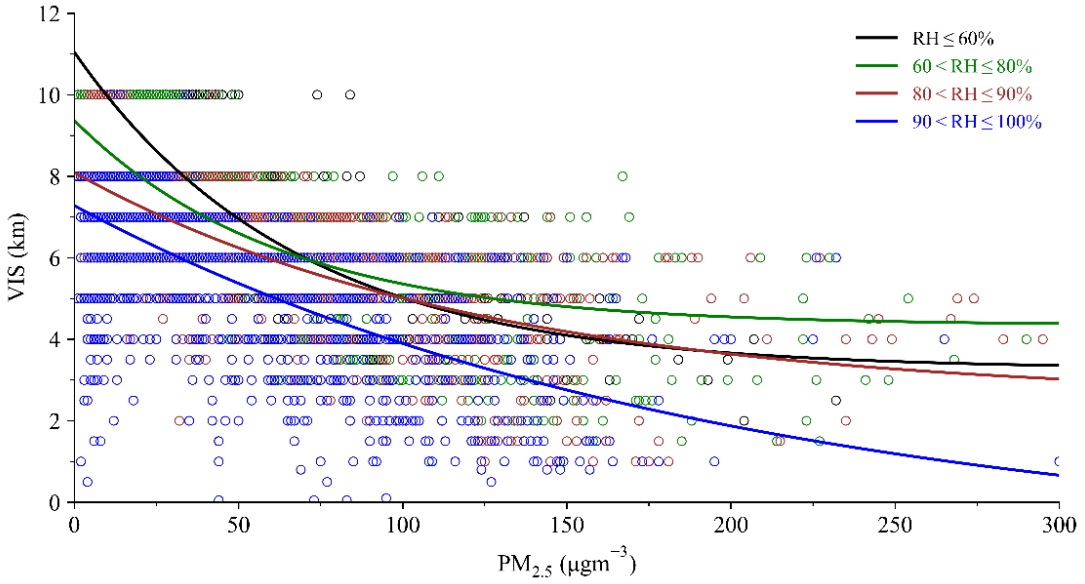

Figure 27: Hourly mean visibility (VIS) vs. hourly average PM2.5 concentration at TIA, Kathmandu in 2020 according to different relative humidity (RH) categories. Data points are color-coded by RH.

Initially, VIS decreases sharply with increased PM2.5; however, when PM2.5 concentration exceeds certain levels (e.g., 100 μg/m^3)—different for different RH ranges—the change in VIS is not as sensitive as a change in PM2.5. A lower correlation between PM2.5 and VIS was also observed with increasing RH (**Table 13**). This suggests that even with low PM2.5 concentration, VIS is lower at greater relative humidity (> 80%). In this scenario, abundant water vapor covers the particle surfaces, increasing aerosol scattering efficiency and severely reducing visibility. Furthermore, when RH increases, the maximum visibility decreases for various RH ranges.

A single-parameter regression equation like the above (**Eq. (50)**) cannot forecast VIS in other locations or times. It does not include the effect of other environmental variables, like, NO_2, O_3, CO, T, WS, etc. Nevertheless, the above exponential relationship between PM2.5 and VIS shall form the basis of the forecasting visibility model under different RH ranges.

Table 13: Regression models of atmospheric visibility under different RH in Tribhuvan International Airport, Kathmandu (Jan–Dec 2020). Where; T, VIS, WS, RH, and PM2.5 denote ambient temperature (ºC), atmospheric visibility (km), wind speed (m/s) and relative humidity (%), fine mass concentration (PM2.5 (μg/m3)) respectively. R2 refers to the coefficient of determination of the regression model, "r" refers to the Pearson correlation coefficient between VIS and PM2.5, and "p" refers to the p-value.

Stepwise Regression model	**RH Category**	R^2	R
$VIS = (8.292 \pm 0.004)e^{-(0.02)PM_{2.5}} + (0.026 \pm 0.006)T + (3.181 \pm 0.005)$	RH ⩽60%	0.63	−0.77, p<0.001
$VIS = (5.822 \pm 0.003)e^{-(0.01)PM_{2.5}} - (0.021 \pm 0.004)T - (0.029 \pm 0.005)RH - (0.06 \pm 0.02)WS + (5.9 \pm 0.3)$	60% < RH ⩽ 80%	0.59	−0.74, p<0.001
$VIS = (6.0 \pm 0.1)e^{-(0.009)PM_{2.5}} - (0.04 \pm 0.01)RH + (5.8 \pm 1.1)$	80% < RH ⩽ 90%	0.54	−0.71, p<0.001
$VIS = (6.55 \pm 1.11)e^{-(0.006)PM_{2.5}} - (0.17 \pm 0.01)RH + (0.035 \pm 0.005)T + (16.3 \pm 2.4)$	RH > 90 %	0.52	−0.64, p<0.001

In the process of developing a brief model capable of predicting VIS at TIA airport, it was presumed that apparent VIS at the airport is the result of a combination of various factors affecting air pollution as well as meteorological variables as shown in the following equation:

$$\text{VIS} = f(PM_{2.5}) + f(RH, T, NO_2, O_3, \ldots)) \quad (51)$$

Or,

$$VIS = f(PM_{2.5}) + \sum_i a_i x_i + \varepsilon$$

(Zhang *et al.*, 2019)

Here, x_i denotes any important factor affecting VIS; a_i represents a coefficient of linear regression, and ε is the error term.

Equivalently,

$$\text{VIS} - f(PM_{2.5}) = \sum_i a_i x_i + \varepsilon \quad (52)$$

(Zhang *et al.*, 2019)

Therefore, the difference between VIS and the functional relation between VIS and PM2.5 can be expressed as a linear sum of the rest of the factors.

Firstly, regression parameters were obtained from exponential fitting (**Figure 27**). These parameters were used as the initial values of modeling fit. Then, a multiple linear regression between residues of prediction (LHS of **Eq.(52)**) and the remaining parameters was carried out. Based on their importance determined by stepwise procedure, we chose and included each independent parameter (s) into the final multiple nonlinear regression model. After many rounds of regression and iteration, a model was eventually developed that incorporates the main affecting factors besides PM2.5 (**Table 13**). It showed that under different RH ranges, the main contributors to the VIS are different and their influence is additive. It is seen that PM2.5 is the main contributor in all RH ranges. Besides it, T contributes to VIS when RH ≤ 60%; T, RH, and WS contribute when 60% < RH ≤ 80%; RH contributes to VIS when 80% < RH ≤ 90%; and RH and T contribute when RH > 90%. At high RH (RH > 90%), temperature shall affect VIS by influencing the condensation of water vapor.

The validity of the nonlinear model combining exponential and multiple linear regression was examined using test data spanning a year (Jan–Dec 2019) observed at TIA. **Figure 28** presents observed VIS versus simulated VIS based on the models (**Table 13**). Compared to the single parameter regression models (**Figure 27**), the nonlinear multiple regression model (**Table 13**) performs better in predicting VIS with generally higher R^2.

Figure 29 shows a time series plot of the daily averages of observed visibility (VIS_{obs}) and the predicted visibility (VIS_{sim}) by the nonlinear regression model. It was noticed that observed visibility at TIA is higher in wet months (Jun Jul Aug Sep) when the PM2.5 level is lower in the atmosphere, and lower in dry months (Oct–May) when PM2.5 elevates in Kathmandu's atmosphere. The simulated visibility also follows suit. Thus, simulated visibility is highly consistent with observed one, i.e., it closely captures day-to-day variation and seasonal changes that may occur in observed visibility.

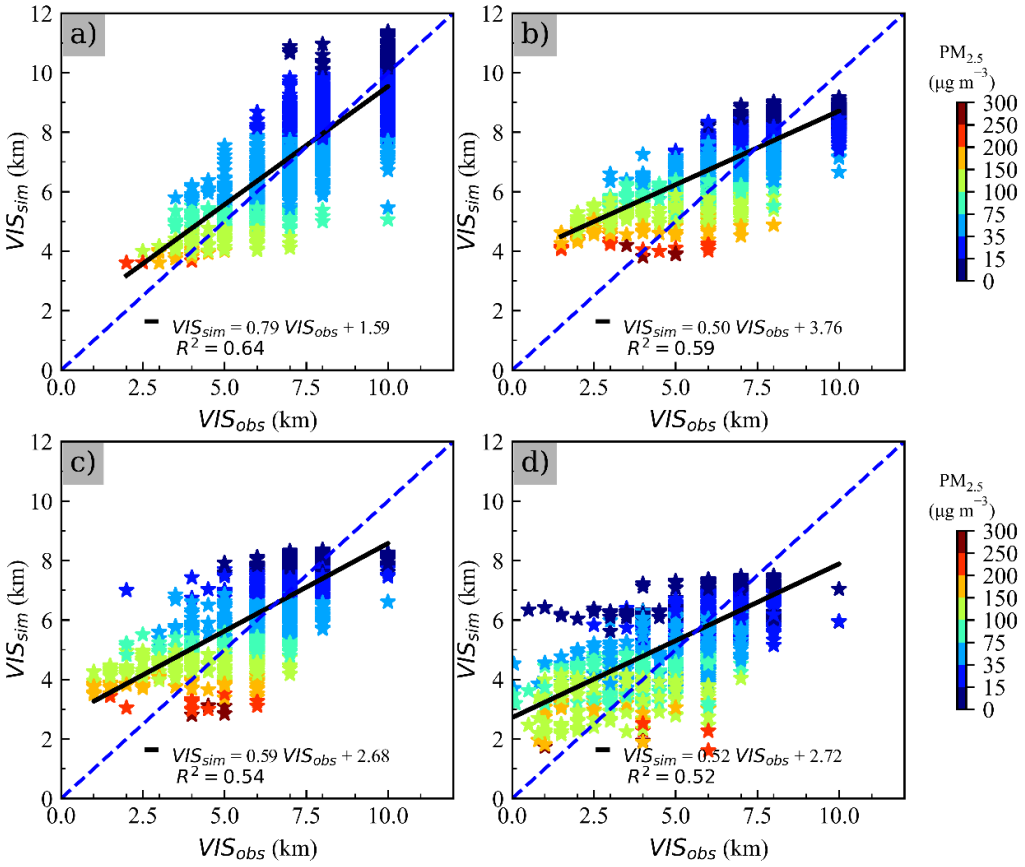

Figure 28: Comparison between hourly-observed visibility (VIS_{obs}) and model-simulated visibility (VIS_{sim}) during 2020 in Kathmandu: **(a)** RH ≤ 60%, **(b)** 60% < RH ≤ 80%, **(c)** 80% < RH ≤ 90%, **(d)** RH > 90 %**.** Data points are color-coded according to the level of PM2.5.

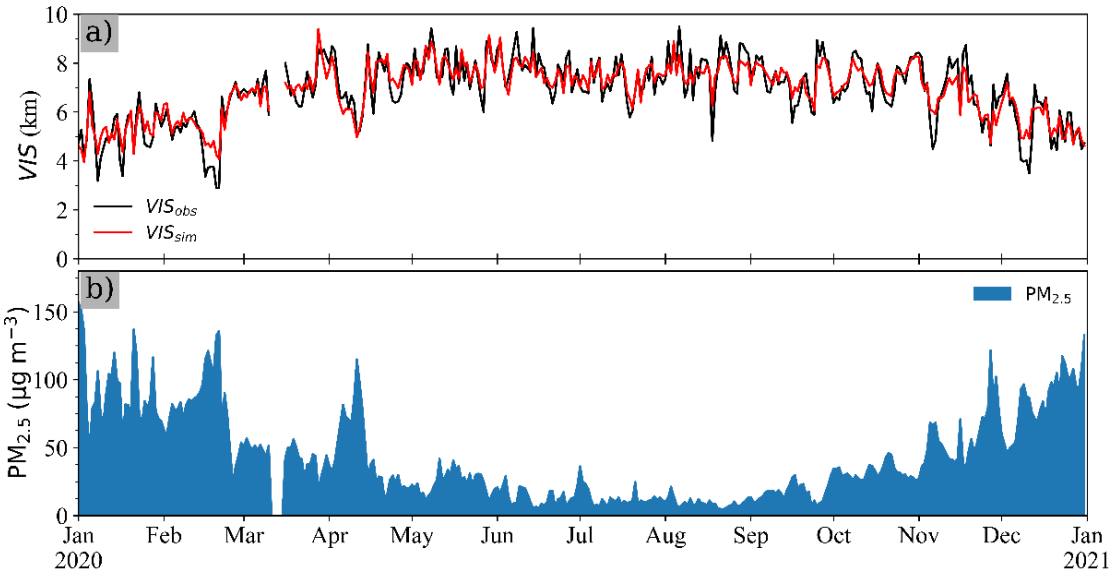

Figure 29: Time series of: **(a)** daily-observed visibility (VIS_{obs}) and daily-simulated visibility (VIS_{sim}) by the stepwise regression model, and **(b)** PM2.5 in Kathmandu (2020)

There are many advanced models available for visibility predictions. Numerical Weather Prediction (NWP) Models have been widely used in the past (e.g., Arun *et al.*, 2022; Gultepe *et al.*, 2006; Singh *et al.*, 2018) for visibility predictions, elsewhere. As artificial intelligence and Internet of Things (IoT) sensor technologies continue to advance, intelligent identification and analysis based on video data is becoming more and more popular in visibility prediction and detection (Babari *et al.*, 2011; Zhai and Cheng, 2020). Several authors (e.g., Liu *et al.*, 2022; Wang *et al.*, 2020) have used deep learning technology in visibility forecasts, too.

Similar to this study, various researchers (e.g., Wen and Yeh, 2010; Zhang *et al.*, 2018) also have developed simple multiple linear regressions illustrating the effect of air pollutants and meteorological conditions on visibility elsewhere in the past. Furthermore, various empirical regression models employing logarithm of coarse particle concentration were developed for visibility in Guangzhou, Shanghai, and Beijing (e.g., Lin *et al.*, 2012; Tsai, 2005). Additionally, several studies have suggested that visibility is a linear response to the exponential function of PM2.5 concentrations in specific ranges of RH (e.g., Cao *et al.*, 2012; Yu *et al.*, 2016; Shen *et al.*, 2016). These papers collectively suggest that the impact of meteorological and air pollution on visibility is complex and non-linear.

The regression model that we developed in this study is an extended work aiming to develop a simple equation connecting basic factors affecting visibility as done by previous researchers, mentioned above. However, the acceptable degree of consistency of our regression model implies that this model using air quality and meteorological variables as inputs may serve as a practical approach to predict visibility at TIA. To our knowledge, though simple, this model is the first of its kind in TIA for visibility predictions. It may serve as a foundation stone for developing a more sophisticated visibility model in the future.

4.3 Winter haze and fog in Kathmandu

4.3.1 Long-term trend of haze and fog

Interannual variation of frequency of haze during winter (DJF) over the study period (**Figure 30**(a)) reveals that haze occurrence in Kathmandu's atmosphere was very little (< 30% of winter days) up until the year 1990. This suggests Kathmandu had a clear sky with good visibility. The haze frequency gradually rose, attaining a value (< 60%) about double the preceding period until the year 2000. The year 2000 marks a sudden jump in haze frequency near its saturation (~ 100% of winter days). It has remained more or less the same (max number of haze days) since the year 2000. Thus, the whole data was divided into two periods 1976–2000 (regime-I) and 2001–2022 (regime-II), and further analyzed. Trend results (**Table 14**) also reveal a definitive increase in haze day frequency for this study period (2.36% day yr^{-1} at 0.001 significance level before the year 2000 and 0.36% day yr^{-1} at 0.05 significance level after the year 2000). However, the frequency of winter fog in Kathmandu (**Figure 30**(b)) remained mostly below 20% until the year 1998, which rose to 66% in the year 2001, and again declined to 13% in the year 2006.

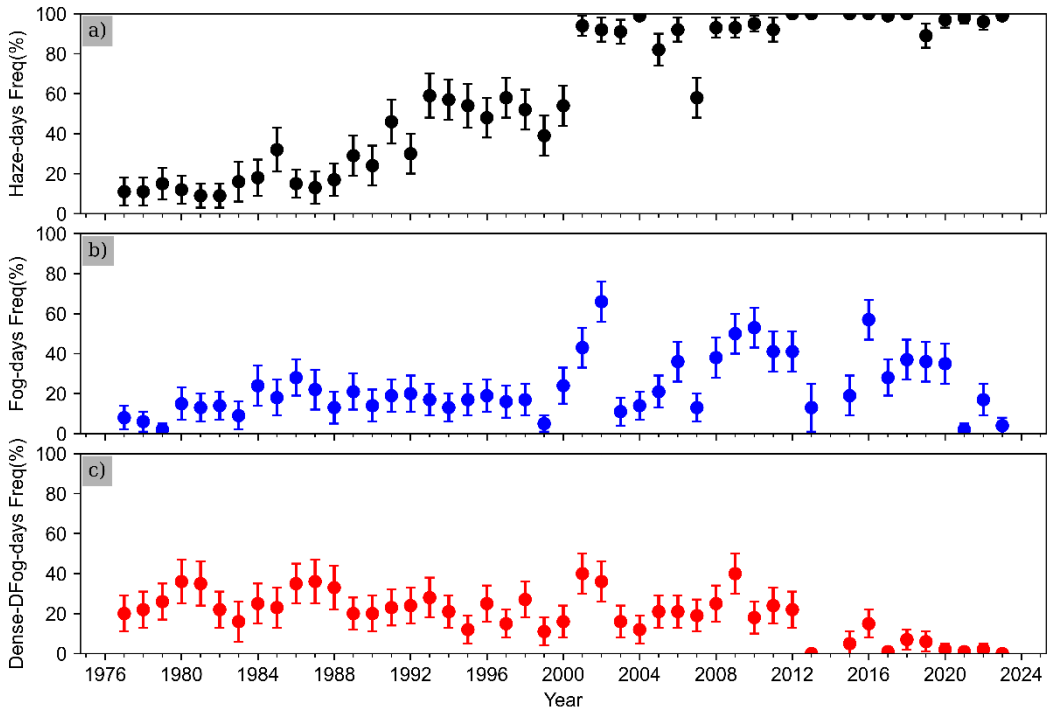

Figure 30: Time evolution in the percentage frequency of: (a) haze days, (b) fog days, and (c) dense-fog days in the winter season (DJF) at Tribhuvan International Airport (TIA), Kathmandu, from 1976 to 2023. The error bars indicate the Margin of Error (MoE)

Table 14: Trend results of occurrence frequency of haze, fog, and dense fog days in winter (DJF) at Tribhuvan International Airport (TIA) in Kathmandu from 1976 to 2022 using MK-Test and Sen's slope. CI denotes the confidence interval.

	Period	Mann-Kendall		Sen's slope	
		Z_{MK}	p –value	Trend Q (% yr^{-1})	CI %
Occurrence frequency of haze days (%)	1976-2000	4.79	< 0.001	2.36*	[1.00, 3.69]
	2001-2022	2.01	0.044	0.36†	$[-0.12, 1.75]$
	1976-2022	7.34	< 0.001	2.34*	[1.79, 3.00]
Occurrence frequency of fog days (%)	1976-2000	1.92	0.055	0.46†	$[-0.45, 1.25]$
	2001-2022	−0.91	0.364	-0.56^{ns}	$[-2.78, 3.83]$
	1976-2022	2.52	0.012	0.46†	$[-0.06, 1.04]$
Occurrence frequency of dense-fog-days (%)	1976-2000	−0.89	0.374	-0.25^{ns}	$[-0.75, 0.25]$
	2001-2022	−3.23	0.001	−1.28**	$[-1.84, 0.13]$
	1976-2022	−4.07	< 0.001	−0.53*	$[-0.79, 0.00]$

*- 0.001, ** - 0.01, and † – 0 .05 level of significance ; ns – non significant

It displayed a secondary peak value (57%) in the year 2015 and started declining. Surprisingly, only 2 days out of 88 winter days (data available) during the winter of 2020 witnessed fog. It rose to 17% in the year 2021. Again, in the winter of 2022, only four foggy days were observed out of 90 days. Trend result of fog days revealed an upward trend (0.46% day yr^{-1} at 0.05 significance level) in regime I.

Although the yearly relative frequency of fog days is usually higher than in the previous period, there is no such significant trend in regime II (**Table 14**). On the contrary, the relative frequency of dense-fog days showed no trend in the previous period but a declining trend (-1.28% day yr^{-1} at 0.01 significance level) in regime II. There was little variation (variance = 0.6%) in occurrence frequency up until the year 2011(**Figure 30**(c)). During this period, the year 1998 saw the fewest dense-fog episodes (11% of available winter days), while the year 2000 saw the most (40%) of these episodes. Dense fog events were below 10% after the year 2016. Dense fog was observed in only one day in the winter of 2020, two days in 2021, and none in the year 2022.

Other studies (De & Dandekar, 2001; Saikawa *et al.,* 2019; Sarkar *et al.,* 2006; Syed *et al.,* 2012) have also documented a rise in regional haze and fog occurrences over time in Hindu Kush Himalayan (HKH)—the region where the KTM valley lies.

The level of air pollution in the atmosphere is detrimental to the existence and intensity of haze. Due to its distinct bowl-shaped topography, atmospheric conditions, and an increase in local emission sources, the Kathmandu Valley is particularly vulnerable to air pollution (Becker *et al.*, 2021; Mool *et al.*, 2020; Panday *et al.*, 2009). During winter, the valley's atmosphere experiences the highest levels of ground-level air pollution (Aryal *et al.*, 2008; Becker *et al.*, 2021; Putero *et al.*, 2015) makes KTM Valley occasionally rank as having the worst particulate air pollution levels worldwide (Becker *et al.*, 2021). Wintertime particulate pollution in the valley comes from diverse local emission sources, e.g., traffic fleets (Mool *et al.*, 2020; e.g., Shrestha *et al.*, 2013), refuse burning, industries, dust from poor road networks, brick kilns, open burning of municipal solid waste (Saikawa *et al.*, 2020; Zhong *et al.*, 2019), domestic biofuel usages (Zhong *et al.*, 2019). Besides local emissions, the transboundary flow of air pollutants emitted in the IGP—a global hotspot of air pollution—too affects level of the air pollution in the valley (Khanal *et al.*, 2022; Mahapatra *et al.*, 2019) under favorable synoptic conditions.

In KTM, meteorology also a vital role in air pollution mixing, diffusion, and scavenging. Near-surface temperature and wind speed are the lowest in **Table 15** in the winter months at Kathmandu. Strong temperature inversions during the night cause a cold air pool to form above the valley basin, trapping air pollution close to the ground and causing a high level of air pollution; as the day goes on, the cold air pool dissipates as incoming solar radiation heats the surface, lowering particulate matter (Panday *et al.*, 2009; Panday & Prinn, 2009). Mues *et al.* (2017) also reported having a low Mixing Layer Height (MLH) and Ventilation Coefficient (VC) during wither in the valley that suppresses buoyant vertical transport of air pollutants. Rain scarcely occurs in the valley during winter—making precipitation scavenging a rare seasonal phenomenon. All of the above factors—air pollution emissions and meteorological—contribute to the intensification of winter haze.

Through the analysis of Copernicus Atmosphere Monitoring Services (CAMS)-PM2.5 reanalysis data of Kathmandu for 2003–2019, Becker *et al.* (2021) revealed that the winter season witnessed the highest increase in PM2.5 levels ($\sim 2\ \mu g\ m^{-3}$) annually. Considering visibility as a proxy of air pollution, the present study using multi-decadal data, also suggests similar deteriorating winter air quality in the valley.

Table 15: Seasonal average values of different meteorological parameters namely, visibility, temperature, dew-point temperature, relative humidity, and wind speed at Tribhuvan International Airport (TIA) in Kathmandu from Nov 1976 to 2023. The bold-faced numeric values are the highest and lowest monthly averages

Parameter	Jan	Feb	Mar	Apr	May	Jun	Jul	Aug	Sep	Oct	Nov	Dec
Visibility (km)	**5.83±**	6.41±	6.85±	7.13±	8.35±	8.69±	8.50±	**8.70±**	8.57±	8.44±	7.41±	6.24±
	0.06	0.07	0.07	0.07	0.07	0.07	0.06	**0.06**	0.06	0.07	0.07	0.06
Temperature (°C)	**10.51±**	13.39±	17.29±	20.81±	22.38±	24.10±	23.82±	**23.94±**	22.93±	20.23±	15.47±	11.59±
	0.07	0.08	0.08	0.08	0.06	0.05	0.04	**0.04**	0.04	0.06	0.07	0.07
Dew point	**5.00±**	6.85±	9.05±	11.62±	16.05±	19.67±	20.95±	**20.93±**	19.76±	15.33±	10.12±	6.25±
Temperature (°C)	**0.03**	0.03	0.05	0.06	0.04	0.03	0.02	**0.02**	0.02	0.05	0.04	0.04
Relative Humidity (%)	73.6±	70.1±	64.1±	**62.4±**	72.0±	79.1±	**85.8±**	84.9±	84.1±	76.8±	74.9±	74.4±
	0.3	0.3	0.3	**0.3**	0.3	0.2	**0.2**	0.2	0.2	0.3	0.3	0.3
Wind Speed (m/s)	**2.3±**	2.8±	3.6±	**3.8±**	2.9±	2.7±	2.7±	3.0±	2.4±	2.7±	2.5±	2.5±
	0.3	0.3	0.5	**0.5**	0.3	0.3	0.4	0.4	0.2	0.4	0.4	0.4

Possible reasons could be either an increase in wintertime air-pollution-activities—local and/or transboundary—or a meteorological impact. Looking at the trend of possible meteorological parameters (**Table 16**), a slight upward trend (0.28% /year at α = 0.05) of RH in regime-I was seen, which might have played a contributory role in haze enhancement. In regime II, RH reversed the trend (-0.46 %/year at α = 0.01); already a higher level of air pollution should have outplayed the role of RH in this period. Though little, slowing down of the wind since 2000 (-0.02 m/s/year at $\alpha = 0.05$) might have contributed to the intensification of winter haze in Kathmandu in regime II. Detailed analysis of the increase in air pollution emission is beyond the framework of the current study. Deterioration of visibility over long periods can be seen as a manifestation of changing air pollution rather than meteorological effects (P. Zhao *et al.*, 2011). Thus, it is reasonable to mainly link this to a significant increase in anthropogenic air pollution sources ranging from road/air traffic, and industrial activities, to refuse burnings—commensurate with the rapid increase in population (~ 4% per annum) (Timsina *et al.*, 2020) of the valley. Intensification of haze in the IGP region during the same period has been reported in tens of papers (e.g., (De & Dandekar, 2001; Kathayat *et al.*, 2023; Saikawa *et al.*, 2019; Sarkar *et al.*, 2006)).

Table 16: Trend results of meteorological parameters: Relative Humidity (RH), temperature (T), and Wind Speed (WS) in winter (DJF) at Tribhuvan International Airport (TIA) in Kathmandu from 1976 to 2022 using MK Test and Sen's slope . CI denotes the confidence interval.

		Mann-Kendall		**Sen's slope**	
	Period	Z_{MK}	p –value	Trend Q (% yr^{-1})	CI %
Relative Humidity (RH) (%)	1976-2000	2.55	0.011	0.28†	[−0.10, 0.65]
	2001-2022	−2.87	0.004	−0.46**	[−0.94,0.64]
	1976-2022	−1.24	0.215	-0.06^{ns}	[−0.20, 0.18]
Temperature (T) (℃)	1976-2000	0	1.0	0.00^{ns}	[−0.13, 0.13]
	2001-2022	−1.48	0.14	-0.06^{ns}	[−016, 0.12]
	1976-2022	3.06	0.002	0.04**	[0.01, 0.09]
Wind Speed (WS) (m/s)	1976-2000	0.37	0.708	0.01^{ns}	[−0.06, 0.47]
	2001-2022	−1.96	0.049	−0.02†	[−0.03,0.01]
	1976-2022	−3.37	<0.001	−0.02*	[−0.03,0.00]*

*- 0.001, ** - 0.01, and † – 0 .05 level of significance ; ns – non significant

Thus, the observed haze uptrend in KTM can also be attributed to the transboundary transport of IGP haze especially from Crop Residue Burning (CRB) from northern parts of India and Pakistan after post-monsoon rice harvest.

Fog requires sufficient moisture and cloud condensation nuclei (CCN) as key ingredients for its formation (Gultepe *et al.*, 2007). Kathmandu Valley experiences radiation fog early the next morning after a cold, calm, and clear-sky previous night when the land surface cools below the dew point temperature by loss of heat by radiation cooling—creating a temperature inversion. The occurrence of widespread radiation fog in the IGP plains is a well-studied winter phenomenon.

Tens of papers have reported increasing frequency of both fog types (fog and dense-fog) elsewhere in the IGP region (e.g., Ghude *et al.*, 2017; Jenamani, 2007; Kathayat *et al.*, 2023; Shrestha *et al.*, 2018; Syed *et al.*, 2012) as well as central and eastern China (Niu *et al.*, 2010). Many (Kathayat *et al.*, 2023; Niu *et al.*, 2010; Sarkar *et al.*, 2006; Syed *et al.*, 2012) have attributed this to the increase in air pollution and thus abundance of CCN, resulting in more water droplets with higher optical depth (Syed *et al.*, 2012). According to Yan *et al.* (2020), aerosols increase droplet concentration and Liquid Water Content (LWC) while reducing effective droplet size, which in turn promotes fog. Some works of literature have also pointed out the possible change in land cover use and irrigation area (Kathayat *et al.*, 2023; Shrestha *et al.*, 2018), and regional meteorological change (Niu *et al.*, 2010). In addition to the looking at trend of plausible parameters (e.g., RH and WS), the trend in Dew-point Depression (T_{dep})—the difference between ambient temperature (T) and dew-point temperature (T_d)—was estimated, similar to the work of Kutty *et al.* (2020). If dew point depression is low, the saturation of air is more likely, and hence the fog formation provided other conditions are met. In addition to elevated air pollution, declining nighttime T_{dep} (-0.03 ℃/year at $\alpha = 0.05$) (**Table 17**) might have contributed to the observed increased trend of fog during 1976–2000. Whereas, the decreased RH (-0.70 % /year at $\alpha = 0.001$), and increase in T_{dep} (0.13 ℃ /year at $\alpha = 0.001$) should have contributed to the decline in dense fog occurrence since 2000. An increase in average nighttime temperature (0.14 ℃ /year at $\alpha = 0.01$) was observed in the later period (2001–2022).

Table 17: Trend results of winter-season average values of nighttime meteorological parameters, namely, Relative Humidity (RH), Temperature (T), Dew-point Depression (T_{dep}), and Wind Speed (WS) in winter (DJF) at Tribhuvan International Airport (TIA) in Kathmandu from 1976 to 2022 using Mann-Kendall and Sen's slope estimator. CI denotes the confidence interval.

	Period	Mann-Kendall		Sen's slope	
		Z_{MK}	p –value	Trend Q (% yr^{-1})	CI %
Relative Humidity (RH) (%)	1976-2000	1.89	0.059	0.18 ^{ns}	[−0.17,0.43]
	2001-2022	−3.44	<0.001	−0.70*	[−1.13, 0.18]
	1976-2022	−1.93	0.05	−0.11^{ns}	[−0.29, 0.10]
Temperature (T) (℃)	1976-2000	0.58	0.559	0.01^{ns}	[−0.05,0.10]
	2001-2022	2.68	0.007	0.14**	[0.06, 0.34]
	1976-2022	3.75	<0.001	0.07*	[0.01, 0.11]
Dew point Depression (T_{dep}) (℃)	1976-2000	−2.19	0.028	−0.03†	[−0.05, 0.00]
	2001-2022	3.29	<0.001	0.13*	[0.03, 0.25]
	1976-2022	1.67	0.10	0.02^{ns}	[−0.01, 0.06]
Wind Speed (WS) (m/s)	1976-2000	0.53	0.597	0.01^{ns}	[−0.03, 3.43]
	2001-2022	−1.43	0.153	−0.01^{ns}	[−0.09, 0.03]
	1976-2022	0.47	0.64	0.00^{ns}	[0.00,0.00]

*- 0.001, ** - 0.01, and † – 0 .05 level of significance ; ns – non significant

Kathmandu Valley is one of the fastest-growing metro cities in South Asia (Timsina *et al.*, 2020). Because of the increased population, agricultural land and other vegetation land coverage have shrunk considerably in later periods. This can be visible in satellite imagery of Kathmandu taken 60 years apart (**Figure 31**). This vast change in land cover use led to a diminished source of moisture—one of the most important ingredients for the genesis of fog—as evidenced by a decrement in RH. Decreased moisture content in the atmosphere results in decreased dew point temperature and increased dew point depression as seen above. This may explain the reduced occurrence of dense fog in the later period.

This study leads us to the reasonable conclusion that rising aerosol pollution should have been the cause of the observed upward trend of general fog (regime-I) in Kathmandu. Whereas, the more rapid declining trend in dense-fog occurrence (regime-II) should be the result of the reduction in agricultural land and vegetation cover resulting in reduced evapotranspiration and thus a reduction in the source of ambient moisture.

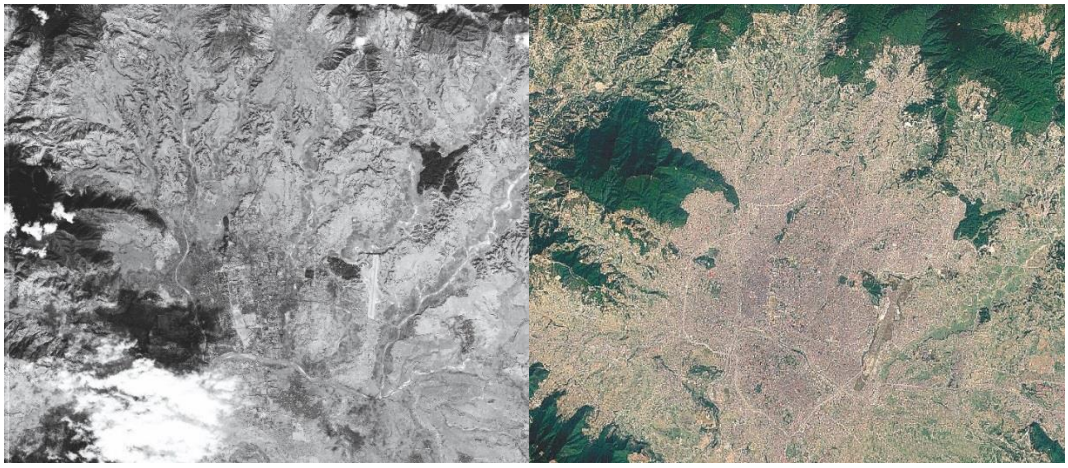

Figure 31: Satellite image taken on 5 February 1967 (left) showing the broad floodplains of rivers flowing through the Valley floor and open areas and agricultural lands in and around TIA and Google Earth map taken on 20 April 2022 (right) showing urbanization of the Valley (Dixit, 2022)

With the reduced occurrence of dense fog in KTM, morning visibility in winter is usually above the minimum visibility required to operate flights at the airport. This has made it easier to operate morning flights in recent years based on the experience of the author himself and other pilots who have operated flights during later periods in TIA.

4.3.2 Microclimatic properties of fog

Figure 32 shows the occurrence frequency of fog (dense-fog) days having witnessed fog of a certain duration at a stretch and intensity. It was observed that most of the fog (~86% of fog days) and dense fog (~95% of dense fog days) at TIA lasted a very brief period (< 1 hour). Although there were some days having fog continuously occurring for up to 6 hours, these were very rare for dense fog. Winter fog onset and dispersal timing are shown in **Figure 33**. In December, fog usually starts to form as early as 04:45 am local time (LT) until 09:45 am in and around TIA. A very small percentage of fog occurrences were even recorded at 11:00 pm too. The most favorable time was 05:15 am when about 23% of all fog onsets occurred. Whereas, fog onset takes place between 03:15 to 09:45 am in January with the most favorable onset time being 06:45 am when more than 16% of all onset happen. The fog onset window is narrow in February; it occurs between 04:45 am and 09:15 am, with the highest onset at 06:45 am. Regarding dispersion of fog, it occurs during 05:45–10:45 LT in Dec, 04:45–12:15 LT in Jan, and 05:45–10:15 in Feb. The most favorable times of dispersion of fog are 06:15 LT in Dec and 07:45 LT in January and February. Likewise, the onset and dispersal time of dense fog during winter at TIA has been shown in **Figure 34**.

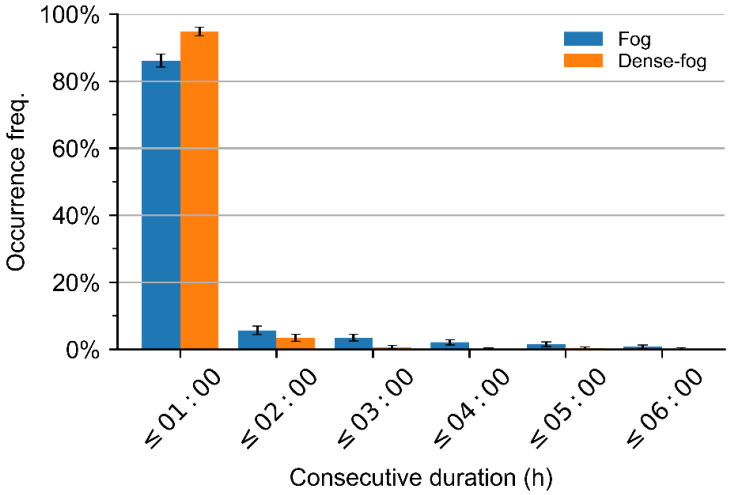

Figure 32: Consecutive duration of fog and dense fog in winter (DJF) at Tribhuvan International Airport, Kathmandu from 1976 through 2023. The error bars represent a 95% confidence interval of a single proportion

Dense-fog onset usually occurs in 03:45–08:45 am in Dec, 02:15–09:15 am in Jan, and 05:15–08:15 am in Feb. Most of the dense fog onset occurs at 05:15 and 08:15 am in all three months. Dispersal timings are 04:45–09:45, 03:45–10:15, and 06:15–09:45 am in Dec, Jan, and Feb respectively. Most of the dense fog dispersal takes place at 06:15 and 09:15 am in all three-winter months. This is in line with previous observations of the highest percentage of dense-fog onset at 05:15 and 08:15 am.

Investigation of the consecutive duration of winter fog in Kathmandu revealed that the maximum percentage of fog (dense fog) events in Kathmandu do not last long—less than one hour. Only very few days witnessed fog (dense fog) lasting up to 6 h (2 h). Fog in Kathmandu exhibits a sharp contrast to fog in the IGP region. Jenamani (2012) reported having a higher duration fog of up to 18 hours over Indira Gandhi International Airport (IGI) in Delhi. Persistent fog spells (also called '*seetlahar*') lasting up to a few days in a stretch is a common phenomenon in the IGP region, including in the Terai plains of Nepal, during December and January. It was found that the onset of fog in the valley occurs in the early morning and dispersal occurs before noon. The onset of fog usually takes a longer duration, as the ambient temperature gradually falls overnight and reaches dew point temperature before the fog starts forming. However, the dispersal takes a shorter duration as the increase in ambient temperature occurs faster when the sun passes overhead or the wind becomes stronger (Jenamani, 2012).

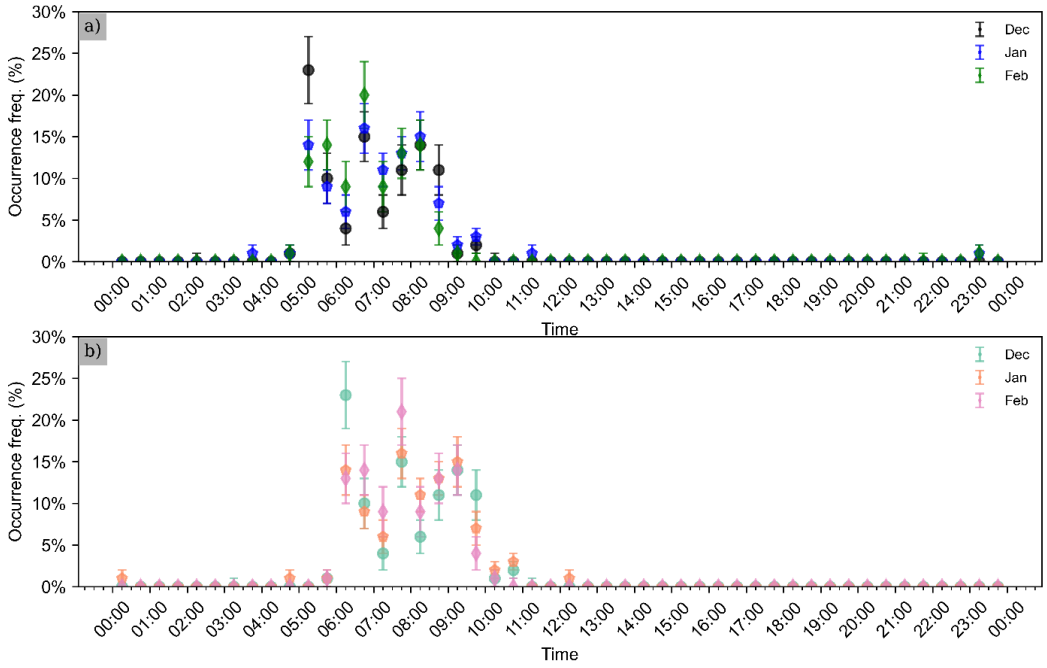

Figure 33: Occurrence frequency of: (a) onset, and (b) dispersal of winter fog (general) in Tribhuvan International Airport (TIA), Kathmandu, from 1976 to 2023. The error bars represent a 95% confidence interval of a single proportion

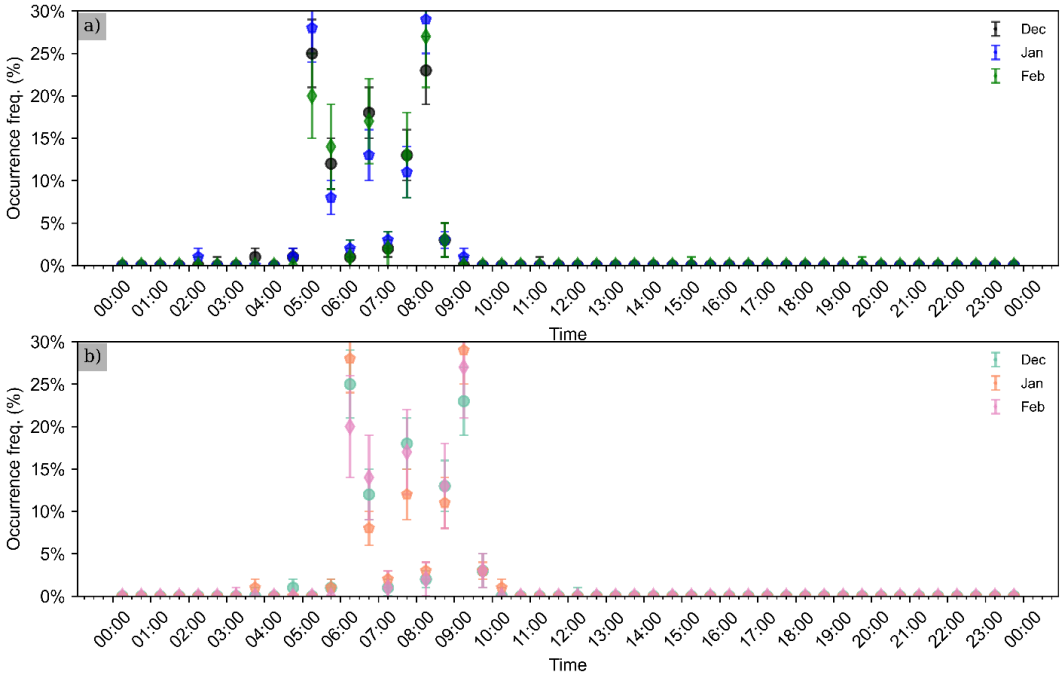

Figure 34: Occurrence frequency of: (a) onset, and (b) dispersal of winter dense fog in Tribhuvan International Airport (TIA), Kathmandu, from 1976 to 2023. The error bars represent a 95% confidence interval of a single proportion

Winter fog (dense fog) was found to have a wider onset/dispersal window at Bhairahawa Airport (Kathayat *et al.*, 2023).

CHAPTER 5

CONCLUSIONS AND RECOMMENDATIONS

This study assessed the temporal (in different time scales: seasonal, interannual) variability of atmospheric visibility (VIS), the impact of most plausible factors on visibility, and the implication to aviation in Nepal using a climatological dataset spanning over four decades (1976–2022), air pollution data set (in-situ, remote sensing and reanalysis) and most recent radio soundings measurements (November 2019–March 2022). Based on the availability of data and previous research, and the strategic significance of aviation in Nepal, two international airports: Tribhuvan International Airport (TIA) in Kathmandu (KTM) and Gautam Buddha International Airport (GBIA)—a recently upgraded international airport—at Bhairahawa (BWA) were chosen. For better preparedness to lessen damage potential to aviation, some of the key microclimatic behaviors of winter fog—one of the biggest challenges in winter flight operations in Nepal—were also evaluated at both airport stations. Meanwhile, as an initial effort to obtain sounding-based PBLH climatology in Nepal, different algorithms were developed and validated to estimate boundary layer heights from vertical profiles of L-band radiosonde measurements. Based on the findings of this study, the following conclusions and recommendations are made.

5.1 Conclusions

There is obvious diurnal, seasonal, and inter-annual variation in atmospheric visibility at both GBIA and TIA, commensurate with variation in solar radiation flux, atmospheric pollution level, and dispersion mechanisms. It was found that haze, specifically in winter and post-/pre- monsoon season impairs visibility, whereas winter fog limits visibility during winter.

There has been a consistent decline in visibility over GBIA in all seasons. Poor visibility events and haze days increased in all seasons—the biggest rise in post-monsoon season—and winter-fog day frequency has almost doubled. The increased uptrend of haze and overall poor visibility events have resulted from regionally increased air pollution in Indo-Gangetic Plains (IGP). In winter, an increase in fog and haze frequency results from increased seasonal RH and a slowing down of surface wind speed. A comparison of poor-visibility occurrences in winter among four neighboring

airports in IGP revealed that BWA witnessed a gradual increase while the rest of the airports showed already peaked occurrences. This is attributed to the changes in the level of local air pollution in the respective cities.

Kathmandu Valley also witnessed a sharp increment in the number of haze days in winter. Haze intensifies during winter in the Kathmandu valley owing to the intensified air pollution, weaker air-pollution-dispersion-mechanism (colder air, slower wind, shallow boundary layer, and no rain), and unique topography of the valley. This has increased exceedingly over the study period mainly because of increased local air pollution. Increased RH in the winter season in regime I (1976–2000), and slowing down of wind in regime II (2001–2022) could have partly contributed to the intensification of winter haze over the years. Fog events have increased in the valley, though not a lot, due to the effect of enhanced aerosols (more Cloud Condensation Nuclei (CCN)) in the air. However, it appears that dense fog may have disappeared largely in the recent period (regime II) because of a reduction in agricultural land and vegetation cover and increased dew point depression in Kathmandu.

An inverse power-function relationship was explored between AOD and VIS (even better between PM2.5 and VIS at BWA. The negative correlation was strongly reliant on ambient relative humidity and was most noticeable during the monsoon, then the post-monsoon, winter, and pre-monsoon seasons. Similar is the relationship between PM2.5 and VIS at KTM.

PBLH derived from radiosonde measurements represents a unique dataset and vital information for the analysis of air quality and meteorological conditions in Kathmandu Valley. It was found that surface-based temperature inversions occur in >90% of all early morning soundings, suggesting that the majority of nocturnal SBL occur under clear-sky conditions. After inter-comparison and performance assessment of each method, it is concluded that the SBI method, which is used as the benchmark method of estimating PBLH from SBL classification elsewhere, is the best method for estimation of nocturnal SBL top and GM_θ is as robust as the SBI method. Whereas, RM also yields reasonable estimates of PBLH in SBL classifications provided appropriate use of Ri_c . However, the reliability of ERA5 reanalysis products on PBLH—especially in mountainous terrain like Kathmandu—is highly questionable. This might be because of the spatial resolution of the reanalysis data (0.25º × 0.25º, or, ~ 28 × 28 km). This is

much coarser than the topographic variations in the valley. The strongest and deepest nocturnal SBIs were found in winter and the weakest in monsoon. These seasonal differences are explained by distinct seasonal meteorological conditions: solar radiation (temperature), precipitation, and wind speed.

The statistical results reveal a good association between PM2.5 concentration, nocturnal stable-boundary-layer height, and visibility in Kathmandu. A notable impact of PBL structure on the distribution of PM2.5 concentration was found; a clear positive correlation suggests a higher concentration of air pollution when the nocturnal-stable-boundary layer is stronger. Because it inhibits the vertical mixing of pollutants, a deep and robust surface inversion layer combined with low wind speed had a major role in the buildup of PM2.5 close to the surface. Deeper SBL heights are associated with more frequent stratification and sporadic turbulent boundary layer conditions, which are frequently brought on by enhancement in ground-based PM2.5 measurements. Likewise, airport VIS is weakly anti-correlated with SBL Height (SBLH). This suggests that the deeper and stronger the SBL, the lower the surface visibility at the airport because of a weak vertical dispersion of near-surface air pollution. Seasonal highest visibility at the KTM airport is observed during the wet monsoon season because of reduced air pollution emission, the active scavenging of particles by monsoon rain, and shallower SBL that promotes convective transport of air pollution. Increased fine mass concentration from October through February of next year in the valley and lower visibility at the airport are partly attributed to increased biomass burning emissions including brick kiln operations under a deep SBL in winter.

This study on the effects of optical properties of aerosols (specifically PM2.5) and their hygroscopic effect on visibility at TIA revealed that airport VIS decreases sharply with increased extinction coefficient and mass extinction efficiency (MEE), and hygroscopic growth factor (f(RH)) grows exponentially with the RH and results in the reduction of VIS.

Other key meteorological factors that affect visibility at TIA are relative humidity and wind. Higher ambient humidity results in lower visibility through the change in optical properties of hygroscopic aerosol species in the valley's atmosphere. Similarly, faster surface wind disperses local air pollution and improves visibility. The directional dependence of wind on airport visibility was found such that wind with a speed of 1–2

m/s flowing from the eastern quadrant of the airport (more specifically from Northeast through South) impairs visibility in winter.

After analyzing the climatological dataset, for microclimatic behavior of winter fog in Kathmandu, it was found that ~ 86% (~95%) of fog (dense fog) days witnessed fog lasting not more than an hour. The onset of fog occurs in the early morning—usually between 05:00 to 09:45 am—in all three winter months and disperses before noon. The most favorable onset times for fog are 05:15 am in December and 06:45 am in January and February, while the dense fog onset window is between 05:00 and 09:00 am. The highest percentage of dense fog onset occurs at 05:15 and 08:15 am and dissipates at 06:15 and 09:15 am.

Poor visibility occurrence severely affects aviation at GBIA and TIA that seems to continue; especially the alarming increase of poor visibility conditions in post-monsoon and winter seasons are more concerning to flight operations at these airports.

5.2 Recommendations

The rapid rise in the occurrence of poor visibility in various forms in major airport locations in Nepal is alarming. Based on the comprehensive study using a vast set of historical data, the major precursors of visibility impairment in Nepal is found to be enhanced air pollution over the years. The adverse impact of severe air pollution is not only limited to impaired visibility but also many other areas ranging from human health, climate, cryosphere, ecosystem, agriculture, and water availability to tourism in the region (Saikawa *et al.*, 2019). Some of the limitations that this study faced could be addressed in future studies. Thus, below are some recommendations for the policy and academia/ researchers:

5.2.1 Policy recommendation

To lessen the impact of visibility impairment in the aviation sector, and that of enhanced air pollution in many other sectors (mentioned above) the following policy recommendations have been advised:

- Investment in technologies and equipment to mitigate potential damage to the aviation sector resulted from visibility decline at airports. As of now, implementation of an instrument landing system (ILS), preferably CAT-II/III,

and an advanced surface movement guidance and control system (A-SMGCS) at GBIA to mitigate the damage potential to aviation, especially in winter.

- Designing policies and measures to address the anthropogenic causes of visibility decline. This includes controlling air pollution emissions at sources, such as vehicular and brick kiln emissions, open garbage fires, etc. in Kathmandu, and industrial and crop residue burning in Bhairahawa and Indo Gangetic Plains. Special care is to be taken to control the emission of precursors of secondary hygroscopic aerosols such as sulfates, nitrates, ammonium, etc. at the source.

- Understanding physical and chemical properties (e.g., concentration, type) of aerosols while implementing measures to control air pollution in pollution-vulnerable areas, such as Kathmandu and Bhairahawa.

5.2.2 Recommendation for future work

This work has achieved some insights into previously unexplored aspects of atmospheric visibility in our country. However, many limitations were faced in terms of data, methods, and scope of this research, which can be addressed in future studies that would enhance our scientific understanding. Here are some of the recommendations for researchers/ academia for further work:

- Understanding aerosol-visibility relationship at GBIA and TIA using more precise and high temporal-resolution routine visibility measurements from various instruments like, Transmissometers, Forward Scatter Sensors, Nephelometer etc.

- Exploring different advances in visibility studies in our country, such as measurement techniques, atmospheric modeling, impact of secondary aerosols, impact of climate change, technological integration, and policy and mitigation strategies.

- Development of visibility prediction models using big data analytics and machine learning algorithms in Nepalese airports

- Use of artificial intelligence in visibility monitoring and forecast at Nepalese airports

- Study on the mechanism of winter fog in Kathmandu valley by using models and the effect of UHI on fog
- It is challenging to elucidate the underlying complex mechanism of the relationship between PBLH, aerosols, and meteorology via observational studies alone. This also merits further future work using explicit model simulations.

CHAPTER 6

SUMMARY

Air pollution in the atmosphere poses many adverse socio-economic problems. Among them, visibility impairment especially at the airports is one of its serious consequences—since this may incur huge economic losses to the aviation sector and may lead to fatal aircraft accidents in the worst-case scenario. Yet, this perspective remains an unexplored but important issue to be addressed in our region. Thus, this study aims to cater to this research gap in the aviation sector of our country by choosing two of the major international airports: Tribhuvan International Airport (TIA) at Kathmandu (KTM) and Gautam Buddha International Airport (GBIA) at Bhairahawa (BWA).

A vast set of climatological data—spanning more than four decades—was used supplemented by in-situ measurements, remote sensing and reanalysis data of air pollution, and vertical profile measurements of the atmosphere using radiosondes. The vast dataset has been analyzed using Python and 'R' programming languages. We used very robust statistical methods: Mann-Kendall (MK) test, Sen's Slope indicators, and Ordinary Least Square (OLS) regression tests for quantifying the changes in visibility and Pearson's correlation and other regression metrics (**APPENDIX B**), etc. for quantification of relationship and performance validation respectively.

It was found that haze and fog are the two major weather types reducing visibility in Nepal, both of which display a significant uptrend. At BWA, the most alarming increase in the haze is witnessed in the post-monsoon season. Whereas, KTM witnessed a serious intensification of haze in winter as well as a notable increase in fog occurrence during regime-I (1976–2000). Winter-haze plateaued and dense fog occurrence declined later in regime II (2001–2022) in KTM. Obvious local and regional air pollution at both sites would drive the intensification of both weather types in all seasons. After further careful examination of all plausible climatological drivers of the change, increased moisture, and decreased wind speed appear to support the intensification of winter haze and fog at BWA, while decreased ambient moisture level and increased dew point depression after the year 2000 appear to support decreased dense fog occurrence in KTM.

It was found that the level of air pollution is the highest in dry and lowest in wet seasons, while airport visibility is just the opposite. Thus, a reciprocal relationship between the level of air pollution and visibility was established at the airports. The best anti-correlation was observed for the monsoon season at GBIA.

Aerosol water effect on visibility was observed at both the airports—increased ambient moisture content in the atmosphere leading to the reduced visibility—and also found the RH and PM2.5 thresholds beyond which the effect displayed prominence. A negative association between airport visibility and the WS and wind-directional dependence of visibility was also found.

As a first effort to obtain sounding-based PBLH climatology in Nepal and study the relationship of PBLH on air pollution dispersion and airport visibility, radiosonde measurements launched from a suburban site in KTM were analyzed. It was concluded that Surface Based Temperature inversion (SBI) is the best estimation technique for SBL classification, while, reanalysis data proves to be not reliable in high-terrain topography. It was found that the strongest and deepest surface inversions occur during winter and pre-monsoon months and the weakest and shallowest stable boundary layer occurs in the early morning of monsoon. A positive correlation between SBL height and PM2.5 was seen. Similarly, a negative correlation between PM2.5 and visibility pair, and SBL height and airport visibility pair were seen.

Some of the salient microclimatic properties of winter fog were also studied at both of the airports. It was observed that the onset of fog usually occurs overnight up until early morning on cold and clear-sky nights in winter and starts to disperse with the progression of the day after sunrise. Dense fog occurrences are very short spells. The occurrence and intensity of fog peaks typically in January.

REFERENCE

Accident Investigation Commission (AIC). (2015). *Final Report on the Investigation of the Accident of TC-JOC, A330-303, at TIA, KTM on 4 March 2015*. https://reports.aviation-safety.net/2015/20150304-0_A333_TC-JOC.pdf

Ahmad, I., Tang, D., Wang, T., Wang, M., & Wagan, B. (2015). Precipitation Trends over Time Using Mann-Kendall and Spearman's rho Tests in Swat River Basin, Pakistan. *Advances in Meteorology*, **2015:** e431860. https://doi.org/10.1155/2015/431860

Alperson-Afil, N. (2008). Continual Fire Making by Hominins at Gesher Benot Ya ʻAqov, Israel. *Quaternary Science Reviews*, **27**(17): 1733–1739. https://doi.org/10.1016/j.quascirev.2008.06.009

American Meteorological Society (AMS). (2023). *Visibility*. Glossary of Meteorology. https://glossary.ametsoc.org/wiki/Visibility

Anderson, T. L., & Ogren, J. A. (1998). Determining Aerosol Radiative Properties Using the TSI 3563 Integrating Nephelometer. *Aerosol Science and Technology*, **29**(1): 57–69. https://doi.org/10.1080/02786829808965551

Arun, S. H., Singh, C., John, S., Diwakar, S. K., Sankhala, D. K., Nigam, N., Tomar, C. S., & Kumar, G. (2022). A Study to Improve the Fog/Visibility Forecast at IGI Airport, New Delhi during the Winter Season 2020–2021. *Journal of Earth System Science*, **131**(2), 124. https://doi.org/10.1007/s12040-022-01874-5

Aryal, R. K., Lee, B.-K., Karki, R., Gurung, A., Kandasamy, J., Pathak, B. K., Sharma, S., & Giri, N. (2008). Seasonal PM10 dynamics in Kathmandu Valley. *Atmospheric Environment*, **42**(37): 8623–8633. https://doi.org/10.1016/j.atmosenv.2008.08.016

Aryee, J. N. A., Amekudzi, L. K., Preko, K., Atiah, W. A., & Danuor, S. K. (2020). Estimation of Planetary Boundary Layer Height from Radiosonde Profiles over West Africa During the AMMA Field Campaign: Inter Comparison of Different Methods. *Scientific African*, **7:** e00228. https://doi.org/10.1016/j.sciaf.2019.e00228

Babari, R., Hautiere, N., Dumont, E., Brémond, R., & Paparoditis, N. (2011). A Model-Driven Approach to Estimate Atmospheric Visibility with Ordinary Cameras. *Atmospheric environment*, **45**(30), 5316-5324. https://doi.org/10.1016/j.atmosenv.2011.06.053

Baidya, S. K., Shrestha, M. L., & Sheikh, M. M. (2008). Trend in Daily Climatic Extremes of Temperature and Precipitation in Nepal. *Journal of Hydrology and Meteorology*, **5**(1): 38–51.

Bäumer, D., Vogel, B., Versick, S., Rinke, R., Möhler, O., & Schnaiter, M. (2008). Relationship of Visibility, Aerosol Optical Thickness and Aerosol Size Distribution in an Ageing Air Mass over South-West Germany. *Atmospheric Environment*, **42**(5): 989–998. https://doi.org/10.1016/j.atmosenv.2007.10.017

Becker, S., Sapkota, R. P., Pokharel, B., Adhikari, L., Pokhrel, R. P., Khanal, S., & Giri, B. (2021). Particulate Matter Variability in Kathmandu Based on In-Situ Measurements, Remote Sensing, and Reanalysis Data. *Atmospheric Research*, **258**, 105623. https://doi.org/10.1016/j.atmosres.2021.105623

Beyrich, F., & Leps, J.P. (2012). An Operational Mixing Height Data Set from Routine Radiosoundings at Lindenberg: Methodology. *Meteorologische Zeitschrift*, **21**: 337–348. https://doi.org/10.1127/0941-2948/2012/0333

Bhushan, B., Trivedi, H. K. N., Bhatia, R. C., Dube, R. K., Giri, R. K., & Negi, R. S. (2003). On The Persistence of Fog over Northern Parts of India. *Mausam*, **54**(4): 851–860. https://doi.org/10.54302/mausam.v54i4.1585

Bi, J., Huang, J., Hu, Z., Holben, B. N., & Guo, Z. (2014). Investigating the Aerosol Optical and Radiative Characteristics of Heavy Haze Episodes in Beijing during January Of 2013. *Journal of Geophysical Research: Atmospheres*, **119**(16): 9884–9900. https://doi.org/10.1002/2014JD021757

Bian, Q. (2011). *Study of visibility degradation over the Pearl River delta region: Source apportionment and impact of chemical characteristics*. Hong Kong University of Science and Technology (Hong Kong). https://search.proquest.com/openview/2f26952b3d33d69646c668436479628f/1?pq-origsite=gscholar&cbl=18750

Bosilovich, M. G., Lucchesi, R., & Suarez, M. (2015). *MERRA-2: File Specification*. https://ntrs.nasa.gov/citations/20150019760

Boyouk, N., Léon, J.-F., Delbarre, H., Podvin, T., & Deroo, C. (2010). Impact of the Mixing Boundary Layer on the Relationship between PM2.5 and Aerosol Optical Thickness. *Atmospheric Environment*, **44**(2): 271–277. https://doi.org/10.1016/j.atmosenv.2009.06.053

Bradley, R. S., Keimig, F. T., & Diaz, H. F. (1992). Climatology of Surface-based Inversions in the North American Arctic. *Journal of Geophysical Research: Atmospheres*, **97**(D14): 15699–15712. https://doi.org/10.1029/92JD01451

Bradley, R. S., Keimig, F. T., & Diaz, H. F. (1993). Recent Changes in the North American Arctic Boundary Layer in winter. *Journal of Geophysical Research: Atmospheres*, **98**(D5): 8851–8858. https://doi.org/10.1029/93JD00311

Buchard, V., Randles, C. A., Silva, A. M. da, Darmenov, A., Colarco, P. R., Govindaraju, R., Ferrare, R., Hair, J., Beyersdorf, A. J., Ziemba, L. D., & Yu, H. (2017). The MERRA-2 Aerosol Reanalysis, 1980 Onward. Part II: Evaluation and Case Studies. *Journal of Climate*, **30**(17): 6851–6872. https://doi.org/10.1175/JCLI-D-16-0613.1

Busch, N., Ebel, U., Kraus, H., & Schaller, E. (1982). *The structure of the subpolar inversion-capped ABL*. https://pascal-francis.inist.fr/vibad/index.php?action=getRecordDetail&idt=PASCAL82X0220171

CAAN. (2022). *Aeronautic Information Publication (8th edition)*. Civil Aviation Authority of Nepal. https://e-aip.caanepal.gov.np/_uploads/_pdf/0819d46e68f7b2a1edde6ec55ae00105.pdf

Cao, J., Wang, Q., Chow, J. C., Watson, J. G., Tie, X., Shen, Z., Wang, P., & An, Z. (2012). Impacts of Aerosol Compositions on Visibility Impairment in Xi'an, China. Atmospheric Environment, **59**: 559–566. https://doi.org/10.1016/j.atmosenv.2012.05.036

Carrico, C. M., Rood, M. J., & Ogren, J. A. (1998). Aerosol Light Scattering Properties at Cape Grim, Tasmania, During the First Aerosol Characterization

Experiment (ACE 1). *Journal of Geophysical Research: Atmospheres*, **103**(D13): 16565–16574. https://doi.org/10.1029/98JD00685

Carrico, C. M., Rood, M. J., Ogren, J. A., Neususs, C., Wiedensohler, A., & Heintzenberg, J. (2000). Aerosol Optical Properties at Sagres, Portugal during ACE-2. *Tellus B*, **52**(2): 694–715. https://doi.org/10.1034/j.1600-0889.2000.00049.x

Chandiramani, W., Pradhan, S. K., Gurunadham, G., Kishan, D., & Manral, N. (1975). A Case Study of Poor Visibility Over Bombay Airport. *MAUSAM*, **26**(2): 208–210.

Chang, D., Song, Y., & Liu, B. (2009). Visibility Trends in Six Megacities in China 1973–2007. *Atmospheric Research*, **94**(2): 161–167. https://doi.org/10.1016/j.atmosres.2009.05.006

Charlson, R. J., Schwartz, S. E., Hales, J. M., Cess, R. D., Coakley, J. A., Hansen, J. E., & Hofmann, D. J. (1992). Climate Forcing by Anthropogenic Aerosols. *Science*, **255**(5043): 423–430. https://doi.org/10.1126/science.255.5043.423

Che, H., Zhang, X., Li, Y., Zhou, Z., & Qu, J. J. (2007). Horizontal Visibility Trends in China 1981 – 2005. *Geophysical Research Letters*, **34**(24): L24706. https://doi.org/10.1029/2007GL031450

Chen, J., Zhao, C. S., Ma, N., Liu, P. F., Göbel, T., Hallbauer, E., Deng, Z. Z., Ran, L., Xu, W. Y., & Liang, Z. (2012). A Parameterization of Low Visibilities for Hazy Days in the North China Plain. *Atmospheric Chemistry and Physics*, **12**(11): 4935–4950. https://doi.org/10.5194/acp-12-4935-2012

Chen, Y., & Xie, S. (2013). Long-Term Trends and Characteristics of Visibility in Two Megacities in Southwest China: Chengdu and Chongqing. *Journal of the Air & Waste Management Association*, **63**(9): 1058–1069. https://doi.org/10.1080/10962247.2013.791348

Cheng, Z., Ma, X., He, Y., Jiang, J., Wang, X., Wang, Y., Sheng, L., Hu, J., & Yan, N. (2017). Mass Extinction Efficiency and Extinction Hygroscopicity of Ambient PM2.5 in Urban China. *Environmental Research*, **156:** 239–246. https://doi.org/10.1016/j.envres.2017.03.022

Chmielecki, R. M., & Raftery, A. E. (2011). Probabilistic Visibility Forecasting Using Bayesian Model Averaging. *Monthly Weather Review*, **139**(5): 1626–1636. https://doi.org/10.1175/2010MWR3516.1

Chou, C. C. K., Lee, C.-T., Chen, W. N., Chang, S. Y., Chen, T. K., Lin, C. Y., & Chen, J. P. (2007). Lidar Observations of the Diurnal Variations in the Depth of Urban Mixing Layer: A Case Study on the Air Quality Deterioration in Taipei, Taiwan. *Science of the Total Environment*, **374**(1): 156–166. https://doi.org/10.1016/j.scitotenv.2006.11.049

Collaud Coen, M., Praz, C., Haefele, A., Ruffieux, D., Kaufmann, P., & Calpini, B. (2014). Determination and Climatology of the Planetary Boundary Layer Height above the Swiss Plateau By in Situ and Remote Sensing Measurements as well as by the COSMO-2 Model. *Atmospheric Chemistry and Physics*, **14**(23): 13205–13221. https://doi.org/10.5194/acp-14-13205-2014

Covert, D. S., Charlson, R. J., & Ahlquist, N. C. (1972). A Study of the Relationship of Chemical Composition and Humidity to Light Scattering By Aerosols. *Journal of Applied Meteorology and Climatology*, **11**(6): 968–976. https://doi.org/10.1175/1520-0450(1972)011<0968:ASOTRO>2.0.CO;2

Davis, R. E. (1991). A Synoptic Climatological Analysis of Winter Visibility Trends in the Mideastern United States. *Atmospheric Environment. Part B. Urban Atmosphere*, **25**(2): 165–175. https://doi.org/10.1016/0957-1272(91)90052-G

Dayan, U., & Levy, I. (2005). The Influence of Meteorological Conditions and Atmospheric Circulation Types on PM10 and Visibility in Tel Aviv. *Journal of Applied Meteorology*, **44**(5): 606–619. https://doi.org/10.1175/JAM2232.1

De, U. S., & Dandekar, M. M. (2001). Natural Disasters in Urban Areas. *Deccan Geographer*, **39**(2): 1–12.

De, U. S., Rao, G. P., & Jaswal, A. K. (2001). Visibility over Indian Airports during Winter Season. *Mausam*, **52**(4): 717–726.

Deng, H., Tan, H., Li, F., Cai, M., Chan, P. W., Xu, H., Huang, X., & Wu, D. (2016). Impact of Relative Humidity on Visibility Degradation during a Haze Event: A

Case Study. *Science of the Total Environment*, **569:** 1149–1158. https://doi.org/10.1016/j.scitotenv.2016.06.190

Deng, J., Wang, T., Jiang, Z., Xie, M., Zhang, R., Huang, X., & Zhu, J. (2011). Characterization of Visibility and Its Affecting Factors over Nanjing, China. *Atmospheric Research*, **101**(3): 681–691. https://doi.org/10.1016/j.atmosres.2011.04.016

Dey, S., & Di Girolamo, L. (2010). A Climatology of Aerosol Optical and Microphysical Properties over the Indian Subcontinent from 9 Years (2000 – 2008) Of Multiangle Imaging Spectroradiometer (MISR) Data. *Journal of Geophysical Research*, **115**(D15): D15204. https://doi.org/10.1029/2009JD013395

Dhungel, S., Kathayat, B., Mahata, K., & Panday, A. (2018). Transport of Regional Pollutants through a Remote Trans-Himalayan Valley in Nepal. *Atmospheric Chemistry and Physics*, **18**(2): 1203–1216. https://doi.org/10.5194/acp-18-1203-2018

Diederen, H., Guicherit, R., & HolLonder, J. C. T. (1985). Visibility Reduction by Air Pollution in the Netherlands. *Atmospheric Environment (1967)*, **19**(2): 377–383.

Ding, A. J., Huang, X., Nie, W., Sun, J. N., Kerminen, V. -M., Petäjä, T., Su, H., Cheng, Y. F., Yang, X. -Q., Wang, M. H., Chi, X. G., Wang, J. P., Virkkula, A., Guo, W. D., Yuan, J., Wang, S. Y., Zhang, R. J., Wu, Y. F., Song, Y., … Fu, C. B. (2016). Enhanced Haze Pollution by Black Carbon in Megacities in China. *Geophysical Research Letters*, **43**(6): 2873–2879. https://doi.org/10.1002/2016GL067745

Ding, Y., & Liu, Y. (2014). Analysis of Long-Term Variations of Fog and Haze in China in Recent 50 Years and Their Relations with Atmospheric Humidity. *Science China Earth Sciences*, **57**(1): 36–46. https://doi.org/10.1007/s11430-013-4792-1

Dixit, K. (2022, June 17). *60 Years of Living Dangerously*. https://nepalitimes.com/here-now/60-years-of-living-dangerously

Doran, J. A., Roohr, P. J., Beberwyk, D. J., Brooks, G. R., Gayno, G. A., Williams, R. T., Lewis, J. M., & Lefevre, R. J. (1999). The MM 5 at the AF Weather Agency- New Products to Support Military Operations. *Conference on Aviation, Range, and Aerospace Meteorology, 8th, Dallas, TX*, 115–119.

Doyle, M., & Dorling, S. (2002). Visibility Trends in the UK 1950–1997. *Atmospheric Environment*, **36**(19): 3161–3172. https://doi.org/10.1016/S1352-2310(02)00248-0

Du, K., Mu, C., Deng, J., & Yuan, F. (2013). Study on Atmospheric Visibility Variations and the Impacts of Meteorological Parameters Using High Temporal Resolution Data: an Application of Environmental Internet of Things in China. *International Journal of Sustainable Development & World Ecology*, **20**(3): 238–247. https://doi.org/10.1080/13504509.2013.783886

Duda, R. O., & Hart, P. E. (1972). Use of the Hough Transformation to Detect Lines and Curves in Pictures. *Communications of the ACM*, **15**(1): 11–15. https://doi.org/10.1145/361237.361242

Eck, T. F., Holben, B. N., Reid, J. S., Sinyuk, A., Dubovik, O., Smirnov, A., Giles, D., O'Neill, N. T., Tsay, S. -C., Ji, Q., Al Mandoos, A., Ramzan Khan, M., Reid, E. A., Schafer, J. S., Sorokine, M., Newcomb, W., & Slutsker, I. (2008). Spatial and Temporal Variability of Column‐Integrated Aerosol Optical Properties in the Southern Arabian Gulf and United Arab Emirates in summer. *Journal of Geophysical Research: Atmospheres*, **113**(D1): 2007JD008944. https://doi.org/10.1029/2007JD008944

Elias, T., Haeffelin, M., Drobinski, P., Gomes, L., Rangognio, J., Bergot, T., Chazette, P., Raut, J.-C., & Colomb, M. (2009). Particulate Contribution to Extinction of Visible Radiation: Pollution, Haze, and Fog. *Atmospheric Research*, **92**(4): 443–454. https://doi.org/10.1016/j.atmosres.2009.01.006

Engelhart, G. J., Hildebrandt, L., Kostenidou, E., Mihalopoulos, N., Donahue, N. M., & Pandis, S. N. (2011). Water Content of Aged Aerosol. *Atmospheric Chemistry and Physics*, **11**(3): 911–920. https://doi.org/10.5194/acp-11-911-2011

Folini, D., & Wild, M. (2011). Aerosol Emissions and Dimming/Brightening in Europe: Sensitivity studies with ECHAM5-HAM: Dimming/Brightening in Europe. *Journal of Geophysical Research: Atmospheres*, **116**(D21). https://doi.org/10.1029/2011JD016227

Founda, D., Kazadzis, S., Mihalopoulos, N., Gerasopoulos, E., Lianou, M., & Raptis, P. I. (2016). Long-Term Visibility Variation in Athens (1931 – 2013): A Proxy for Local and Regional Atmospheric Aerosol Loads. *Atmospheric Chemistry and Physics*, **16**(17):11219–11236. https://doi.org/10.5194/acp-16-11219-2016

Foye, K. (2019). *An Algorithm with an Eye for Visibility Helps Pilots in Alaska*. https://dspace.mit.edu/handle/1721.1/128256

Fu, G. Q., Xu, W., Yang, R. F., Li, J. B., & Zhao, C. S. (2014). The Distribution and Trends of Fog and Haze in the North China Plain over the Past 30 Years. *Atmospheric Chemistry and Physics*, **14**(21): 11949–11958. https://doi.org/10.5194/acp-14-11949-2014

Fu, X., Wang, X., Hu, Q., Li, G., Ding, X., Zhang, Y., He, Q., Liu, T., Zhang, Z., & Yu, Q. (2016). Changes in Visibility with PM2.5 Composition and Relative Humidity at a Background Site in the Pearl River Delta Region. *Journal of Environmental Sciences*, **40:** 10–19. https://doi.org/10.1016/j.jes.2015.12.001

Gautam, R., Hsu, N. C., Kafatos, M., & Tsay, S. (2007). Influences of Winter Haze on Fog/Low Cloud over the Indo-Gangetic Plains. *Journal of Geophysical Research: Atmospheres*, **112**(D5): 2005JD007036. https://doi.org/10.1029/2005JD007036

Gautam, R., Liu, Z., Singh, R. P., & Hsu, N. C. (2009). Two Contrasting Dust-Dominant Periods over India Observed from MODIS and CALIPSO Data. *Geophysical Research Letters*, **36**(6): L06813. https://doi.org/10.1029/2008GL036967

Gebhart, K. A., & Malm, W. C. (1990). *An Investigation of the Size Distributions of Particulate Sulfate Concentrations Measured During WHITEX.*

Gelaro, R., McCarty, W., Suárez, M. J., Todling, R., Molod, A., Takacs, L., Randles, C. A., Darmenov, A., Bosilovich, M. G., & Reichle, R. (2017). The Modern-

Era Retrospective Analysis for Research and Applications, Version 2 (MERRA-2). *Journal of Climate*, **30**(14): 5419–5454.

Ghim, Y. S., Moon, K.-C., Lee, S., & Kim, Y. P. (2005). Visibility Trends in Korea during the Past Two Decades. *Journal of the Air & Waste Management Association*, **55**(1): 73–82. https://doi.org/10.1080/10473289.2005.10464599

Ghude, S. D., Bhat, G. S., Prabhakaran, T., Jenamani, R. K., Chate, D. M., Safai, P. D., Karipot, A. K., Konwar, M., Pithani, P., & Sinha, V. (2017). Winter Fog Experiment over the Indo-Gangetic Plains of India. *Current Science*, **112**(4): 767–784. https://www.jstor.org/stable/24912578

Giles, D. M., Sinyuk, A., Sorokin, M. G., Schafer, J. S., Smirnov, A., Slutsker *et al.* (2019). Advancements in the Aerosol Robotic Network (AERONET) Version 3 Database – Automated Near-Real-Time Quality Control Algorithm With Improved Cloud Screening for Sun Photometer Aerosol Optical Depth (AOD) Measurements. *Atmospheric Measurement Techniques*, **12**(1), 169-209. https://doi.org/10.5194/amt-12-169-2019

Global Modeling and Assimilation Office (GMAO). (2015). *MERRA-2 tavg1_2d_lnd_Nx: 2d, 1-Hourly, Time-Averaged, Single-Level, Assimilation, Land Surface Diagnostics V5.12.4* [dataset]. Greenbelt, MD, USA, Goddard Earth Sciences Data and Information Services Center (GES DISC). https://doi.org/10.5067/FH9A0MLJPC7N

Google Earth Pro. (2023). *Version 7.3.6.9345*. Google Earth. https://www.google.com/earth/about/versions/

Griffins, J., Houghton, D. D., & Sons, J. W. (1985). Handbook of Applied Meteorology. *DD Houghton, and JW Sons, Eds*.

Gultepe, I., Müller, M. D., & Boybeyi, Z. (2006). A New Visibility Parameterization for Warm-Fog Applications in Numerical Weather Prediction Models. *Journal of Applied Meteorology and Climatology*, **45**(11), 1469-1480. https://doi.org/10.1175/JAM2423.1

Gultepe, I., Tardif, R., Michaelides, S. C., Cermak, J., Bott, A., Bendix, J., Müller, M. D., Pagowski, M., Hansen, B., Ellrod, G., Jacobs, W., Toth, G., & Cober, S. G.

(2007). Fog Research: A Review of Achievements and Future Perspectives. *Pure and Applied Geophysics*, **164**(6–7): 1121–1159. https://doi.org/10.1007/s00024-007-0211-x

Gultepe, I., Zhou, B., Milbrandt, J., Bott, A., Li, Y., Heymsfield, A. J., Ferrier, B., Ware, R., Pavolonis, M., & Kuhn, T. (2015). A Review on Ice Fog Measurements and Modeling. *Atmospheric Research*, **151**: 2–19. https://doi.org/10.1016/j.atmosres.2014.04.014

Guo, J., Miao, Y., Zhang, Y., Liu, H., Li, Z., Zhang, W., He, J., Lou, M., Yan, Y., & Bian, L. (2016). The Climatology of Planetary Boundary Layer Height in China Derived from Radiosonde and Reanalysis Data. *Atmospheric Chemistry and Physics*, **16**(20): 13309–13319. https://doi.org/10.5194/acp-16-13309-2016

Guo, J., Zhang, J., Chen, T., Bai, K., Shao, J., Sun, Y., Li, N., Wu, J., Li, R., & Li, J. (2022). A Merged Continental Planetary Boundary Layer Height Dataset Based on High-Resolution Radiosonde Measurements, ERA5 Reanalysis, and GLDAS. *Earth System Science Data Discussions*, **16** (1): 1–33. https://doi.org/10.5194/essd-16-1-2024

Hadjimitsis, D. G., Clayton, C., & Toulios, L. (2010). Retrieving Visibility Values Using Satellite Remote Sensing Data. *Physics and Chemistry of the Earth, Parts A/B/C*, **35**(1): 121–124. https://doi.org/10.1016/j.pce.2010.03.002

Hameed, S., Mirza, M. I., Ghauri, B. M., Siddiqui, Z. R., Javed, R., Khan, A. R., Rattigan, O. V., Qureshi, S., & Husain, L. (2000). On The Widespread Winter Fog in Northeastern Pakistan and India. *Geophysical Research Letters*, **27**(13): 1891–1894. https://doi.org/10.1029/1999GL011020

Han, Y., Lü, D., Rao, R., & Wang, Y. (2009). Determination of the Complex Refractive Indices of Aerosol from Aerodynamic Particle Size Spectrometer and Integrating Nephelometer Measurements. *Applied Optics*, **48**(21): 4108–4117. https://doi.org/10.1364/AO.48.004108

Hand, J. L., Prenni, A. J., Schichtel, B. A., Malm, W. C., & Chow, J. C. (2019). Trends in Remote PM2.5 Residual Mass across the United States: Implications

for Aerosol Mass Reconstruction in the IMPROVE Network. *Atmospheric Environment*, **203**: 141–152. https://doi.org/10.1016/j.atmosenv.2019.01.049

Harrison, R. M., Jones, A. M., & Lawrence, R. G. (2004). Major Component Composition of PM10 and PM2.5 from Roadside and Urban Background Sites. *Atmospheric Environment*, **38**(27): 4531–4538. https://doi.org/10.1016/j.atmosenv.2004.05.022

Hassoon, A., Ibraheem, B., Al-Temimi, W., Khishala, A. D., & Altemimi, B. (2018). Visibility Trends in Baghdad City during the Period 2005–2014. *Civil and Environmental Research,* **10**(5): 76 – 84. https://doi.org/10.13140/RG.2.2.22147.86565

Hegde, P., Pant, P., Naja, M., Dumka, U. C., & Sagar, R. (2007). South Asian Dust Episode in June 2006: Aerosol Observations in the Central Himalayas. *Geophysical Research Letters*, **34**(23). https://doi.org/10.1029/2007GL030692

Helsel, D. R., & Hirsch, R. M. (1992). *Statistical methods in water resources* (Vol. 49). Elsevier.

Henry, R. C., Mahadev, S., Urquijo, S., & Chitwood, D. (2000). Color Perception through Atmospheric Haze. *Journal of the Optical Society of America A*, **17**(5): 831–835. https://doi.org/10.1364/JOSAA.17.000831

Herman, G. R., & Schumacher, R. S. (2016). Using Reforecasts to Improve Forecasting of Fog and Visibility for Aviation. *Weather and Forecasting*, **31**(2): 467–482. https://doi.org/10.1175/WAF-D-15-0108.1

Hess, A., Iyer, H., & Malm, W. C. (2001). Linear Trend Analysis: A Comparison of Methods. *Atmospheric Environment*, **35**(30): 5211–5222. https://doi.org/10.1016/S1352-2310(01)00342-9

Holzworth, G. C. (1964). Estimates of Mean Maximum Mixing Depths in the Contiguous United States. *Monthly Weather Review*, **92**(5): 235–242. https://doi.org/10.1175/1520-0493(1964)092<0235:EOMMMD>2.3.CO;2

Horvath, H. (1971). On the Applicability of the Koschmieder Visibility Formula. *Atmospheric Environment (1967)*, **5**(3): 177–184.

Horvath, H. (1981). Atmospheric visibility. *Atmospheric Environment (1967)*, **15**(10–11): 1785–1796. https://doi.org/10.1016/0004-6981(81)90214-6

Horvath, H., & Kaller, W. (1994). Calibration of Integrating Nephelometer in the Post-Halocarbon Era. *Atmospheric Environment*, **28**(6): 1219–1223. https://doi.org/10.1016/1352-2310(94)90299-2

Hu, Y., Yao, L., Cheng, Z., & Wang, Y. (2017). Long-term Atmospheric Visibility Trends in Megacities of China, India and the United States. *Environmental Research*, **159**: 466–473. https://doi.org/10.1016/j.envres.2017.08.018

Hunova, I., Brabec, M., Malỳ, M., Dumitrescu, A., & Geletič, J. (2021). Terrain and Its Effects on Fog Occurrence. *Science of the Total Environment*, **768**: 144359. https://doi.org/10.1016/j.scitotenv.2020.144359

Hunova, I., Brabec, M., Malỳ, M., & Valeriánová, A. (2020). Long-Term Trends in Fog Occurrence in the Czech Republic, Central Europe. *Science of the Total Environment*, **711**: 135018. https://doi.org/10.1016/j.scitotenv.2019.135018

Hussain, M., & Mahmud, I. (2019). PyMannKendall: A Python Package for Non-Parametric Mann Kendall Family of Trend Tests. *Journal of Open Source Software*, **4**(39): 1556. doi:10.21105/joss.01556

Hyslop, N. P. (2009). Impaired Visibility: The Air Pollution People See. *Atmospheric Environment*, **43**(1): 182–195. https://doi.org/10.1016/j.atmosenv.2008.09.067

ICAO. (2005). *ICAO Annex 2: Rules of Air, Tenth Edition*. International Civil Aviation Organization (ICAO). https://www.icao.int/Meetings/anconf12/Document%20Archive/an02_cons%5B1%5D.pdf

ICAO. (2017). *ICAO Doc 9365: Manual of All-Weather Operations*. International Civil Aviation Organization (ICAO).

Igini, M. (2022, October 23). *History of Air Pollution: Have We Reached the Point of No Return?* Earth.Org. https://earth.org/history-of-air-pollution/

Inhaber, H. (1976). Changes in Canadian National Visibility. *Nature*, **260**(5547): 129–130.

Islam, Md. R., Li, T., Mahata, K., Khanal, N., Werden, B., Giordano, M. R., Praveen, P. S., Dhital, N. B., Gurung, A., Panday, A. K., Joshi, I. B., Poudel, S. P., Wang, Y., Saikawa, E., Yokelson, R. J., DeCarlo, P. F., & Stone, E. A. (2021). Wintertime Air Quality in Lumbini, Nepal: Sources of Fine Particle Organic Carbon. *ACS Earth and Space Chemistry*, **5**(2): 226–238. https://doi.org/10.1021/acsearthspacechem.0c00269

Izhar, S., Gupta, T., Qadri, A. M., & Panday, A. K. (2021). Wintertime Chemical Characteristics of Aerosol and Their Role in Light Extinction during Clear and Polluted Days in Rural Indo Gangetic Plain. *Environmental Pollution*, **282:** 117034. https://doi.org/10.1016/j.envpol.2021.117034

Jacob, D. J. (1999). *Introduction to atmospheric chemistry*. Princeton university press.

Jacobson, M. Z. (2002). *Atmospheric Pollution: History, Science, and Regulation*. Cambridge University Press.

Jaswal, A. K., Kumar, N., Prasad, A. K., & Kafatos, M. (2013). Decline in Horizontal Surface Visibility over India (1961 – 2008) and Its Association with Meteorological Variables. *Natural Hazards*, **68**(2): 929–954. https://doi.org/10.1007/s11069-013-0666-2

Jenamani, R. K. (2007). Alarming Rise in Fog and Pollution causing a fall in Maximum Temperature over Delhi. *Current Science*, **3**: 314–322. https://www.jstor.org/stable/24099461

Jenamani, R. K. (2012). Micro-Climatic Study and Trend Analysis of Fog Characteristics at IGI Airport New Delhi Using Hourly Data (1981-2005). *Mausam*, **63**(2): 203–218.

Jenamani, R. K., & Kumar, A. (2013). Bad Weather and Aircraft Accidents – Global Vis-À-Vis Indian Scenario. *Current Science*, **104**(3): 316–325. https://www.jstor.org/stable/24089632

Jeričević, A., & Grisogono, B. (2006). The Critical Bulk Richardson Number in Urban Areas: Verification and Application in a Numerical Weather Prediction Model. *Tellus A: Dynamic Meteorology and Oceanography*, **58**(1): 19–27. https://doi.org/10.1111/j.1600-0870.2006.00153.x

Jethva, H., Torres, O., Field, R. D., Lyapustin, A., Gautam, R., & Kayetha, V. (2019). Connecting Crop Productivity, Residue Fires, and Air Quality over Northern India. *Scientific Reports*, **9**(1): 16594.

Jung, J., Lee, H., Kim, Y. J., Liu, X., Zhang, Y., Gu, J., & Fan, S. (2009). Aerosol Chemistry and the Effect of Aerosol Water Content on Visibility Impairment and Radiative Forcing In Guangzhou during the 2006 Pearl River Delta Campaign. *Journal of Environmental Management*, **90**(11): 3231–3244. https://doi.org/10.1016/j.jenvman.2009.04.021

Kafle, D. N. (1997). *A study of visibility in Kathmandu valley*. Central Department of Physics, Institute of Science and Technology, Tribhuvan University, Kathmandu, Nepal.

Kahya, E., & Kalaycı, S. (2004). Trend Analysis of Streamflow in Turkey. *Journal of Hydrology*, **289**(1–4): 128–144. https://doi.org/10.1016/j.jhydrol.2003.11.006

Kaskaoutis, D. G., Singh, R. P., Gautam, R., Sharma, M., Kosmopoulos, P. G., & Tripathi, S. N. (2012). Variability and Trends of Aerosol Properties over Kanpur, Northern India Using AERONET Data (2001–10). *Environmental Research Letters*, **7**(2): 024003. doi: 10.1088/1748-9326/7/2/024003

Kathayat, B., Panday, A. K., Pokharel, B., Kumar, V., & Chapagain, N. P. (2023). Four Decades of Aviation Visibility at Bhairahawa Airport, Gateway to Buddha's Birthplace Lumbini, Nepal. *Atmospheric Research*, **288**: 106746. https://doi.org/10.1016/j.atmosres.2023.106746

Kedia, S., Ramachandran, S., Holben, B. N., & Tripathi, S. N. (2014). Quantification of Aerosol Type, And Sources of Aerosols over the Indo-Gangetic Plain. *Atmospheric Environment*, **98**: 607–619. https://doi.org/10.1016/j.atmosenv.2014.09.022

Khanal, S., Pokhrel, R. P., Pokharel, B., Becker, S., Giri, B., Adhikari, L., & LaPlante, M. D. (2022). An Episode of Transboundary Air Pollution in the Central Himalayas during Agricultural Residue Burning Season in North India. *Atmospheric Pollution Research*, **13**(1): 101270. https://doi.org/10.1016/j.apr.2021.101270

Kim, C. K., Yum, S. S., Kim, H.-G., & Kang, Y.-H. (2019). A WRF Modeling Study on the Effects of Land Use Changes on Fog off the West Coast of the Korean Peninsula. *Pure and Applied Geophysics*, **176**(10): 4623–4640. https://doi.org/10.1007/s00024-019-02242-z

Kitada, T., & Regmi, R. P. (2003). Air Pollutants Distribution and Their Dynamics Over the Kathmandu Valley, Nepal: As Revealed With Numerical Simulation. *J. Appl. Meteo*, **42**: 1770–1789. https://doi.org/10.1175/1520-0450(2003)042<1770:DOAPTI>2.0.CO;2

Kompalli, S. K., Babu, S. S., Moorthy, K. K., Manoj, M. R., Kumar, N. K., Shaeb, K. H. B., & Joshi, A. K. (2014). Aerosol Black Carbon Characteristics over Central India: Temporal Variation and Its Dependence on Mixed Layer Height. *Atmospheric Research*, **147**: 27–37. https://doi.org/10.1016/j.atmosres.2014.04.015

Koschmieder, H. (1924). Theorie Der Horizontalen Sichtweite. *Beitrage zur Physik der freien Atmosphare*, 33-53.

Kotchenruther, R. A., Hobbs, P. V., & Hegg, D. A. (1999). Humidification Factors for Atmospheric Aerosols off The Mid-Atlantic Coast of the United States. *Journal of Geophysical Research: Atmospheres*, **104**(D2): 2239–2251. https://doi.org/10.1029/98JD01751

Krishnamurthy, R., Newsom, R. K., Berg, L. K., Xiao, H., Ma, P. L., & Turner, D. D. (2021). On The Estimation of Boundary Layer Heights: A Machine Learning Approach. *Atmospheric Measurement Techniques*, **14**(6): 4403–4424. https://doi.org/10.5194/amt-14-4403-2021

Kulesa, G. (2003). Weather and Aviation: How Does Weather Affect the Safety and Operations of Airports and Aviation, and How Does FAA Work To Manage Weather-Related Effects? *The Potential Impacts of Climate Change on Transportation US Department of Transportation Center for Climate Change and Environmental Forecasting; US Environmental Protection Agency; US Department of Energy; and US Global Change Research Program*. https://trid.trb.org/view/663829

Kulkarni, R., Jenamani, R. K., Pithani, P., Konwar, M., Nigam, N., & Ghude, S. D. (2019). Loss to Aviation Economy Due To Winter Fog in New Delhi during the winter of 2011–2016. *Atmosphere*, **10**(4): 198. doi: 10.3390/atmos10040198

Kulkarni, S. H., Ghude, S. D., Jena, C., Karumuri, R. K., Sinha, B., Sinha, V., Kumar, R., Soni, V. K., & Khare, M. (2020). How Much Does Large-Scale Crop Residue Burning Affect the Air Quality in Delhi? *Environmental Science & Technology*, **54**(8): 4790–4799. https://doi.org/10.1021/acs.est.0c00329

Kumar, V., Beirle, S., Dörner, S., Mishra, A. K., Donner, S., Wang, Y., Sinha, V., & Wagner, T. (2020). Long-term MAX-DOAS Measurements of NO2, HCHO, and Aerosols and Evaluation of Corresponding Satellite Data Products over Mohali in the Indo-Gangetic Plain. *Atmospheric Chemistry and Physics*, **20**(22): 14183–14235. https://doi.org/10.5194/acp-20-14183-2020

Kutty, S. G., Dimri, A. P., & Gultepe, I. (2020). Climatic Trends in Fog Occurrence over the Indo-Gangetic Plains. *International Journal of Climatology*, **40**(4): 2048–2061. https://doi.org/10.1002/joc.6317

Larson, S. M., & Cass, G. R. (1989). Characteristics of Summer Midday Low-Visibility Events in the Los Angeles Area. *Environmental Science & Technology*, **23**(3): 281–289. https://doi.org/10.1021/es00180a003

Larssen, S., Gram, F., Haugsbakk, I., Jansen, H., Olsthoorn, X., Giri, A. S., Shah, R., Shrestha, M. L., Shrestha, B., & Shah, J. J. (1997). *Urban air quality management strategy in Asia-Kathmandu Valley report*. The World Bank.

Li, H., Liu, B., Ma, X., Jin, S., Ma, Y., Zhao, Y., & Gong, W. (2021). Evaluation of Retrieval Methods for Planetary Boundary Layer Height Based on Radiosonde Data. *Atmospheric Measurement Techniques*, **14**(9): 5977–5986. https://doi.org/10.5194/amt-14-5977-2021

Li, M., Tang, G. Q., Huang, J., Liu, Z. R., An, J. L., & Wang, Y. S. (2015). Characteristics of Winter Atmospheric Mixing Layer Height in Beijing-Tianjin-Hebei Region and Their Relationship with the Atmospheric Pollution. *Huan Jing Ke Xue= Huanjing Kexue*, **36**(6): 1935–1943.

Lin, M., Tao, J., Chan, C.Y., Cao, J.J., Zhang, Z. S., Zhu, L. H., & Zhang, R. J. (2012). Regression Analyses between Recent Air Quality and Visibility Changes in Megacities at Four Haze Regions in China. *Aerosol and Air Quality Research*, **12**(6), 1049–1061. https://doi.org/10.4209/aaqr.2011.11.0220

Lin, T. H., Christina Hsu, N., Tsay, S.-C., & Huang, S.J. (2011). Asian Dust Weather Categorization with Satellite and Surface Observations. *International Journal of Remote Sensing*, **32**(1): 153–170. https://doi.org/10.1080/01431160903439932

Liu, F., Tan, Q., Jiang, X., Yang, F., & Jiang, W. (2019). Effects of Relative Humidity and PM2.5 Chemical Compositions on Visibility Impairment in Chengdu, China. *Journal of Environmental Sciences*, **86**: 15–23. https://doi.org/10.1016/j.jes.2019.05.004

Liu, J., Xia, X., Wang, P., Li, Z., Zheng, Y., Cribb, M., & Chen, H. (2007). Significant Aerosol Direct Radiative Effects during a Pollution Episode in Northern China: Aerosol Radiative Effects in China. *Geophysical Research Letters*, **34**(23). https://doi.org/10.1029/2007GL030953

Liu, N., Luo, T., Han, Y., Yang, K., Zhang, K., Wu, Y., Weng, N., & Li, X. (2022). Analysis of the Atmospheric Visibility Influencing Factors under Sea-Land Breeze Circulation. *Optics Express*, **30**(5): 7356–7371. https://doi.org/10.1364/OE.447141

Liu, P. F., Zhao, C. S., Göbel, T., Hallbauer, E., Nowak, A., Ran, L., Xu, W. Y., Deng, Z. Z., Ma, N., & Mildenberger, K. (2011). Hygroscopic Properties of Aerosol Particles at High Relative Humidity and Their Diurnal Variations in the North China Plain. *Atmospheric Chemistry and Physics*, **11**(7): 3479–3494. https://doi.org/10.5194/acp-11-3479-2011

Liu, S., & Liang, X. Z. (2010). Observed Diurnal Cycle Climatology of Planetary Boundary Layer Height. *Journal of Climate*, **23**(21): 5790–5809. https://doi.org/10.1175/2010JCLI3552.1

Liu, X., Cheng, Y., Zhang, Y., Jung, J., Sugimoto, N., Chang, S.Y., Kim, Y. J., Fan, S., & Zeng, L. (2008). Influences of Relative Humidity and Particle Chemical

Composition on Aerosol Scattering Properties during the 2006 PRD Campaign. *Atmospheric Environment*, **42**(7): 1525–1536. https://doi.org/10.1016/j.atmosenv.2007.10.077

Liu, X., Zhang, Y., Cheng, Y., Hu, M., & Han, T. (2012). Aerosol Hygroscopicity and Its Impact on Atmospheric Visibility and Radiative Forcing In Guangzhou during the 2006 PRIDE-PRD Campaign. *Atmospheric Environment*, **60**: 59–67. https://doi.org/10.1016/j.atmosenv.2012.06.016

Liu, Z., Chen, Y., Gu, X., Yeoh, J. K. W., & Zhang, Q. (2022). Visibility Classification and Influencing-Factors Analysis of Airport: A Deep Learning Approach. *Atmospheric Environment*, **278**, 119085. https://doi.org/10.1016/j.atmosenv.2022.119085

Lou, M., Guo, J., Wang, L., Xu, H., Chen, D., Miao, Y., Lv, Y., Li, Y., Guo, X., Ma, S., & Li, J. (2019). On The Relationship between Aerosol and Boundary Layer Height in summer in China under Different Thermodynamic Conditions. *Earth and Space Science*, **6**(5): 887–901. https://doi.org/10.1029/2019EA000620

Luan, T., Guo, X., Guo, L., & Zhang, T. (2018). Quantifying the Relationship Between PM2.5 Concentration, Visibility and Planetary Boundary Layer Height for Long-Lasting Haze and Fog-Haze Mixed Events in Beijing. *Atmospheric Chemistry and Physics*, **18**(1): 203–225. https://doi.org/10.5194/acp-18-203-2018

Lüthi, Z. L., Škerlak, B., Kim, S.W., Lauer, A., Mues, A., Rupakheti, M., & Kang, S. (2015). Atmospheric Brown Clouds Reach the Tibetan Plateau by Crossing the Himalayas. *Atmospheric Chemistry and Physics*, **15**(11): 6007–6021. https://doi.org/10.5194/acp-15-6007-2015

Mahadev, S., & Henry, R. C. (1999). Application of a Color-Appearance Model to Vision through Atmospheric Haze. *Color Research & Application*, **24**(2): 112–120. https://doi.org/10.1002/(SICI)1520-6378(199904)24:2<112::AID-COL6>3.0.CO;2-J

Mahapatra, P. S., Puppala, S. P., Adhikary, B., Shrestha, K. L., Dawadi, D. P., Paudel, S. P., & Panday, A. K. (2019). Air Quality Trends of the Kathmandu Valley: A

Satellite, Observation and Modeling Perspective. *Atmospheric Environment*, **201:** 334–347. https://doi.org/10.1016/j.atmosenv.2018.12.043

Maji, S., Ghosh, S., & Ahmed, S. (2018). Association of Air Quality with Respiratory and Cardiovascular Morbidity Rate in Delhi, India. *International Journal of Environmental Health Research*, **28**(5): 471–490. https://doi.org/10.1080/09603123.2018.1487045

Malm, W. C. (1999). *Introduction to visibility* [PhD Thesis, Colorado State University. Libraries]. https://mountainscholar.org/bitstream/handle/10217/235501/CIRA_040.pdf?sequence=1

Malm, W. C. (2016). *Visibility: The seeing of near and distant landscape features*. Elsevier. https://books.google.com/books?hl=en&lr=&id=aPMqCgAAQBAJ&oi=fnd&pg=PP1&dq=Malm,+W.+(2016).+Visibility:+The+seeing+of+near+and+distant+landscape+features.+Elsevier.&ots=EMZjntHzkq&sig=PY2RYg0BtNg4q10xSs5er-PpRrg

Malm, W. C., & Day, D. E. (2001). Estimates of Aerosol Species Scattering Characteristics as a Function of Relative Humidity. *Atmospheric Environment*, **35**(16): 2845–2860. https://doi.org/10.1016/S1352-2310(01)00077-2

Malm, W. C., Gebhart, K. A., Latimer, D., Cahill, T., Eldred, R., Pielke, R., Stocker, R., & Watson, J. (1989). *The Winter Haze Intensive Tracer Experiment (WHITEX)*. National Park Service. http://vista.cira.colostate.edu/Improve/the-winter-haze-intensive-tracer-experiment-whitex/

Malm, W. C., Kelley, K., Molenar, J., & Daniel, T. (1981). Human Perception of Visual Air Quality (Uniform Haze). *Atmospheric Environment (1967)*, **15**(10–11): 1875–1890.

Malm, W. C., Molenar, J., & Chan, L. L. (1983). Photographic Simulation Techniques for Visualizing the Effect of Uniform Haze on a Scenic Resource. *Journal of the Air Pollution Control Association*, **33**(2): 126–129. https://doi.org/10.1080/00022470.1983.10465554

Malm, W. C., Molenar, J. V., Eldred, R. A., & Sisler, J. F. (1996). Examining the Relationship among Atmospheric Aerosols and Light Scattering and Extinction in the Grand Canyon Area. *Journal of Geophysical Research: Atmospheres*, **101**(D14): 19251–19265. https://doi.org/10.1029/96JD00552

Malm, W. C., Sisler, J. F., Huffman, D., Eldred, R. A., & Cahill, T. A. (1994). Spatial and Seasonal Trends in Particle Concentration and Optical Extinction in the United States. *Journal of Geophysical Research: Atmospheres*, **99**(D1): 1347–1370. https://doi.org/10.1029/93JD02916

Manandhar, K. B. (2006). The Fog Episode in Southern Terai Plains of Nepal: Some Observations and Concepts. *Journal of Hydrology and Meteorology*, **3**(1). http://soham.org.np/wp-content/uploads/2006/03/v3-95-100.pdf

Mann, H. B. (1945). Nonparametric Tests against Trend. *Econometrica: Journal of the Econometric Society*, **13**(3): 245–259. https://doi.org/10.2307/1907187

Markowicz, K. M., Flatau, P. J., Quinn, P. K., Carrico, C. M., Flatau, M. K., Vogelmann, A. M., Bates, D., Liu, M., & Rood, M. J. (2003). Influence of Relative Humidity on Aerosol Radiative Forcing: An ACE‐Asia Experiment Perspective. *Journal of Geophysical Research: Atmospheres*, **108**(D23): 2002JD003066. https://doi.org/10.1029/2002JD003066

Martinez, J. (2019). Great Smog of London. *Encyclopedia Britannica*, *9*.

Meteorology, J. (2004). JAA ATPL Training. *Jeppessen Sanderson Inc., ISBN 0.88487*, *350*.

Middleton, W. E. K. (1952). *Vision through the atmosphere*. University of Toronto Press.

Miller, M. E., Canfield, N. L., Ritter, T. A., & Weaver, C. R. (1972). Visibility Changes in Ohio, Kentucky, and Tennessee from 1962 to 1969. *Monthly Weather Review*, **100**(1): 67–71.

MoF. (2020). *Economic Survey 2019/20*. Government of Nepal, Ministry of Finance. https://www.mof.gov.np/uploads/document/file/Economic%20Survey%202019_20201125024153.pdf

Mohan, M., & Payra, S. (2014). Aerosol Number Concentrations and Visibility during Dense Fog over a Subtropical Urban Site. *Journal of Nanomaterials*, **2014**: 15–15. https://doi.org/10.1155/2014/495457

Mool, E., Bhave, P. V., Khanal, N., Byanju, R. M., Adhikari, S., Das, B., & Puppala, S. P. (2020). Traffic Condition and Emission Factor from Diesel Vehicles within the Kathmandu Valley. *Aerosol and Air Quality Research*, **20**(3): 395–409. Doi: 10.4209/aaqr.2019.03.0159

Morisset, T., & Odoni, A. (2011). Capacity, Delay, and Schedule Reliability at Major Airports in Europe and the United States. *Transportation Research Record: Journal of the Transportation Research Board*, **2214**(1): 85–93. https://doi.org/10.3141/2214-11

Mues, A., Rupakheti, M., Münkel, C., Lauer, A., Bozem, H., Hoor, P., Butler, T., & Lawrence, M. G. (2017). Investigation of The Mixing Layer Height Derived from Ceilometer Measurements in the Kathmandu Valley and Implications for Local Air Quality. *Atmospheric Chemistry and Physics*, **17**(13): 8157–8176. https://doi.org/10.5194/acp-17-8157-2017

Mukherjee, A. K., Daniel, C. E. J., & Sethumadhavan, K. (1980). Deterioration of Visibility at Bombay Airport due to Atmospheric Pollutants. *Mausam*, **31**(2): 287–290. https://doi.org/10.54302/mausam.v31i2.3864

Münkel, C. (2007). Mixing Height Determination with Lidar Ceilometers Results from Helsinki Testbed. *Meteorologische Zeitschrift*, 451–459.

Munn, R. E. (1973). Secular Increases in Summer Haziness in the Atlantic Provinces. *Atmosphere*, **11**(4): 156–161. https://doi.org/10.1080/00046973.1973.9648357

Nabat, P., Somot, S., Mallet, M., Chiapello, I., Morcrette, J. J., Solmon, F., Szopa, S., Dulac, F., Collins, W., & Ghan, S. (2013). A 4-D Climatology (1979 – 2009) of the Monthly Tropospheric Aerosol Optical Depth Distribution over the Mediterranean Region from a Comparative Evaluation and Blending Of Remote Sensing and Model Products. *Atmospheric Measurement Techniques*, **6**(5): 1287–1314. https://doi.org/10.5194/amt-6-1287-2013

Naegele, P. S., & Sellers, W. D. (1981). A Study of Visibility in Eighteen Cities in the Western and Southwestern United States. *Monthly Weather Review*, **109**(11): 2394–2399. https://doi.org/10.1175/1520-0493(1981)109<2394:ASOVIE>2.0.CO;2

Nakajima, C., SR, C., & ML, S. (1980). On the fog in Kathmandu Valley Glaciological Expedition of Nepal, Contribution No. 75. *Journal of the Japanese Society of Snow and Ice*, **41**(Special): 90–99.

National Statistics Office. (2021). *National Population and Housing Census 2021* (Volume 01). National Statistics Office, Government of Nepal. https://censusnepal.cbs.gov.np/results/files/result-folder/National%20Report_English.pdf

NCDC. (2010). *Federal climate complex data documentation for integrated surface data*. National Climatic Data Center (NCDC), Air Force Combat Climatology Center, Fleet Numerical Meteorology and Oceanography Detachment. https://www.itl.nist.gov/div898/winds/NIST_TN/doc/ish-format-document.pdf

Nieuwstadt, F. T. (1984). The turbulent structure of the stable, nocturnal boundary layer. *Journal of Atmospheric Sciences*, *41*(14), 2202–2216.

Niu, F., Li, Z., Li, C., Lee, K.-H., & Wang, M. (2010). Increase of Wintertime Fog in China: Potential Impacts of Weakening of the Eastern Asian Monsoon Circulation and Increasing Aerosol Loading. *Journal of Geophysical Research*, **115**: D00K20. https://doi.org/10.1029/2009JD013484

Oleniacz, R., Bogacki, M., Szulecka, A., Rzeszutek, M., & Mazur, M. (2016). Assessing the Impact of Wind Speed and Mixing-Layer Height on Air Quality in Krakow (Poland) In the Years 2014–2015. *JCEEA*, **33**: 315–342.

Padmanabhamurty, B. (1986). Some aspects of the urban climates of India. *WMO Proceedings of the Technical Conference on Urban Climatology and Its Applications with Special Regard to Tropical Areas p 136-165(SEE N 87-10636 01-47)*.

Pan, X. L., Yan, P., Tang, J., Ma, J. Z., Wang, Z. F., Gbaguidi, A., & Sun, Y. L. (2009). Observational Study of Influence of Aerosol Hygroscopic Growth on

Scattering Coefficient over Rural Area near Beijing Mega-City. *Atmospheric Chemistry and Physics*, **9**(19): 7519–7530. https://doi.org/10.5194/acp-9-7519-2009

Panday, A. K., Praveen, P. S., Adhikary, B., Bhave, P., Banmali Pradhan, B., Dhungel, S., Mehra, M., & Mahapatra, P. S. (2016). Who is Polluting the Himalaya? *AGU Fall Meeting Abstracts*, *2016*, A53E-0344. https://ui.adsabs.harvard.edu/abs/2016AGUFM.A53E0344P/abstract

Panday, A. K., & Prinn, R. G. (2009). Diurnal cycle of air pollution in the Kathmandu Valley, Nepal: Observations. *Journal of Geophysical Research: Atmospheres*, **114**(D9): 2008JD009777. https://doi.org/10.1029/2008JD009777

Panday, A. K., Prinn, R. G., & Schär, C. (2009). Diurnal Cycle of Air Pollution in the Kathmandu Valley, Nepal: 2.-Modeling Results. *Journal of Geophysical Research: Atmospheres*, **114**(D21): 2008JD009808. https://doi.org/10.1029/2008JD009808

Pandithurai, G., Dipu, S., Dani, K. K., Tiwari, S., Bisht, D. S., Devara, P. C. S., & Pinker, R. T. (2008). Aerosol Radiative Forcing During Dust Events over New Delhi, India. *Journal of Geophysical Research: Atmospheres*, **113**(D13): 2008JD009804. https://doi.org/10.1029/2008JD009804

Pasricha, P. K., Gera, B. S., Shastri, S., Maini, H. K., John, T., Ghosh, A. B., Tiwari, M. K., & Garg, S. C. (2003). Role of the Water Vapour Greenhouse Effect in the Forecasting Of Fog Occurrence. *Boundary-Layer Meteorology*, **107**(2): 469–482. https://doi.org/10.1023/A:1022128800130

Pilinis, C., Seinfeld, J. H., & Grosjean, D. (1989). Water Content of Atmospheric Aerosols. *Atmospheric Environment (1967)*, **23**(7): 1601–1606. https://doi.org/10.1016/0004-6981(89)90419-8

Pitchford, M., Malm, W. C., Schichtel, B., Kumar, N., Lowenthal, D., & Hand, J. (2007). Revised Algorithm for Estimating Light Extinction from IMPROVE Particle Speciation Data. *Journal of the Air & Waste Management Association*, **57**(11): 1326–1336. https://doi.org/10.3155/1047-3289.57.11.1326

Poulos, G. S., Blumen, W., Fritts, D. C., Lundquist, J. K., Sun, J., Burns, S. P., Nappo, C., Banta, R., Newsom, R., & Cuxart, J. (2002). CASES-99: A Comprehensive Investigation of the Stable Nocturnal Boundary Layer. *Bulletin of the American Meteorological Society*, **83**(4): 555–582. https://doi.org/10.1175/1520-0477(2002)083<0555:CACIOT>2.3.CO;2

Putero, D., Cristofanelli, P., Marinoni, A., Adhikary, B., Duchi, R., Shrestha, S. D., Verza, G. P., Landi, T. C., Calzolari, F., & Busetto, M. (2015). Seasonal Variation of Ozone and Black Carbon Observed at Paknajol, An Urban Site in the Kathmandu Valley, Nepal. *Atmospheric Chemistry and Physics*, **15**(24): 13957–13971. https://doi.org/10.5194/acp-15-13957-2015

Qu, W. J., Wang, J., Zhang, X. Y., Wang, D., & Sheng, L. F. (2015). Influence of Relative Humidity on Aerosol Composition: Impacts on Light Extinction and Visibility Impairment at Two Sites in Coastal Area of China. *Atmospheric Research*, **153:** 500–511. https://doi.org/10.1016/j.atmosres.2014.10.009

Quan, J., Zhang, Q., He, H., Liu, J., Huang, M., & Jin, H. (2011). Analysis of the Formation of Fog and Haze in North China Plain (NCP). *Atmospheric Chemistry and Physics*, **11**(15): 8205–8214. https://doi.org/10.5194/acp-11-8205-2011

Quan, J., Gao, Y., Zhang, Q., Tie, X., Cao, J., Han, S., Meng, J., Chen, P., & Zhao, D. (2013). Evolution of Planetary Boundary Layer under Different Weather Conditions, And Its Impact on Aerosol Concentrations. *Particuology*, **11**(1): 34–40. https://doi.org/10.1016/j.partic.2012.04.005

Ram, K., Sarin, M. M., & Hegde, P. (2010). Long-Term Record of Aerosol Optical Properties and Chemical Composition from a High-Altitude Site (Manora Peak) In Central Himalaya. *Atmospheric Chemistry and Physics*, **10**(23): 11791–11803. https://doi.org/10.5194/acp-10-11791-2010

Ramachandran, S., Kedia, S., & Sheel, V. (2015). Spatiotemporal Characteristics of Aerosols in India: Observations and Model Simulations. *Atmospheric Environment*, **116**: 225–244. https://doi.org/10.1016/j.atmosenv.2015.06.015

Ramachandran, S., & Rupakheti, M. (2022). Trends in the Types and Absorption Characteristics of Ambient Aerosols over the Indo-Gangetic Plain and North

China Plain in Last Two Decades. *Science of the Total Environment*, **831**: 154867. https://doi.org/10.1016/j.scitotenv.2022.154867

Ramanathan, V., Li, F., Ramana, M. V., Praveen, P. S., Kim, D., Corrigan, C. E., Nguyen, H., Stone, E. A., Schauer, J. J., Carmichael, G. R., Adhikary, B., & Yoon, S. C. (2007). Atmospheric Brown Clouds: Hemispherical and Regional Variations in Long-Range Transport, Absorption, and Radiative Forcing. *Journal of Geophysical Research: Atmospheres*, **112**(D22): 2006JD008124. https://doi.org/10.1029/2006JD008124

Randles, C. A. (2004). Hygroscopic and Optical Properties of Organic Sea Salt Aerosol and Consequences for Climate Forcing. *Geophysical Research Letters*, **31**(16): L16108. https://doi.org/10.1029/2004GL020628

Randles, C. A., Da Silva, A. M., Buchard, V., Colarco, P. R., Darmenov, A., Govindaraju, *et al.* (2017). The MERRA-2 Aerosol Reanalysis, 1980 Onward. Part I: System Description and Data Assimilation Evaluation. *Journal of climate*, **30**(17), 6823-6850.

Ranter, H. (1992). *ASN Aircraft accident Airbus A300B4-203 AP-BCP Kathmandu-Tribhuvan Airport (KTM)*. https://aviation-safety.net/database/record.php?id=19920928-0

Ranter, H. (1997). *ASN Aircraft accident Airbus A300B4-220 PK-GAI Medan-Polonia Airport (MES)*. https://aviation-safety.net/database/record.php?id=19970926-0

Ratajczak, A., Badyda, A., Czechowski, P. O., Czarnecki, A., Dubrawski, M., & Feleszko, W. (2021). Air Pollution Increases The Incidence of Upper Respiratory Tract Symptoms among Polish Children. *Journal of Clinical Medicine*, **10**(10): 2150. https://doi.org/10.3390/jcm10102150

Ray, D., Ghosh, A., Chatterjee, A., Ghosh, S. K., & Raha, S. (2019). Size-Specific PAHs and Associated Health Risks over a Tropical Urban Metropolis: Role of Long-Range Transport and Meteorology. *Aerosol and Air Quality Research*, **19**(11): 2446–2463. https://doi.org/10.4209/aaqr.2019.06.0312

Regmi, G., Shrestha, S., Maharjan, S., Khadka, A. K., Regmi, R. P., & Kaphle, G. C. (2020). The Weather Hazards Associated with the US-Bangla Aircraft

Accident at the Tribhuvan International Airport, Nepal. *Weather and Forecasting*, **35**(5): 1891–1912. https://doi.org/10.1175/WAF-D-19-0183.1

Ribeiro, F. N., de Oliveira, A. P., Soares, J., de Miranda, R. M., Barlage, M., & Chen, F. (2018). Effect of Sea Breeze Propagation on the Urban Boundary Layer of the Metropolitan Region of Sao Paulo, Brazil. *Atmospheric Research*, **214:** 174–188. https://doi.org/10.1016/j.atmosres.2018.07.015

Rienecker, M. M., Suarez, M. J., Gelaro, R., Todling, R., Bacmeister, J., Liu, E., Bosilovich, M. G., Schubert, S. D., Takacs, L., & Kim, G.-K. (2011). MERRA: NASA's Modern-Era Retrospective Analysis for Research and Applications. *Journal of Climate*, **24**(14): 3624–3648. https://doi.org/10.1175/JCLI-D-11-00015.1

Ross, D. M., Malm, W. C., & Iyer, H. K. (1997). Human Visual Sensitivity to Plumes with a Gaussian. *Journal of the Air & Waste Management Association*, **47**(3): 370–382. https://doi.org/10.1080/10473289.1997.10464448

Rupakheti, D., Adhikary, B., Praveen, P. S., Rupakheti, M., Kang, S., Mahata, K. S., Naja, M., Zhang, Q., Panday, A. K., & Lawrence, M. G. (2017). Pre-Monsoon Air Quality over Lumbini, a World Heritage Site along the Himalayan Foothills. *Atmospheric Chemistry and Physics*, **17**(18): 11041–11063. https://doi.org/10.5194/acp-17-11041-2017

Rupakheti, D., Kang, S., Cong, Z., Rupakheti, M., Tripathee, L., Panday, A. K., & Holben, B. (2018). Study of Aerosol Optical Properties over Two Sites in the Foothills of the Central Himalayas. *The International Archives of the Photogrammetry, Remote Sensing and Spatial Information Sciences*, **42:** 1493–1497. https://doi.org/10.5194/isprs-archives-XLII-3-1493-2018

Rupakheti, D., Kang, S., Rupakheti, M., Cong, Z., Tripathee, L., Panday, A. K., & Holben, B. N. (2018). Observation of Optical Properties and Sources of Aerosols at Buddha's Birthplace, Lumbini, Nepal: Environmental Implications. *Environmental Science and Pollution Research*, **25**(15): 14868–14881. https://doi.org/10.1007/s11356-018-1713-z

Safai, P. D., Ghude, S., Pithani, P., Varpe, S., Kulkarni, R., Todekar, K., Tiwari, S., Chate, D. M., Prabhakaran, T., & Jenamani, R. K. (2019). Two-Way

Relationship between Aerosols and Fog: A Case Study at IGI Airport, New Delhi. *Aerosol and Air Quality Research*, **19**(1): 71–79. https://doi.org/10.4209/aaqr.2017.11.0542

Saikawa, E., Panday, A., Kang, S., Gautam, R., Zusman, E., Cong, Z., Somanathan, E., & Adhikary, B. (2019). Air Pollution in the Hindu Kush Himalaya. In P. Wester, A. Mishra, A. Mukherji, & A. B. Shrestha (Eds.), *The Hindu Kush Himalaya Assessment* (pp. 339–387). Springer International Publishing. https://doi.org/10.1007/978-3-319-92288-1_10

Saikawa, E., Wu, Q., Zhong, M., Abramov, A., & Panday, A. K. (2020). *Garbage Burning in South Asia: How Important Is It to Regional Air Quality? | Environmental Science & Technology*. https://pubs.acs.org/doi/10.1021/acs.est.0c02830

Sapart, C. J., Monteil, G., Prokopiou, M., van de Wal, R. S., Kaplan, J. O., Sperlich, P., Krumhardt, K. M., Van der Veen, C., Houweling, S., & Krol, M. C. (2012). Natural and Anthropogenic Variations in Methane Sources during the Past Two Millennia. *Nature*, **490**(7418): 85–88.

Sapkota, B. (2002). Suspended Matter in the Urban Air of Kathmandu Valley. *Proceedings of the Regional Workshop on Better Air Quality in Asian and Pacific Rim Cities, 16-18 December 2002 (BAQ 2002)*. https://citeseerx.ist.psu.edu/document?repid=rep1&type=pdf&doi=114697d2fe22b486a8c622d7554aefe8815b1c1e

Sapkota, B. K. (1996). Study of Visibility and Particulate Pollution Over Kathmandu Valley. *Project Report, Institute of Engineering, Pulchowk Campus*.

Sarkar, S., Chokngamwong, R., Cervone, G., Singh, R. P., & Kafatos, M. (2006). Variability of Aerosol Optical Depth and Aerosol Forcing Over India. *Advances in Space Research*, **37**(12): 2153–2159. https://doi.org/10.1016/j.asr.2005.09.043

Schichtel, B. A., Husar, R. B., Falke, S. R., & Wilson, W. E. (2001). Haze Trends over the United States, 1980–1995. *Atmospheric Environment*, **35**(30): 5205–5210. https://doi.org/10.1016/S1352-2310(01)00317-X

Schmid, P., & Niyogi, D. (2012). A Method for Estimating Planetary Boundary Layer Heights and Its Application over The ARM Southern Great Plains Site. *Journal of Atmospheric and Oceanic Technology*, **29**(3): 316–322. https://doi.org/10.1175/JTECH-D-11-00118.1

Seabold, S., & Perktold, J. (2010). Statsmodels: Econometric and statistical modeling with python. *Proceedings of the 9th Python in Science Conference*, **57**(61): 10–25080. https://pdfs.semanticscholar.org/3a27/6417e5350e29cb6bf04ea5a4785601d5a215.pdf

Seibert, P., Beyrich, F., Gryning, S.-E., Joffre, S., Rasmussen, A., & Tercier, P. (1998). Mixing Height Determination for Dispersion Modelling. Report of Working Group 2. In *Harmonisation of the pre-processing of meteorological data for atmospheric dispersion models. COST action 710. Final report*. Office for Official Publications of the European Communities. https://orbit.dtu.dk/en/publications/mixing-height-determination-for-dispersion-modelling-report-of-wo

Seibert, P., Beyrich, F., Gryning, S.-E., Joffre, S., Rasmussen, A., & Tercier, P. (2000). Review and Intercomparison of Operational Methods for the Determination of the Mixing Height. *Atmospheric Environment*, **34**(7): 1001–1027. https://doi.org/10.1016/S1352-2310(99)00349-0

Seidel, D. J., Ao, C. O., & Li, K. (2010). Estimating Climatological Planetary Boundary Layer Heights from Radiosonde Observations: Comparison of Methods and Uncertainty Analysis. *Journal of Geophysical Research*, **115**(D16): D16113. https://doi.org/10.1029/2009JD013680

Seidel, D. J., Zhang, Y., Beljaars, A., Golaz, J., Jacobson, A. R., & Medeiros, B. (2012). Climatology of the Planetary Boundary Layer over the Continental United States and Europe. *Journal of Geophysical Research: Atmospheres*, **117**(D17): 2012JD018143. https://doi.org/10.1029/2012JD018143

Seinfeld, J. H., & Pandis, S. N. (2016). *Atmospheric chemistry and physics: From air pollution to climate change*. John Wiley & Sons.

Sen, P. K. (1968). Estimates of the Regression Coefficient Based on Kendall's Tau. *Journal of the American Statistical Association*, **63**(324): 1379–1389. https://doi.org/10.1080/01621459.1968.10480934

Sequeira, R., & Lai, K. H. (1998). The Effect of Meteorological Parameters and Aerosol Constituents on Visibility in Urban Hong Kong. *Atmospheric Environment*, **32**(16): 2865–2871. https://doi.org/10.1016/S1352-2310(97)00494-9

Shahzad, M. I. (2014). *Estimation of surface visibility over Hong Kong using remote sensing* [Department of Land surveying and Geo-Informatics, Hong Kong Polytechnic University]. https://theses.lib.polyu.edu.hk/handle/200/7420

Sharma, C. K. (1997). Urban air quality of Kathmandu Valley "Kingdom of Nepal." *Atmospheric Environment*, **31**(17): 2877–2883.

Sharma, M., Kaskaoutis, D. G., Singh, R. P., & Singh, S. (2014). Seasonal Variability of Atmospheric Aerosol Parameters over Greater Noida Using Ground Sunphotometer Observations. *Aerosol and Air Quality Research*, **14**(3): 608–622. https://doi.org/10.4209/aaqr.2013.06.0219

Shen, Z., Cao, J., Zhang, L., Zhang, Q., Huang, R.-J., Liu, S., Zhao, Z., Zhu, C., Lei, Y., Xu, H., & Zheng, C. (2016). Retrieving Historical Ambient PM2.5 Concentrations using Existing Visibility Measurements in Xi'an, Northwest China. *Atmospheric Environment*, **126:** 15–20. https://doi.org/10.1016/j.atmosenv.2015.11.040

Shin, J., Kim, D., & Noh, Y. (2022). Estimation of Aerosol Extinction Coefficient Using Camera Images and Application in Mass Extinction Efficiency Retrieval. *Remote Sensing*, **14**(5): 1224. https://doi.org/10.3390/rs14051224

Shrestha, A. B., Bajracharya, S. R., Sharma, A. R., Duo, C., & Kulkarni, A. (2017). Observed Trends and Changes in Daily Temperature and Precipitation Extremes over the Koshi River Basin 1975–2010. *International Journal of Climatology*, **37**(2): 1066–1083. https://doi.org/10.1002/joc.4761

Shrestha, S., Moore, G. A., & Peel, M. C. (2018). Trends in Winter Fog Events in the Terai Region of Nepal. *Agricultural and Forest Meteorology*, **259:** 118–130. https://doi.org/10.1016/j.agrformet.2018.04.018

Shrestha, S., Peel, M. C., & Moore, G. A. (2023). Cold Waves in Terai Region of Nepal and Farmer's Perception of the Effect of Fog Events and Cold Waves on Agriculture. *Theoretical and Applied Climatology*, **151**(1–2): 29–45. https://doi.org/10.1007/s00704-022-04262-7

Shrestha, S. R., Kim Oanh, N. T., Xu, Q., Rupakheti, M., & Lawrence, M. G. (2013). Analysis of the Vehicle Fleet in the Kathmandu Valley for Estimation of Environment and Climate Co-Benefits of Technology Intrusions. *Atmospheric Environment*, **81:** 579–590. https://doi.org/10.1016/j.atmosenv.2013.09.050

Shrestha, S., Shrestha, S., Maharjan, S., & Regmi, R. P. (2015a). Boundary Layer Characteristics over Aindanda Low-Mountain Pass of Kathmandu Valley, Nepal. *Journal of Institute of Science and Technology*, **20**(2): 22–30.

Shrestha, S., Shrestha, S., Maharjan, S., & Regmi, R. P. (2015b). Boundary Layer Characteristics over Central Area of the Kathmandu Valley As Revealed By Sodar Observations. *Journal of Institute of Science and Technology*, **20**(1): 28–35.

Singh, A., Avis, W. R., & Pope, F. D. (2020). Visibility as a Proxy for Air Quality in East Africa. *Environmental Research Letters*, **15**(8): 084002. Doi: 10.1088/1748-9326/ab8b12

Singh, A., Bloss, W. J., & Pope, F. D. (2017). 60 Years of UK Visibility Measurements: Impact of Meteorology and Atmospheric Pollutants on Visibility. *Atmospheric Chemistry and Physics*, **17**(3): 2085–2101. https://doi.org/10.5194/acp-17-2085-2017

Singh, A., & Dey, S. (2012). Influence of aerosol composition on visibility in megacity Delhi. *Atmospheric Environment*, **62:** 367–373. https://doi.org/10.1016/j.atmosenv.2012.08.048

Singh, A., George, J. P., & Iyengar, G. R. (2018). Prediction of Fog/Visibility over India using NWP Model. *Journal of Earth System Science*, **127**(2), 26. https://doi.org/10.1007/s12040-018-0927-2

Singh, J., Giri, R. K., & Kant, S. (2007). Radiation fog viewed by INSAT–1 D and Kalpana Geo-Stationary satellite. *Mausam*, **58**(2): 251–260. https://doi.org/10.54302/mausam.v58i2.1228

Sivaraman, C., McFarlane, S., Chapman, E., Jensen, M., Liu, S., & Fischer, M. (2013). *Planetary boundary layer height (PBL) value added product (VAP): Radiosonde retrievals*. DOE Office of Science Atmospheric Radiation Measurement (ARM) Program user facility, United States. https://www.osti.gov/biblio/1808688

Sloane, C. S. (1982). Visibility trends—II. Mideastern United States 1948—1978. *Atmospheric Environment (1967)*, **16**(10): 2309–2321. https://doi.org/10.1016/0004-6981 (82)90117-2

Sloane, C. S. (1983). Summertime visibility declines: Meteorological influences. *Atmospheric Environment (1967)*, **17**(4): 763–774.

Sloane, C. S. (1984). Meteorologically adjusted air quality trends: Visibility. *Atmospheric Environment (1967)*, **18**(6): 1217–1229.

Sloane, C. S., Watson, J., Chow, J., Pritchett, L., & Richards, L. W. (1991). Size-Segregated Fine Particle Measurements by Chemical Species and Their Impact on Visibility Impairment in Denver. *Atmospheric Environment. Part A. General Topics*, **25**(5–6): 1013–1024. https://doi.org/10.1016/0960-1686(91)90143-U

Smadja, J., Aubriot, O., Puschiasis, O., Duplan, T., Grimaldi, J., Hugonnet, M., & Buchheit, P. (2015). Climate Change and Water Resources in the Himalayas. Field Study in Four Geographic Units of the Koshi Basin, Nepal. *Journal of Alpine Research| Revue de Géographie Alpine*, **103**: *2*. https://journals.openedition.org/rga/2910

Smirnov, A., Holben, B. N., Dubovik, O., O'Neill, N. T., Eck, T. F., Westphal, D. L., Goroch, A. K., Pietras, C., & Slutsker, I. (2002). Atmospheric Aerosol Optical

Properties in the Persian Gulf. *Journal of the Atmospheric Sciences*, **59**(3): 620–634. https://doi.org/10.1175/1520-0469(2002)059<0620:AAOPIT>2.0.CO;2

Smith, T. L., Benjamin, S. G., & Brown, J. M. (2002). Visibility Forecasts from the RUC20. *Preprints, 10th Conf. on Aviation, Range, and Aerospace Meteorology, Portland, OR, Amer. Meteor. Soc., JP1*, *27*. https://citeseerx.ist.psu.edu/document?repid=rep1&type=pdf&doi=5df3a3c7b404032efbd07ae8b4fede187f99db4b

Srivastava, A. K., Dey, S., & Tripathi, S. N. (2012). Aerosol Characteristics over the Indo-Gangetic Basin: Implications to Regional Climate. *Atmospheric Aerosols-Regional Characteristics-Chemistry and Physics*, **10:** 47782.

Srivastava, S. K., Sharma, A. R., & Sachdeva, K. (2016). A Ground Observation Based Climatology of Winter Fog: Study over the Indo-Gangetic Plains, India. *International Journal of Environmental and Ecological Engineering*, **10**(7): 742–753. doi.org/10.5281/zenodo.1125465

Steyn, D. G., Baldi, M., & Hoff, R. M. (1999). The Detection of Mixed Layer Depth and Entrainment Zone Thickness from Lidar Backscatter Profiles. *Journal of Atmospheric and Oceanic Technology*, **16**(7): 953–959. https://doi.org/10.1175/1520-0426(1999)016<0953:TDOMLD>2.0.CO;2

Stjern, C. W., Stohl, A., & Kristjánsson, J. E. (2011). Have Aerosols Affected Trends In Visibility And Precipitation In Europe? *Journal of Geophysical Research*, **116**(D2): D02212. https://doi.org/10.1029/2010JD014603

Streets, D. G., Wu, Y., & Chin, M. (2006). Two-Decadal Aerosol Trends as a Likely Explanation of the Global Dimming/Brightening Transition. *Geophysical Research Letters*, **33**(15): L15806. https://doi.org/10.1029/2006GL026471

Stull, R. B. (1988). *An introduction to boundary layer meteorology* (Vol. 13). Springer Science & Business Media.

Sun, Y., Song, T., Tang, G., & Wang, Y. (2013). The Vertical Distribution of PM2.5 and Boundary-Layer Structure during Summer Haze in Beijing. *Atmospheric Environment*, **74**: 413–421. https://doi.org/10.1016/j.atmosenv.2013.03.011

Syed, F. S., Körnich, H., & Tjernström, M. (2012). On The Fog Variability over South Asia. *Climate Dynamics*, **39**(12): 2993–3005. https://doi.org/10.1007/s00382-012-1414-0

Szintai, B. (2010). *Improving the turbulence coupling between high-resolution numerical weather prediction models and Lagrangian particle dispersion models*. EPFL. https://infoscience.epfl.ch/record/150277

Tabari, H., & Marofi, S. (2011). Changes of Pan Evaporation in the West of Iran. *Water Resources Management*, **25**(1): 97–111. https://doi.org/10.1007/s11269-010-9689-6

Tang, I. N. (1996). Chemical and Size Effects of Hygroscopic Aerosols on Light Scattering Coefficients. *Journal of Geophysical Research: Atmospheres*, **101**(D14): 19245–19250. https://doi.org/10.1029/96JD03003

Tang, I. N., Wong, W. T., & Munkelwitz, H. R. (1981). The Relative Importance of Atmospheric Sulfates and Nitrates in Visibility Reduction. *Atmospheric Environment (1967)*, **15**(12): 2463–2471. https://doi.org/10.1016/0004-6981(81)90062-7

Tare, V., Tripathi, S. N., Chinnam, N., Srivastava, A. K., Dey, S., Manar, M., Kanawade, V. P., Agarwal, A., Kishore, S., Lal, R. B., & Sharma, M. (2006). Measurements of Atmospheric Parameters during Indian Space Research Organization Geosphere Biosphere Program Land Campaign II at a Typical Location in the Ganga Basin: 2. Chemical Properties. *Journal of Geophysical Research: Atmospheres*, **111**(D23): 2006JD007279. https://doi.org/10.1029/2006JD007279

Tiao, G. C., Box, G. E. P., & Hamming, W. J. (1975). Analysis of Los Angeles Photochemical Smog Data: A Statistical Overview. *Journal of the Air Pollution Control Association*, **25**(3): 260–268. https://doi.org/10.1080/00022470.1975.10470082

Timsina, N. P., Shrestha, A., Poudel, D. P., & Upadhyaya, R. (2020). Trend of Urban Growth in Nepal with a Focus in Kathmandu Valley: A Review of Processes and Drivers of Change. https://era.ed.ac.uk/handle/1842/37436

Tripathee, L., Kang, S., Rupakheti, D., Cong, Z., Zhang, Q., & Huang, J. (2017). Chemical Characteristics of Soluble Aerosols over the Central Himalayas: Insights into Spatiotemporal Variations and Sources. *Environmental Science and Pollution Research*, **24**(31): 24454–24472. https://doi.org/10.1007/s11356-017-0077-0

Tsai, H.-H., Yuan, C.-S., Hung, C.-H., Lin, C., & Lin, Y.-C. (2011). Influence of Sea-Land Breezes on the Tempo-spatial Distribution of Atmospheric Aerosols over Coastal Region. *Journal of the Air & Waste Management Association*, **61**(4): 358–376. https://doi.org/10.3155/1047-3289.61.4.358

Tsai, Y. I. (2005). Atmospheric Visibility Trends in an Urban Area in Taiwan 1961–2003. *Atmospheric Environment*, **39**(30): 5555–5567. https://doi.org/10.1016/j.atmosenv.2005.06.012

Tsai, Y. I., Kuo, S.-C., Lee, W.-J., Chen, C.-L., & Chen, P.-T. (2007). Long-Term Visibility Trends in One Highly Urbanized, One Highly Industrialized, and Two Rural Areas of Taiwan. *Science of the Total Environment*, **382(**2–3): 324–341. https://doi.org/10.1016/j.scitotenv.2007.04.048

UNEP, SAARC, & DA. (2014). *South Asia Environment Outlook 2014*. UNEP Regional Office for Asia and the Pacific (UNEP/ROAP). http://www.sacep.org/pdf/Reports-Technical/2014-South-Asia-Environment-Outlook-2014.pdf

Vajanapoom, N., Shy, C. M., Neas, L. M., & Loomis, D. (2001). Estimation of Particulate Matter from Visibility in Bangkok, Thailand. *Journal of Exposure Science & Environmental Epidemiology*, **11**(2): 97–102.

Van Beelen, A. J., & Van Delden, A. J. (2012). Cleaner air brings better views, more sunshine and warmer summer days in the Netherlands. *Weather*, **67**(1): 21–25. Doi: 10.1002/wea.836

Van Belle, G., & Hughes, J. P. (1984). Nonparametric Tests for Trend in Water Quality. *Water Resources Research*, **20**(1): 127–136. https://doi.org/10.1029/WR020i001p00127

Vautard, R., Yiou, P., & Van Oldenborgh, G. J. (2009). Decline of Fog, Mist and Haze in Europe over the Past 30 Years. *Nature Geoscience*, **2**(2): 115–119.

Vogelezang, D. H. P., & Holtslag, A. A. M. (1996). Evaluation and Model Impacts of Alternative Boundary-Layer Height Formulations. *Boundary-Layer Meteorology*, **81**(3–4): 245–269. https://doi.org/10.1007/BF02430331

Wallace, J. M., & Hobbs, P. V. (2006). *Atmospheric science: an introductory survey* (Vol. 92). Elsevier.

Wan, X., Kang, S., Li, Q., Rupakheti, D., Zhang, Q., Guo, J., Chen, P., Tripathee, L., Rupakheti, M., & Panday, A. K. (2017). Organic Molecular Tracers in the Atmospheric Aerosols from Lumbini, Nepal, In the Northern Indo-Gangetic Plain: Influence of Biomass Burning. *Atmospheric Chemistry and Physics*, **17**(14): 8867–8885. https://doi.org/10.5194/acp-17-8867-2017

Wang, H., Shen, K., Yu, P., Shi, Q., & Ko, H. (2020). Multimodal Deep Fusion Network for Visibility Assessment with a Small Training Dataset. *IEEE Access*, **8**, 217057–217067. IEEE Access. https://doi.org/10.1109/ACCESS.2020.3031283

Wang, J., & Martin, S. T. (2007). Satellite Characterization of Urban Aerosols: Importance of Including Hygroscopicity and Mixing State in the Retrieval Algorithms. *Journal of Geophysical Research: Atmospheres*, **112**(D17): 2006JD008078. https://doi.org/10.1029/2006JD008078

Wang, K., Dickinson, R. E., & Liang, S. (2009). Clear Sky Visibility has Decreased over Land Globally from 1973 to 2007. *Science*, **323**(5920): 1468–1470. https://doi.org/10.1126/science.1167549

Wang, X. Y., & Wang, K. C. (2014). Estimation of Atmospheric Mixing Layer Height from Radiosonde Data. *Atmospheric Measurement Techniques*, **7**(6): 1701–1709. https://doi.org/10.5194/amt-7-1701-2014

Wang, X., Zhang, R., & Yu, W. (2019). The Effects of PM2.5 Concentrations and Relative Humidity on Atmospheric Visibility in Beijing. *Journal of Geophysical Research: Atmospheres*, **124**(4): 2235–2259. https://doi.org/10.1029/2018JD029269

Watson, J. G. (2002). Visibility: Science and Regulation. *Journal of the Air & Waste Management Association*, **52**(6): 628–713. https://doi.org/10.1080/10473289.2002.10470813

Wen, C. C., & Yeh, H.H. (2010). Comparative Influences of Airborne Pollutants and Meteorological Parameters on Atmospheric Visibility and Turbidity. *Atmospheric Research*, **96**(4): 496–509. https://doi.org/10.1016/j.atmosres.2009.12.005

White, W. H. (1990). The Components of Atmospheric Light Extinction: A Survey of Ground-Level Budgets. *Atmospheric Environment. Part A. General Topics*, **24**(10): 2673–2679. https://doi.org/10.1016/0960-1686(90)90147-F

World Bank. (2014). *Diesel Power Generation: Inventories and Black Carbon Emissions in Nigeria*. World Bank. https://doi.org/10.1596/28419

World Health Organization (WHO). (2016). *Air quality database 2016*. https://www.who.int/data/gho/data/themes/air-pollution/who-air-quality-database/2016#cms

World Meteorological Organization (WMO). (2023). *International Cloud Atlas*. International Cloud Atlas. https://cloudatlas.wmo.int/home.html

World Meteorological Organization (WMO), A. (1996). *Exchanging meteorological data: Guidelines on relationships in commercial meteorological activities; WMO policy and practice*. Secretariat of the World Meteorological Organization, Geneva.

Wu, D. (2006). More Discussions on the Differences between Haze and Fog in City. *Guangdong Meteorology*, **32:** 9–15. Doi: 10.7519/j.issn.1000-0526.2006.4.002

Wu, J., Fu, C., Zhang, L., & Tang, J. (2012). Trends of Visibility on Sunny Days in China in the Recent 50 Years. *Atmospheric Environment*, **55:** 339–346. https://doi.org/10.1016/j.atmosenv.2012.03.037

Xing, Y.-F., Xu, Y.-H., Shi, M.-H., & Lian, Y.-X. (2016). The Impact of PM2.5 on the Human Respiratory System. *Journal of Thoracic Disease*, **8**(1): E69. Doi: 10.3978/j.issn.2072-1439.2016.01.19

Yao, W., Gui, K., Wang, Y., Che, H., & Zhang, X. (2021). Identifying the Dominant Local Factors of 2000–2019 Changes in Dust Loading Over East Asia. *Science of the Total Environment*, **777:** 146064. https://doi.org/10.1016/j.scitotenv.2021.146064

Yu, X., Ma, J., An, J., Yuan, L., Zhu, B., Liu, D., Wang, J., Yang, Y., & Cui, H. (2016). Impacts of Meteorological Condition and Aerosol Chemical Compositions on Visibility Impairment in Nanjing, China. *Journal of Cleaner Production*, **131:** 112–120. https://doi.org/10.1016/j.jclepro.2016.05.067

Yuan, C. S., Lee, C.-G., Liu, S.-H., Yuan, C., Yang, H.-Y., & Chen, C.-T. A. (2002). Developing Strategies for Improving Urban Visual Air Quality. *Aerosol and Air Quality Research*, **2**(1): 9–22.

Yue, S., & Wang, C. (2004). The Mann-Kendall Test Modified by Effective Sample Size to Detect Trend in Serially Correlated Hydrological Series. *Water Resources Management*, **18**(3): 201–218. https://doi.org/10.1023/B:WARM.0000043140.61082.60

Zajonc, A. (1993). *Catching the light: The entwined history of light and mind*. Oxford University Press, USA.

Zhai, W., & Cheng, C. (2020). A Long Short-Term Memory Approach to Predicting Air Quality Based on Social Media Data. *Atmospheric Environment*, **237**, 117411. https://doi.org/10.1016/j.atmosenv.2020.117411

Zhang, J., Tong, L., Peng, C., Zhang, H., Huang, Z., He, J., & Xiao, H. (2019). Temporal Variability of Visibility and Its Parameterizations in Ningbo, China. *Journal of Environmental Sciences*, **77**: 372-382. https://doi.org/10.1016/j.jes.2018.09.015

Zhang, L., Sun, J. Y., Shen, X. J., Zhang, Y. M., Che, H., Ma, Q. L., Zhang, Y. W., Zhang, X. Y., & Ogren, J. A. (2015). Observations of Relative Humidity Effects on Aerosol Light Scattering In the Yangtze River Delta of China. *Atmospheric Chemistry and Physics*, **15**(14): 8439–8454. https://doi.org/10.5194/acp-15-8439-2015

Zhang, M., Tian, P., Zeng, H., Wang, L., Liang, J., Cao, X., & Zhang, L. (2021). A Comparison of Wintertime Atmospheric Boundary Layer Heights Determined By Tethered Balloon Soundings and Lidar at the Site of SACOL. *Remote Sensing*, **13**(9): 1781. https://doi.org/10.3390/rs13091781

Zhang, Q. H., Zhang, J. P., & Xue, H. W. (2010). The Challenge of Improving Visibility in Beijing. *Atmospheric Chemistry and Physics*, **10**(16): 7821–7827. https://doi.org/10.5194/acp-10-7821-2010

Zhang, W., Guo, J., Miao, Y., Liu, H., Song, Y., Fang, Z., He, J., Lou, M., Yan, Y., & Li, Y. (2018). On The Summertime Planetary Boundary Layer With Different Thermodynamic Stability in China: A Radiosonde Perspective. *Journal of Climate*, **31**(4): 1451–1465. https://doi.org/10.1175/JCLI-D-17-0231.1

Zhang, Y., Seidel, D. J., & Zhang, S. (2013). Trends in Planetary Boundary Layer Height over Europe. *Journal of Climate*, **26**(24): 10071–10076. https://doi.org/10.1175/JCLI-D-13-00108.1

Zhang, Y. L., & Cao, F. (2015). Fine Particulate Matter (PM2.5) in China at a City Level. *Scientific Reports*, **5**(1): 14884.

Zhao, C., Yu, Y., Kuang, Y., Tao, J., & Zhao, G. (2019). Recent Progress of Aerosol Light-scattering Enhancement Factor Studies in China. *Advances in Atmospheric Sciences*, **36**(9): 1015–1026. https://doi.org/10.1007/s00376-019-8248-1

Zhao, P., Zhang, X., Xu, X., & Zhao, X. (2011). Long-Term Visibility Trends and Characteristics in the Region of Beijing, Tianjin, and Hebei, China. *Atmospheric Research*, **101**(3): 711–718. https://doi.org/10.1016/j.atmosres.2011.04.019

Zhong, M., Saikawa, E., Avramov, A., Chen, C., Sun, B., Ye, W., Keene, W. C., Yokelson, R. J., Jayarathne, T., Stone, E. A., Rupakheti, M., & Panday, A. K. (2019). Nepal Ambient Monitoring and Source Testing Experiment (NAMaSTE): Emissions of Particulate Matter and Sulfur Dioxide from Vehicles and Brick Kilns and Their Impacts on Air Quality in The Kathmandu Valley, Nepal. *Atmospheric Chemistry and Physics*, **19**(12): 8209–8228. https://doi.org/10.5194/acp-19-8209-2019

APPENDIX

APPENDIX A

A.1 IFR and VFR Airport Operations

The visibility condition at the airport with visibility of more than 5 km is referred to as a Visual Meteorological Condition (VMC), i.e., nice and clear weather; and the applicable rules for flight operations are Visual Flight Rules (VFR) (ICAO, 2005).

Instrument meteorological conditions (IMC) are "meteorological conditions in terms of visibility distance from cloud, and cloud ceiling less than the minimum specified for VMC" (ICAO, 2005). The corresponding applicable rules are Instrument Flight Rules (IFR). However, aircraft can choose to fly under IFR in VMC conditions for orderly air –air-traffic-flow-management. Most of the large aircraft, especially jets, opt to fly under IFR in all weather conditions in most of the airports.

A.2 Controlled Flight into Terrain (CFIT)

It happens when an airworthy aircraft that the pilot is fully controlling erroneously flies into a body of water, terrain, or an obstruction. Usually, the pilots do not realize there is a threat until it is too late.

A.3 Different types of approaches at the airports for aircraft landing (VOR, RNP, ILS)

Every airport requires having minimum visibility (visibility minima) level to function properly for aircraft take-off and landing, which is determined by local authority based on various factors: terrains, regulations, and most importantly available navigation facilities at the airport. Each of the navigation facilities has different operational minima that are aircraft-type specific. VHF Omnidirectional Radio Range collated with Distance Measuring Equipment (VOR-DME or simply VOR) is one of the most widely used navigation facilities at the airport that assists with aircraft take-off and landing in normal (aircraft flying under IFR rules) and impaired visibility conditions. Many of the airports in Nepal including both of our study sites are equipped with VOR DMEs.

Table A.1: ILS categories and corresponding runway visual range (RVR) as per ICAO standards. (ICAO, 2017)

ILS categories (CATs)	ICAO Runway visual range (RVR) (m)
CAT I	> 550
CAT II	550 - 300
CAT IIIA	300 - 175
CAT IIIB	175 - 50
CAT IIIC	< 50

Instrument Landing System, ILS in short form, facilitates aircraft to land in even worse weather conditions, e.g., lower visibility and cloud ceiling conditions. Different categories of ILS and the corresponding minimum visibility conditions—expressed in terms of Runway Visual Range (RVR)—have been shown in **Table A.1**. The term Runway Visual Range (RVR) describes the range at which a pilot seated in an aircraft on the runway centerline can see the surface markers.

The higher the category, the better is its lading guidance. Although this technology is highly advanced and efficient in catering to most unfavorable weather conditions that reduce visibility at airports, e.g., dense haze and dense fog, it requires a huge monetary investment and suitable topography. Thus, in our country, only two of the recent international airports GBIA and Pokhara Regional International Airport are equipped with these CAT-I ILS systems. Nonetheless, one at GBIA is yet to get operational permission from the southern neighboring country.

TIA has been equipped with VOR-DME facilities for tens of years. GoN has recently invested in a Localizer (LOC) facility at TIA, which also gives lateral guidance to the lading aircraft with lower visibility and cloud ceiling threshold than VOR (**Table A.2**). Installation of ILS in TIA is quite unlikely because of not so suitable topography. The best-performing approach and landing facility available in TIA is Required Navigation Performance-Authorization Required (RNP-AR), which has been in effect there since 2012, together with a VOR (**Table A.2**). However, RNP-AR type of approaches require some special equipment on board the aircraft, complex training procedures for pilots, and complicated approval processes. This implies that not all aircraft and all pilots are capable and authorized to conduct such procedures. Thus, the basic mode of approach guidance system in TIA is VOR.

Table A.2: Different lading facilities available at GBIA and TIA along with required visibility thresholds and their operational status

Airport	Landing Facility	Minimum Required Visibility (m)	Remarks
GBIA, Bhairahawa	VOR Runway 10	1800	Operational
	RNP Runway 10	1800	Operational
	RNP Runway 28	2200	Operational
	ILS	-	Not Operational
TIA, Kathmandu	VOR-DME Runway 02	2800	Operational
	RNP-AR Runway 02	1100	Operational
	LOC Runway 02	2000	Operational

APPENDIX B

B.1 Pearson correlation coefficient (r)

Pearson correlation coefficient in statistics gives a measure of linear relationship between two different variables. It is the ratio of covariance of two variables and the product of their standard deviation, i.e., normalized covariance.

For a given random variable pair (X, Y), the Pearson correlation coefficient (r_{xy}) is given by:

$$r_{xy} = \frac{cov(X,Y)}{\sigma_x \sigma_y} \tag{B.1}$$

Where, $cov(X,Y)$ stands for the covariance of X and Y; σ_x and σ_y are standard deviations of X and Y respectively.

In this given paired data $\{(x_1, y_1), \dots, (x_n, y_n)\}$ consisting of n pairs, r_{xy} is:

$$r_{xy} = \frac{\sum_{i=1}^{n}(x_i - \bar{x})(y_i - \bar{y})}{\sqrt{\sum_{i=1}^{n}(x_i - \bar{x})^2}\sqrt{\sum_{i=1}^{n}(y_i - \bar{y})^2}} \tag{B.2}$$

Where n is the size of the sample; x_i and y_i are individual sample points; and $\bar{x}$ and $\bar{y}$ are sample mean values such that:

$$\bar{x} = \frac{1}{n}\sum_{i=1}^{n} x_i \tag{B.3}$$

$$\bar{y} = \frac{1}{n}\sum_{i=1}^{n} y_i \tag{B.4}$$

B.2 Coefficient of determination (R^2)

This statistic is generally used in the context of statistical models that have the main purpose of predicting future outcomes or testing of hypothesis based on other related

information. It gives the measure of the proportion of variation in the dependent variable that can be predicted from the independent variable(s).

If $\{(f_1, y_1), \ldots, (f_n, y_n)\}$ represent modeled (predicted), and observed data (target) pair, coefficient of determination is:

$$R^2 = 1 - \frac{\sum_i (y_i - f_i)^2}{\sum_i (y_i - \bar{y})^2} \tag{B.5}$$

Or,

$$R^2 = 1 - \frac{SS_{res}}{SS_{tot}} \tag{B.6}$$

Where,

SS_{res} is the sum of squares of residuals ($e_i = (y_i - f_i)$):

$$SS_{res} = \sum_i (y_i - f_i)^2 = \sum_i e_i^2 \tag{B.7}$$

Moreover, SS_{tot} is the total sum of squares of the variable and the mean value.

$$SS_{tot} = \sum_i (y_i - \bar{y})^2 \tag{B.8}$$

B.3 Mean absolute error (MAE)

It gives the measure of errors between paired observations that express the same phenomena. It is calculated as the ratio of the sum of absolute errors to the sample size. It uses the same scale as the measured data—a scale-dependent accuracy measure. Thus, it is not appropriate to make a comparison between predicted values that use different scales. It is one of the common measures of forecast error in time series analysis.

$$MAE = \frac{\sum_{i=1}^{n} |y_i - f_i|}{n} = \frac{\sum_{i=1}^{n} |e_i|}{n} \tag{B.9}$$

B.4 Median absolute error (MedAE)

This is particularly robust to the outliers and calculated as a median of all absolute differences between the target and the prediction. The smaller the error better the performance of a model.

$$MedAE(y, f) = median(|y_1 - f_1|, \ldots, |y_n - f_n|) \tag{B.10}$$

Where, f_i is the predicted value of i-th sample and y_i is the corresponding true value (observed value) as discussed above.

B.5 Root mean squared error (RMSE)

This is the standard deviation of residuals (e_i) and it gives us a measure of how spread out the residuals are, i.e., it tells us how near the data around the best fit is. RMSE finds its most common application in forecasting and regression analysis of climatology to verify experimental results. The working formula of RMSE is:

$$RMSE = \sqrt{\frac{1}{n}\sum_{i=1}^{n}(y_i - f_i)^2} \tag{B.11}$$

APPENDIX C

C.1 Papers published in international journals

Kathayat, B., Panday, A. K., Pokharel, B., Kumar, V., & Chapagain, N. P. (2023). Four decades of aviation visibility at Bhairahawa airport, gateway to Buddha's birthplace Lumbini, Nepal. *Atmospheric Research*, *288*, 106746. https://doi.org/10.1016/j.atmosres.2023.106746

Dhungel, S., **Kathayat, B**., Mahata, K., & Panday, A. (2018). Transport of regional pollutants through a remote trans-Himalayan valley in Nepal. *Atmospheric Chemistry and Physics*, *18*(2), 1203–1216. https://doi.org/10.5194/acp-18-1203-2018

C.2 Papers published in national (peer-reviewed) journals

Kathayat, B., Chapagain, N. P., & Lamsal, Y. R. (2022). Influence of ambient relative humidity on horizontal visibility in the two cities of western Nepal having contrasting urban-cum-industrial backgrounds and study of long-term variation. *Journal of Nepal Physical Society*, ***8***(1): 55–62. https://doi.org/10.3126/jnphyssoc.v8i1.48287

Kathayat, B., Panday, A. K., Pokharel, B., & Chapagain, N. P. (2024). Intensifying Haze and Disappearing Dense Fog in Winter at Tribhuvan International Airport, Kathmandu: Impacts in Aviation. *Journal of Institute of Science and Technology*, **29**(1): 35-45.

C.3 Manuscripts

1) **Kathayat, B.**, Panday, A. K., Pokharel, B., & Chapagain, N. P. (----). Nocturnal boundary layer height in the mountainous terrain of Kathmandu from radiosonde instruments—retrieval methods, temporal variations and relationship with air pollution and visibility. *Waiting for submission to an international journal.*

2) **Kathayat, B.**, Panday, A. K., Pokharel, B., & Chapagain, N. P. (----). Characterization and parametrization of atmospheric visibility at Tribhuvan International Airport, Kathmandu. *Drafting a manuscript for an international journal*.

C.4 Conferences, seminars, workshop participation

Oral/ poster presentations

Kathayat, B., Chapagain, N., Panday, A. & Lamsal, Y.R. (5–9 June 2017). *Factors Influencing Aviation Visibility in Nepal* [Poster Presentation] Third Atmospheric Composition and Asian Monsoon, Guangzhou, China

Kathayat, B., Chapagain, N., Panday, A., Adhikari, B.R. & Rupakheti, D. (2–3 September 2017). *Study of Atmospheric Visibility in Biratnagar Airport* [Poster Presentation]. International Conference in Physics of Space and Matter (ICPSM), Saint Xavier's College, Kathmandu, Nepal

Kathayat, B., Chapagain, N., Panday, A. (27-30 November 2017) *Variability of Atmospheric Visibility in Kathmandu, Nepal: Analysis of Aviation Routine Weather Reports (METAR)* [Poster presentation]. Air Pollution, Climate and Health in Southern Asia and the HKH: Workshop & Science-Policy Dialogue, ICIMOD, NEPAL

Kathayat, B., Chapagain, N., Panday, A., Lamsal, Y.R. (18 July 2020). *Long-term atmospheric visibility variation in two cities of West Nepal (1977-2020): A proxy for local and regional atmospheric aerosol loads* [Oral Presentation].Association of Nepalese Physicists in America (ANPA)

Kathayat, B., Panday, A.K., Kumar, V., Chapagain, N.P. (22 January 2022). *Four Decades of Aviation Visibility at Bhairahawa Airport, Gateway to Buddha's Birthplace Lumbini* [Oral Presentation]. International Conference on Frontier of Physics (ICFP), Nepal Physical Society (NPS), Kathmandu, Nepal

Kathayat, B., Panday, A.K., Pokharel, B., Kumar, V., Chapagain, N.P. (9–10 October 2023). *Four Decades of Aviation Visibility at Bhairahawa Airport, Gateway to Buddha's Birthplace Lumbini, Nepal* [Poster Presentation]. Institute of Science and Technology (IoST), Tribhuvan University, Kathmandu, Nepal

Trainings/ Lecturers/ Courses

1) 'Programming for Everybody (Getting Started with Python)' (May 2016) [Online Course completed]. University of Michigan, hosted by Coursera

2) Second ACAM Training School on 'Observations and Modeling of Atmospheric Chemistry and Aerosols in the Asian Monsoon region' (10–12 June 2017) [Training attended]. Atmospheric Composition and Asian Monsoon (ACAM), Guangzhou, China

3) Non-credit lecturer series on 'Research Methodology' by Prof. Dr. Subodh R. Shenoy (ICTP & TIFR) (6 Nov–22 Dec 2017) [Lecturer attended]. Central Department of Physics, Kirtipur, Kathmandu, Nepal

4) 'MET service for Flight Operations', Recurrent Training for Met Observers, MET forecast Division (30 March 2018) [Training delivered]. Gauchar, Kathmandu, Nepal

5) 'Python Programming for data analysis' course, NPS School of Computing -2020 (4 July-31 January 2021) [Course completed]. Nepal Physical Society (NPS), Kathmandu, Nepal

6) Specialization course on 'Statistics with Python' (June 2020) [Course completed]. University of Michigan, hosted by Coursera. Modules included: understanding and visualizing data with Python, inferential statistical analysis with Python, and fitting statistical models to data with Python

7) 'How to write an impressive research proposal and ISP promoting equal opportunity in science' (9 June 2021) [Workshop attended]. Atmospheric and Material Research Center, Department of Physics, Amrit Campus, Kathmandu, Nepal with the support of International Science Programme (ISP), Uppsala University, Sweden

8) 'Quantum computing' (24–30 July 2021) [Course completed]. LOCUS, Institute of Engineering (IOE), Pulchowk, Lalitpur, Nepal

9) 'Satellite data retrieval from NASA ARSET/ EUMETSAT, and atmospheric modeling' (July 2022) [Online training attended]. EUMETSAT/ESA/ECMWF, Germany

10) ‘ArcGIS’ course (4–28 September 2021) [Course completed]. Skill corner and consultation, Kathmandu, Nepal

11) ‘Machine learning for climate science and earth observation’ (19 October 2021) [online workshop attended]. Climate change AI (https://www.climatechange.ai/)

12) ‘Proficient Manuscript Writing: Author’s and Editor’s Perspective’ (17 July 2022) [Online workshop attended]. Association of Nepali Physicists in America (ANPA) and Nepal Physical Society (NPS)

13) ‘Hydro-Met Master Plan of Nepal’ (6 April 2023) [Workshop attended]. Department of Hydrology and Meteorology (DHM) and World Bank, Kathmandu, Nepal

APPENDIX D

D.1 Attachments

Influence of Ambient Relative Humidity on Horizontal Visibility in the Two Cities of Western Nepal having Contrasting Urban-Cum-Industrial Backgrounds and Study of Long-Term Variation

Bhogendra Kathayat, Narayan Prasad Chapagain and Yash Raj Lamsal

Journal of Nepal Physical Society
Volume 8, No 1, 2022
(Special Issue: ICFP 2022)
ISSN: 2392-473X (Print), 2738-9537 (Online)

JNPS, **8** (1), 55-62 (2022)
DOI: http://doi.org/10.3126/jnphyssoc.v8i1.48287

Published by: Nepal Physical Society
P.O. Box: 2934
Tri-Chandra Campus
Kathmandu, Nepal
Email: nps.editor@gmail.com

ICFP 2022
ISSN:2392-473X (Print)
2738-9537 (Online)

Research Article ©Nepal Physical Society
DOI:http://doi.org/10.3126/jnphyssoc.v8i1.48287

Influence of Ambient Relative Humidity on Horizontal Visibility in the Two Cities of Western Nepal having Contrasting Urban-Cum-Industrial Backgrounds and Study of Long-Term Variation

Bhogendra Kathayat,[1, a)] Narayan Prasad Chapagain,[2, b)] and Yash Raj Lamsal[3, c)]

[1)] *Central Department of Physics, Tribhuvan University, Kathmandu, Nepal*
[2)] *2Department of Physics, Amrit Campus, Tribhuvan University, Kathmandu, Nepal*
[3)] *Department of Management Informatics and communication, Kathmandu University, Dhulikhel, Nepal*

[a)] *Corresponding author: bhogendra.735711@cdp.tu.edu.np*
[b)] *Electronic mail: npchapagain@gmail.com*
[c)] *Electronic mail: yashrajlamsal@gmail.com*

Abstract. Atmospheric visibility, a measure of horizontal distance one can distinctly see with unaided eye, is affected by the scattering and absorption of visible light by the tiny particles (aerosols), or different gases present in the atmosphere. Thus, visibility is commonly considered a proxy for ambient air quality. The long-term trend of visibility may reflect the change in the air quality of a place over the period. In our study, we have analyzed historic climatological data (1977-2020) from the National Oceanic and Atmospheric Administration (NOAA) global hourly archive, for the two cities of west Nepal, namely, Bhairahawa (BWA, 27.506N, 83.416 E) and Surkhet (SKH, 28.6 N, and 81.617 E). We have found that both of the synoptic stations exhibited persistent degraded visibility. BWA had poorer visibility conditions (poor air quality) than that of SKH since the beginning of the study period. Since 2014, the 'annual good day' (V10 km) at BWA is steadily near 0%, and the 'annual bad day' (V<5 km) is 60 %, suggesting a degraded air quality. Similarly, we observed a notable decline in the 50th percentile of visibility in the mid-1980s at SKH, and a sharp decline of 'good day' since 2011. Meteorology modifies the optical properties of aerosol/ gaseous in the atmosphere, thereby, resulting in a change in visibility. In our study, we have investigated the influence of relative humidity (RH) on prevailing visibility. Although the relationship between them exists in both of the stations, it is more distinctly visible at BWA. We observed lower visibility conditions (V 3 km) occurring at an RH level as low as 50% at BWA. This indicates an abundance of specific hygroscopic aerosols, whose light extinction thresholds are as low. At BWA, the impact of RH is evident during the dry season. In contrast, the threshold value of RH is quite high (80%) at SKH and the relationship is prominent during the wet season. This alarmingly poor air quality at both stations requires a serious concern because of its adverse impact on various sectors like aviation, tourism, and public health.

Received:20 March,2022 ; **Revised**:20 April 200; **Accepted**:3 May 2022

Keywords: air pollution, meteorology, relative humidity, trend, visibility.

INTRODUCTION

Atmospheric visibility is a key element in meteorological observation. Very good atmospheric visibility (up to > 100 km) can be observed in unpolluted circumstances in clear sky conditions [1, 2]. Whereas, the low visibility is observed when there is heavy air pollution in the atmosphere and, or bad meteorological conditions [1, 3]. Thus, the status of atmospheric visibility, good or bad, is an important indicator of the status of atmospheric optics [4, 5, 6, 7, 8, 9, 10, 11, 12]. This makes visibility an important proxy for particulate matter pollution [13, 14]. Atmospheric visibility can decrease because of the scattering and absorption of visible light by particles and gases present in the atmosphere [10, 15, 16]. Several studies in the past have confirmed that visibility extinction is related to fine particles PM2.5, and PM10, especially particles with a diameter of less than 1 mm [10]. The total light

extinction resulting from atmospheric particles can be apportioned to the major components of particles, which includes sulfate, nitrate, organic carbon (OC), black carbon (BC), soil, and the coarse mass fraction (PM10 and PM2.5) [17]. Several studies have shown that countries like the United States, China, and India having vast territories, large populations and giant economies have faced problems of poor visibility conditions and hence the poor air quality in different periods because of industrial revolutions [18]. Serious sulfur and organics pollution in the mid-eastern and western urban regions [6, 17, 19, 20] were attributed to the poor air quality in the US during those periods. Population and economic explosions in their mega-cities, and the associated air pollution are attributed as the reason behind the significant decline in visibility in India [18, 21, 22, 23, 24] and China [1, 3, 12, 25, 26, 27, 28, 29, 30, 31, 32, 33]. Meteorological factors, especially relative humidity (RH), have a great influence on visibility [17, 34, 35]. As the RH increases, hygroscopic particles progressively uptake ambient water vapor leading to increased scattering cross-sections and hence refractive index. For instance, the scattering cross-section of ammonium sulfate could be increased by a factor of five or more above that of dry particles when RH increases above 90% [17]. This very property, hygroscopicity; inevitably affects the light radiation in the horizontal direction; and influences atmospheric visibility [4, 11, 36]. This is how; the understanding of the mechanism of visibility variations plays a key role in air pollution, emergency response, and regional air quality management. In this study, we have investigated the long-term variation of visibility in two cities Bhairahawa and Surkhet. The variations in visibility were investigated using 43 years of data collected from the National Climatic Data Center (NCDC). Two different statistical approaches have been adopted for the investigation of the trend: (a) trend of 50th, 90th, and 10th percentile and (b) annual percentage of good and bad days. Lastly, we have attempted to study the dependence of visibility on RH.

DATA AND METHODS

Bhairahawa (BWA) and Surkhet (SKH), two cities in the western region of Nepal (Figure.1; Table I), have contrasting geographic and meteorological features and were chosen as the representative sites for the investigation. Bhairahawa, a municipal city is an administrative headquarter of the Rupandehi district, lies in the outer flat plains of Nepal, 265 km west of the capital city, Kathmandu. This city borders India towards the south. The nearest mountain foothill to the city lies about 25 km north. The city is highly urbanized, and among the major industrial powerhouse in the country influencing major economic aspects of Nepal. In contrast, Surkhet station

TABLE I. Details of the selected synoptic station in West Nepal

Station	Lat.(°)	Lon.(°)	Elev.(m)	Available data duration
ine Bhairahawa(BWA)	27.506 N	83.416 E	109.1	1977-2020
Surkhet (SKH)	28.6 N	81.617 E	720	1976-2020

(28.6 N, 81.617 E; elevation: 720 m) lies in the valley of Surkhet, about 600 km west of Kathmandu. It is surrounded all around by hills. Surkhet is a comparatively less populated city and it lags Bhairahawa in terms of industrial establishments.

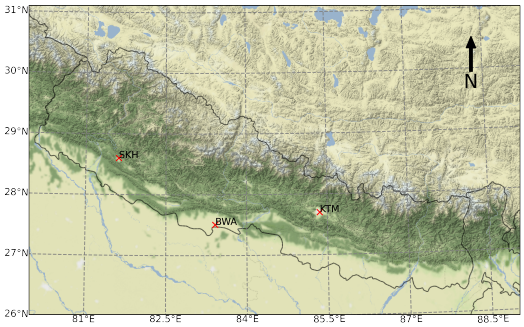

FIGURE 1. Bhairahawa and Surkhet stations, in country map of Nepal and their relative position w.r.t. Kathmandu (KTM), the capital city of Nepal

Visibility and other key meteorological parameters like wind speed, wind direction, air temperature, and dew-point temperature of these two sites with at least 3 hr. intervals from 1977 to 2020 were collected from the online repository of the National Climate Data Center (NCDC)(source: https://www7.ncdc.noaa.gov/CDO/cdoselect.cmd). NCDC is an authentic data source, used by many researchers as the main data source. It archives historical climatological datasets on a global scale. The data has been subjected to extensive automated quality control to correctly decode as much synoptic data as possible and to eliminate many of the random errors found in the original data. A series of processes were performed to get quality-controlled data that could accurately reflect the relationship between visibility and air pollution. Relative humidity (RH) was calculated through the equation [37]:

$$RH \approx 100 \left(\frac{112 - 0.1T + T_d}{112 + 0.9T} \right)^8 \quad (1)$$

Where T (°C) represents the air temperature and T_d (°C) represents the dew point temperature.

Visibility trend analysis

Naturally, the low visibility observations may occur because of specific weather conditions such as mist, precipitation, and fog, which have high relative humidity (RH). In this study, we have narrowed down our purpose of trend analysis to detect any inadvertent alteration of air quality resulting from human activities only, rather than the synergetic effect of human activities and natural influences. Similar to the work of many other researchers like [7, 11, 25], we have made a minor attempt to offset meteorological factors while carrying out the trend analysis. As all of these specific weather conditions bear one property in common, i.e. high moisture content (RH), we have removed all visibility observations when relative humidity (RH) equals or exceeds 90%. This is how; we have screened our data for precipitation, fog, and mist. In addition, we have screened the data for the time of day, i.e. data between 00:00 to 12:15 UTC (5:45-18:00 LT). Using visibility observation from 1980 to 2019 (inclusive), we have used two common statistical methods as described in the following sections.

Trend analysis by cumulative percentile

The observed visibility is the lower limit to prevailing visibility. The trend of a particular percentile of visibility can reflect the change in visibility level [11] over a long period. The Nth cumulative percentile of a visibility distribution is the visibility that equaled or exceeded N percent of the time according to [7, 8] . Usually, the fiftieth percentile is compared to establish the trend of visibility observation at a place. For a continuous and widespread frequency distribution, the 50th percentile would correspond to a median, a familiar concept. However, when applied to the visibility data, the 50th percentile need not necessarily correspond to the median, rather it represents the visibility one may expect to be equal to or exceed half of the considered period. Many researchers (e.g. [11]) have used other percentile levels, like the 10th percentile and 90th percentile to establish the trend in visibility data, since these percentile levels are inherently more representative of optical air quality compared to the 50th percentile. Here, the 10th percentile of visibility represents 'good visibility' and the 90th percentile represents "poor visibility". We also have attempted to report a trend in these percentile levels in our study. It is worthwhile to note here that the notion of percentile in this analysis follows reverse order to the statistical meaning of percentile of a continuous and widely spread frequency distribution because of the definition of visibility itself ([7, 8]). In this method, we also have grouped the visibility data into non-overlapping five-year periods to lessen the effect of large seasonal fluctuation in a given year.

Annual good and bad day percentage

The original dataset contains a combination of data from two different standard methods of measurement: SYNOP (Surface Synoptic Observations) and METAR (Meteorological Terminal Air Report). The major difference between these two methods is the recording time of their observations and observation standard. METAR data are encoded by automated airport weather stations (AWS) and SYNOP data are encoded by both manned and automated weather stations. The upper limit of METAR is 10 miles (or,10 km) whereas that of SYNOP could reach 30 miles or higher ([38]). Additionally, the time resolution of SYNOP is 3 hr, and METAR is 1 hr or half an hour. Thus, measurements of percentile, averages, etc. from the mixed data may not reflect the actual picture. Our dataset is mixed-type and primarily occupied by METAR in the later stages of recordings. This may lead to a sharp decrease in percentile values. Thus, a conclusion drawn based only on the analytical method described in the above section may not accurately reflect the actual status of visibility. To compensate for the influences caused by METAR records, we have adopted a more stringent analysis. In this method, we define a 'good day' as a day having daily average visibility equaled or exceeded the 10 km visibility threshold and a 'bad day' as one having daily average visibility of less than 5 km. We have calculated bad visibility frequency directly based on the data points rather than daily mean visibility values similar to the work of [18]. Finally, we have calculated the annual percentage of good and bad days for the entire period at both locations. According to [11, 18, 39] this method can more accurately indicate a long-term variation of air pollution status in a place.

RESULTS AND DISCUSSION

The 50th, 90th, and 10th cumulative percentiles of visibility

The long-term trends of visibility differed between the measurement locations as we can see from the grouped percentile charts (Figure.2) in three different percentiles levels. It is to be noted that the maximum value of visibility reported in our observation is 75.5 km. At the beginning of the five-year interval (1980 –1984), a very high 50th percentile of visibility nearing a maximum reported (75.5 km) was observed (Figure.2 [a]) in SKH. We observe an initially sharp (1985-1989) followed by a gradual decline in visibility until the end of our study period. Thus, the deterioration of general visibility is witnessed at SKH since the mid-80s. Figure 2[a] also depicts BWA having far less 50th percentile i.e., visibility observed dur-

ing half of the considered period, in comparison to that of SKH, the difference being appreciable initially. The 50th percentile and 10th percentile values of visibility at SKH (Figure.2 [b]) are both 75.5 km at the beginning period indicating excellent visibility conditions. In contrast, only 10% of the time during the period BWA witnessed that excellent visibility. We witness a decline in good visibility condition abruptly since mid- 90s at SKH and as early as mid - 80s in BWA. We also can see strong evidence of deterioration of visibility in SKH (Figure.2 [c]). Visibility used to be more than 10 km, 90% of the time before the year 2010, which is reduced to as low as 4 km in the later interval. The marked difference in studied percentile levels at these two sites suggests the regionality of the atmospheric aerosols. The typical poor visibility is reflected by the trend of the 90th percentile, as discussed. These plots show that visibility in SKH is much higher than that of BWA. All of these percentile levels display an overall marked declining trend of visibility indicating a worsening of air quality at both locations.

Percentage of annual good days and bad days

Figure 3 depicts that more than 55% of annual days witness good visibility before the year 1985 at BWA in line with our observation of the high value of the 50th percentile in Figure (2[a]). It exhibits gradual decline until reaching nil annual good day percentage since the year 2014. There is no recovery ever since it dropped to its lowest. Meanwhile, except for one year since 1980, all years before the year 2007 witnessed good visibility conditions, with a good day percentage of over 85%. It has recently reached the lowest after 2018. Annual bad day percentages at BWA are higher throughout, in comparison to SKH. It displayed a gradual rise from 20% (in 1980) to 60% (in 2014), and remained steady ever since with minor fluctuation. These findings suggest long periods of "general good visibility" in SKH compared to BWA. This method too clearly indicates a notable declining trend of visibility at both locations. SKH witnessed a better overall visibility condition throughout. A marked decline in the annual good day percentage is seen in the year 2011. Since our analysis has screened the influence of specific meteorological phenomena, any change in visibility should be a direct manifestation of the extent of air pollutants content in the atmosphere. Hence, we can certainly view visibility as a proxy for air pollution. Our findings, thus, imply a cleaner atmosphere in SKH. This can be attributed to the combined effect of lesser local-air-pollution-emission and/or diminished influence of transboundary air pollution, which agrees with its location and rural settings relative to BWA.

Influence of relative humidity on Visibility

Water vapor in the atmosphere does not have any direct effect on visibility since it does not scatter or absorb visible light by itself. The effect of RH on visibility results from the hygroscopic growth or shrink of atmospheric particles leading to light extinction. Thus, water vapor does not affect visibility unless pollutants are present. To gain more insight into the relationship between RH and visibility at the studied sites, we have categorized RH into seven bins [<40, 40-50, 50-60, 60-70, 70-80, 80-90,>90]. Likewise, observed visibilities have been classified into the following six specific ranges: visibility 1 km, 1 km < visibility 2 km, 2 km < visibility 3 km, 3 km visibility < 5 km, 5 km visibility < 10 km, and visibility 10 km or higher. In the stacked bars (Figure 4), we have shown the percentage occurrence of visibility categories (distinguished by different colors bar) that fall into a particular RH bin. These plots also display the respective frequency distribution of RH. Figure 4 shows that with growing RH, the percentage of low visibilities (V < 5 km) increases sharply.

As depicted in Figure 4, for RH exceeding 80% in BWA, more than 78% of visibility observations are below 10 km and over 40% of the observation are below 5 km. When RH >90%, about 67% of visibility observations are low visibility (V < 5 km) and 40% of the visibilities are below 2 km. Similarly, Figure 4(b) clearly shows that the percentage of low visibility increases with an increase in RH at SKH as well. For RH < 90% at SKH, more than 50% of visibility observations are above 10 km, indicating a lesser impact of RH on visibility. While comparing Figure 4 (a) and (b), we see that there are some percentage of low visibilities (v < 3 km) observations at RH as low as 50% at BWA, while this is pronounced only in the high RH regime (RH>80%) at SKH. The poor visibilities in the RH regime above 90% could have resulted from either the occurrence of meteorological phenomena like rain, fog, and mist, or the hygroscopic effect of RH on secondary aerosol pollutants present in the atmosphere as discussed earlier. Due to the limitation of our dataset, we could not rule out the rain observations from our dataset. Ruling out the mist and fog observation from the data set is beyond the scope of this research as well. Thus, increased low visibility conditions at higher RH (RH >90%) should be because of the combined effect of meteorological phenomena and hygroscopic growth of secondary aerosol pollutants, more prominent in BWA Focusing on the effect of RH alone on visibility, poor visibility observed even at the lower regime of RH, especially at BWA highlights the prominent effect of hygroscopic aerosols on the extinction of the light. This indicates the presence of a specific type of hygroscopic aerosols at BWA, which can manifest its light extinction behavior even at the low RH regime.

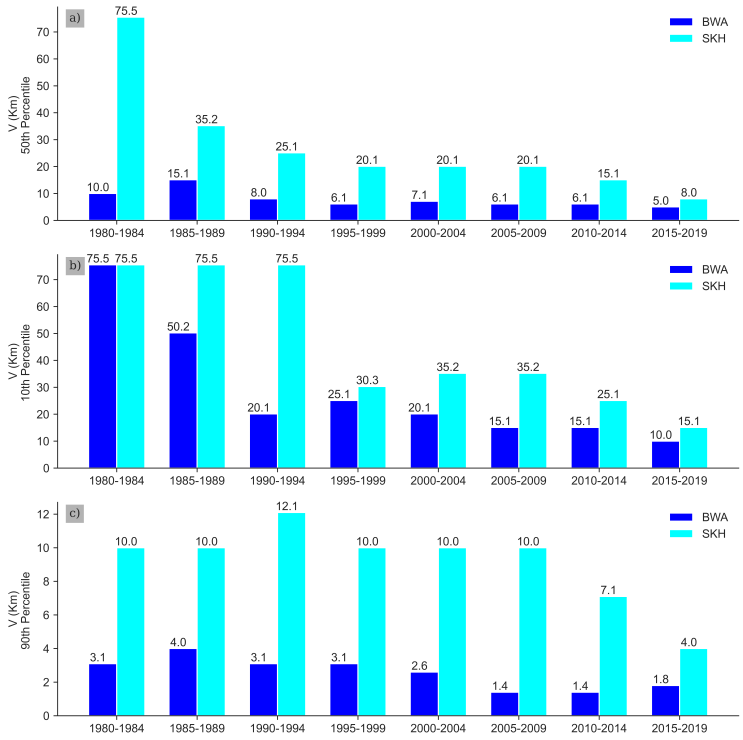

FIGURE 2. The 50th[a], 10th[b], and 90th [c] cumulative percentiles of visibility in Bhairahawa and Surkhet (1980-2020)

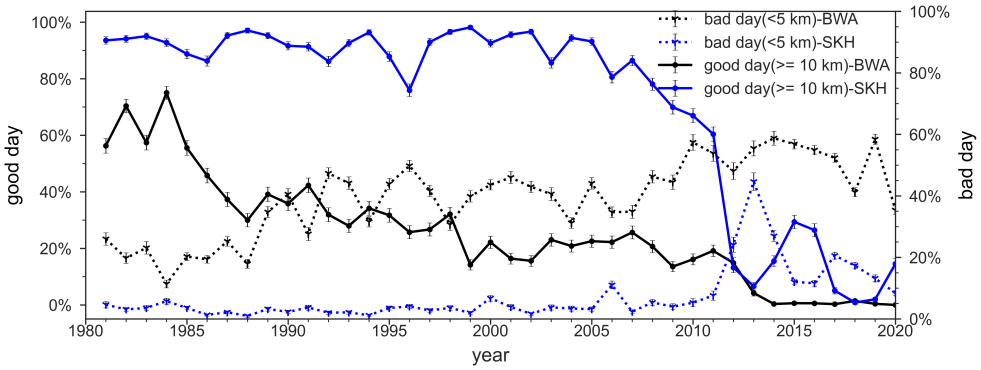

FIGURE 3. Long term variation of the annual good (visibility 10 km) and bad (<5km) day percentage based on visibilities of Bhairahawa (BWA) & Surkhet (SKH) for the period 1980-2020

[35] observed similar behavior of RH and visibility at Xiamen, China using high temporal resolution data during June 2011-May to 2012. They, too, found that percentage of low visibilities (V < 5 km) increases sharply with growing RH. We have also attempted to investigate the seasonal influence of RH on visibility. Seasonal variation of visibility with RH at both of our stations are shown in Figure 5 and their summary statistics have been presented in Table II. The two stations display quite contrasting seasonality concerning the occurrence of good and bad visibility conditions. At BWA the best visibility is observed (Figure. 5[a]) during the wet period of the summer Asian monsoon (June-September) and the poorest during the winter months (Dec-Feb). This might primarily be because of the scavenging of air pollutants by rainfall during the summer monsoon, irrespective of the extent of air pollution, and the occurrence of regionally widespread winter fog during winter (Dec-Feb). Many works of literature have pointed out that the presence of air pollutants enhances the severity of winter fog as well. Thus, RH might have played some role in worsening winter visibility through the hygroscopic growth of secondary

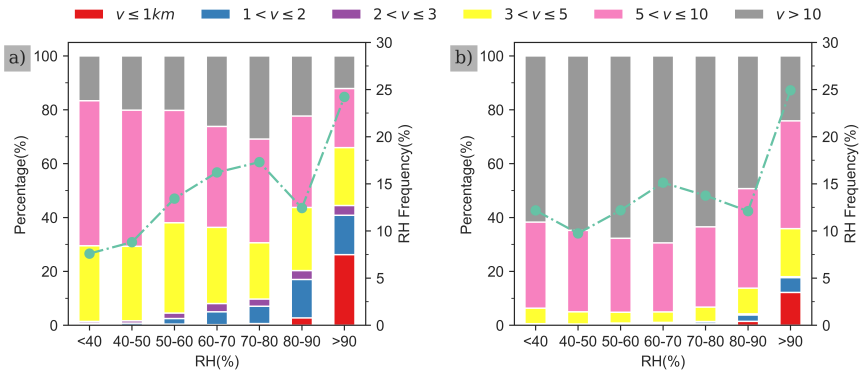

FIGURE 4. Percentage occurrence of different visibility classes (each denoted by a distinct color) at different RH categories represented by stacked bars and corresponding frequency distribution of RH represented by dotted lines and points at (a) Bhairahawa (BWA), and (b) Surkhet (SKH); 1977-2020

aerosols having their origin from local or transboundary emission sources. During dry pre-monsoon season, (Mar-May, RH 50%) and post-monsoon (Oct-Nov, RH70%) visibility generally shows reciprocal relation. Having not so different dispersion criteria during a season, this reciprocal behavior should be resulted from the extinction of light by a specific type of hygroscopic aerosols present in the atmosphere. This is because the RH at or above 50% can show its influence on visibility at BWA. While advancing towards the end of each season (e.g. from Jan-Feb, Apr-May), the relationship between visibility and RH seems more likely to follow the behavior of the upcoming season. This might be evident because of the weakening of the season towards its end and slowly gaining the characteristics of the season that follows. In contrast, the seasonal pattern of SKH exhibited (Figure 5[a]) almost opposite behavior to that of BWA in terms of the seasonal value of visibility. It witnesses a seasonal high value of visibility rather during post-monsoon months (Oct-Nov) and low during wet monsoon months (June-Sept.). In addition to having a cloudy sky during monsoon, a high RH value over 80% might have some influence on reduced visibility during the summer monsoon period, as only RH above 80% can manifest the adverse influence on visibility at SKH. The change in visibility during other seasons cannot be explained by the RH effect alone since typical seasonal RH values are lower than 80%.

CONCLUSION

After accomplishing a detailed study on the trend of visibility at two different locations,SKH and BWA, and exploring relationship between RH and visibility, we have reached to the following conclusions:

- Visibility displayed a significant declining trend at both of the locations during the study period (1980-2020), i.e. the air quality worsened over the period.

- The beginning of a decline in air quality occurred in the mid-1980s at SKH and another sharp decline occurred in 2011.

- The air quality at BWA was already poor since the beginning; this could be because of earlier urbanization and industrialization resulting in higher air pollution emissions. Trans-boundary air pollution also might have a greaterimpact on air quality. BWA airport is the gateway to the birthplace of Lord Buddha, Lumbini, a UNESCO heritage site, and the airport itself is being upgraded to an international airport, it is imminent to improve the air quality there to lessen the adverse effect of air pollution on tourism, health, aviation, etc. sectors. It requires enough attention from policymakers. The successful implementation of air quality control measure at BWA rely on regional coordinated effort.

- Although, the situation in SKH is not as alarming, the visibility condition is in a declining trend there too. Timely implementation of necessary measures to control the air quality is imminent.

- Only RH above 80% can affect reducing visibility by light extinction, meaning that there might be the presence of hygroscopic aerosols whose light extinction threshold for RH is higher than 80%. This effect is prominent during monsoon months. Whereas, the RH threshold for BWA is as low as 50%. The reciprocal relationship between RH and visibility shows its prominence during the dry seasons.

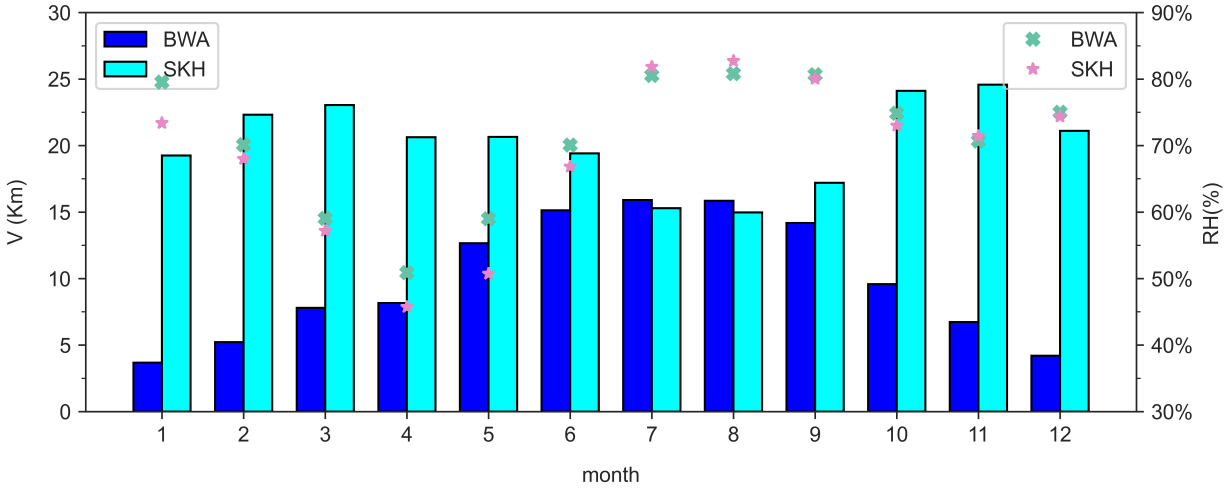

FIGURE 5. Seasonal variation of visibility (v, represented by bars) and relative humidity (RH, represented by points) at Bhairahawa (BWA) and Surkhet (SKH) for the period 1977-2020

TABLE II. Summary statistics of visibility and relative humidity at BWA and SKH

station	met.parameters	annual	pre-monsoon	monsoon	post-monsoon	winter
ine BWA	v(km)	10.7[a]	10.5[a]	10.5[a]	17.0[a]	4.7[a]
		6.1[b]	6.1[b]	6.1[b]	10.0[a]	3.1[a]
	RH(%)	71.7[a]	75.2[a]	57.4[a]	77.8[a]	74.0[a]
		71.0[b]	75.0[b]	53.0[b]	79.0[b]	73.0[b]
ine SKH	v(km)	22.7[a]	24.7[a]	18.9[a]	24.8[a]	24.6[a]
		20.1[b]	20.1[b]	15.1[b]	20.1[a]	20.1[a]
	RH(%)	62.3[a]	42.8[a]	72.1[a]	68.5[a]	65.0[a]
		65.0[b]	41.0[b]	74.0[b]	69.0[b]	63.0[b]

[a] mean
[b] median

ACKNOWLEDGMENTS

We extend our sincere gratitude to the National Climatic Data Center (NCDC) for making highly quality-controlled climatological data easily accessible for this project.

REFERENCES

1. J. Deng, K. Du, K. Wang, C.-S. Yuan, and J. Zhao, "Long-term atmospheric visibility trend in southeast china, 1973–2010," Atmospheric Environment **59**, 11–21 (2012).
2. U. S. E. P. A. O. of Air Quality Planning, Standards, and U. S. E. P. A. O. of Air, *Latest Findings on National Air Quality: 2000 Status and Trends*, Vol. 1 (US Environmental Protection Agency, Office of Air Quality Planning and Standards, 2001).
3. P. Zhao, X. Zhang, X. Xu, and X. Zhao, "Long-term visibility trends and characteristics in the region of beijing, tianjin, and hebei, china," Atmospheric Research **101**, 711–718 (2011).
4. I. N. Tang, "Chemical and size effects of hygroscopic aerosols on light scattering coefficients," Journal of Geophysical Research: Atmospheres **101**, 19245–19250 (1996).
5. M. Doyle and S. Dorling, "Visibility trends in the uk 1950–1997," Atmospheric Environment **36**, 3161–3172 (2002).
6. B. A. Schichtel, R. B. Husar, S. R. Falke, and W. E. Wilson, "Haze trends over the united states, 1980–1995," Atmospheric Environment **35**, 5205–5210 (2001).
7. C. S. Sloane, "Visibility trends—i. methods of analysis," Atmospheric Environment (1967) **16**, 41–51 (1982).
8. C. S. Sloane, "Meteorologically adjusted air quality trends: visibility," Atmospheric Environment (1967) **18**, 1217–1229 (1984).
9. Y. I. Tsai, "Atmospheric visibility trends in an urban area in taiwan 1961–2003," Atmospheric environment **39**, 5555–5567 (2005).
10. J. Watson and J. Chow, "Visibility and air pollution," WIT Transactions on Ecology and the Environment **99** (2006).
11. Y. Chen and S.-d. Xie, "Long-term trends and characteristics of visibility in two megacities in southwest china: Chengdu and chongqing," Journal of the Air & Waste Management Association **63**, 1058–1069 (2013).

12. G. Fu, W. Xu, R. Yang, J. Li, and C. Zhao, "The distribution and trends of fog and haze in the north china plain over the past 30 years," Atmospheric Chemistry and Physics **14**, 11949–11958 (2014).
13. L. Clancy, P. Goodman, H. Sinclair, and D. W. Dockery, "Effect of air-pollution control on death rates in dublin, ireland: an intervention study," The lancet **360**, 1210–1214 (2002).
14. Y. J. Kim, K. W. Kim, S. D. Kim, B. K. Lee, and J. S. Han, "Fine particulate matter characteristics and its impact on visibility impairment at two urban sites in korea: Seoul and incheon," Atmospheric environment **40**, 593–605 (2006).
15. N. P. Hyslop, "Impaired visibility: the air pollution people see," Atmospheric Environment **43**, 182–195 (2009).
16. W. C. Malm, "Characteristics and origins of haze in the continental united states," Earth-Science Reviews **33**, 1–36 (1992).
17. W. C. Malm, J. F. Sisler, D. Huffman, R. A. Eldred, and T. A. Cahill, "Spatial and seasonal trends in particle concentration and optical extinction in the united states," Journal of Geophysical Research: Atmospheres **99**, 1347–1370 (1994).
18. Y. Hu, L. Yao, Z. Cheng, and Y. Wang, "Long-term atmospheric visibility trends in megacities of china, india and the united states," Environmental research **159**, 466–473 (2017).
19. R. E. Davis, "A synoptic climatological analysis of winter visibility trends in the mideastern united states," Atmospheric Environment. Part B. Urban Atmosphere **25**, 165–175 (1991).
20. W. C. Malm and J. V. Molenar, "Visibility measurements lo national parks in the western united states," Journal of the Air Pollution Control Association **34**, 899–904 (1984).
21. K. Dani, P. Ernest Raj, P. Devara, G. Pandithurai, S. Sonbawne, R. Maheskumar, S. Saha, and Y. Jaya Rao, "Long-term trends and variability in measured multi-spectral aerosol optical depth over a tropical urban station in india," International Journal of Climatology **32**, 153–160 (2012).
22. U. De, R. K. Dube, and G. P. Rao, "Extreme weather events over india in the last 100 years," J. Ind. Geophys. Union **9**, 173–187 (2005).
23. A. K. Jaswal, N. Kumar, A. K. Prasad, and M. Kafatos, "Decline in horizontal surface visibility over india (1961–2008) and its association with meteorological variables," Natural hazards **68**, 929–954 (2013).
24. S. Tiwari, S. Payra, M. Mohan, S. Verma, and D. S. Bisht, "Visibility degradation during foggy period due to anthropogenic urban aerosol at delhi, india," Atmospheric Pollution Research **2**, 116–120 (2011).
25. H. Che, X. Zhang, Y. Li, Z. Zhou, and J. J. Qu, "Horizontal visibility trends in china 1981–2005," Geophysical research letters **34** (2007).
26. H. Che, X. Zhang, Y. Li, Z. Zhou, J. J. Qu, and X. Hao, "Haze trends over the capital cities of 31 provinces in china, 1981–2005," Theoretical and Applied climatology **97**, 235–242 (2009).
27. X. Deng, X. Tie, D. Wu, X. Zhou, X. Bi, H. Tan, F. Li, and C. Jiang, "Long-term trend of visibility and its characterizations in the pearl river delta (prd) region, china," Atmospheric Environment **42**, 1424–1435 (2008).
28. L. Gao, G. Jia, R. Zhang, H. Che, C. Fu, T. Wang, M. Zhang, H. Jiang, and P. Yan, "Visual range trends in the yangtze river delta region of china, 1981–2005," Journal of the Air & Waste Management Association **61**, 843–849 (2011).
29. W. Huang, J. Tan, H. Kan, N. Zhao, W. Song, G. Song, G. Chen, L. Jiang, C. Jiang, R. Chen, *et al.*, "Visibility, air quality and daily mortality in shanghai, china," Science of the Total Environment **407**, 3295–3300 (2009).
30. W. Qu, R. Arimoto, X. Zhang, C. Zhao, Y. Wang, L. Sheng, and G. Fu, "Spatial distribution and interannual variation of surface pm 10 concentrations over eighty-six chinese cities," Atmospheric Chemistry and Physics **10**, 5641–5662 (2010).
31. Y. Wang, Q. Wan, W. Meng, F. Liao, H. Tan, and R. Zhang, "Long-term impacts of aerosols on precipitation and lightning over the pearl river delta megacity area in china," Atmospheric Chemistry and Physics **11**, 12421–12436 (2011).
32. J. Wu, C. Fu, L. Zhang, and J. Tang, "Trends of visibility on sunny days in china in the recent 50 years," Atmospheric Environment **55**, 339–346 (2012).
33. R. Zhang, "Getting to the critical nucleus of aerosol formation," Science **328**, 1366–1367 (2010).
34. H. Deng, H. Tan, F. Li, M. Cai, P. Chan, H. Xu, X. Huang, and D. Wu, "Impact of relative humidity on visibility degradation during a haze event: A case study," Science of the Total Environment **569**, 1149–1158 (2016).
35. K. Du, C. Mu, J. Deng, and F. Yuan, "Study on atmospheric visibility variations and the impacts of meteorological parameters using high temporal resolution data: an application of environmental internet of things in china," International Journal of Sustainable Development & World Ecology **20**, 238–247 (2013).
36. X. Liu, Y. Zhang, Y. Cheng, M. Hu, and T. Han, "Aerosol hygroscopicity and its impact on atmospheric visibility and radiative forcing in guangzhou during the 2006 pride-prd campaign," Atmospheric Environment **60**, 59–67 (2012).
37. R. K. Linsley Jr, M. A. Kohler, and J. L. Paulhus, "Hydrology for engineers," (1975).
38. J. Li, C. Li, C. Zhao, and T. Su, "Changes in surface aerosol extinction trends over china during 1980–2013 inferred from quality-controlled visibility data," Geophysical Research Letters **43**, 8713–8719 (2016).
39. B. Gomez and C. Smith, "Visibility at oxford, 1926–1985," Weather **42**, 98–106 (1987).
40. M. Stock, Y. Cheng, W. Birmili, A. Massling, B. Wehner, T. Müller, S. Leinert, N. Kalivitis, N. Mihalopoulos, and A. Wiedensohler, "Hygroscopic properties of atmospheric aerosol particles over the eastern mediterranean: implications for regional direct radiative forcing under clean and polluted conditions," Atmospheric Chemistry and Physics **11**, 4251–4271 (2011).

Atmospheric Research 288 (2023) 106746

Contents lists available at ScienceDirect

Atmospheric Research

journal homepage: www.elsevier.com/locate/atmosres

Four decades of aviation visibility at Bhairahawa airport, gateway to Buddha's birthplace Lumbini, Nepal

Bhogendra Kathayat [a,b,*], Arnico Kumar Panday [c], Binod Pokharel [d,e], Vinod Kumar [f], Narayan Prasad Chapagain [g]

[a] Central Department of Physics, Tribhuvan University, Kathmandu, Nepal
[b] Nepal Airlines Corporation, Kathmandu, Nepal
[c] Institute for Integrated Development Studies, Mandikatar, Kathmandu, Nepal
[d] Central Department of Hydrology and Meteorology, Tribhuvan University, Kathmandu, Nepal
[e] Utah Climate Center, Department of Plants, Soils, and Climate, Utah State University, Logan, UT, USA
[f] Max Planck Institute for Chemistry, Mainz, Germany
[g] Department of Physics, Amrit Campus, Tribhuvan University, Kathmandu, Nepal

ARTICLE INFO

Keywords:
Visibility
Aviation
Fog
AOD
PM2.5
Bhairahawa airport

ABSTRACT

Over four decades of visibility data at Bhairahawa airport (BWA), a recently upgraded international airport near Lumbini, a UNESCO heritage site in Nepal has been analyzed. In this study, we also investigated one of the important microclimatic behavior of fog i.e., onset and dispersal timings, and its implication on aviation. Temporal variations of poor visibility conditions at BWA are found to be primarily associated with variations in haze and fog. Haze at BWA accounts for the highest percentage (~27%) of time and its annual occurrence is increasing (0.57% yr^{-1}). There is a significant upward trend of hazy days in all seasons, the highest (1.46% day yr^{-1}) being in post-monsoon. The overall seasonal poor visibility, too, has increased significantly in all seasons, with the highest trend in post-monsoon (1.57% yr^{-1}). Similarly, fog frequency in the winter season has also increased noticeably for fog days (1.05% day yr^{-1}), dense fog days (0.51% day yr^{-1}), general fog hours (0.55% hour yr^{-1}) and dense fog hours (0.20% hour yr^{-1}). We found that fog at BWA is usually formed overnight and dissipates before noon. Daytime onset and late dispersion of fog are more common in the peak winter months of December and January. Further, we investigated the relationship between visibility and aerosol optical depth (AOD) and found a moderate negative correlation ($r = -0.66$, $p < 0.001$) between them in the monsoon season. However, AOD is found to have a weaker correlation with visibility during winter ($r = -0.36$) and pre-monsoon ($r = -0.23$) seasons, when there is a more pronounced influence of meteorological conditions on the occurrence of visibility. We have observed a better correlation ($r = -0.74$) between fine particulate matter concentration (PM2.5) and visibility. Examining the effect of relative humidity (RH) on AOD (or, PM2.5) and visibility revealed that higher RH tends to lower visibility. Visibility at BWA airport is gradually worsening due to local and regional air pollution emissions and changing meteorological conditions. The degraded visibility at BWA airport will negatively impact flight safety and timeliness. Effective implementation of regionally coordinated air pollution mitigation measures can be a sustainable step towards the improvement of visibility in long run. However, the installation of ground equipment like CAT-II/III Instrument Landing System (ILS) for aircraft take-off and landings, and advanced surface movement guidance and control system (A-SMGCS) are highly advisable to lessen the damage potential to aviation.

1. Introduction

Aviation is a sector that is directly impacted by atmospheric visibility. Better visibility conditions at airports result in safer and more convenient flight operations, from take-off and landings to air-traffic flow management, ground movement, and ground handling operations. When visibility at an airport drops below a certain threshold, instrument meteorological conditions (IMC) are triggered, which creates

* Corresponding author at: Central Department of Physics, Tribhuvan University, Kathmandu, Nepal.
E-mail address: bhogendra.735711@cdp.tu.edu.np (B. Kathayat).

https://doi.org/10.1016/j.atmosres.2023.106746
Received 14 November 2022; Received in revised form 20 February 2023; Accepted 2 April 2023
Available online 4 April 2023

many problems in aviation including a reduction in the airport's overall capacity (Morisset and Odoni, 2011), flight delays (Morisset and Odoni, 2011), diversions, and cancellations, resulting in substantial monetary losses (Kulkarni et al., 2019) in the form of lost time, fuel, and additional aircraft maintenance. The adverse weather condition in the form of reduced visibility has been identified as an important aviation safety hazard (Regmi, 2014a, 2014b; Regmi et al., 2020), and has led to several aircraft incidents and fatal accidents (Gultepe et al., 2015; Jenamani and Kumar, 2013). A typical instance of a major aircraft incident in Nepal, solely because of the reduced visibility, happened on 4 March 2015. A Turkish Airlines aircraft (registration TC-JOC) suffered a runway excursion accident upon landing at Tribhuvan International Airport, Nepal during reduced visibility conditions caused by dense fog over the airport – resulting in damage of million- dollar-brand-new aircraft (Airbus A-330) beyond repair (AIC, 2015). The only international airport in Nepal, then, remained closed for four days because of the blocking of the runway, causing massive disruption in air transport and a huge economic loss.

Gautam Buddha Airport at Bhairahawa, Nepal, hereafter referred to by its IATA code BWA (Fig. 1), is the main gateway to the UNESCO world heritage site of Lumbini, the birthplace of Lord Buddha. The government of Nepal has just completed upgrading BWA to an international airport (CAAN, 2013, p. 2). This airport is expected to relieve the air traffic load at Tribhuvan international airport in Kathmandu (KTM). BWA is also expected to serve as the nearest suitable diversion alternate to KTM for large jet aircraft, whenever weather or any other situation at KTM prevents landings, saving time and money for airlines that to date had to divert to airports in India. To what extent BWA can successfully fulfill this role, and how well it can handle its own scheduled flights, will depend on how badly its own operations will be affected by reduced visibility.

Visibility is reduced by the extinction of light due to absorption or scattering by particles and droplets in the atmosphere (Che et al., 2007; Chen et al., 2013; Doyle and Dorling, 2002; Schichtel et al., 2001). This can happen in several ways: Past studies in China (Du et al., 2013; Fu et al., 2014; Gao et al., 2011), India (Dani et al., 2012; De et al., 2001; Hu et al., 2017; Jaswal et al., 2013; Tiwari et al., 2011) and elsewhere have reported reduced visibility as a consequence of serious air pollution. In addition, meteorological parameters, especially relative humidity (RH), can also have a significant impact on visibility degradation (Chen et al., 2013; Liu et al., 2012; Tang, 1996; Zhang et al., 2010). As RH increases, hygroscopic particles progressively take up more ambient water vapor, leading to increased scattering cross-sections and change in complex refractive index – leading to enhanced extinction efficiency – and finally visibility degradation (Malm et al., 1994). Meanwhile, increased temperature improves visibility by enhancing the dispersion capability in the atmosphere via thermal and mechanical turbulence (Du et al., 2013). Synoptic weather also has a significant impact on air pollution and visibility (Deng et al., 2011). Zhao et al. (2011) argued that the long-term trend in visibility is a manifestation of air pollution, rather than the meteorological effect.

Wang et al. (2009) found that clear sky visibility over the land has been decreasing globally from 1973 to 2007. Visibility over cities in China (Che et al., 2007; Fu et al., 2014, etc.) and India (De et al., 2001; Hu et al., 2017; Jaswal et al., 2013) has declined significantly over the years. In contrast, many cities in the United States (Hu et al., 2017) and Europe (Vautard et al., 2009) have witnessed improved visibility because of the implementation of effective air pollution control measures.

Bhairahawa airport is situated near the northern edge of the Indo-Gangetic Plains (IGP), which stretches over 2000 km across northern South Asia, from eastern Pakistan, through northern and eastern India, southern Nepal (the Terai region), and big parts of Bangladesh. As a hotspot of air pollution, the IGP has become a region of local, regional, and global concern (Ramanathan et al., 2007; UNEP and DA, 2014; WHO, 2016). During the dry season, the IGP region is affected by western disturbances - a series of alternating low and high-pressure systems that move eastwards, and that create ideal conditions for multi-day accumulation of pollutants within the boundary layer, leading to intense haze and fog (Hameed et al., 2000; Gautam et al., 2007). Ramanathan and Carmichael (2008) earlier referred to this thick aerosol haze as the atmospheric brown cloud (ABC). The IGP region has seen an increase in the aerosol haze over the past several decades (De and Dandekar, 2001; Jaswal et al., 2013; Kaskaoutis et al., 2012; Ramanathan and Ramana, 2005; Sarkar et al., 2006; Srivastava et al., 2012; Saikawa et al., 2019; WHO, 2016; Yasmeen et al., 2012). The region has also experienced a large increase in persistent multi-day winter fog events in recent years (De and Dandekar, 2001; Syed et al., 2012; Srivastava et al., 2016; Singh et al., 2004; Saikawa et al., 2019). Syed et al. (2012) found a significant positive trend in fog frequency in the IGP

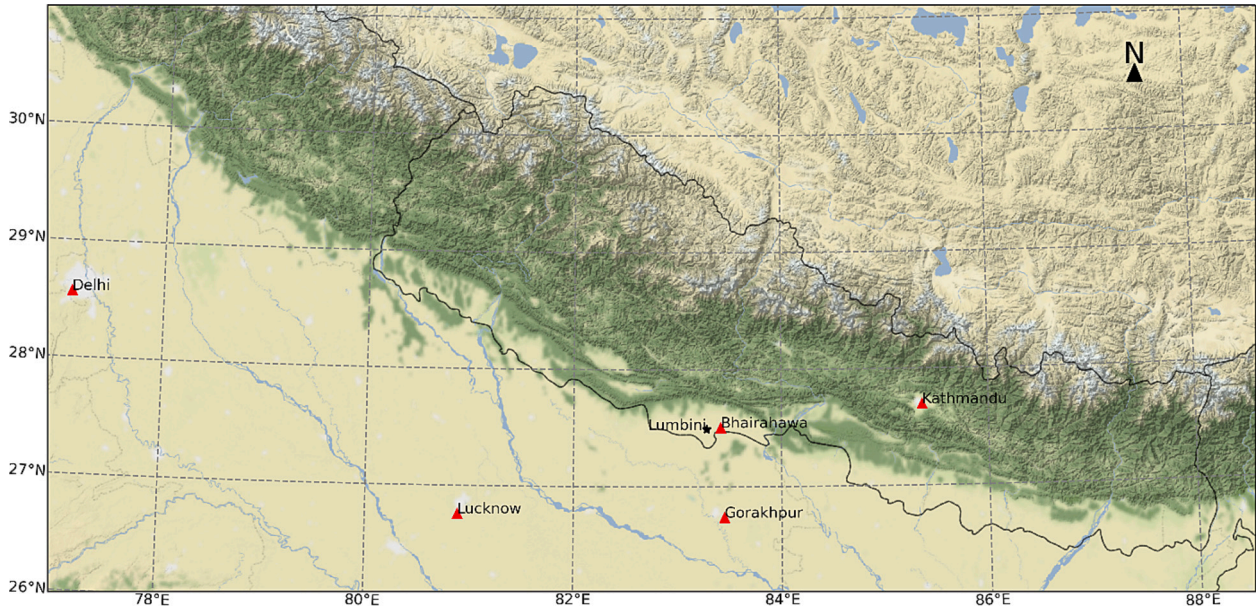

Fig. 1. The geographical location of selected NOAA stations (red triangle) inside Nepal and India. (More details in Supplement, Table. S.1). (For interpretation of the references to color in this figure legend, the reader is referred to the web version of this article.)

region since 1990 and that fog variability over the South Asian region is coupled and governed by some large-scale phenomena. A study by Jenamani (2007) highlighted an alarming increase in fog and its persistence in winter at Indira Gandhi International airport, New Delhi (DEL). Ghude et al. (2017) reported a consistent discovery of the doubling of dense fog hours in the last three decades at the same location. Singh and Singh (2010) noted a similar increasing trend of winter fog at Hisar (an Indian city in western IGP), while Shrestha et al. (2018) reported an increasing trend of opacity and fog-related parameters during winter in four Terai plain stations of Nepal. Several of these studies have attributed changes in fog in the IGP to the changes in irrigation as well as anthropogenic air pollutant emissions patterns in winter.

While we have only found one past study, examining visibility in winter at BWA (Shrestha et al., 2018), nearby Lumbini has seen a significant volume of potentially relevant research on air pollution in recent years. This includes the identification of major sources of air pollution (Islam et al., 2021; Rupakheti et al., 2018b), their temporal behavior (Rupakheti et al., 2017), optical properties (Izhar et al., 2021; Rupakheti et al., 2018a, 2018b), and chemical characteristics (Tripathee et al., 2017; Wan et al., 2017). With the Upgraded BWA airport expected to be operating 24 h a day, understanding the visibility limitations will be a key planning ingredient for the safe and efficient conduct of flight operations at BWA and the investment in suitable navigation equipment, as well as a key starting point to design policies and measures to address the anthropogenic causes of visibility decline. As a first of a series of papers focusing on aviation visibility in Nepal, this paper analyses publicly available datasets to address three questions in relation to aviation and visibility at BWA. First, we examine the long-term changes to atmospheric visibility at BWA and neighboring airports of the IGP, focusing on thresholds relevant to aviation. Next, we examine the microclimatic behavior of fog that reduces visibility during winter, and finally, we examine the relationship between the aerosol optical depth (AOD), PM2.5, relative humidity, and visibility at BWA.

2. Data and methods

The Department of Hydrology and Meteorology (DHM), Nepal manually recorded meteorological data including horizontal visibility – used in this study – at Bhairahawa airport, as a part of the Meteorological Terminal Air Report (METAR) for aviation use. This data is archived as a global hourly database and distributed publicly by National Climate Data Center (NCDC) (https://www.ncei.noaa.gov/maps/hourly/) as a part of the data exchange protocol under the World Meteorological Organization (WMO, Resolution 40(Cg-XII), 1996). Our dataset includes daily observations at 00:00, 03:00, 06:00, 09:00, and 12:00 UTC, from 1977 to 2020. Since the dataset does not have a record of direct relative humidity (RH) measurement, we computed RH using the following equation (Linsley et al., 1988; Chang et al., 2009; Chen and Xie, 2012):

$$RH \approx 100\left(\frac{112 - 0.1T + T_d}{112 + 0.9\,T}\right)^8 \quad (1)$$

where T (°C) represents the air temperature and T_d (°C) represents the dew point temperature.

Analyzing this dataset, we have dropped all the observations with a missing value of visibility from the dataset. Among all the values from the present-weather feature in the dataset, we have decoded only those weather types, that could influence visibility at BWA: haze, fog, mist, and rain. Since our primary dataset from NCDC had many missing values in the precipitation record, we have used another historic climatological repository, ERA5 [European Centre for Medium-Range Weather Forecasts (ECMWF) Reanalysis v5; *data source*: https://cds.climate.copernicus.eu/)] for hourly precipitation since 1981.

To better understand aerosol impacts, we have also obtained AOD time series (version 3, level 1.5 - cloud-screened and quality controlled; *data source*: http://aeronet.gsfc.nasa.gov/) (2013–2018) from nearby Lumbini from the public archive of NASA Aerosol Robotic Network (AERONET). The NASA AERONET collaboration provides globally distributed observation of spectral AOD, inversion products, and perceptible water in diverse aerosol regimes. In this study, we also used ground measurement of PM2.5 (April-Dec 2019) at a nearby location (27° 29′ 22.3“ N, 83° 16’ 44.7” E). The site is primarily managed by the Department of Environment, Government of Nepal, in collaboration with International Center for Integrated Mountain Development (ICIMOD), and the data is accessed through the public domain (https://opendatanepal.com/dataset/realtime-air-quality-datasets). Similarly, we have collected long-term records (Jan-1980 to Feb-2020, bounding box (82° 14′ 25.8“ E, 26° 30’ 57.6” N, 84° 57′ 54.36“ E, 28° 3’ 14.76” N), spatial resolution (0.5° × 0.625°)) of time-averaged 2- dimensional monthly mean PM2.5 reanalysis data from Modern-Era Retrospective analysis for Research and Applications version 2 (MERRA-2) NASA public domain (GMAO, 2015; https://giovanni.gsfc.nasa.gov/giovanni). MEERA-2 is a NASA atmospheric reanalysis that begins in 1980 and replaces the original MEERA reanalysis (Rienecker et al., 2011). It uses an upgraded version of the Goddard Earth Observing System Model, version 5 (GEOS-5, version 5.12.4) data assimilation system which can use newer microwave sounders and hyperspectral infrared radiance instruments as well as other data types (Bosilovich et al., 2015). Gelaro et al. (2017) have provided an overview of the MEERA-2 modeling system. Similarly, Buchard et al. (2017) have given a detailed description of aerosols in the MEERA-2 system. Despite the optimum effort to harmonize observing systems by rigorous quality control, AOD values are affected by differences in data coverage – particularly in pre- and post-NASA Earth Observing System (EOS) periods (1980–1999 and post-2000, respectively) (Randles et al., 2017; Yao et al., 2021).

The number of data records in our meteorological dataset were not uniform across the study period, with fewer records in the early years and more in recent years. We have thus decided to consider the percentage occurrence of weather types over their frequency, similar to the work of Hu et al. (2017). The percentage occurrence mentioned, hereafter, in this paper is the percentage frequency of daytime observation because of having daytime-only METAR data and our aim to have insights on the temporal change of daytime visibility.

2.1. Reduced visibility due to different weather-type

Different weather types were classified according to the criteria described in Appendix B.1 and their hourly occurrence frequency was computed to identify and quantify their contribution. The time resolution of both kinds of datasets i.e., NCDC & ERA5, were matched. As our dataset describes the weather every 3 h, we assumed that the weather type in each observation persists from 1.5 h before to 1.5 h after the time of observation. The hourly occurrence frequency of a particular weather type is computed as the percentage of total hours of the occurrence of the weather type out of the total occurrence hours of all-weather types combined.

2.2. Statistical tests for estimation of a long-term trend

We have chosen some commonly used statistical tools (Appendix B.2): Mann-Kendell Test (MK Test) and Sen’s Slope Estimator (Sen’s Slope) to better understand the trend of the selected parameter over time. Where, the Mann-Kendall Test detects the trend in a time series data, and Sen’s Slope quantifies the trend. Then, we used a parametric test, Ordinary Least Square (OLS) (Appendix B.2) regression method to compare the results from the above two tests. According to (Sen, 1968; Mann, 1945), these non-parametric tests, namely the MK test and Sen’s Slope are appropriate to find the trend of parameters with missing values, data errors, and/or outliers. Hence, the main purpose of using these tests in the present study is to cater for the issue of inhomogeneity

of our dataset, since our data records contain many missing values. Because of these advantages, many previous researchers have widely used these techniques to quantify the trend of climatic and hydrological time series (Kendall, 1975; Mann, 1945; Van Belle and Hughes, 1984; Yue and Wang, 2004).

2.3. Long-term change in poor visibility and haze

The occurrence frequency of poor-visibility events during a given time scale (e.g., season, year) in a year was computed as the percentage of the total number of reported visibility observations that fit the criteria of poor visibility (or, haze) laid down in Appendix B.1.

2.4. Long-term change in winter fog

Winter fog can occur at BWA and elsewhere on the southern plain of Nepal between November and February. As such, we have considered these four months for fog occurrence. A day is qualified as having fog or dense fog if at least one record fulfills the criteria (Appendix B.1). We have used the term 'general fog' and fog interchangeably elsewhere in this paper. As mentioned in Section 2.1, we assumed that if a fog event is detected in a 3-hourly observation, it would have persisted from 1.5 h before to 1.5 h after the timestamp of its observation. The occurrence frequency of fog (dense fog) is the percentage of the total number of days (hours) in the considered winter months that witness fog (dense fog).

2.5. Microclimatic properties of fog

Jenamani (2012) suggested that given its high damage potential to general aviation, it is highly advantageous to develop an intensity and duration-based fog micro-climatological information system using long-term data. Such a system containing information about favorable times for the formation and dispersal of fog, persistence of fog, etc. could be very much useful to various users, including forecasters, airport operators, Air Traffic Controllers (ATC), airlines, and pilots. They would benefit from understanding the vulnerability of airports to various fog conditions so that they can implement better mitigation plans in advance, such as CAT- I/II/III ILS for runways, winter schedules, and training for pilots and ATC. In order to gain a better understanding of the nature of the occurrence timings of winter fog at BWA airport, this paper examines an important microclimatic property of the fog at BWA: onset/dispersal of fog (Appendix B.3).

2.6. Comparison of winter poor visibility and fog among the neighboring airports in the IGP region

The meteorological condition in the winter season (DJF) offers one of the most favorable situations for poor air quality and poor visibility in the IGP region. To obtain a regional comparative understanding of the status of long-term poor visibility and fog during the winter season at BWA airport, we have chosen the airports of Gorakhpur (GOP), Lucknow (LKN), and Delhi (DEL) as representative sites from the Indian side of IGP (Table. S1). The data of all the stations are resampled to match with that of BWA: i.e., only daytime observations from 00:00 to 12:00 UTC were used for further analysis.

2.7. Relationship between the aerosol optical depth (AOD), PM2.5, RH, and visibility

Aerosol optical depth (AOD), a measure of scattering and/or absorption of sunlight (photon) when passing through a vertical or slant column of the atmosphere, is a vertical entity. On contrary, visibility is measured in the horizontal direction. As discussed in earlier sections, visibility is a function of aerosols including type, size distribution, and concentration. Many studies (Bäumer et al., 2008; Founda et al., 2016) have compared visibility with AOD despite their different directional consideration. Thus, we also have attempted to explore the relationship between them. The experimental formula of visibility, the Koschmieder relation, states an inverse relationship between visibility (v) and extinction coefficient b_{ext} (Middleton, 2019; Singh et al., 2020), that can be expressed as:

$$v = K/b_{ext} \tag{2}$$

where, K is the Koschmieder constant (≈3.912), and b_{ext} is a function of position within the sight path and is a property of the atmosphere alone (Malm, 2016).

Similarly, from the definition of AOD,

$$\tau = \int_0^{z_i} b_{ext}\, dz \tag{3}$$

where, z represents the mixing layer height. For the sake of simplicity, we too have assumed that all aerosol is trapped within the mixing layer with a height z_i and the extinction coefficient is uniform across the height as done in past studies (Bäumer et al., 2008; Founda et al., 2016). The solution of Eqs. (2) and (3) yield the required functional relation between visibility (v) and AOD (τ) as follows:

$$v = 3.912\, z_i\, \tau^{-1} \tag{4}$$

More details on their relationship can be found in the supplementary material of this paper (Appendix B.4). We have attempted to include the combined effect of RH and AOD on visibility. We have examined the relationship between PM 2.5, RH, and visibility too.

3. Results

3.1. Reduced visibility due to different weather-type

Fig. 2(a) shows the hourly occurrence frequency of five different weather types (haze, mist, fog, rain, and normal (clear)) that influence visibility at BWA during the period from 1981 to 2020. Among all weather types, which resulted in reduced visibility at BWA, haze accounts for the highest percentage (26.7 ± 0.3%) of the entire period, followed by fog (7.9 ± 0.2%), rain (7.2 ± 0.2%), and mist (3.9 ± 0.1%). Thus, apart from rain, which is the result of many complex local and regional processes, atmospheric conditions at BWA airport are prone to the formation of haze, fog, and mist that result in poor visibility conditions. Further, we have investigated the long-term variation of different weather types (Fig. 2(b); Fig. S1 & Table S2). Results show a significant increase in the occurrence frequency of fog (0.215% yr^{-1}) and haze (0.556% yr^{-1}) events over the past decades. In the meantime, there is a significant decline in the occurrence of normal (clear) weather conditions (−0.931% yr^{-1}). We have singled out haze and fog as the two major weather types that reduce visibility and could have resulted in a decline in normal weather conditions – based on their occurrence frequency and increasing trend. We focus our investigation on only these two weather types henceforth, because of their probable implication on flight operation at BWA.

3.2. Long-term change in poor visibility and haze

Fig. 3 (a-d) presents long-term variations of poor-visibility events (in percentage) at BWA for different seasons, namely winter (DJF), pre-monsoon (MAM), monsoon (JJAS), and post-monsoon (ON) over the study period. Each point in the plots represents the seasonal occurrence frequency of poor visibility in a particular year, and Table 1 shows the respective trend results obtained from different statistical tests (MK test, Sen's Slope & OLS) which are almost close to each other.

Among all the seasons (Fig. 3(a-d)), the highest poor visibility percentage was observed during winter (Fig. 3a). The poor visibility percentage in winter has reached close to 100% since 2007. The overall

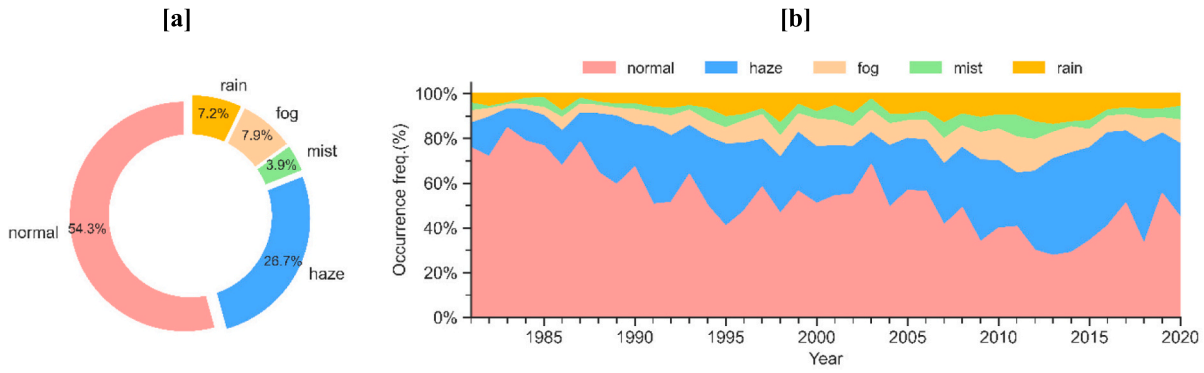

Fig. 2. [a] Hourly total & [b] Annual - occurrence frequency (%) of reduced visibility due to different weather types at BWA (1981–2020). These weather types are defined according to criteria detailed in (Appendix B.1).

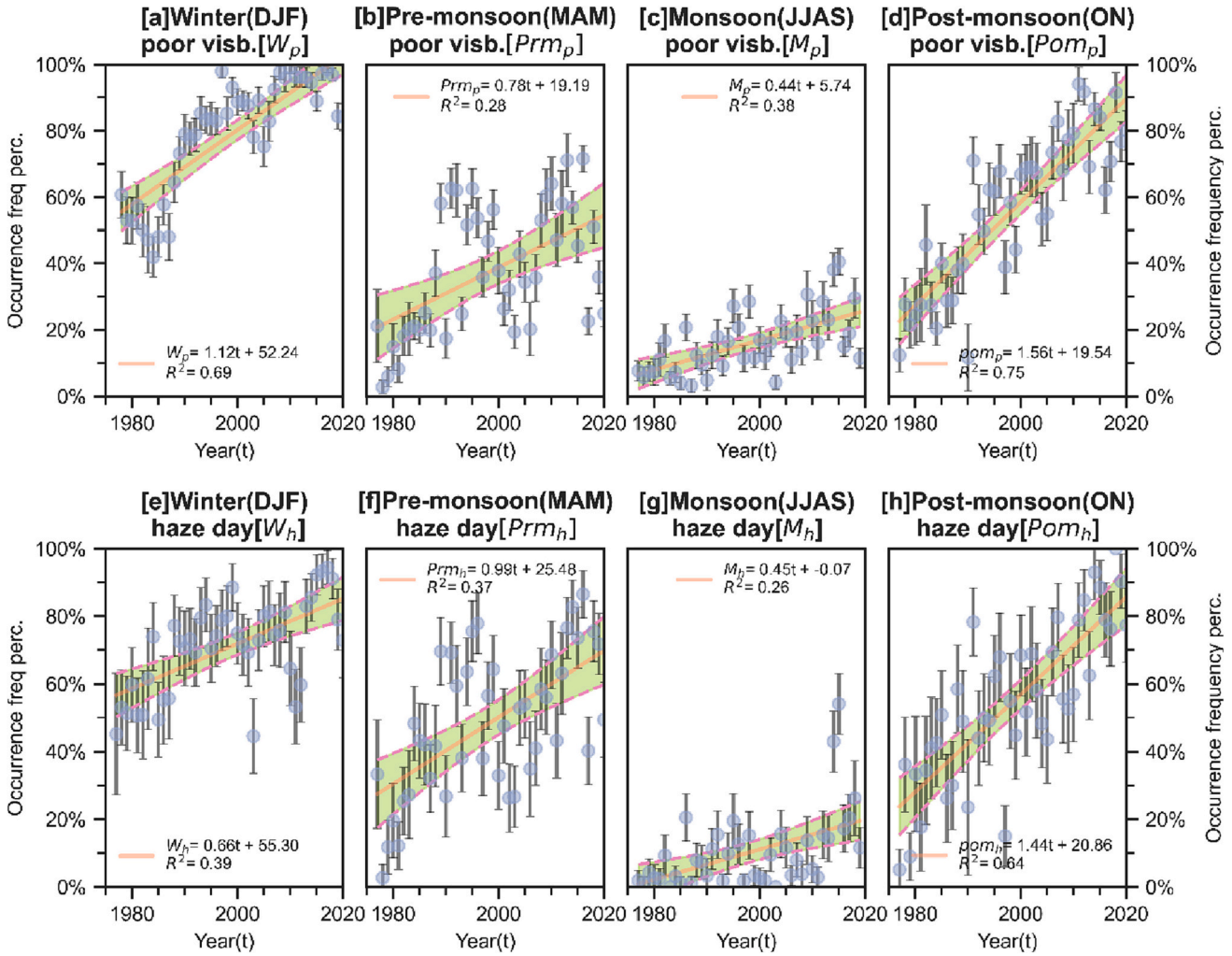

Fig. 3. The time evolution of; the frequency (in percentage) of occurrence of poor-visibility (a-d) events and haze (e-h) during winter (**DJF**), pre-monsoon (**MAM**), monsoon (**JJAS**), and post-monsoon (**ON**) seasons at Bhairahawa airport during (1977–2020). The error bars represent the 95% confidence interval. The linear regression lines (solid), defined by the corresponding equations, are fitted according to the results of OLS regression and the dashed lines represent their 95% confidence interval. R^2 represents corresponding goodness of fit.

increasing trend in the poor-visibility events during the winter season is 1.02%yr^{-1} significant at a 0.001 level of significance (Table. 1). Poor-visibility events during pre-monsoon (Fig. 3b) were very rare events during the early years. This has increased significantly towards the mid to late stages. The overall trend in the poor-visibility percentage in the pre-monsoon is also positive and statistically significant. We also observed a small (Table 1) but significant increase (0.42% yr^{-1}) in poor visibility events during the monsoon season (Fig. 3c). The highest (40 ± 5%) and the lowest (2.3 ± 2%) poor-visibility percentages during monsoon were observed in 2014 and 1991 respectively. The standard deviation in monsoon (8%) is the lowest among all seasons and the median is only 13%, indicating a persistent better visibility condition

Table 1
Results of Mann-Kendall, Sen's slope estimator, and OLS regression test, from 1977 through 2020 at Bhairahawa airport. These results consider winter months (**NDJF**) for fog parameters (fog/dense-fog days/h). The trend represents the slope of the linear fit between the variable of interest and year. The boldface values indicate that the slope is statistically significant given levels of significance(α).

		Mann – Kendall		Sen's slope		OLS regression			
		Z_{MK}	p–value	Trend Q (% yr^{-1})	**[CI]** %	Trend $\hat{\beta}_1$ (% yr^{-1})	**[95% CI]** %	t_s	p-value>|t|
a) Occurrence frequency of poor visibility events (%)	Winter (**DJF**)	5.90*	3.71×10^{-9}	**1.02***	[0.582, 1.481] *	**1.12*** ± 0.116	[0.886, 1.355]	9.66	0.000
	Pre-monsoon (**MAM**)	3.57*	4×10^{-4}	**0.84***	[0.079, 1.576] *	**0.79*** ± 0.192	[0.396, 1.173]	4.08	0.000
	Monsoon (**JJAS**)	4.19*	2.83×10^{-5}	**0.42***	[0.108, 0.780] *	**0.45*** ± 0.09	[0.264, 0.626]	4.97	0.000
	Post-monsoon (**ON**)	6.50*	7.85×10^{-11}	**1.57***	[1.069, 2.076] *	**1.56*** ± 0.139	[1.277, 1.839]	11.18	0.000
	Annual	5.74*	9.27×10^{-9}	**0.94***	[0.524, 1.273] *	**0.90*** ± 0.098	[0.699, 1.094]	9.17	0.000
b) Occurrence frequency of haze days (%)	Winter (**DJF**)	4.58*	4.6×10^{-6}	**0.75***	[0.218, 1.137]	**0.67*** ± 0.127	[0.416, 0.927]	5.31	0.000
	Pre-monsoon (**MAM**)	4.02*	5.92×10^{-5}	**1.09***	[0.274,1.795] *	**0.99*** ± 0.398	[0.584,1.388]	4.95	0.000
	Monsoon (**JJAS**)	3.71†	2.11×10^{-4}	**0.31†**	[0.021, 0.668]	**0. 45†** ± 0.117	[0.209, 0.682]	3.80	0.000
	Post-monsoon (**SON**)	5.96*	2.56×10^{-9}	**1.46***	[0.806,2.106]	**1.44*** ± 0.167	[1.103,1.778]	8.618	0.000
c) Occurrence frequency of fog parameters (%)	fog days	4.95*	7.58×10^{-7}	**1.05***	[0.518,1.577] *	**1.06*** ± 0.243	[0.809,1.311]	8.52	0.000
	dense fog days	5.37*	7.84×10^{-8}	**0.51***	[0.253, 0.776] *	**0.50*** ± 0.141	[0.354,0.645]	6.91	0.000
	fog hour	4.62*	3.80×10^{-6}	**0.55***	[0.229, 0.862] *	**0.52*** ± 0.152	[0.363,0.677]	6.67	0.000
	dense-fog hour	4.06*	5.00×10^{-5}	**0.20***	[0.054, 0.387] *	**0.20*** ± 0.084	[0.112,0.287]	4.61	0.000

* 0.001, † 0.05 - level of significance.

during this season. Meanwhile, we have observed (Fig. 3d, Table 1) the fastest increase (trend of 1.57% yr^{-1}) in poor visibility during the post-monsoon. During the post-monsoon of 1977, poor-visibility events occurred only 12.4 ± 4% of the time; this increased to a maximum of 87 ± 6% in 2018, with the largest standard deviation (19.8%) among all seasons.

Similarly, Fig. 3e illustrates the overall increasing trend of annual poor-visibility percentage at BWA. Likewise, an increase in the percentage of pre-monsoon and post-monsoon haze days (Fig. 3(f - g)) is found over the past four decades at Bhairahawa. The trend is larger for post-monsoon haze days with 1.46% day yr^{-1} significant at 0.001 level, about an increase of 80% over the last 44 years. The occurrence frequency of haze days (Table 1, Fig. S1) in winter is the largest among the seasons, 70.8%, and its annual trend is 0.75% day yr^{-1}.Whereas, occurrence frequency and annual trend of haze days in monsoon are the lowest.

3.3. Long-term change in winter fog

The annual variation of winter (NDJF) fog parameters; namely general-fog days, dense-fog days, general-fog hours, and dense-fog hours, are presented in Fig. 4 and Table 1. The general-fog day's percentage increased faster with a Sen's slope of 1.05% day yr^{-1} significant at 0.001 level (Fig. 4a, Table 1), while the dense fog percentage has a

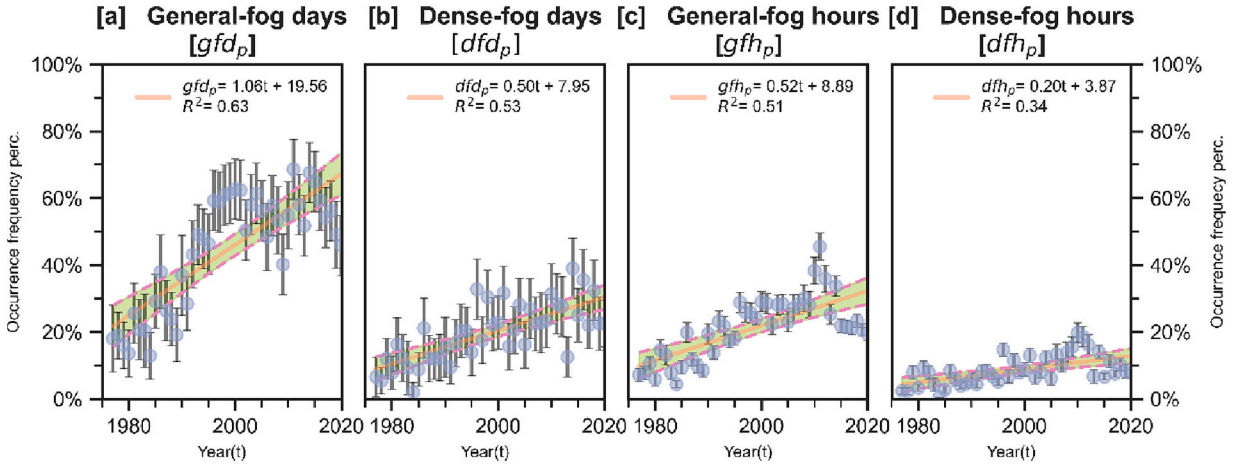

Fig. 4. The time evolution of frequency (in percentage) of occurrence of different winter fog parameters at Bhairahawa airport during (1977–2020): **(a)** general fog days, **(b)** dense fog days, **(c)** general fog hours, and (**d**) dense fog hours. The error bars represent the 95% confidence interval. The linear regression lines (solid), defined by the respective equations, are fitted according to the results of OLS regression and the dashed lines correspond to their 95% confidence interval. R^2 represents corresponding goodness of fit.

trend of 0.51% day yr^{-1}at 0.001 level of significance (Fig. 4b, Table 1).

General fog hour in BWA (Fig. 4c) is clearly seen to have a positive trend with 0.55% hour yr^{-1}at 0.001 level of significance (Table. 1). Though significant, the smallest trend is observed for an annual dense-fog hour i.e., 0.20% hour yr^{-1} (Fig. 4d, Table 1). Like before, the trend results of fog parameters obtained from three different trend tests are very close to each other.

3.4. Microclimatic properties of winter fog

Fig. 5(a-d) shows the timing of onset and dispersal of the fog of different intensities during the winter months at BWA airport. Generally, the time of onset and dispersion of fog and dense fog look similar. The most favorable timing of both types of fog is before 05:45 local time (00:00 UTC), i.e., any time between the previous night and the early next morning. The percentage of general fog onset that occurs before 05:45 local time in November is the highest (91.1 ± 3%) followed by February (82.1 ± 4%), December (72.8 ± 3%), and January (63.7 ± 3%); whereas fog onset that occurs during the early morning (05:46–08:45 local time) is the highest (19.4 ± 3%) in January, December (15.1 ± 3%), February (13.9 ± 4%), and November (7.0 ± 3%). Quite a few percent (1.8 ± 1.6% - Nov, 8.6 ± 2% - Dec, 15 ± 3% - Jan & 4 ± 2% - Feb) of fog onset occur during (08:46–11:45 local time). While fog onset during early afternoon 11:46–14:45 local time (3 events-Dec & 2 events-Jan) is quite a rare event. Interestingly, our data was able to capture a small percentage of general fog onset in the late afternoon (14:46–17:45 local time) during December (3 ± 1.3%) and January (1.5 ± 0.8%), although there is almost no dense fog onset during this period. Thus, there is some possibility of fresh fog formation during the daytime even when the day started with no fog. This phenomenon has prominence during December and January. Fig. 5(b & d) shows that the most favorable period of both types of fog dispersal, for all winter months, in the early morning 05:46–08:44 local time. During November, most, 82.5 ± 4.5%, of the general fog dispersal takes place in the early morning 05:46–08:44 local time, 15.6 ± 4.3% of fog dispersal takes place in 08:46–11:44 local time and the remaining 1.8 ± 1.6% completely dissipates by the early afternoon, 14:45 local time. Similarly, during February 68.9 ± 4.8% of fog dispersal occurs in the early morning, while about 6.8 ± 2.6% dissipates by early afternoon. Further, during the peak foggy months, December and January, the fog dispersal might occur throughout the day, with the lowest dispersal percentage in the late afternoon 14:46–17:44 local time. In December (January), the highest percentage, 60.6 ± 3.7% (45.4 ± 3.7%), of fog dispersal occurs in the early morning, 05:46–08:44 local time, followed by 21.6 ± 3.1% (29.2 ± 3.4%) dispersal in mid to late morning, 08:46–11:44 local time, 13.3 ± 2.6% (22.5 ± 3.1%) dispersal in the early afternoon,11:46–14:44 local time. A very negligible dispersal of 0.7 ± 0.6% (0.7 ± 0.6%) was recorded in the early afternoon, 11:46–14:44 local time. However, a small percentage of 3.8 ± 1.5% (2.1 ± 1.1%) of the dispersal of general fog events was observed in the evening time (>17:46 local time); this dispersal possibly accounts for the dispersal of those fog events that onset during the late afternoon. Thus, most of the fog events that formed overnight as well as some fresh fog events that formed during the daytime disperse before early afternoon, i.e., before 14:44 local time. Likewise, the time of the dispersion of dense fog events is also identical to that of general fog for all winter months.

3.5. Comparison of winter poor visibility and fog among the neighboring airports in the IGP region

Comparing wintertime temporal variation of poor visibility and fog days at BWA to that in other cities in the IGP, we find that cities of GOP, LKN, and DEL had poor visibility since much longer ago while BWA experienced a major decline in visibility in recent years (Fig. 6, Table S.3). The lowest winter poor visibility percentages in GOP, LKN, and DEL are yet very high, i.e., 91.5 ± 2% (2019), 79.6 ± 2% (2005), and 94.7 ± 1% (1998) respectively. The winter poor visibility has already peaked in these cities since the beginning of their data recordings and their interannual variation showed lesser variation. On the other hand, it has increased gradually over the same period at BWA. The results point out a marked positive trend of 1.02%yr^{-1} at 0.001 level of significance at BWA. There is an obvious increasing trend in winter fog days across all these cities over the entire data period (Fig. 6 (e-h)). DEL has the steepest trend of 1.29 % *day* yr^{-1} at 0.001 significance level followed by: BWA 1.19%*day* yr^{-1}at 0.001 level, LKN 0.93%*day* yr^{-1} at 0.05 level, and GOP at 0.62%*day* yr^{-1} at 0.05 significance level.

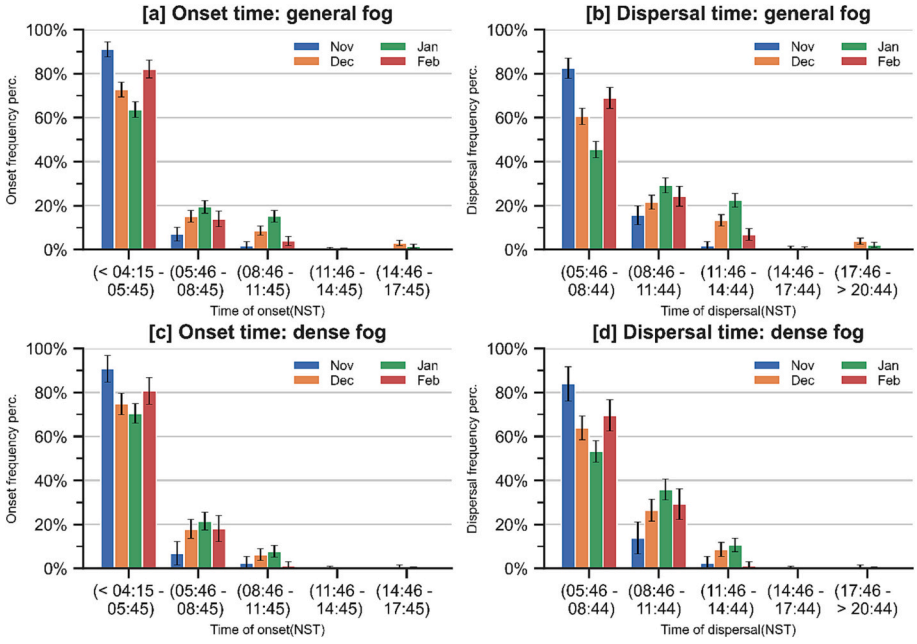

Fig. 5. The occurrence frequency (in percentage) of (a) Onset time of general fog events, (b) Dispersal time of general fog events, (c) Onset time of dense fog events, and (d) Dispersal time of dense fog events - at Bhairahawa airport (1977–2020). The error bars represent a 95% confidence interval for a single proportion of the annual number of respective fog parameters. The endpoints in the ordered time pair representing consecutive duration are included inside the time interval monsoon (0.15%yr^{-1}, *at* $\alpha = 0.05$) only. WS displays a significant declining trend of -0.009 m/s yr^{-1} (at,$\alpha = 0.1$) in winter. T_{min} shows an increasing trend in all seasons except for pre-monsoon.

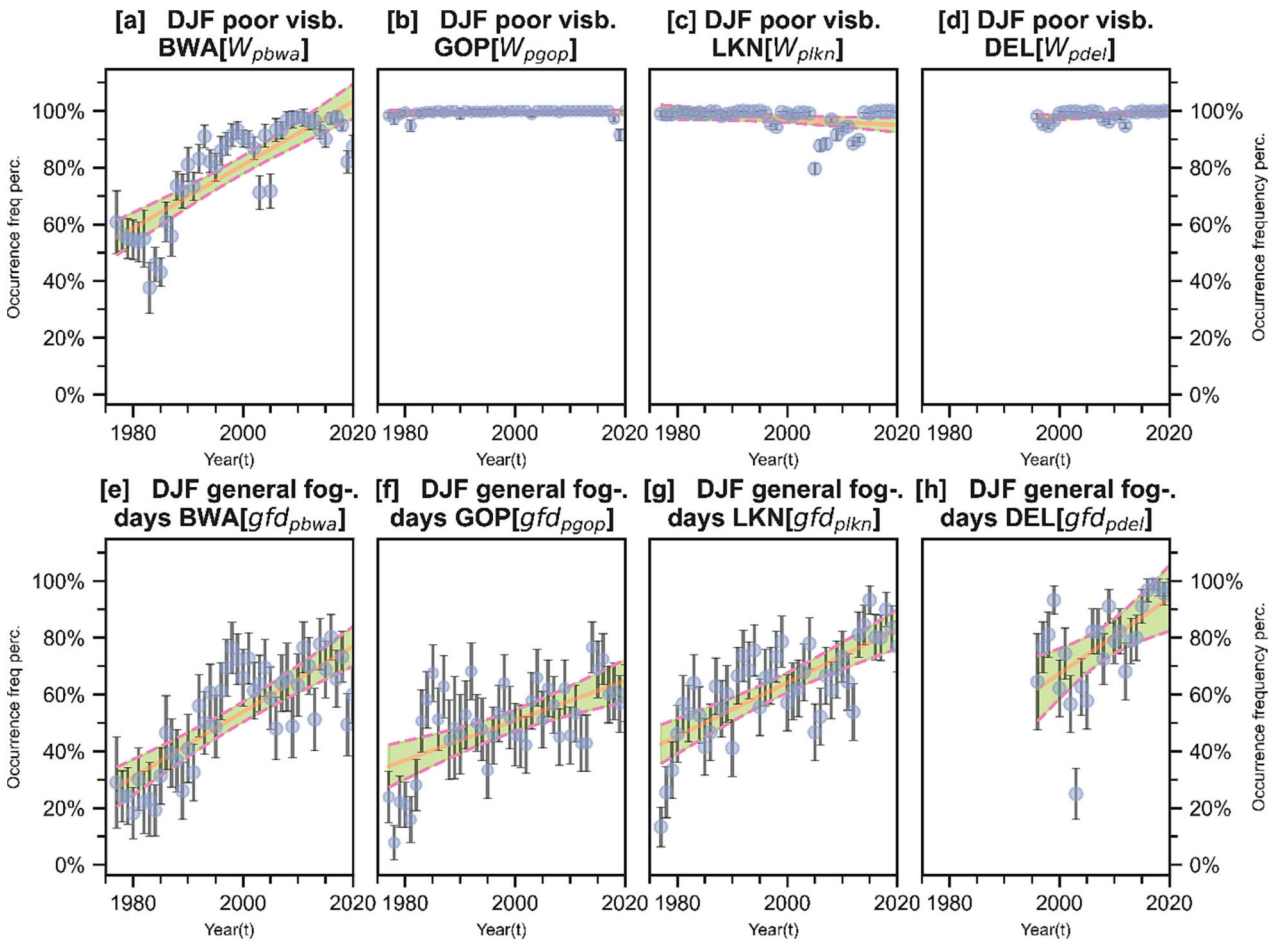

Fig. 6. The time evolution of; the frequency (in percentage) of occurrence of: poor- visibility events [(a), (b), (c) & (d)], and general fog days [(e), (f), (g) & (h)] during winter months (**DJF**) at Bhairahawa (BWA), Gorakhpur (GOP), Lucknow (LKN), and Delhi (DEL) airports. The error bars represent the 95% confidence interval for a single proportion of the annual number of poor visibility events and the annual number of fog days respectively. The solid lines represent the linear fit of the trend results obtained from OLS regression, and the dashed lines represent their 95% confidence interval.

3.6. Relationship between the aerosol optical depth (AOD), PM2.5, RH, and visibility

Fig. 7 (a) shows the daily average values of AOD and visibility for each day of the year aggregated from observation between 2013 and 2018. During winter (DJF), average AOD values gradually increased, reaching their maximum in February (0.80 ± 0.02). Contrary to the empirical relation between visibility and AOD (Eq. (4)), average visibility in February (2.75 ± 0.15 km) is better than in December (2.1 ± 0.13 km) and January (1.89 ± 0.16 km) despite having higher AOD values. The correlation between AOD and visibility during winter was weak ($r = -0.36$, $p = 2.74 \times 10^{-5}$). Temperature is at its lowest (14.68 ± 0.37 °C) and RH is at its highest (82.7 ± 1.28%) in January among the three-winter months (Table S5). As the pre-monsoon season advances, aerosol loading (AOD) starts increasing and the highest AOD value is observed in May (0.75 ± 0.01). Despite the increase in the AOD, visibility also starts improving with the advancement of pre-monsoon season, having the best average visibility in May (6.10 ± 0.14 km). Visibility and AOD display an inverse relation with an even weaker correlation ($r = -0.23$, $p = 4.75 \times 10^{-5}$). With the onset of the South Asian Monsoon system in monsoon, we can see a notable improvement in visibility and a sharp decline in the AOD.

The lowest value of AOD (0.21 ± 0.01) and the highest visibility (7.4 ± 0.21) were observed in July. There is an overall increase in AOD and a decrease in visibility across the season during active monsoon months (JJAS). During these months, visibility and AOD exhibit moderate correlation ($r = -0.66$, $p = 7.23 \times 10^{-20}$), and are in good agreement with the empirical relation (4), the best among all over the year. A gradual decrease in visibility and a sharp rise in AOD is seen during October and November when there is a moderate correlation of ($r = -0.42$, $p = 9.81 \times 10^{-10}$). A graphical representation of the association of AOD with visibility and RH during the monsoon period of 2013–2018 is shown in Fig. 7(b). The curve of best fit (brown line) is similar to the theoretical relation given by Eq. (4) with a goodness of fit (R^2) of about 0.55, meaning that about 55% of the variability in visibility during the monsoon period is explained by the variability of the AOD alone. We can clearly see that the combined effect of RH and AOD on visibility is as expected, with the visibility reduction taking place towards a higher RH regime. When RH is <60% the influence of RH is negligible. Under the condition of high visibility and low RH, the main influencing factor of visibility is particle concentration. When the RH is >60% the influence of RH on visibility continues to increase. A similar power function relationship is seen between PM2.5 and visibility at BWA (Fig. 7(c)), with a strong anti-correlation ($r = -0.74$). Atmospheric visibility provides the public with an estimate of air quality such that they generally believe that the lower the visibility the worse the air pollution. Accordingly, we see that the higher the PM2.5 concentration, the lower the visibility. PM2.5 also has different effects on visibility, under different RH. There is generally good visibility condition at low PM2.5 and RH <50%. However, when RH and PM2.5 get higher, visibility tends to lower. From the figure (Fig. 7(c)), visibility of 5 km, the visual threshold for aviation use, corresponds to a PM2.5 mass of 48 μgm^{-3}.

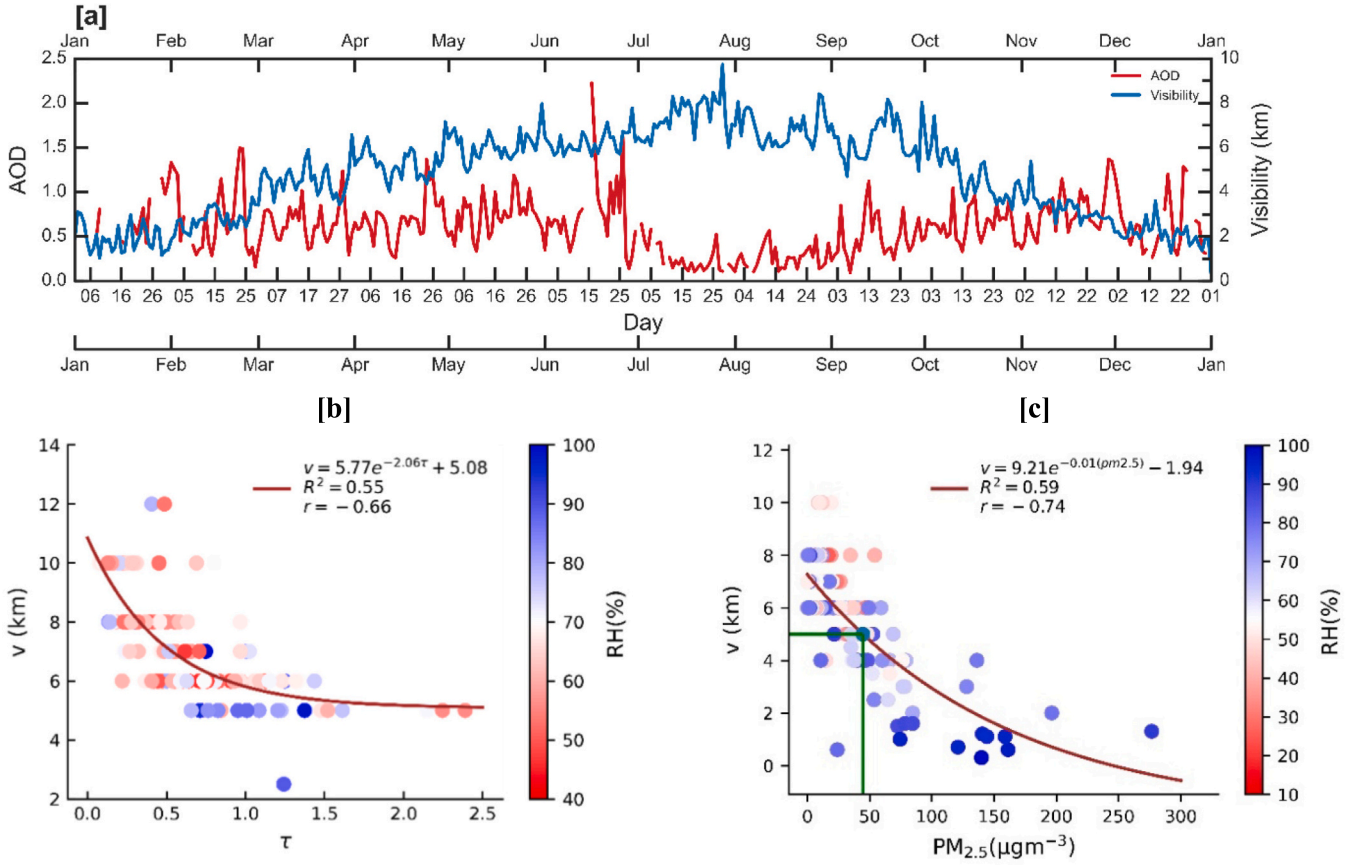

Fig. 7. (a) Average visibility and AOD (τ, *at* $\lambda = 550$ nm) with respect to the Day of the year, and (b) visibility as a function of AOD (τ) – during the South Asian monsoon (JJAS) period from 2013 to 2018 (c) Visibility as a function of $PM_{2.5}$ mass from April to Dec 2019. Data points are color coded for RH in (b) and (c).

3.7. Long-term change of PM2.5, relative humidity, wind speed, and daily minimum temperature

The interannual time series of Total Surface Mass Concentration (PM2.5) in Fig. S2 shows a significant increase of PM2.5 over the period for all seasons. A sudden jump in PM2.5 is observed in the year 2000. The highest value of PM2.5 is observed during winter (DJF) followed by pre-monsoon (MAM), post-monsoon (SON), and monsoon (JJAS) similar to our observation on AOD data (Section 3.6). We found a statistically significant (at 0.001 level) positive trend of PM2.5 in all seasons (Table 2). It shows the highest positive trend in winter ($1.27 \mu g\, m^{-3}\, yr^{-1}$) season and lowest in monsoon ($0.45\ \mu g\, m^{-3}\, yr^{-1}$).

Similarly, we performed a trend analysis of different meteorological parameters, namely relative humidity (RH), Surface Wind Speed (WS),

Table 2
Results of Mann-Kendall, Sen's slope estimator, and OLS regression test of seasonal average values of (a) PM2.5, (b) Relative humidity (RH), (c) wind speed (WS), and (d) Daily minimum temperature (T_{min}) between 1977 and 2020 at Bhairahawa airport. The trend represents the slope of the linear fit between the variable of interest and year. The boldface values indicate that the slope is statistically significant at corresponding levels of significance(α).

		Mann – Kendall		Sen's slope		OLS regression			
		Z_{MK}	*p*–value	Trend Q (yr^{-1})	**[CI]**	Trend $\widehat{\beta}_1$ (yr^{-1})	**[95% CI]**	t_s	*p*-value>|*t*|
a) PM2.5 ($\mu g\, m^{-3}$)	Winter (**DJF**)	6.15*	7.56×10^{-10}	**1.27***	[0.440, 1.835]	**1.42*** ± 0.127	[1.167, 1.679]	11.2	0.000
	Pre-monsoon (**MAM**)	5.80*	6.76×10^{-9}	**0.76***	[0.400, 1.122]	**0.80*** ± 0.088	[0.626, 0.982]	9.14	0.000
	Monsoon (**JJAS**)	5.51*	3.49×10^{-8}	**0.45***	[0.242, 0.699]	**0.49*** ± 0.067	[0.353, 0.625]	7.26	0.000
	Post-monsoon (**ON**)	6.10*	1.07×10^{-9}	**1.26***	[0.723, 1.669]	**1.35*** ± 0.111	[1.122, 1.571]	12.14	0.000
b) RH (%)	Winter (**DJF**)	4.16*	3.22×10^{-5}	**0.36***	[0.084, 0.646]	**0.38*** ± 0.072	[0.230, 0.523]	5.20	0.000
	Pre-monsoon (**MAM**)	2.28†	2.28×10^{-2}	**0.15†**	[−0.093, 0.441]	**0.17**** ± 0.097	[−0.025, 0.365]	1.76	0.086
	Monsoon (**JJAS**)	0.65ns	5.03×10^{-1}	0.029ns	[−0.107, 0.179]	0.30ns ± 0.041	[−0.053, 0.112]	0.73	0.471
	Post-monsoon (**ON**)	1.22ns	2.20×10^{-1}	0.062ns	[−0.132, 0.291]	0.08ns ± 0.061	[−0.046, 0.199]	1.258	0.215
c) WS (m/s)	Winter (**DJF**)	−1.7**	8.74×10^{-2}	**−0.009****	[−0.032, 0.009]	**−0.01**** ± 0.006	[−0.023, 0.001]	−1.78	0.082
	Pre-monsoon (**MAM**)	−1.2ns	2.28×10^{-1}	−0.009ns	[−0.034, 0.016]	−0.01ns ± 0.007	[−0.023, 0.007]	−1.12	0.268
	Monsoon (**JJAS**)	−0.63ns	5.30×10^{-1}	−0.004ns	[−0.013, 0.006]	−0.003ns ± 0.005	[−0.014, 0.008]	−0.59	0.556
	Post-monsoon (**ON**)	−1.18ns	2.31×10^{-1}	−0.006ns	[−0.015, 0.003]	−0.006ns ± 0.005	[−0.017, 0.005]	−1.14	0.261
d) T_{min} (°C)	Winter (**DJF**)	2.41†	1.57×10^{-2}	**0.020†**	[0.004, 0.036]	**0.019† ± 0**.008	[0.003, 0.035]	2.40	0.021
	Pre-monsoon (**MAM**)	1.62ns	1.05×10^{-1}	0.016ns	[−0.004, 0.034]	**0.018† ± 0**.008	[0.001, 0.34]	2.15	0.038
	Monsoon (**JJAS**)	3.27†	1.06×10^{-3}	**0.016†**	[0.007, 0.223]	**0.014† ± 0**.004	[0.008, 0.022]	4.16	0.000
	Post-monsoon (**ON**)	4.13†	3.53×10^{-5}	**0.032†**	[0.019, 0.046]	**0.030† ± 0**.008	[0.014, 0.047]	3.75	0.001

* 0.001, † 0.05, **0.1 - level of significance; ns - non-significant.

and Daily Minimum Temperature (T_{min}) and presented their test results in Table 2. Upon the trend analysis, we found that RH displays an increasing trend during winter ($0.36\%yr^{-1}$, *at* $\alpha = 0.001$) and pre-.

4. Discussion

The region around BWA airport is one of Nepal's larger industrial centers, influencing major economic aspects of Nepal. In addition to agricultural fields and villages, the region contains the city of Bhairahawa, as well as brick kilns, cement factories, steel mills, and other industries. Across the border in India, the region is also densely populated and contains agricultural fields and industries. The city of BWA, its surrounding area, and the area across the southern border with India have witnessed rapid urbanization and industrialization in recent decades. A study by Ramachandran and Rupakheti (2022), found a positive trend of urban/ industrial aerosol type on the annual scale over Kanpur, indicating worsening air quality and visibility in the IGP region. Different studies (Dhungel et al., 2018; Khanal et al., 2022; Lüthi et al., 2015; Panday et al., 2016; Rupakheti et al., 2017) which involve models, satellite, and observation data have reported a long-range and transboundary transport of air pollutants from IGP region to higher Himalayas via southern plains of Nepal, especially in dry seasons. Thus, the worsening of air quality and visibility during dry seasons can also be attributed to the transport of transboundary air pollution. Power cuts during dry months have been a common phenomenon in the IGP region in and around BWA until recently. Emissions from distributed generator sets (World Bank, 2014) and irrigation pump has been significant during winter and pre-monsoon season and have contributed to local and regional air pollution.

We have found that BWA experiences the highest air pollution, both AOD and PM2.5, during the winter season (DJF) (Fig. 7(a) & Fig. S2) similar to the findings of previous studies (Rupakheti et al., 2018a; Kedia et al., 2014; Sharma et al., 2014). A significant buildup of air pollution in the atmosphere of IGP starts in the post-monsoon season particularly because of agricultural residue burning after rice crop harvest in large parts of the region (Saikawa et al., 2019; Khanal et al., 2022), in addition to other regular emission sources and intensifies in December and January (Dey and Di Girolamo, 2010). The low correlation between AOD and visibility ($r = -0.36$) during winter suggests that aerosol loading only is not sufficient to explain the visibility reduction in winter. We have also found the steepest positive trend ($1.27\mu g\, m^{-3}\ yr^{-1}$) of air pollution, more specifically, PM2.5, during winter for our study period. Many previous studies have reported a similar increasing trend of haze (Jaswal et al., 2013; Kaskaoutis et al., 2012; Sarkar et al., 2006; Saikawa et al., 2019; Srivastava et al., 2012) elsewhere in the IGP region in winter. Burning wood and fossil fuels are still primary sources for heating and cooking in Nepal. Burning of wood is more common in rural areas whereas fossil fuel burning is common in urban areas. Such activities are higher during cold winter days, especially in lowland areas of Nepal and adjacent areas across the border. According to Kedia et al. (2014) and Ramachandran et al. (2015), in addition to vehicular/ industrial emissions, an increase in anthropogenic emissions due to biomass burning in winter – especially for residential heating – results in more amount of Black Carbon (BC) over IGP. Thus, such activity in winter worsens the air quality as well as visibility in the area. Through their study of climatology and trends in absorbing aerosols type – on seasonal and annual time scales – Ramachandran and Rupakheti (2022) found a significant positive trend in biomass burning (BB) aerosol type during winter over Kanpur, a city in IGP, located at about 313 km southwest of BWA. This upward trend of BB during winter shall contribute to a worsening trend of air quality and visibility at BWA.

Similarly, winter months in the Terai plains of Nepal are characterized by special meteorological conditions – slower wind, adequate moisture content (RH) (Table S5), and low-level temperature inversion episodes. These conditions result in a shallow planetary boundary layer (PBL), hence, suppressed buoyant vertical transport of the pollutants (Tare et al., 2006). Because of the trapping of pollutants within a shallow layer, with low WS, an optically thick layer of haze on a regional scale builds up in winter. There is also a statistically significant increase in RH ($0.36\%yr^{-1}$ *at* $\alpha = 0.001$) and a decrease in surface wind speed (-0.009 m/s yr^{-1} at $\alpha = 0.1$) during winter (Table 2). A recent study by Islam et al. (2021) reported that secondary inorganic ions (ammonium, nitrate, and sulfate) comprise $20 \pm 6\%$ of the total chemical composition of PM2.5 nearby BWA. Under a high RH regime, as generally observed during winter, optical properties of such secondary aerosols are altered leading to increased extinction efficiency, i.e., haze, and reduced visibility. Thus, RH is also an important meteorological parameter to influence winter season visibility at BWA. Similarly, decreasing WS in winter reduces the horizontal dispersion of air pollution.

Across IGP, the winter haze and fog are strongly coupled systems. The meteorological conditions in winter also offer an ideal condition for the occurrence of widespread and persistent radiation fog along the stretch of the IGP region. The key ingredients for the formation of the fog are sufficient moisture, and enough hygroscopic aerosol particles onto which moisture can condense (also known as cloud condensation nuclei, or CCN) (Gultepe et al., 2007). Apart from the addition of water vapor on a regional scale by western- disturbances (Gautam, 2014), the moisture for winter-time fog formation in some parts of IGP could have originated from the irrigation of a large swathe of agricultural fields of Uttar Pradesh, Haryana, and Punjab (Jenamani, 2007). According to a report by MoF (2020), the irrigation area of BWA has expanded manifold during the last few decades, which might have resulted in the observed upward trend of RH. There is still a lack of scientific consensus on why persistent winter fog has increased across the IGP in recent decades (Saikawa et al., 2019), however, we found that the increasing trend in frequency and intensity of winter fog is consistent with the increasing trend of air pollution (PM2.5, ($1.27\mu g\, m^{-3}\ yr^{-1}$)), RH ($0.36\%yr^{-1}$), and decreased WS ($-0.009$ m/s yr^{-1}). Several other studies (e.g., Ghude et al., 2017; Jenamani, 2007; Syed et al., 2012; Mohan and Payra, 2014; Shrestha et al., 2018) conducted elsewhere in IGP have also reported the increasing tendency of fog (fog - days/h) in winter. These results also agree with the general perception of local people in the Terai region, about the main climatic variation during the winter season, that "fog occurs more frequently and denser", and "cold spells are getting more intense" (Smadja et al., 2015). Further, we have observed an increasing trend in average daily minimum temperature (T_{min})($0.020\ ^{\circ}\ C\ yr^{-1}$) in winter similar to the findings of Baidya et al. (2008), Shrestha et al. (2017), and Shrestha et al. (2018). This could be because of the increased occurrence of fog and haze which reduce the loss of long-wave solar insolation at night resulting in surface warming. In essence, we observed the seasonal highest occurrence of poor visibility events in winter in the form of haze and fog because of the combination of the highest level of air pollution and the influence of specific meteorological conditions i.e., low temperature, temperature inversion, RH, and WS. The increased poor visibility events eventually resulted from the upward trend of occurrence of haze and fog. The lowest temperature and highest RH in January, among the three-winter months, cause the duration and intensity of fog to peak in January resulting in the lowest visibility. Because of a sharp temperature rise – increasing dew point depression – leading to elevated PBL height and a decrease in RH, the duration, and intensity of fog diminish and visibility tends to improve as the winter season advances. We further looked at the frequency of cold days and nights during the winter season and found that the frequency of cold days is slightly increasing while the frequency of cold nights is decreasing (result not shown). This also supports that the duration and frequency of fog and haze are increasing which reveals the increasing cold day and enhancing of the poor visibility.

The onset of fog takes several hours because the ambient temperature falls gradually overnight, creating meteorological conditions conducive to the formation of fog. However, the dispersal of fog takes a shorter duration because an increase in temperature occurs faster as the sun passes overhead or the wind speeds up, dispersing or clearing the

fog. Our findings on the onset and dispersal of fog events are consistent with the finding of Jenamani (2012) and Mishra and Mohapatra (2004).

During the pre-monsoon season (MAM), the atmosphere at BWA becomes warmer, drier, and turbulent (Table S5), and the top of the PBL rises because of the warmer atmosphere as the season advances. This phenomenon should have resulted in the observed improved visibility, in comparison to the winter season. Since aerosols are trapped within a shallow mixing layer in winter and still in pre-monsoon, the columnar distribution of aerosol is not uniform and so is the light extinction, as has been assumed during the formulation of the relation (Eq. (4)). Thus, the relationship between AOD and visibility is not so strong. The majority of visibility reduction during MAM occurs when the haze becomes denser. Regional haze episodes are frequent during this season because of the accumulation of aerosol plumes from different sources as discussed in earlier sections. Besides having these regular emission sources, many previous studies (Dey and Di Girolamo, 2010; Gautam et al., 2009; Hegde et al., 2007; Ram et al., 2010) have reported a likelihood of additional contribution from wind-blown desert dust originating as far from the Thar Desert during this season. A study by Pandithurai et al. (2008) has also reported a deterioration of visibility in IGP by contribution from desert-dust air pollution. In this study, we have found a significant increase in air pollution, more specifically PM2.5 (0.76 $\mu g\ m^{-3}\ yr^{-1}$), and RH (0.15%yr^{-1}), at BWA in the pre-monsoon season. Thus, the increment in aerosol loading and RH could have led to the observed increasing trend of pre-monsoon-haze and overall poor-visibility conditions in the pre-monsoon season.

Most importantly, the precipitation scavenging of pollutants is dominant during the monsoon season (JJAS). It occurs either by rainout (in-cloud capture of particulates as condensation nuclei) or washout (below-cloud capture of particulates and gaseous pollutants by falling raindrops) (American Meteorological Society, 2006). The highest amount of precipitation at BWA airport is witnessed in July, which gradually declines as the monsoon season advances. This results in an abrupt decline in the AOD value in July and lower values of AOD during other monsoon months. Since we do not notice a marked variation in any other meteorological parameters except for the rain while advancing from the pre-monsoon (Table S5), the air pollution scavenging process by the monsoon system should be the governing factor of visibility. In addition, the visibility condition is usually the best of all seasons also because of having high temperature, high WS, (Table S5), and elevated PBL height – probably the highest – leading to stronger convective mixing and horizontal dispersion of air pollution. Based on our findings on the relationship between visibility, AOD/PM2.5, and RH (Section 3.6), the RH, especially in higher regimes (>60%), has an indirect but notable influence on visibility by changing the optical properties of the aerosols. Since the seasonal average RH is higher than 60% (Table S5), we can expect a significant role of RH. Because of air pollution scavenged by this seasonal rainfall during monsoon, the measured level of air pollution is the lowest. The rise of the AOD level in early June could be resulted from the pushing of regional aerosol plumes in the IGP towards the northern IGP by the southwesterly winds related to the onset of the monsoon. Among all, the best anti-correlation between AOD/PM2.5 and visibility occurs and the power function relationship between them is observed because this season offers meteorological conditions closely matching our assumption – all aerosols are trapped within the mixing layer and the extinction coefficient is uniform across it – while deriving the empirical relationship. A similar reciprocal relation between AOD and visibility was detected from the in-situ measurements for 5 days over South-West Germany (Bäumer et al., 2008). Lin et al. (2011) also observed an exponential relationship with a high correlation coefficient (about −0.75) between AOD and visibility during April 2006 in over 200 locations in Asia. The upward trend of PM2.5 (0.45 $\mu g\, m^{-3}\ yr^{-1}$) at the BWA region supports the increase in the occurrence of monsoon-haze (0.314%yr^{-1}) and poor visibility conditions. Dey and Di Girolamo (2010) also suggested that visibility reduction during the monsoon usually results from absorbing and scattering visible light by cloud and rain droplets or by aerosols during the occasional haze that occurs during the monsoon break.

With the onset of the post-monsoon (ON) season, many air pollution activities, especially the operation of brick kilns, in the BWA and elsewhere in the IGP region resume their operation. They are normally shut down during the monsoon season to avoid potential damage by rain. Haze – sometimes referred to as atmospheric brown cloud – start to build up in the IGP region, due to paddy residue burning, mostly in the upwind sites of IGP, like Pakistan, the Indian states of Punjab, and Hariyana after the rice harvest (Kulkarni et al., 2020; Jethva et al., 2019). Slow eastward transport of thus produced pollutants contributes to air pollution in the downwind sites, as found by Kulkarni et al. (2020) in Delhi. A study by Wan et al. (2017) in the post-monsoon months at Lumbini also reported that the organic carbon (OC) derived from biomass burning contributed a significant fraction (as high as 40%) of the total aerosol OC in Lumbini, which confirms the regional influence of agricultural residue burning on the aerosol concentration at BWA. The seasonal air temperature, wind speed, and rainfall (Table S5) diminish, and PBL height starts to shrink as the season advances and aerosol concentration in the atmosphere increases. Since there is little to no rainfall during this season, there is a lack of active scavenging processes. Thus, air pollution is further intensified as the season advances resulting in a gradual reduction in visibility from the combined contribution of increased air pollution emission, a lower air temperature, and wind speed. The observed significant increase in poor visibility conditions and haze during this season might be explained by the upward trend of PM2.5 (1.26 $\mu g\ m^{-3}\ yr^{-1}$). Similarly, the observed sudden drop in the occurrence of poor visibility since the pre-monsoon period of 2020 can be attributed to the slowing down of air pollution emission activities after the COVID lockdown in the region, which started in March 2020.

Almost similar meteorological conditions exist during winter in all of the studied nearby airports in IGP. The perceivable difference at BWA is the extent of local air pollution and proximity to the major sources of emissions in the upwind sector of the IGP region. In comparison to GOP, LKN, and DEL airports, BWA is a smaller city with a lesser population and industrial setup from the beginning of our study period. Thus, local air pollution emissions at BWA were lesser and had better visibility conditions initially. With urbanization and industrialization in the area, which occurred lately, local air pollution emissions at BWA also increased manifold in the recent decades, resulting in worsening visibility conditions during winter. Poor visibility conditions existed in the rest of the megacities because of having a higher level of air pollution emissions since the beginning.

Besides many other sectors, the occurrence of poor visibility in different forms includes serious impacts on the air transport system at BWA. One of the major challenges for aviation at BWA airport is that flight operations are highly influenced by poor visibility conditions due to both regional haze and winter fog. Analysis of climatological data at BWA (Fig. 8), shows a significant decline in the fraction of time when aircraft could land using Visual Flight Rules (VFR) (Appendix A.1). Airport's Instrument Flight Rules (IFR) (Appendix A.1) operation and closure frequency, solely due to reduced visibility, has also increased significantly at the same period. The currently operational navigation systems at BWA, including VOR and recently implemented RNP (Appendix C.1), generally enable airport IFR operation in hazy conditions. However, both fail to enable airport operation, i.e., especially aircraft landing, in general fog (visibility <1 km) conditions, let alone dense fog (visibility <200 m). This results in inconvenience to the passengers and added financial burden to the airlines because of delay or cancellation of scheduled flights, which are yet to depart from BWA airport, or in-flight holding or diversion of the flights bound to BWA airport. The financial loss will be immense when the airport operates international air traffic at its full capacity. Especially during winter, BWA airport and KTM airport are highly unlikely to serve as alternate airports for each other (Appendix C.3 & Fig. S3) in case of visibility conditions at one airport reduce below the minimum visibility required for landing. According to

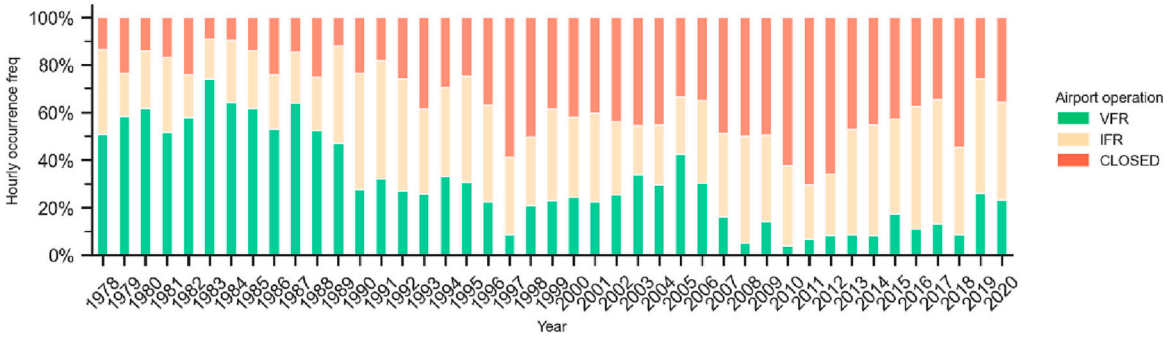

Fig. 8. Winter season (DJF) hourly frequency (in percentage) of different types of flight operation conditions at Bhairahawa airport during the period (1978–2020). The normal Visual Flight Rules (VFR) operation occurs when the visibility of the airport is >5 km.; Instrument Flight Rules (IFR) occur when visibility at BWA airport is between 5 and 1.6 km, and the airport is closed when visibility is lesser than 1.6 km under presently available landing aid i.e., VOR-DME.

CAAN (2022), while being upgraded to the international airport, the government of Nepal has already invested in installing a sophisticated landing guidance system, called Category- I (CAT —I) (Table S.4) Instrument Landing System (ILS) (Appendix C.1) at BWA airport based on its topographic suitability. However, the airport authority of BWA is waiting for permission from the Indian authority before its operation. When it comes to function, it helps BWA airport be able to operate in lower visibility regimes, e.g., during foggy conditions. After further investment in upgrading the ILS to the higher category (CAT – II/III) (Table S.4) and advanced surface movement guidance and control system (A-SMGCS), BWA airport will be capable of operation during very low visibility conditions such as during dense fog. This would justify one of its main objectives of international up-gradation, i.e., the nearest suitable alternate airport to KTM for international air traffics, inside Nepalese territory.

5. Conclusion

This study considered 44 years of visibility data from Bhairahawa airport (BWA) and analyzed the interannual and intra-seasonal variation of visibility that impacts the flight operation at a recently upgraded international airport in Nepal. Haze and fog are the two main weather conditions for reducing visibility, mainly during the winter season and the frequency of annual-poor-visibility events and haze days increased exceedingly over the study period in all seasons. Here are the main conclusions of this study:

- Visibility is consistently decreasing at BWA in all seasons.
- Higher relative humidity and lower wind speed have caused the increased frequency of winter haze and fog.
- The upward trend of haze and poor visibility events are mainly driven by regionally increased air pollution.
- Winter visibility is mainly associated with lengthy fog hours that are caused by the radiational cooling in the stagnant night.

Aviation at BWA airport shows that aviation at BWA airport has been severely affected by the occurrence of poor visibility and is going to be more affected in the future, provided the uncurbed poor visibility conditions persist. The alarming increase in poor visibility conditions in post-monsoon and winter because of the increased haze and fog is of serious concern to aviation. This highlights the importance of immediate implementation of instrument landing system (ILS), preferably CAT- II/III, equipment at BWA airport. Thus, earlier operation of the ILS system is highly advisable.

More in-depth and enhanced studies are needed in the future at BWA airport. Installation of visibility sensors; Runway Visual Range (RVR) measuring equipment like Transmissometers and Forward Scatter Sensors; would yield more precise measurements of visibility. This would be very useful while studying fog characteristics and especially microclimatic behavior. This study highlights a statistical result, which cannot provide detailed physical processes that control the interaction between aerosol particles and weather conditions. Thus, there is a need for an in-depth study with field measurement data, to understand the interaction of aerosol on the lifecycle of fog/ haze for efficient day-to-day flight management. It will help to improve scientific knowledge and proper planning of investments in aviation infrastructure at BWA airport.

Declaration of Completed Interest

The authors declare that they have no known competing financial interests or personal relationships that could have appeared to influence the work reported in this paper.

Funding

This research did not receive any specific grant from funding agencies in the public, commercial, or not-for-profit sectors.

CRediT authorship contribution statement

Bhogendra Kathayat: Conceptualization, Methodology, Software, Formal analysis, Investigation, Data curation, Writing – original draft, Visualization. **Arnico Kumar Panday:** Conceptualization, Methodology, Validation, Supervision, Writing – review & editing. **Binod Pokharel:** Supervision, Writing – review & editing. **Vinod Kumar:** Data curation, Visualization, Writing – review & editing. **Narayan Prasad Chapagain:** Supervision, Writing – review & editing.

Declaration of Competing Interest

None.

Data availability

Data will be made available on a reasonable request.

Acknowledgments

The authors are very much thankful to the Department of Hydrology and Meteorology (DHM), Department of Environment, and the Civil Aviation Authority of Nepal (CAAN). We would like to extend gratitude to the National Climatic Data Center (NCDC), European Centre for Medium-Range Weather Forecasts (ECMWF) Reanalysis v5 (ERA5), and Global Modeling and Assimilation Office (GMAO) (Goddard Earth Sciences Data and Information Services Center (GES DISC), USA) for making various data publicly accessible for this research. We also thank the principal investigator(s) of the AERONET site at Lumbini, whose

data has been used in this study, for their efforts in establishing and maintaining the site. Lastly, we are highly thankful to the anonymous reviewers for their, time and effort in reviewing our manuscript. Their insightful comments and suggestions immensely helped to improve the quality of our paper.

Appendix A. Supplementary data

Supplementary data to this article can be found online at https://doi.org/10.1016/j.atmosres.2023.106746.

References

AIC, 2015. Final Report on the Investigation of Runway Excursion Accident of Turkish Airlines TC-JOC, A330–303, At TIA, Kathmandu, Nepal on 4th March 2015. https://reports.aviation-safety.net/2015/20150304-0_A333_TC-JOC.pdf.

American Meteorological Society, 2006. AMS Glossary of Meteorology. Available online at. https://glossary.ametsoc.org/wiki/Scavenging_by_precipitation.

Baidya, S.K., Shrestha, M.L., Sheikh, M.M., 2008. Trends in daily climatic extremes of temperature and precipitation in Nepal. J. Hydrol. Meteorol. 5 (1), 38–51.

Bäumer, D., Vogel, B., Versick, S., Rinke, R., Möhler, O., Schnaiter, M., 2008. Relationship of visibility, aerosol optical thickness and aerosol size distribution in an ageing air mass over South West Germany. Atmos. Environ. 42, 989–998.

Bosilovich, M.G., Lucchesi, R., Suarez, M., 2015. MERRA-2: File specification (No. GSFC-E-DAA-TN27096).

Buchard, V., Randles, C.A., da Silva, A.M., Darmenov, A., Colarco, P.R., Govindaraju, R., Ferrare, R., Hair, J., Beyersdorf, A.J., Ziemba, L.D., Yu, H., 2017. The MERRA-2 aerosol reanalysis, 1980 onward. Part II: Evaluation and case studies. J. Clim. 30, 6851–6872. https://doi.org/10.1175/JCLI-D-16-0613.1.

CAAN, 2013. Initial Environmental Examination Report. Civil Aviation Authority of Nepal. Government of Nepal. https://caanepal.gov.np/storage/app/media/uploaded-files/SATIDP%20AF%20IEE%20Nov%20013.pdf.

CAAN, 2022. Aeronautical Information Publication, eighth edition. Civil Aviation Authority of Nepal, Government of Nepal, Nepal. https://e-aip.caanepal.gov.np/_uploads/_pdf/0819d46e68f7b2a1edde6ec55ae00105.pdf.

Chang, D., Song, Y., Liu, B., 2009. Visibility trends in six megacities in China 1973–2007. Atmos. Res. 94 (2), 161–167.

Che, H., Zhang, X., Li, Y., Zhou, Z., Qu, J.J., 2007. Horizontal visibility trends in China 1981–2005. Geophys. Res. Lett. 34 (24).

Chen, Y., Xie, S., 2012. Temporal and spatial visibility trends in the Sichuan Basin, China, 1973 to 2010. Atmos. Res. 112, 25–34.

Chen, Y., Xie, S., dong., 2013. Long-term trends and characteristics of visibility in two megacities in Southwest China: Chengdu and Chongqing. J. Air Waste Manage. Assoc. 63 (9), 1058–1069. https://doi.org/10.1080/10962247.2013.791348.

Dani, K.K., Ernest Raj, P., Devara, P.C.S., Pandithurai, G., Sonbawne, S.M., Maheskumar, R.S., Jaya Rao, Y., et al., 2012. Long-term trends and variability in measured multi-spectral aerosol optical depth over a tropical urban station in India. Int. J. Climatol. 32 (1), 153–160.

De, U.S., Dandekar, M.M., 2001. Natural disasters in urban areas. Deccan Geogr. 39 (2), 1–12.

De, U.S., Rag, G.P., Jaswal, A.K., 2001. Visibility over Indian airports during winter season. Mausam 52 (4), 717–726.

Deng, J., Wang, T., Jiang, Z., Xie, M., Zhang, R., Huang, X., Zhu, J., 2011. Characterization of visibility and its affecting factors over Nanjing, China. Atmos. Res. 101 (3), 681–691.

Dey, S., Di Girolamo, L., 2010. A climatology of aerosol optical and microphysical properties over the Indian subcontinent from 9 years (2000–2008) of Multiangle Imaging Spectroradiometer (MISR) data. J. Geophys. Res.-Atmos. 115 (D15).

Dhungel, S., Kathayat, B., Mahata, K., Panday, A., 2018. Transport of regional pollutants through a remote trans-Himalayan valley in Nepal. Atmos. Chem. Phys. 18 (2), 1203–1216.

Doyle, M., Dorling, S., 2002. Visibility trends in the UK 1950-1997. Atmos. Environ. 36, 3161–3172. https://doi.org/10.1016/S1352-2310(02)00248-0.

Du, K., Mu, C., Deng, J., Yuan, F., 2013. Study on atmospheric visibility variations and the impacts of meteorological parameters using high temporal resolution data: an application of environmental internet of things in China. Int. J. Sustain. Developm. World Ecol. 20 (3), 238–247.

Founda, D., Kazadzis, S., Mihalopoulos, N., Gerasopoulos, E., Lianou, M., Raptis, P.I., 2016. Long-term visibility variation in Athens (1931–2013): a proxy for local and regional atmospheric aerosol loads. Atmos. Chem. Phys. 16 (17), 11219–11236.

Fu, G.Q., Xu, W., Yang, R.F., Li, J.B., Zhao, C.S., 2014. The distribution and trends of fog and haze in the North China Plain over the past 30 years. Atmos. Chem. Phys. 14 (21), 11949–11958.

Gao, L., Jia, G., Zhang, R., Che, H., Fu, C., Wang, T., Yan, P., et al., 2011. Visual range trends in the Yangtze River Delta region of China, 1981–2005. J. Air Waste Manage. Assoc. 61 (8), 843–849.

Gautam, R., 2014. Challenges in early warning of the persistent and widespread winter fog over the Indo-Gangetic Plains: a satellite perspective. In: Reducing Disaster: Early Warning Systems for Climate Change. Springer, Dordrecht, pp. 51–61.

Gautam, R., Hsu, N.C., Kafatos, M., Tsay, S.C., 2007. Influences of winter haze on fog/low cloud over the Indo-Gangetic plains. J. Geophys. Res.-Atmos. 112 (5), 1–11. https://doi.org/10.1029/2005JD007036.

Gautam, R., Liu, Z., Singh, R.P., Hsu, N.C., 2009. Two contrasting dust-dominant periods over India observed from MODIS and CALIPSO data. Geophys. Res. Lett. 36 (6).

Gelaro, R., McCarty, W., Suárez, M.J., Todling, R., Molod, A., Takacs, L., Randles, C.A., Darmenov, A., Bosilovich, M.G., Reichle, R., Wargan, K., Coy, L., Cullather, R., Draper, C., Akella, S., Buchard, V., Conaty, A., da Silva, A.M., Gu, W., Kim, G.K., Koster, R., Lucchesi, R., Merkova, D., Nielsen, J.E., Partyka, G., Pawson, S., Putman, W., Rienecker, M., Schubert, S.D., Sienkiewicz, M., Zhao, B., 2017. The modern-era retrospective analysis for research and applications, version 2 (MERRA-2). J. Clim. 30, 5419–5454. https://doi.org/10.1175/JCLI-D-16-0758.1.

Ghude, S.D., Bhat, G.S., Prabhakaran, T., Jenamani, R.K., Chate, D.M., Safai, P.D., Karipot, A.K., Konwar, M., Pithani, P., Sinha, V., Rao, P.S.P., Dixit, S.A., Tiwari, S., Todekar, K., Varpe, S., Srivastava, A.K., Bisht, D.S., Murugavel, P., Ali, K., Mina, U., Dharua, M., Rao, J., Padmakumari, B., Hazra, A., Nigam, N., Shende, U., Chandra, B. P., Mishra, A.K., Kumar, A., Hakkim, H., Pawar, H., Acharga, P., Kulkarni, R., Subharthi, C., Balaji, B., Varghese, M., Bera, S., Rajeevan, M., 2017. Winter fog experiment over the Indo-Gangetic plains of India. Curr. Sci. 112, 767–784. https://doi.org/10.18520/cs/v112/i04/767-784.

Global Modeling and Assimilation Office (GMAO) (2015). MERRA-2 tavgM_2d_aer_Nx: 2d, Monthly mean, Time-averaged, Single-Level, Assimilation, Aerosol Diagnostics V5.12.4, Greenbelt, MD, USA, Goddard Earth Sciences Data and Information Services Center (GES DISC), Accessed: [2023.01.25]. doi: 10.5067/FH9A0MLJPC7N.

Gultepe, I., Tardif, R., Michaelides, S.C., Cermak, J., Bott, A., Bendix, J., Mullar, M.D., Pagwoski, M., Hansen, B., Ellrod, G., Jacobs, W., Toth, G., Cober, S.G., 2007. Fog research: a review of past achievements and future perspectives. Pure Appl. Geophys. 164 (6), 1121–1159.

Gultepe, I., Zhou, B., Milbrandt, J., Bott, A., Li, Y., Heymsfield, A.J., Ferrier, B., Ware, R., Pavolonis, M., Kuhn, T., Cermak, J., 2015. A review on ice fog measurements and modeling. Atmos. Res. 151, 2–19.

Hameed, S., Mirza, M.I., Ghauri, B.M., Siddiqui, Z.R., Javed, R., Khan, A.R., Rattigan, O. V., Qureshi, S., Husain, L., 2000. On the widespread winter fog in Northeastern Pakistan and India. Geophys. Res. Lett. 27, 1891–1894.

Hegde, P., Pant, P., Naja, M., Dumka, U.C., Sagar, R., 2007. South Asian dust episode in June 2006: aerosol observations in the Central Himalayas. Geophys. Res. Lett. 34 (23).

Hu, Y., Yao, L., Cheng, Z., Wang, Y., 2017. Long-term atmospheric visibility trends in megacities of China, India and the United States. Environ. Res. 159, 466–473.

Islam, M.R., Li, T., Mahata, K., Khanal, N., Werden, B., Giordano, M.R., Stone, E.A., et al., 2021. Wintertime air quality in Lumbini, Nepal: sources of fine particle organic carbon. ACS Earth Space Chem. 5 (2), 226–238.

Izhar, S., Gupta, T., Qadri, A.M., Panday, A.K., 2021. Wintertime chemical characteristics of aerosol and their role in light extinction during clear and polluted days in rural Indo Gangetic plain. Environ. Pollut. 282, 117034.

Jaswal, A.K., Kumar, N., Prasad, A.K., Kafatos, M., 2013. Decline in horizontal surface visibility over India (1961–2008) and its association with meteorological variables. Nat. Hazards 68 (2), 929–954.

Jenamani, R.K., 2007. Alarming rise in fog and pollution causing a fall in maximum temperature over Delhi. Curr. Sci. 314–322.

Jenamani, R.K., 2012. Micro-climatic study and trend analysis of fog characteristics at IGI airport New Delhi using hourly data (1981-2005). Mausam 63 (2), 203–218.

Jenamani, R.K., Kumar, A., 2013. Bad weather and aircraft accidents - global vis-a-vis Indian scenario. Curr. Sci. 104 (3), 316–325.

Jethva, H., Torres, O., Field, R.D., Lyapustin, A., Gautam, R., Kayetha, V., 2019. Connecting crop productivity, residue fires, and air quality over northern India. Sci. Rep. 9 (1), 1–11.

Kaskaoutis, D.G., Singh, R.P., Gautam, R., Sharma, M., Kosmopoulos, P.G., Tripathi, S.N., 2012. Variability and trends of aerosol properties over Kanpur, northern India using AERONET data (2001−10). Environ. Res. Lett. 7 (2), 024003.

Kedia, S., Ramachandran, S., Holben, B.N., Tripathi, S.N., 2014. Quantification of aerosol type, and sources of aerosols over the Indo-Gangetic Plain. Atmos. Environ. 98, 607–619.

Kendall, M.G., 1975. Rank Correlation Measures. Charles Griffin, London.

Khanal, S., Pokhrel, R.P., Pokharel, B., Becker, S., Giri, B., Adhikari, L., LaPlante, M.D., 2022. An episode of transboundary air pollution in the Central Himalayas during agricultural residue burning season in North India. Atmosph. Pollut. Res. 13 (1), 101270.

Kulkarni, R., Jenamani, R.K., Pithani, P., Konwar, M., Nigam, N., Ghude, S.D., 2019. Loss to aviation economy due to winter fog in New Delhi during the winter of 2011–2016. Atmosphere 10 (4), 198.

Kulkarni, S.H., Ghude, S.D., Jena, C., Karumuri, R.K., Sinha, B., Sinha, V., Kumar, R., Soni, V.K., Khare, M., 2020. How much does large-scale crop residue burning affect the air quality in Delhi? Environ. Sci. Technol. 54 (8), 4790–4799.

Lin, T.H., Christina Hsu, N., Tsay, S.C., Huang, S.J., 2011. Asian dust weather categorization with satellite and surface observations. Int. J. Remote Sens. 32 (1), 153–170.

Linsley, R.K., Kohler, M.A., Paulhus, J.L.H., 1988. Hydrology for Engineers. McGraw-Hill, New York.

Liu, X., Zhang, Y., Cheng, Y., Hu, M., Han, T., 2012. Aerosol hygroscopicity and its impact on atmospheric visibility and radiative forcing in Guangzhou during the 2006 PRIDE-PRD campaign. Atmos. Environ. 60, 59–67.

Lüthi, Z.L., Škerlak, B., Kim, S.W., Lauer, A., Mues, A., Rupakheti, M., Kang, S., 2015. Atmospheric brown clouds reach the Tibetan Plateau by crossing the Himalayas. Atmos. Chem. Phys. 15 (11), 6007–6021.

Malm, W., 2016. Visibility: The Seeing of near and Distant Landscape Features. Elsevier.

Malm, W.C., Sisler, J.F., Huffman, D., Eldred, R.A., Cahill, T.A., 1994. Spatial and seasonal trends in particle concentration and optical extinction in the United States. J. Geophys. Res.-Atmos. 99 (D1), 1347–1370.

Mann, H.B., 1945. Non-parametric tests against trend. Econometrica 13, 245–259.
Middleton, W.E.K., 2019. Vision through the Atmosphere. University of Toronto Press.
Mishra, S., Mohapatra, M., 2004. Some climatological characteristics of fog over Bhubaneswar airport. Mausam 55 (4), 695–698.
MoF, 2020. Economic Survey 2019/2020. Ministry of Finance, Government of Nepal, Kathmandu, Nepal. https://www.mof.gov.np/uploads/document/file/Economic%20Survey%202019_20201125024153.pdf.
Mohan, M., Payra, S., 2014. Aerosol number concentrations and visibility during dense fog over a subtropical urban site. J. Nanomater. 2014.
Morisset, T., Odoni, A., 2011. Capacity, delay, and schedule reliability at major airports in Europe and the United States. Transp. Res. Rec. 2214 (1), 85–93. https://doi.org/10.3141/2214-11.
Panday, A.K., Praveen, P.S., Adhikary, B., Bhave, P., Banmali Pradhan, B., Dhungel, S., Mehra, M., Mahapatra, P.S., 2016, December. Who is polluting the Himalaya?. In: AGU Fall Meeting Abstracts, 2016 A53E-0344.
Pandithurai, G., Dipu, S., Dani, K.K., Tiwari, S., Bisht, D.S., Devara, P.C.S., Pinker, R.T., 2008. Aerosol radiative forcing during dust events over New Delhi, India. J. Geophys. Res.-Atmos. 113 (D13).
Ram, K., Sarin, M.M., Hegde, P., 2010. Long-term record of aerosol optical properties and chemical composition from a high-altitude site (Manora Peak) in Central Himalaya. Atmos. Chem. Phys. 10 (23), 11791–11803.
Ramachandran, S., Rupakheti, M., 2022. Trends in the types and absorption characteristics of ambient aerosols over the Indo-Gangetic Plain and North China Plain in last two decades. Sci. Total Environ. 831, 154867.
Ramachandran, S., Kedia, S., Sheel, V., 2015. Spatiotemporal characteristics of aerosols in India: Observations and model simulations. Atmos. Environ. 116, 225–244.
Ramanathan, V., Carmichael, G., 2008. Global and regional climate changes due to black carbon. Nat. Geosci. 1 (4), 221–227.
Ramanathan, V., Ramana, M.V., 2005. Persistent, widespread, and strongly absorbing haze over the Himalaya. Pure Appl. Geophys. 162, 1609–1626.
Ramanathan, V., Li, F., Ramana, M.V., Praveen, P.S., Kim, D., Corrigan, C.E., Yoon, S.C., et al., 2007. Atmospheric brown clouds: Hemispherical and regional variations in long-range transport, absorption, and radiative forcing. J. Geophys. Res.-Atmos. 112 (D22).
Randles, C.A., Da Silva, A.M., Buchard, V., Colarco, P.R., Darmenov, A., Govindaraju, R., Smirnov, A., Holben, B., Ferrare, R., Hair, J., Shinozuka, Y., Flynn, C.J., 2017. The MERRA-2 aerosol reanalysis, 1980 onward. Part I: System description and data assimilation evaluation. J. Clim. 30 (17), 6823–6850.
Regmi, R.P., 2014a. Aviation hazards over the Jomsom Airport of Nepal as revealed by numerical simulation of local flows. J. Inst. Sci. Technol. 19 (1), 111–120.
Regmi, R.P., 2014b. Aviation hazards in the sky over Thada as revealed by meso-scale meteorological modeling. J. Inst. Sci. Technol. 19 (2), 65–70.
Regmi, G., Shrestha, S., Maharjan, S., Khadka, A.K., Regmi, R.P., Chandra Kaphle, G., 2020. The Weather Hazards Associated with the US-Bangla Aircraft Accident at the Tribhuvan International Airport, Nepal. Weather Forecast. 35 (5), 1891–1912.
Rienecker, M.M., Suarez, M.J., Gelaro, R., Todling, R., Bacmeister, J., Liu, E., Bosilovich, M.G., Schubert, S.D., Takacs, L., Kim, G., Bloom, S., Chen, J., Collins, D., Conaty, A., da Silva, A., Gu, W., Joiner, J., Koster, R.D., Lucchesi, R., Molod, A., Owens, T., Pawson, S., Pegion, P., Redder, C.R., Reichle, R., Robertson, F.R., Ruddick, A.G., Sienkiewicz, M., Woollen, J., 2011. MERRA: NASA's modern-era retrospective analysis for research and applications. J. Clim. 24 (14), 3624–3648. Retrieved Feb 14, 2023, from. https://journals.ametsoc.org/view/journals/clim/24/14/jcli-d-11-00015.1.xml. Retrieved Feb 14, 2023, from.
Rupakheti, D., Adhikary, B., Praveen, P.S., Rupakheti, M., Kang, S., Mahata, K.S., Naja, M., Zhang, Q., Panday, A.K., Lawrence, M.G., 2017. Pre-monsoon air quality over Lumbini, a world heritage site along the Himalayan foothills. Atmos. Chem. Phys. 17 (18), 11041–11063.
Rupakheti, D., Kang, S., Cong, Z., Rupakheti, M., Tripathee, L., Panday, A.K., Holben, B., 2018a. Study of aerosol optical properties over two sites in the foothills of the Central Himalayas. Int. Archiv. Photogram. Rem. Sens. Spat. Inform. Sci. 42 (3).
Rupakheti, D., Kang, S., Rupakheti, M., Cong, Z., Tripathee, L., Panday, A.K., Holben, B. N., 2018b. Observation of optical properties and sources of aerosols at Buddha's birthplace, Lumbini, Nepal: environmental implications. Environ. Sci. Pollut. Res. 25 (15), 14868–14881.
Saikawa, E., Panday, A., Kang, S., Gautam, R., Zusman, E., Cong, Z., Somnathan, E., Adhikary, B., 2019. Air pollution in the Hindu Kush Himalaya. The Hindu Kush Himalaya Assessment 339–387.
Sarkar, S., Chokngamwong, R., Cervone, G., Singh, R.P., Kafatos, M., 2006. Variability of aerosol optical depth and aerosol forcing over India. Adv. Space Res. 37 (12), 2153–2159. https://doi.org/10.1016/j.asr.2005.09.043.
Schichtel, B.A., Husar, R.B., Falke, S.R., Wilson, W.E., 2001. Haze trends over the United States, 1980–1995. Atmos. Environ. 35 (30), 5205–5210.
Sen, P.K., 1968. Estimates of the regression coefficient based on Kendall's tau. J. Am. Stat. Assoc. 63 (324), 1379–1389.
Sharma, M., Kaskaoutis, D.G., Singh, R.P., Singh, S., 2014. Seasonal variability of atmospheric aerosol parameters over Greater Noida using ground sunphotometer observations. Aerosol Air Qual. Res. 14 (3), 608–622.
Shrestha, A.B., Bajracharya, S.R., Sharma, A.R., Duo, C., Kulkarni, A., 2017. Observed trends and changes in daily temperature and precipitation extremes over the Koshi river basin 1975–2010. Int. J. Climatol. 37 (2), 1066–1083.
Shrestha, S., Moore, G.A., Peel, M.C., 2018. Trends in winter fog events in the Terai region of Nepal. Agric. For. Meteorol. 259 (August 2017), 118–130. https://doi.org/10.1016/j.agrformet.2018.04.018.
Singh, S., Singh, D., 2010, July. Recent fog trends and its impact on wheat productivity in NW plains in India. In: 5th International Conference on Fog, Fog Collection and Dew Münster, Germany, pp. 25–30.
Singh, S., Singh, R., Rao, V.U.M., 2004. Temporal dynamics of dew and fog events and their impact on wheat productivity in semi-arid Region of India. In: The Third International Conference on Fog, Fog Collection and Dew, 11–15 October 2004, South Africa, Temporal Dynamics of Dew and Fog Events and their Impact on Wheat Productivity in Semi-Arid Region of India.
Singh, A., Avis, W.R., Pope, F.D., 2020. Visibility as a proxy for air quality in East Africa. Environ. Res. Lett. 15 (8), 084002.
Smadja, J., Aubriot, O., Puschiasis, O., Duplan, T., Grimaldi, J., Hugonnet, M., Buchheit, P., 2015. Climate change and water resources in the Himalayas. J. Alp. Res. Rev. Géogr. Alp. 0–25 https://doi.org/10.4000/rga.2910.
Srivastava, A.K., Dey, S., Tripathi, S.N., 2012. Aerosol characteristics over the Indo-Gangetic Basin: implications to regional climate. Atmosph. Aerosols-Region. Charact. Chem. Phys. 10, 47782.
Srivastava, S.K., Sharma, A.R., Sachdeva, K., 2016. A ground observation based climatology of winter fog: study over the Indo-Gangetic Plains, India. Int. J. Environ. Ecol. Eng. 10 (7), 742–753.
Syed, F.S., Körnich, H., Tjernström, M., 2012. On the fog variability over South Asia. Clim. Dyn. 39 (12), 2993–3005.
Tang, I.N., 1996. Chemical and size effects of hygroscopic aerosols on light scattering coefficients. J. Geophys. Res.-Atmos. 101 (D14), 19245–19250.
Tare, V., Tripathi, S.N., Chinnam, N., Srivastava, A.K., Dey, S., Manar, M., et al., 2006. Measurements of atmospheric parameters during Indian Space Research Organization Geosphere Biosphere Program Land Campaign II at a typical location in the Ganga Basin: 2. Chemical properties. J. Geophys. Res.-Atmos. 111 (D23) https://doi.org/10.1029/2006JD007279.
Tiwari, S., Payra, S., Mohan, M., Verma, S., Bisht, D.S., 2011. Visibility degradation during foggy period due to anthropogenic urban aerosol at Delhi, India. Atmosph. Pollut. Res. 2 (1), 116–120.
Tripathee, L., Kang, S., Rupakheti, D., Cong, Z., Zhang, Q., Huang, J., 2017. Chemical characteristics of soluble aerosols over the Central Himalayas: insights into spatiotemporal variations and sources. Environ. Sci. Pollut. Res. 24 (31), 24454–24472.
UNEP and DA, 2014. South Asia Environment Outlook 2014. United Nations Environment Programme (UNEP) South Asian Association for Regional Cooperation (SAARC) and Development Alternatives (DA). http://www.sacep.org/pdf/Reports-Technical/2014-South-Asia-Environment-Outlook-2014.pdf.
Van Belle, G., Hughes, J.P., 1984. Nonparametric tests for trend in water quality. Water Resour. Res. 20 (1), 127–136.
Vautard, R., Yiou, P., Van Oldenborgh, G.J., 2009. Decline of fog, mist and haze in Europe over the past 30 years. Nat. Geosci. 2 (2), 115–119.
Wan, X., Kang, S., Li, Q., Rupakheti, D., Zhang, Q., Guo, J., Cong, Z., et al., 2017. Organic molecular tracers in the atmospheric aerosols from Lumbini, Nepal, in the northern Indo-Gangetic Plain: influence of biomass burning. Atmos. Chem. Phys. 17 (14), 8867–8885.
Wang, K., Dickinson, R.E., Liang, S., 2009. Clear sky visibility has decreased over land globally from 1973 to 2007. Science 323 (5920), 1468–1470.
WHO, 2016. Ambient Air Pollution Database, WHO, May 2016. http://www.who.int/phe/health_topics/outdoorair/databases/cities/en/ (Accessed 2. July.17).
WMO, Resolution 40(Cg-XII), 1996. Exchanging Meteorological Data: Guidelines on Relationships in Commercial Meteorological Activities; WMO Policy and Practice. Secretariat of the World Meteorological Organization, Geneva.
World Bank, 2014. Diesel Power Generation.
Yao, W., Gui, K., Wang, Y., Che, H., Zhang, X., 2021. Identifying the dominant local factors of 2000–2019 changes in dust loading over East Asia. Sci. Total Environ. 777, 146064.
Yasmeen, Z., Rasul, G., Zahid, M., 2012. Impact of aerosols on winter fog of Pakistan. Pakistan J. Meteorol. 8 (16).
Yue, S., Wang, C.Y., 2004. The Mann–Kendall test modified by effective sample size to detect trend in serially correlated hydrological series. Water Res. Manage. 18, 201–218.
Zhang, Q.H., Zhang, J.P., Xue, H.W., 2010. The challenge of improving visibility in Beijing. Atmos. Chem. Phys. 10 (16), 7821–7827.
Zhao, P., Zhang, X., Xu, X., Zhao, X., 2011. Long-term visibility trends and characteristics in the region of Beijing, Tianjin, and Hebei, China. Atmos. Res. 101 (3), 711–718.

Supplement of

Four decades of aviation visibility at Bhairahawa airport, gateway to Buddha's birthplace Lumbini, Nepal

Appendix A: Introduction

A.1. IFR and VFR Airport Operations

In the normal visual condition, visibility > 5 km (ICAO, 2005, p.15), also called Visual Meteorological Conditions (VMC), airport authority typically allows the use of Visual Flight Rules (VFR) for airport operations. It offers ideal flight conditions in terms of flight safety, time, cost, comfort, air-traffic flow management, need for navigation and landing aids at the airport, etc. Whenever the visibility gets lower than that specified for VMC, i.e., Instrument Meteorological Condition (IMC) - the flights are not permitted to operate under the VFR rules. Rather, flights can operate up to a certain minimum visibility level under different but more stringent flight rules known as Instrument-Flight rules (IFR). Although IFR operations provide orderly progress of aircraft taking off and landing, typically it reduces the capacity per runway compared to VFR operations. The separation requirement between two air traffics is less relaxed. It demands an extra workload and situational awareness of the pilots and the ATCs. The poor visibility condition resulting from the haze, dust, smoke, mist, or fog may create many problems in aviation, like delay, diversion, or stop in air traffic, resulting in substantial monetary loss to the commercial airlines in lost time, fuel, additional aircraft maintenance, etc. In the worst-case scenario, poor visibility conditions may lead to aircraft incidents or fatal accidents.

While operating under IFR conditions in very low visibility conditions, especially during fog or dense fog events, there are (1) Slow ground movements of air traffics, (2) an increase in runway occupancy time (ROT), and (3) an increase in spacing between landing and taking off aircraft, reducing the airport capacity by ~ 40% (Kulkarni et al., 2019). Moreover, if a Low Visibility Operation (LVO) is in progress at an airport, especially with ILS CAT-II/III, there is a certain area towards the approach end of the runway, called ILS critical area, which shall be protected from any aircraft or vehicular movement to avoid possible interference to the ILS signal. ATC shall ensure that the area is clear of any vehicles, including departing and arriving air traffic. This mandatory requirement causes further delays in departure and arrival. Thus, there is a high likelihood that a scheduled flight may be either held at the origin, diverted back to another airport, or canceled.

Appendix B: Data and Methods

B.1. Classification of weather types

Previous studies have classified weather conditions into several categories based on different thresholds of visibility, RH, and precipitation. There has been some overlap in conditions while transitioning from one condition to another. In our study, we have followed the following classification scheme:

1. **Poor-visibility event** - visibility ≤ 5 km (Hu et al., 2017) and precipitation = 0
2. **Haze** - visibility ≤ 5 km (Vautard et al., 2009), RH ≤ 90% (Wu et al., 2006), and precipitation = 0 (Du et al., 2013)
3. **Mist** -1 km < visibility ≤ 2 km (Vautard et al., 2009; Quan et al., 2011 used visibility ≤ 2 km), RH ≥ 90% (Wu et al., 2006), and precipitation = 0
4. **General-fog** – visibility ≤ 1 km (Vautard et al., 2009; Shrestha et al., 2018; Jenamani et al.,2012), RH ≥ 90% (Wu et al., 2006), and precipitation = 0
5. **Dense-fog** - visibility ≤ 200 m (Shrestha et al., 2018), RH ≥ 90%, and precipitation = 0
6. **Rain** - precipitation > 0
7. **Normal** – Other than all above

B.2. Statistical tests for estimation of a long-term trend

B.2.1. The Mann- Kendall Test

This technique of testing the randomness against the trend in climatic and hydrological time series has been widely used (Kendall, 1975; Mann, 1945; Van Belle and Hughes, 1984; Yue and Wang, 2004). In this method, the null hypothesis (H_0) is that the trend in the studied parameter (visibility or fog parameter) over time does not exist; the alternate hypothesis (H_1) obviously is that there exists a trend (increasing or decreasing) over time. Statistical equations for calculating Mann-Kendall Statistics(S), the variance of MK statistics, and standardized test statistics (Z_{MK}) are (Ahmad et al., 2015; Shrestha et al., 2018):

$$S = \sum_{i=1}^{n-1} \sum_{j=i+1}^{n} sig(X_j - X_i) \quad \text{Eq. (B.1)}$$

$$sig(X_j - X_i) = \begin{cases} +1 \; if(X_j - X_i) > 0 \\ 0 \; if(X_j - X_i) = 0 \\ -1 \; if(X_j - X_i) < 0 \end{cases} \quad \text{Eq. (B.2)}$$

$$V(S) = \frac{1}{18}\left[n(n-1)(2n+5) - \sum_{p=1}^{q} tp\,(t_p - 1)(2t_p + 5)\right] \quad \text{Eq. (B.3)}$$

$$Z_{MK} = \begin{cases} \frac{S-1}{\sqrt{VAR(S)}} & if\ S > 0 \\ 0 \quad if\ S = 0 \\ \frac{S+1}{\sqrt{VAR(S)}} & if\ S < 0 \end{cases} \quad \text{Eq. (B.4)}$$

Where, X_j and X_i are time series observations in chronological order, n is the length of the time series, t_p is the number of ties for the *p*th value and *q* is the number of tied values. Positive, negative, and zero values of *Z* indicate the upward, negative, and no trend in the time series. When, $|Z_{MK}| > Z_{1-\alpha/2}$, or *p-value* less than the level of significance (α); we reject (H_0). Thus, statistically significant trends exist in the time series. The critical value of $Z_{1-\alpha/2}$ at the level of significance (α) 0.05, from the standard normal table is 1.96.

B.2.2. *Sen's Slope estimator*

This technique finds the most common application in finding the linear trend of time-series data in climatological, hydrological, and air pollution studies (Kahya and Kalayci, 2004; Shrestha et al., 2018; Tabari and Marofi 2011;

Van Belle and Hughes, 1984). This non-parametric method is used in our study to estimate the magnitude of trends in poor visibility conditions and different fog parameters. This method is robust to handle single data errors and outliers (Sen, 1968) in which the trend is assumed linear. The equation of the trend line of Sen's slope is given by:

$$f(t) = Qt + B \quad \text{Eq. (B.5)}$$

Where *Q* is the slope and *B* is the intercept.

The slope of the *i*th value pair in the distribution is calculated by using the following equation:

$$Q_i = \frac{x_j - x_k}{j - k} \quad \text{Eq. (B.6)}$$

Where, x_j and x_k represent values of data at time *j* and *k*, respectively in chronological order.

Sen's slope estimator *Q* is obtained by computing of median value of all Q_i such that;

$$Q = \begin{cases} Q_{\frac{N+1}{2}} \ when, \quad N \ is \ odd \\ \frac{1}{2}\left(Q_{(N)/2} + Q_{(N+2)/2}\right) when, \quad N \ is \ even \end{cases} \quad \text{Eq. (B.7)}$$

A positive, negative, and zero value of Q represents increasing, decreasing, and no trend over time (Ahmad et al., 2015).

B.2.3. Ordinary least squares (OLS) regression

This parametric test is one of the most commonly used and powerful statistical methods for estimating trends in time series data (Hess et al., 2001). However, the normality, non-autocorrelation, and homoscedasticity of residuals are some of the basic requirements in this method (H and Hirsch, 1992). OLS tests for the detection of the linear trend by examining the relationship between time *t* and variable of interest *X*.

The statistical model of simple linear regression of *X* on time, used in this technique is given by (Hess et al., 2001):

$$X_i = \beta_0 + \beta_1 t_i + \varepsilon_i \quad \text{Eq. (B.8)}$$

Where X_i is the response for the time t_i, and $1 \leq i \leq n$ with n as the length of the time series. Similarly, β_0, β_1 and ε_i are the intercept, slope, and random error. The errors are assumed independent and identically distributed.

The fitted line represents a predicted value for *X* given a value for t; and it involves minimizing the sum of the square of the difference between the fitted line and the observed data points in the y-direction (Cantrell, 2008). The estimates of slope and intercept of the regression line are given by:

$$\hat{\beta}_1 = \frac{\sum_{i=1}^{n}(t_i - \hat{t})(X_i - \hat{X})}{\sum_{i=1}^{n}(t_i - \hat{t})} \quad \text{Eq. (B.9)}$$

$$\hat{\beta}_0 = \hat{X} - \beta_1 \hat{t} \quad \text{Eq. (B.10)}$$

Where, $\hat{t}$ and $\hat{X}$ are the expected values of the predictor and response variable respectively.

The standard error of the slope is given by:

$$se(\hat{\beta}_1) = \sqrt{\frac{\sum_{i=1}^{n}(X_i - \hat{\beta}_0 - \hat{\beta}_1 t_i)^2}{(n-2)\sum_{i=1}^{n}(t_i - \hat{t})^2}} \quad \text{Eq. (B.11)}$$

A null hypothesis $H_0 : \beta_1 = 0$ is tested using the t-statistic (t_s) with n-2 degree of freedom:

$$t_s = \frac{\hat{\beta}_1}{se(\hat{\beta}_1)} \qquad \text{Eq. (B. 12)}$$

The null hypothesis H_0 is rejected if t_s is greater than the critical value of two-tail t- distribution with α level of significance or the *p-value* is less than the level of significance (α) or if 0 is not contained in the confidence interval ($\hat{\beta}_1 \pm t^*_{[\alpha,n-2]}\, se(\hat{\beta}_1)$). Where, $t^*_{[\alpha,n-2]}$ is the t^* multiplier at α level of significance and $(n-2)$ degree of freedom.

B.3. Microclimatic properties of fog

Onset and dispersal of fog

Because of the limitation of our data, i.e., the coarser time resolution of 3 h and not having nighttime observation, we face difficulty determining, mostly, the exact timing of fog onsets in the previous nighttime and the actual dispersal time also. Thus, we have made some assumptions: instead of considering that an onset/ dispersal takes place in a fixed timestamp, we consider it to occur within time intervals of 3 h, matching with our data time resolution.

The onset timing of a fog event is determined in such a way that if a fog event is reported in observation, the onset of that fog could have happened any time before the observation time, not overlapping the previous onset. If a fog event of the same intensity were recorded in consecutive recordings, the onset of the fog is always in the first instance when the fog onset was recorded, no matter how long the fog lasts.

For instance, if a fog event is observed on the first observation of the day, 05:45 local time (00:00 UTC), the onset of the fog might have been any time of the previous night, earlier than 05:45 local time. Likewise, for the onset timings of a fog event observed at 08:45 local time (03:00 UTC), we have assumed it was any time between 05:46 to 08:45 local time.

Similarly, the dispersal of a fog event is determined in such a way that if a fog event of a given intensity were recorded in an earlier measurement, but not in the next; then the dispersal of the fog could have occurred any time in between these two consecutive measurements. For example, if we observe a fog event in the first observation of the day, 05:45 local time (00:00 UTC), but not in the next observation at 08:45 local time (03:00 UTC), the fog might have dispersed anytime within the time interval 05:46-08:44 local time (00:01-02:59 UTC). Other dispersal intervals follow the same argument; except for the last dispersal time of the day, >17:46 local time (> 12:01 UTC), which assumes that the dispersal could have occurred anytime in the early evening until the next morning.

Firstly, the onset and dispersal time of fog of different intensities were determined, then the occurrence frequency (in percentage), which is the total number of fog onset/dispersal during the interval out of the total number of onsets/ dispersals in the whole data period.

The most favorable time interval of onset/dispersals of fog is a time interval when the highest number of onset/dispersals occurs in comparison to other intervals. In a likely manner, the favorable period of onset/ dispersals of fog is the period during which the cumulative percentage of onset/ dispersals is more than 90%.

B.4. Relationship between the aerosol optical depth (AOD) and visibility

Although the two measurement sites, BWA and Lumbini, are not collocated (about 14 km apart), it is assumed, here, that the aerosol composition and their optical properties remain the same between these two neighboring locations. To determine optical properties, like scattering and transmission of the atmosphere, the sunphotometer makes automatic measurements of direct-sun irradiance and sky radiance in eight spectral channels (340, 380, 440, 500, 675, 870, 940, and 1020 nm) (Holben et al., 1998).

We have calculated the Ångström exponent (AE) (α) between 340 and 1020 nm based on the formula (Kumar et al., 2020; Liu et al., 2011):

$$AE = -\frac{\log(AOD_{340}/AOD_{1020})}{\log(340/1020)}$$ Eq. (B.13)

Finally, we have converted AERONET AOD at 500 nm to AOD at 550 nm using the spectral data as follows (Nabat et al., 2013):

$$AOD_{550} = AOD_{500}\left(\frac{550}{500}\right)^{-\alpha}$$ Eq. (B.24)

Table S1
Details of selected stations

NOAA Site ID.	Station Name	Location identifier	Country	Lat. (N)	Lon. (E)	Elev. (m)	Data availability
444380	Bhairahawa	BWA	Nepal	27° 30' 21.6"	83° 24' 57.5994"	109.1	1977-2020
444540	Kathmandu	KTM	Nepal	27° 41' 49.1994"	85° 21' 32.3994"	1338.1	1973-2020
423790	Gorakhpur	GOP	India	26° 44' 22.9488"	83° 26' 58.9488"	78.94	1944-2020
423690	Lucknow	LKN	India	26° 45' 38.1384"	80° 53' 21.6204"	124.96	1944-2020
421810	Delhi	DEL	India	28° 33' 59.4"	77° 6' 11.1162"	236.82	1996-2020
-	Lumbini AERONET	-	Nepal	27° 29' 24"	83° 16' 48"	110.0	2012-2018

NOAA station ID is the United States Air force (USAF) catalog station number, unique to each station. Lat., Lon., Elev., m, N, and E denote latitude, longitude, elevation, meters, North, and East respectively. All of our stations are airports. Location identifiers are the three-letter geocode, designating many airports around the world defined by the International Air Transport Association (IATA).

Appendix C: Results and Discussion

C.1. Type of Approaches for aircraft landings (VOR, RNP, ILS, etc.)

The minimum visibility level, above which normal operation of the airport is possible, is airport and aircraft type-specific; determined by regulations set by international and local governing authorities based on various factors, like available navigational facilities at the airport/ aircraft, terrain, training requirement of pilots and Air Traffic Controllers (ATC), etc. Thus, different landing facilities offer different take-off and landing minima for an airport. VHF Omnidirectional Radio Range collated with Distance Measuring Equipment (VOR-DME or simply VOR), and Instrument Landing System (ILS) is one of the most common radio navigation and landing aid ground installations worldwide to aid take-off and landing in marginal visibility conditions. In between the two, ILS offers much lower IFR minima, i.e. aircraft can take off and land in a much lower visibility threshold. According to the International Civil Aviation Organization (ICAO), ILS has been classified into different categories based on its capability to permit landings under given visibility conditions as presented in Table.T3 (K, 2017, p. App- C3). There is not even a single airport in Nepal with an operational ILS, let alone the country's only international airport, Tribhuvan international airport (TIA) at Kathmandu (KTM).

Although TIA does not have sophisticated landing aids like ILS, which would otherwise help airport operation in much lower visibility conditions, another precise satellite-based navigation and approach system, suiting local topography, known as Required Navigation Performance-Authorization Required (RNP-AR), is in effect there since 2012, together with a VOR. It offers lower minima (1100 m) than the VOR (2800 m); but there are some difficulties with its operational use, e.g., lengthy approval process, additional training requirements for the operating crew, requirement of the onboard instruments, etc. Thus, not all aircraft and crew are qualified to conduct an RNP-AR approach in Kathmandu. Thus, VOR is yet the basic mode of aid for take-off and landing in Kathmandu in IFR weather conditions.

After the recent up-gradation to the international operation in May 2022, VOR-DME and RNP approach only are available at BWA, for which the minimum visibility requirement for aircraft landings at BWA are 1600m and 1900m (or even higher depending on the Runway) respectively. However, before the upgradation, VOR was the only mode of landing aid.

C.2. Hourly frequency of airport operation at BWA during winter

In this study, although hours of operation of BWA airport differ slightly during the winter (16 Feb - 15 Nov) from the rest of the year (CAAN, 2018, p. AD 2-1); we have considered airport operation hours of 06:00-18:00 local time (00:15-12:15 UTC), throughout the year for the sake of analytical ease. When the visibility reduces below 1600m, the airport remains closed for operation. Towards a better understanding of how many hours in a year, the flight operation at BWA is affected by low visibility, the hourly frequency of airport-operation-type was computed, which is the percentage of hours of the particular type of airport operation in winter (VFR, IFR or CLOSED), out of total hours of operation in the winter.

C.3. Can BWA and KTM airports serve as landing alternate airports for each other?

In order to find the instances when both TIA and BWA airports cannot serve as alternate airports to each other, we have chosen VOR approaches in both airports. This is because the majority of aircraft and crew are capable of performing VOR approaches. When the visibility at TIA reduces below 2800 m (KTM VOR minima), an aircraft bound for TIA cannot make a diversion to BWA unless visibility at the latter is more than 1600 m (BWA VOR minima) and vice-versa. Unlike three-hourly observations at BWA, TIA publishes a Meteorological Terminal Air Report (METAR) every half an hour. In order to figure out the number of hours for which aircraft bound for one airport (say, TIA) cannot proceed to another (say, BWA), in case of weather at the former deteriorates below landing minima, an assumption is made:

- If visibility at a given time in TIA is less than 2800 m and that in BWA (at the nearest observation made within 1.5 hours of the given time) is less than 1600 m; a diversion from one airport to another is not possible. For instance, if visibility in TIA at, say, 02:20 UTC (or, 03:50 UTC) is, say, 2500 m (or, 2700 m) and visibility at BWA at 03:00 UTC (the nearest timestamp at BWA within 1.5 hours interval of 02:20 UTC and 03:50 UTC) is 1200 m only, diversion is not possible.

From Fig. S3, we see that during the winter months there is very little chance that BWA serves as a suitable alternate airport to Kathmandu, if visibility in one goes below the minimum, under the existing landing guidance system VOR at both places. The chance is higher during autumn. For the rest of the seasons, visibility is usually not an issue for the diversion.

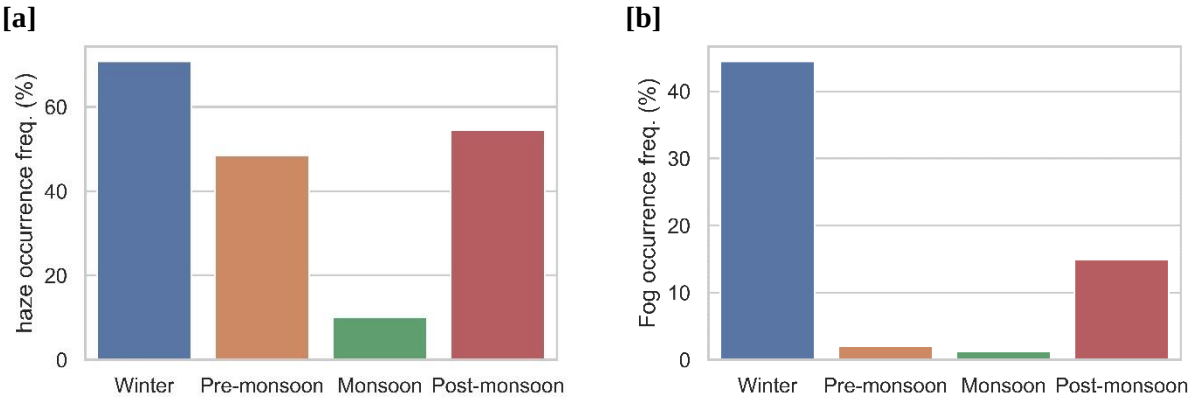

Fig. S1 Occurrence frequency of: (a) haze and (b) fog at Bhairahawa (BWA) airport in different seasons during the period (1978–2020).

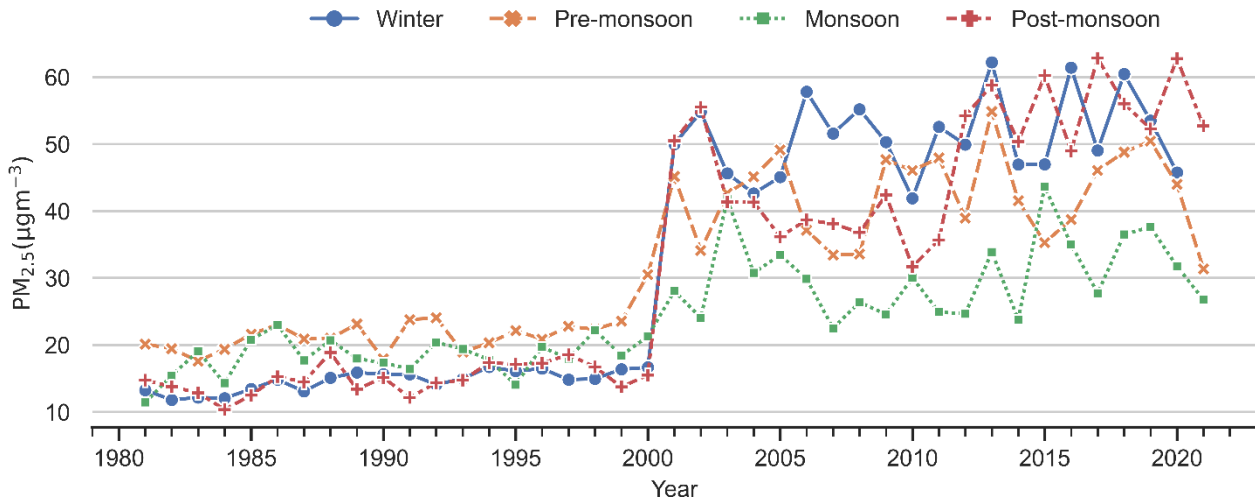

Fig. S2 Interannual Time Series of Average Total Surface Mass Concentration – PM2.5 monthly 0.5 × 0.625 deg. [MEERA-2 Model M2TMNXAER v5.12.4] $\mu g\ m^{-3}$ for 1980-Jan – 2020-Feb, Region 82.2405E, 26.516N, 84.9651E, 28.0541N. (*Data source* MEERA-2 Model using NASA's online Giovanni tool (https://giovanni.gsfc.nasa.gov/giovanni/))

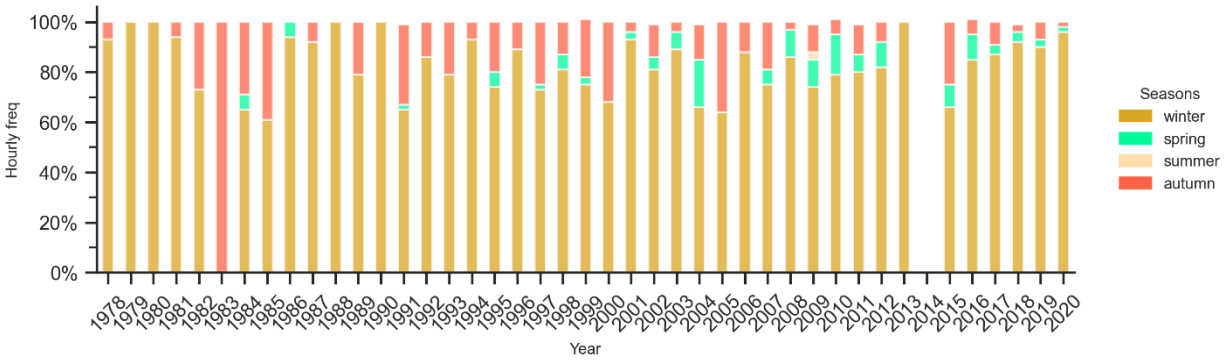

Fig. S3 Yearly frequency of hours (%) during which Bhairahawa airport (BWA) and Tribhuvan International Airport (TIA) cannot serve as a diversion alternate to each other, under presently available landing facility (VOR-DME), during the period (1978–2020) owing to airport visibility conditions in different seasons. When visibility conditions in BWA and TIA are less than 1600 m and 2800 m respectively flights are not permitted to land under the existing navigation and landing guidance system (VOR) installation at these airports.

Table S2
Results of Mann-Kendall, Sen's slope estimator, and OLS regression test of annual occurrence frequency (%) of different weather types for the period of 1981 – 2020 at Bhairahawa airport. The trend represents the slope of the linear fit between the variable of interest and year. The boldface values indicate that the slope is statistically significant at a defined level of significance (α).

		Mann – Kendall		**Sen's slope**		**OLS regression**			
		Z_{MK}	p –value	Trend Q ($\%yr^{-1}$)	**[CI]** %	Trend $\hat{\beta}_1$ ($\%yr^{-1}$)	[**95% CI**] %	t_s	p -value $>\|t\|$
Weather -type	Haze	4.41*	1.0×10^{-5}	**0.57***	[0.213, 0.926]	**0.57*** ± 0.095	[0.374, 0.759]	5.97	0.000
	Mist	3.13†	1.7×10^{-3}	**0.08**†	[0.031, 0.138]	**0.08** † ± 0.024	[0.033, 0.131]	3.41	0.002
	Fog	4.60*	4.18×10^{-6}	**0.22***	[0.064, 0.354]	**0.20*** ± 0.034	[0.127, 0.263]	5.80	0.000
	Rain	3.76*	1.7×10^{-4}	**0.18***	[0.027, 0.322]	**0.16*** ± 0.038	[0.082, 0.234]	4.20	0.000
	Normal	-5.34*	8.9×10^{-8}	**-0.94***	[-1.351, -0.462]	**-0.90*** ± 0.110	[-1.118, -0.673]	-8.15	0.000

* 0.001, † 0.05, ** 0.1 - level of significance; *ns* non-significant

Table S3
Results of the Mann-Kendall test and Sen's slope estimator for Occurrence frequency (%) of: (**a)** poor-visibility events, and **(b)** fog days, in **the** winter season (**DJF**) at Bhairahawa (**BWA**), Gorakhpur (**GOP**), Lucknow (**LKN**) and Delhi (**DEL**) airports. The trend represents the slope of the linear fit between the variable of interest and the year. The boldface values in the trend indicate that the slope is statistically significant at a defined level of significance(α).

			Mann - Kendall		**Sen's slope**	
	Site	**Data period**	Z_{MK}	p -value	Trend Q ($\%yr^{-1}$)	**[CI]**(%)
a) Occurrence frequency of poor visibility events (%)	**BWA**	1977-2020	5.98*	2.27×10^{-9}	**1.02***	[0.523, 1.506]
	GOP	1977-2020	3.72	1.97×10^{-4}	**0.01**	[0.000, 0.020]
	LKN	1977-2020	-0.58	0.563	0.00	[-0.061, 0.010]
	DEL	1996-2020	2.85**	4.34×10^{-3}	**0.06****	[0.005, 0.210]
b) Occurrence frequency of fog - days (%)	**BWA**	1977-2020	5.44*	5.28×10^{-8}	**1.19***	[0.573, 1.723]
	GOP	1977-2020	3.07	2.17×10^{-3}	**0.62**	[0.261, 0.979]
	LKN	1977-2020	5.20	1.99×10^{-7}	**0.93**	[0.630, 1.212]
	DEL	1996-2020	3.32*	8.95×10^{-4}	**1.29****	[0.000, 2.798]

* 0.001 level of significance, ** 0.01 level of significance

Table S4
ILS categories and corresponding runway visual range (RVR) as per ICAO standards. RVR is the range over which the pilot of an aircraft on the centerline of a runway can see the runway surface markings of the lights delineating the runway or identifying its centerline (ICAO, 2017, p. Glossary).

ILS categories (CATs)	ICAO Runway visual range (RVR) (m)
CAT I	> 550
CAT II	550 - 300
CAT IIIA	300 - 175
CAT IIIB	175 - 50
CAT IIIC	< 50

Table S5
Monthly average values of meteorological parameters, namely, visibility, temperature, relative humidity, and wind speed at Bhairahawa airport from 2013 to 2018. The bold faced values are the highest and lowest monthly averages

Met parameter	Jan	Feb	Mar	Apr	May	Jun	Jul	Aug	Sep	Oct	Nov	Dec
Visibility (km)	**1.89 ± 0.16**	2.75 ± 0.15	4.50 ± 0.18	5.26 ± 0.14	6.10 ± 0.14	6.26 ± 0.13	**7.34 ± 0.21**	6.88 ± 0.19	6.35 ± 0.21	4.80 ± 0.21	3.29 ± 0.16	2.11 ± 0.13
Temperature (°C)	**14.68 ± 0.37**	20.24 ± 0.44	25.38 ± 0.46	30.22 ± 0.48	31.78 ± 0.35	**31.86 ± 0.31**	30.46 ± 0.27	30.63 ± 0.27	30.29 ± 0.27	27.88 ± 0.37	23.37 ± 0.43	17.78 ± 0.38
Relative Humidity (%)	**82.72 ± 1.28**	71.02 ± 1.49	57.54 ± 1.62	**47.08 ± 1.67**	56.06 ± 1.35	68.34 ± 1.24	78.59 ± 0.98	79.57 ± 0.97	78.07 ± 0.98	74.06 ± 1.36	67.80 ± 1.68	77.28 ± 1.44
Wind Speed (m/s)	2.33 ± 0.20	2.43 ± 0.11	3.51 ± 0.24	**4.77 ± 0.27**	4.20 ± 0.22	3.43 ± 0.23	3.75 ± 0.30	3.05 ± 0.13	3.09 ± 0.19	2.56 ± 0.36	**1.97 ± 0.11**	2.20 ± 0.17

References

Ahmad, I., Tang, D., Wang, T., Wang, M., & Wagan, B. (2015). Precipitation trends over time using Mann-Kendall and spearman's rho tests in swat river basin, Pakistan. *Advances in Meteorology*, *2015*.

Cantrell, C. A. (2008). Review of methods for linear least-squares fitting of data and application to atmospheric chemistry problems. *Atmospheric Chemistry and Physics*, *8*(17), 5477-5487.

Helsel, D. R., & Hirsch, R. M. (1992). *Statistical methods in water resources* (Vol. 49). Elsevier.

Hess, A., Iyer, H., & Malm, W. (2001). Linear trend analysis: a comparison of methods. *Atmospheric Environment*, *35*(30), 5211-5222.

Holben, B. N., Eck, T. F., Slutsker, I. A., Tanre, D., Buis, J. P., Setzer, A., Vermote, E., Jankowiak, I., & Smirnov, A. (1998). AERONET—A federated instrument network and data archive for aerosol characterization. *Remote sensing of environment*, *66*(1), 1-16.

ICAO. (2005). Annex 2 (Rules of the air), Tenth Edition (July 2005). International Civil Aviation Organization

ICAO. (2017). Doc 9365 (Manual of All-weather Operations). International Civil Aviation Organization. http://amc.namem.gov.mn/juram/icao/20.pdf

Kahya, E., & Kalaycı, S. (2004). Trend analysis of streamflow in Turkey. *Journal of Hydrology*, *289*(1-4), 128-144.

Kumar, V., Beirle, S., Dörner, S., Mishra, A. K., Donner, S., Wang, Y., Sinha, V., Wagner, T. (2020). Long-term MAX-DOAS measurements of NO 2, HCHO, and aerosols and evaluation of corresponding satellite data products over Mohali in the Indo-Gangetic Plain. *Atmospheric Chemistry and Physics*, *20*(22), 14183-14235.

Nabat, P., Somot, S., Mallet, M., Chiapello, I., Morcrette, J. J., Solmon, F., Szopa, S., Dulae, F., Collins, W., Ghan, S., Horowitz, L.W., Lamarque, J.F., Lee, Y.H., Naik, V., Nagashima, T., Shindell, D., Skeie, R. (2013). A 4-D climatology (1979–2009) of the monthly tropospheric aerosol optical depth distribution over the Mediterranean region from a comparative evaluation and blending of remote sensing and model products. *Atmospheric Measurement Techniques*, *6*(5), 1287-1314.

Quan, J., Zhang, Q., He, H., Liu, J., Huang, M., & Jin, H. (2011). Analysis of the formation of fog and haze in North China Plain (NCP). Atmospheric Chemistry and Physics, 11(15), 8205-8214.

Tabari H, Marofi S (2011) Changes of pan evaporation in the west of Iran. Water Resour Manag 25(1):97–111

Wu, D. (2006). More discussions on the differences between haze and fog in city. *Guangdong Meteorology*, *32*, 9-15.

Journal of Institute of Science and Technology, 29(1), 35-45 (2024)
ISSN: 2467-9062 (print), e-ISSN: 2467-9240
https://doi.org/10.3126/jist.v29i1.56933

Research Article

INTENSIFYING HAZE AND DISAPPEARING DENSE FOG IN WINTER AT TRIBHUVAN INTERNATIONAL AIRPORT, KATHMANDU: IMPACTS IN AVIATION

Bhogendra Kathayat[1,2*], Arnico Kumar Panday[3], Binod Pokharel[4, 5], Narayan Prasad Chapagain[6]

[1]Central Department of Physics, Institute of Science and Technology, Tribhuvan University, Kathmandu, Nepal
[2]Nepal Airlines Corporation, Kathmandu, Nepal
[3] National Planning Commission, Government of Nepal
[4]Central Department of Hydrology and Meteorology, Institute of Science and Technology, Tribhuvan University, Kathmandu, Nepal
[5]Department of Plants, Soils, and Climate, Utah State University, Logan, UT, USA
[6]Department of Physics, Amrit Campus, Tribhuvan University, Kathmandu, Nepal
**Correspondence: bhogendra.735711@cdp.tu.edu.np*

(***Received**: July 25, 2023; **Final Revision**: February 29, 2024; **Accepted**: April 13, 2024)*

ABSTRACT
In winter, Tribhuvan International Airport (TIA) in Kathmandu, Nepal, is badly affected by poor visibility conditions due to the occurrence of thick haze and dense fog. In this study, we examined the microclimatic behaviors (e.g., consecutive duration and onset/dispersal) of the winter fog. Alongside, we analyzed the trend in the occurrence of fog, dense fog, and winter haze in TIA from a historic global hourly climatological dataset (1976–2022) from TIA. We found that radiation fog in the valley is mostly short spells having a consecutive duration of less than an hour (~86% of fog, ~95% of dense fog). The onset of fog starts most favorably in the early morning (05:45–09:00 am) and disperses mostly before noon. To ascertain the synergetic effect of enhanced natural and anthropogenic forcing, urbanization, and meteorological changes on winter haze and fog, we assessed their trend for the same period. There was a marked change in visibility around the year 2000 together with important changes in humidity and dew point depression. We observed an upward trend of winter haze frequency (2.36% day/year, at 0.001 level of significance (a)) and fog frequency (0.46% day/year, at $a = 0.05$) in regime-I (1976–2000). Whereas the trend of winter haze flattened to 0.36% day/year (at $a = 0.05$) and dense fog declined at the rate of −1.28% day per annum (at $a = 0.01$) in regime-II (2001–2022). By careful examination of all plausible climatological drivers of the change (relative humidity, temperature, wind speed, and dew point depression), we found strong evidence of decreasing humidity and increasing dew point depression after the year 2000. Effective air pollution and urbanization control measures are imminent to lessen the adverse impact of the increased frequency of haze and fog at the country's major international airport, TIA.

Keywords: Aviation, fog, haze, Kathmandu, visibility

INTRODUCTION
Haze and fog over an airport reduce visibility, making it difficult for pilots to land an aircraft visually (Hanesiak & Wang, 2005). Resulted from the suspension of aerosols in the atmosphere, haze reduces visibility to lower than 5 km under a relatively dry atmosphere (Du *et al.*, 2013; Kathayat *et al.*, 2023; Vautard *et al.*, 2009; Wu, 2006). Whereas, fog and dense fog—obscurity caused by the suspension of water droplets near the surface layer of the atmosphere—reduces visibility to lower than 1 km and 200 m respectively (Jenamani, 2007; Kathayat *et al.*, 2023; Vautard *et al.*, 2009; Wu, 2006). Such low visibility events at the airport affect the safety, timeliness, and efficiency of flight operations as well as add extra financial burden (Gultepe *et al.*, 2007; Jenamani & Kumar, 2013; Kulkarni *et al.*, 2019; Morisset & Odoni, 2011). Like elsewhere (Jenamani & Kumar, 2013), low visibility contributed many aviation accidents and incidents in Nepal (Kathayat *et al.*, 2023; Regmi *et al.*, 2020). Typical evidence of such occurrence in Nepal is a runway excursion after the landing of Turkish Airlines wide-body aircraft (TC-JOC, Airbus-A330) at Tribhuvan International Airport (TIA) in Kathmandu (KTM) under very dense-fog conditions over the airport (AIC, 2015).

Atmospheric constituents (gaseous molecules, aerosols, and water vapor) attenuate incoming solar radiation by scattering and absorption, leading to visibility reduction (Y. Chen & Xie, 2013; Malm, 1999; Vautard *et al.*, 2009; Zhang *et al.*, 2010) in the form of haze. Many past studies have reported a decline in visibility in global (e.g., Wang *et al.*, 2009) and regional scale (Y. Chen & Xie, 2013; Fu *et al.*, 2016; Jaswal *et al.*, 2013; A. Singh & Dey, 2012). On the contrary, there has been an improvement in visibility in regions like Europe, the USA, and Canada (Inhaber, 1976; Munn, 1973; Stjern *et al.*, 2011; Streets *et al.*, 2006; Vautard *et al.*, 2009).

The occurrence of fog—a complex and interesting boundary layer phenomenon—depends on several factors, such as meteorology, air pollution, land use, terrain, and topography (Gultepe *et al.*, 2007; Hunova *et al.*, 2020, 2021; Kim *et al.*, 2019; Safai *et al.*, 2019). Because of the high damage potential of fog to general

aviation, developing an intensity and duration-based fog microclimatic information system using long-term data is highly advantageous benefiting forecasters, air traffic controllers (ATC), airlines, and pilots (Jenamani, 2012). Various researchers studied various aspects of fog occurrences in different places in India (Bhushan *et al.*, 2003; Jenamani, 2007; J. Singh *et al.*, 2007; Srivastava *et al.*, 2016) and elsewhere (Hameed *et al.*, 2000; Hunova *et al.*, 2020; Liu *et al.*, 2012; Vautard *et al.*, 2009). Because of the severity of the fog problem, most of the fog studies in our region focus on the occurrence of fog in cities and airports of Indo Gangetic Plains (IGP)—a region stretching more than 2000 km across northern South Asia including eastern Pakistan, northern and eastern India, southern Nepal and large parts of Bangladesh. The region has experienced a notable increase in fog events over the years (Saikawa *et al.*, 2019; Srivastava *et al.*, 2016; Syed *et al.*, 2012). Through the analysis of climatological data at Indira Gandhi International Airport (IGI) in New Delhi, India, Jenamani (2007) reported an alarming rise and persistence of fog at the airport. Another comprehensive study conducted by Ghude *et al.* (2017) at the same airport also supported it by finding that dense fog hours doubled over the last three decades.

Nevertheless, our country lacks dedicated studies of haze and fog despite their significance in various sectors; most of these studies are localized within the IGP section of Nepal (Kathayat *et al.*, 2023; Manandhar, 2006; Shrestha *et al.*, 2018, 2023). Analyzing multi-decadal meteorological data, we (Kathayat *et al.*, 2023) also found almost a doubling of winter fog days and a substantial uptrend in other fog parameters at Gautam Buddha International Airport (GBIA) at BWA—an airport located in the IGP section of Nepal. In this paper, we also highlighted the impact of low visibility (caused by haze and fog) on aviation. In KTM, a handful of studies have occurred regarding haze and fog occurrence (e.g., Larssen *et al.*, 1997; Nakajima *et al.*, 1980; B. Sapkota, 2002; B. K. Sapkota, 1996; Sharma, 1997). Using photographs and meteorological data, Nakajima *et al.* (1980) investigated the mechanism of fog formation in KTM. On the onset and dispersal timing of winter fog over the valley, Sharma (1997) reported that fog covering the valley basin usually restricts visibility until 10 or 11 am. Larssen *et al.* (1997) reported increased fog and the largest decline in visibility in winter. A study by Sapkota (2002) reported declining visibility (1.58 km year^{-1}) using three years of data (1996, 1998, and 1999). Most of the papers are quite old; various factors affecting haze and fog including undeniable increase in regional air pollution level and possibly some meteorological changes could have happened ever since. To cater for this research gap, this paper uses a multi-decadal dataset to investigate the long-term trend of haze and fog in winter at TIA. We also aim to shed light on the microclimatic behavior of fog and its implication on flight operations.

MATERIALS AND METHODS

In this study, we used meteorological data (Jan 1976–Feb 2023) obtained from the National Climatic Data Center (NCDC) of the National Oceanic and Atmospheric Administration (NOAA) for Tribhuvan International Airport in Kathmandu (NOAA station ID: 444540, 27° 41' 49.1994" N, 85° 21' 32.3994", elevation: 1338.1 m). Our data includes 3-hourly synoptic records until 1996, one-hourly until 2015, and half-hourly onwards Meteorological Weather Report (METAR) records—used especially for aviation use. Such historic and long-term global hourly data are archived and publicly distributed (https://www.ncei.noaa.gov/maps/hourly). Each of them includes the measurement of surface air temperature, dew point temperature, visibility, wind speed, wind direction, and present weather among many other meteorological parameters. The present weather code gives observed weather phenomena like rain, fog, hail, thunder, etc. during the time of measurement. The station reports fog according to the definition of WMO (WMO, 1992). Although records in the years 2013 and 2014 were completely missing from this dataset, more than 45 years of data were used in this study. This dataset does not include a direct measurement of relative humidity (RH), thus, we computed one using the following equation (Chang *et al.*, 2009; J. Chen *et al.*, 2012).

$$RH \approx 100\left(\frac{112 - 0.1T + T_d}{112 + 0.9\,T}\right)^8 \quad (1)$$

Where T & T_d denote air temperature and dew point temperature respectively.

Similar to previous studies (Du *et al.*, 2013; Kathayat *et al.*, 2023; Vautard *et al.*, 2009; Wu, 2006), we classified weather types based on a threshold of observed visibility, RH, and precipitation. This study considers only haze and fog among different weather types. They have been defined according to the following classification scheme:

1. Haze: precipitation = 0 , visibility ≤ 5 km & RH ≤ 90%
2. Fog: precipitation = 0, visibility ≤ 1 km & RH ≥ 90%
3. Dense-fog: precipitation = 0, visibility ≤ 200 m & RH ≥ 90%

Microclimatic properties of fog: consecutive duration, onset, and dispersal

To gain a better insight into fog occurrence timing and its duration in winter at TIA, this paper examines two important microclimatic properties, namely consecutive duration and onset/ dispersal of fog episodes. Because of the coarse and uneven time resolution of our dataset, we assumed that if a fog event were detected in a record, it would have persisted from half of the period (time resolution) before and after the timestamp of observation. For example, if the fog were observed in a half-hourly observation, it would have persisted from 15 minutes before to 15 minutes after the observation time. Consecutive duration of fog is the cumulative period

when a fog event of a given intensity continuously occurs. According to our previous assumption, an isolated fog observation could last for a period equal to or less than the time resolution of data during that period. On that basis, if we observe another same-intensity fog, then consecutive duration is the cumulative duration lasting less than double the time resolution, and so on. Its occurrence frequency (percentage) is the percentage of the total number of days with a given consecutive duration to a total of all fog days.

A fog observed in a record could have started any time before. When the same intensity fog is observed in the next record, the onset of the fog should be the first instance when it was recorded. Similarly, if a fog event were recorded earlier but not in the successive measurement, it could have dispersed anytime in between. Their occurrence frequency is the ratio of the number of fog onset/dispersal during the period to total onset/dispersal in the whole of the study period.

Long-term change in haze and fog

In this study, we have defined a day as having haze/fog/dense fog, if at least one record of the day fulfills the respective criteria as mentioned above. Since our data is not uniform across our study period, in terms of time resolution and annual measurement frequency, we opted to use percentage occurrence frequency rather than number frequency similar to the work of Hu *et al.* (2017) and Kathayat *et al.* (2023). Where occurrence frequency (percentage) of haze/fog/dense fog in a year is the number of days with respective weather types to the total number of days of available data in the winter season (DJF) of that year. To detect and quantify the long-term trend in the occurrence of the weather type in the subject, we used Mann-Kendell Test (MK Test) and Sen's Slope Estimator (Sen's Slope) similar to many previous studies (e.g., Kathayat *et al.*, 2023; Shrestha *et al.*, 2018; Yue & Wang, 2004). These two non-parametric tests are particularly preferred statistical tools to detect the trend in climatic and hydrological time series when the data is inhomogeneous and/or bears some errors and outliers (Sen, 1968) as our data does. In the Mann-Kendall test, the null hypothesis (H_0) is that there is no trend in the subjected parameter over the considered period. Following are the governing equations of the Mann-Kendall test.

Mann-Kendall Statistics (S):

$$S = \sum_{i=1}^{n-1} \sum_{j=i+1}^{n} sig(X_j - X_i) \tag{2}$$

$$sig(X_j - X_i) = \begin{cases} +1 \; if(X_j - X_i) > 0 \\ 0 \; if(X_j - X_i) = 0 \\ -1 \; if(X_j - X_i) < 0 \end{cases} \tag{3}$$

The variance of MK statistics:

$$V(S) = \frac{1}{18}\left[n(n-1)(2n+5) - \sum_{p=1}^{q} tp\,(t_p - 1)(2t_p + 5)\right] \tag{4}$$

Standardized test statistics (Z_{MK}):

$$Z_{MK} = \begin{cases} \dfrac{S-1}{\sqrt{VAR(S)}} & if\ S > 0 \\ 0 \quad if\ S = 0 \\ \dfrac{S+1}{\sqrt{VAR(S)}} & if\ S < 0 \end{cases} \tag{5}$$

Where n is the length of the considered time series, X_j and X_i are time series observations (in chronological order), t_p is the number of ties for the p_{th} value and q is the number of tied values. Zero, positive, and negative values of Z respectively indicate none, upward, negative trend. We reject H_0 when $p < a$ (the significance level) or, $|Z_{MK}| > Z_{1-\alpha/2}$ indicating statistically significant trend value. From the standard normal table, the critical value, $Z_{1-\alpha/2}$, at $a = 0.05$ is 1.96.

Similarly, the trend line equation of Sen's slope (Sen, 1968) is given by

$$f(t) = Qt + B \tag{6}$$

Here, Q is the slope and B represents the intercept.

In a time series, the slope of the ith value pair x_j and x_k observed at time j and k, respectively (in chronological order) is

$$Q_i = \frac{x_j - x_k}{j - k} \tag{7}$$

The median value of all such Q_i gives the Sen's slope estimator Q such that:

$$Q = \begin{cases} Q_{\frac{N+1}{2}} & when, \quad N\ is\ odd \\ \dfrac{1}{2}\left(Q_{(N)/2} + Q_{(N+2)/2}\right) when, & N\ is\ even \end{cases} \tag{8}$$

It may take zero, negative, or positive values representing none, positive and negative trends, respectively.

RESULTS AND DISCUSSION

Microclimatic properties of fog: Consecutive duration, onset, and dispersal

Figure 1 shows the occurrence frequency of fog (dense-fog) days having witnessed fog of a certain duration at a stretch and intensity. We observed that most of the fog (~86% of fog days) and dense fog (~95% of dense fog days) at TIA lasted a very brief period (< 1 hour). Only ~6% (~3%) of fog (dense-fog) days witness fog lasting up to two hours. ~4% (~1%) of fog (dense fog) lasted for up to 3 hours. Although there were some days having fog continuously occurring for up to 6 hours, these were very rare for dense fog.

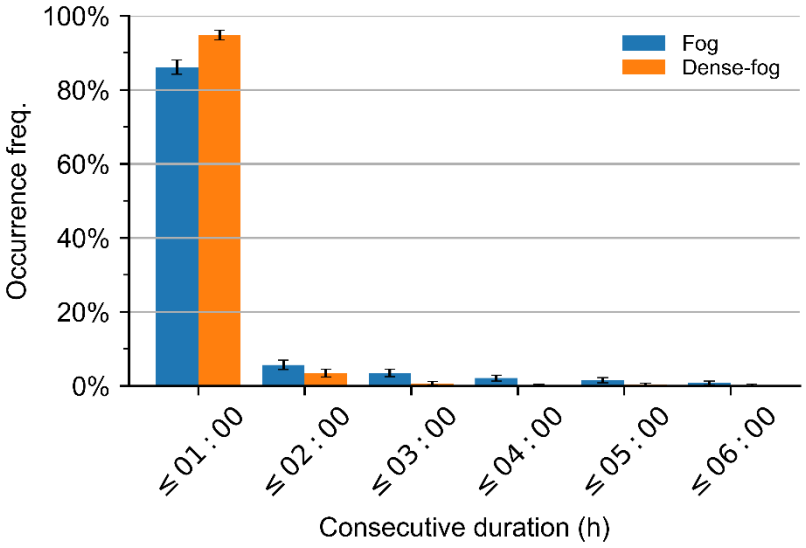

Figure 1. Consecutive duration of fog and dense fog in winter (DJF) at Tribhuvan international airport, Kathmandu from 1976 through 2023. The error bars represent a 95% confidence interval of a single proportion

Winter fog onset and dispersal timing are shown in Figure 2. In December, fog usually starts to form as early as 04:45 am local time (LT) until 09:45 am in and around TIA. A very small percentage of fog occurrences were even recorded at 11:00 pm too. The most favorable time was 05:15 am when about 23% of all fog onsets occurred. Whereas fog onset takes place between 03:15 am to 09:45 in January with the most favorable onset time being 06:45 am when more than 16% of all onsets happen.

The fog onset window is narrow in February; it occurs between 04:45 am and 09:15 am, with the highest onset at 06:45 am. Regarding dispersion of fog, it occurs during 05:45–10:45 LT in Dec, 04:45–12:15 LT in Jan, and 05:45–10:15 in Feb. The most favorable times of dispersion of fog are 06:15 LT in Dec and 07:45 LT in January and February. Likewise, the onset and dispersal time of dense fog during winter at TIA has been shown in Figure 3. Dense-fog onset usually occurs in 03:45–08:45 am in Dec, 02:15–09:15 am in Jan, and 05:15–08:15 am in Feb. Most of the dense fog onset occurs at 05:15 and 08:15 am in all three months. Dispersal timings are 04:45–09:45, 03:45–10:15, and 06:15–09:45 am in Dec, Jan, and Feb respectively. Most of the dense fog dispersal takes place at 06:15 and 09:15 am in all three winter months. This is in line with previous observations of the highest percentage of dense-fog onset at 05:15 and 08:15 am.

Our investigation of the consecutive duration of winter fog in Kathmandu revealed that the maximum percentage of fog (dense fog) events in Kathmandu do not last long—less than one hour. Only very few days witnessed fog (dense fog) lasting up to 6 h (2 h). Fog in Kathmandu exhibits a sharp contrast to fog in the IGP region. Jenamani (2012) reported having a higher duration fog up to 18 hours over Indira Gandhi International Airport (IGI) in Delhi.

Persistent fog spells (also called '*seetlahar*') lasting up to a few days in a stretch is a common phenomenon in the IGP region, including in the Terai plains of Nepal, during December and January. We found that the onset of fog in the valley occurs in the early morning and dispersal occurs before noon. The onset of fog usually takes a longer duration, as the ambient temperature gradually falls overnight and reaches dew point temperature before the fog starts forming. However, the dispersal takes a shorter duration as the increase in ambient temperature occurs faster when the sun passes overhead, or the wind becomes stronger (Jenamani, 2012).

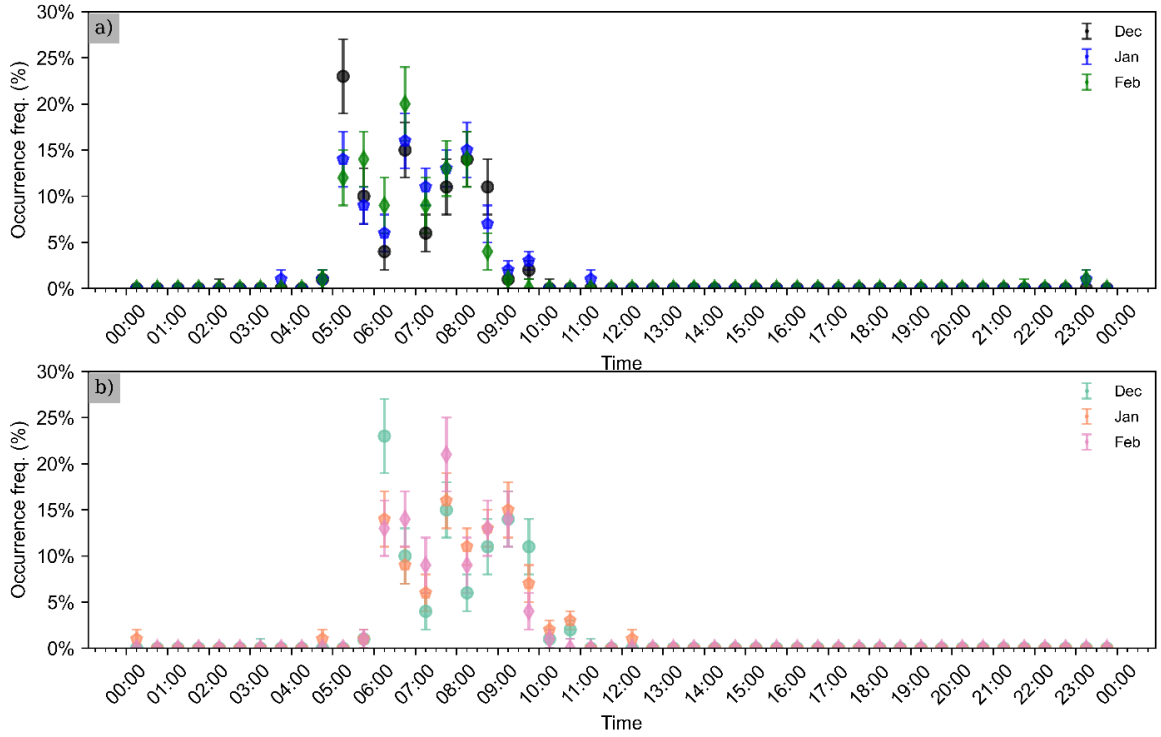

Figure 2. Occurrence frequency of: (a) onset, and (b) dispersal of winter fog (general) in Tribhuvan International Airport (TIA), Kathmandu, from 1976 to 2023. The error bars represent a 95% confidence interval of a single proportion

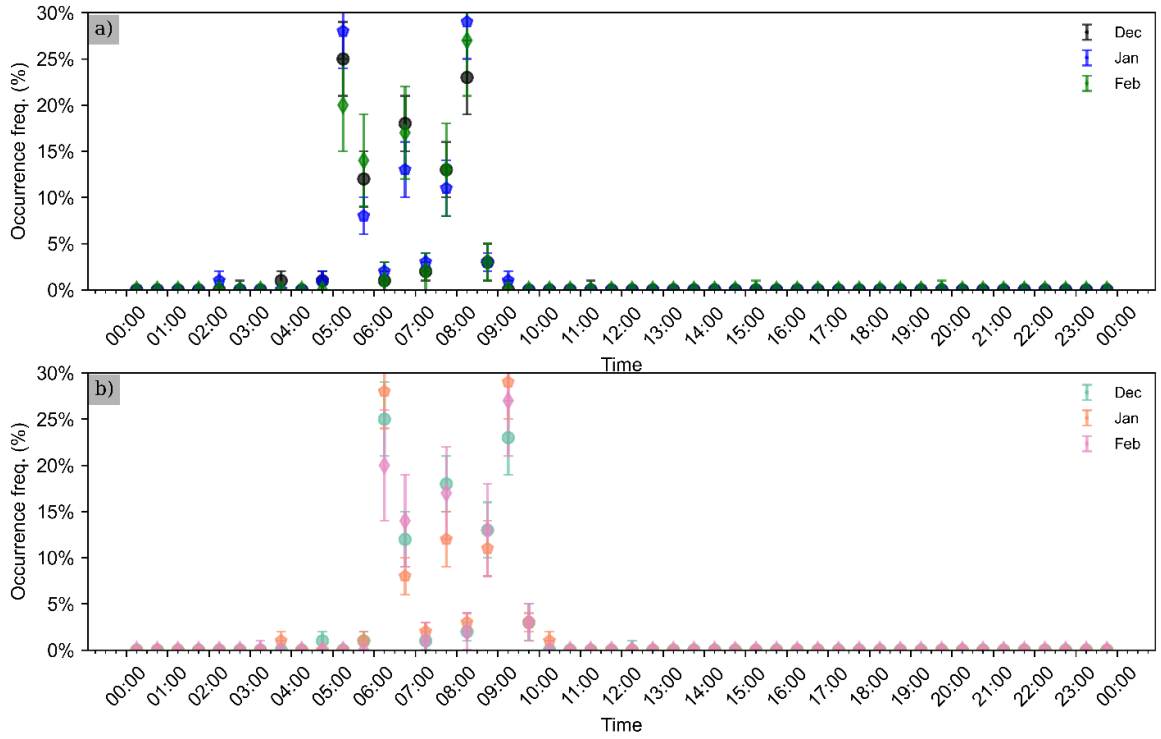

Figure 3. Occurrence frequency of: (a) onset, and (b) dispersal of winter dense fog in Tribhuvan International Airport, Kathmandu, from 1976 to 2023. The error bars represent a 95% confidence interval of a single proportion

Long-term change in haze and fog

Interannual variation of frequency of haze during winter (DJF) over the study period (Figure 4a) reveals that haze occurrence in TIA atmosphere was very little (< 30% of winter days) up until the year 1990. This suggests Kathmandu had a clear sky with good visibility. The haze

frequency gradually rose, attaining a value (< 60%) about double the preceding period until the year 2000. The year 2000 marks a sudden jump in haze frequency near its saturation (~ 100% of winter days). It has remained more or less the same (max number of haze days) since the year 2000.

Thus, we have divided the whole data into two periods 1976–2000 (regime-I) and 2001–2022 (regime-II), and further analyzed. Trend results in Table 1 also reveal a definitive increase in haze day frequency for our study period (2.36% day yr^{-1}, a = 0.001 before the year 2000 and 0.36% day yr^{-1} at a = 0.05 after the year 2000). However, the frequency of winter fog in TIA (Figure 4b) remained mostly below 20% until the year 1998, which rose up to 66% in the year 2001, and again declined to 13% in the year 2006. It displayed a secondary peak value (57%) in the year 2015 and started declining. Surprisingly, only 2 days out of 88 winter days (data available) during the winter of 2020 witnessed fog. It rose to 17% in the year 2021. Again, in the winter of 2022, we observed only four foggy days out of 90 days. Trend result of fog days revealed an upward trend (0.46% day yr^{-1} at a = 0.05) in regime-I. Although the yearly relative frequency of fog days is usually higher than in the previous period, there is no such significant trend in regime II (Table 1). On the contrary, the relative frequency of dense-fog days showed no trend in the previous period but a declining trend (-1.28% day yr^{-1} at a = 0.01) in regime II.

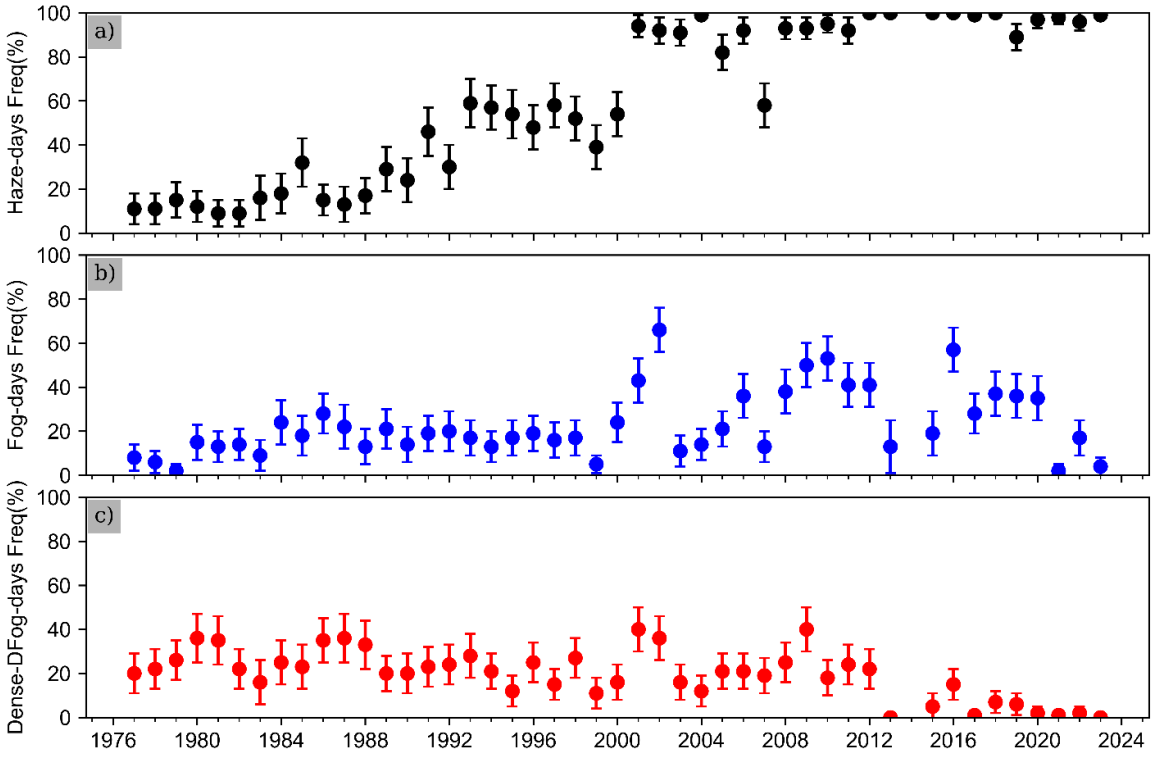

Figure 4. Time evolution in the percentage frequency of: (a) haze days, (b) fog days, and (c) dense-fog days in the winter season (DJF) at Tribhuvan International Airport (TIA), Kathmandu, from 1976 to 2023. The error bars indicate the Margin of Error (MoE)

There was little variation (variance = 0.6%) in occurrence frequency up until the year 2011 (Figure 4c). In this period, the lowest number of dense-fog episodes (11 % of available winter days) were observed in the year 1998 and the highest (40%) in the year 2000. Dense fog events were below 10% after the year 2016. We observed dense fog in only one day in the winter of 2020, two days in 2021, and none in the year 2022. Likewise, the annual fog and dense fog days over the study period have been shown in **Figure S.1** (Supplementary material).

Several previous research works (e.g., De & Dandekar, 2001; Saikawa *et al.*, 2019; Sarkar *et al.*, 2006; Syed *et al.*, 2012) also reported increased regional haze and fog episodes over the years elsewhere in Hindu Kush Himalayan (HKH)—where the KTM valley lies. Kathmandu Valley is highly vulnerable to air pollution due to its unique bowl-shaped topography (Panday *et al.*, 2009), atmospheric conditions (Becker *et al.*, 2021), and increased sources of local emissions (Mool *et al.*, 2020). During winter, the valley's atmosphere experiences the highest levels of ground-level air pollution (Aryal *et al.*, 2008; Becker *et al.*, 2021; Putero *et al.*, 2015) that makes KTM Valley occasionally rank as having the worst particulate air pollution levels worldwide (Becker *et al.*, 2021). Near-surface temperature and wind speed in KTM are the lowest in the winter months (Supplementary material, Table S.1). In winter, strong

nighttime inversions form cold air pool above the valley basin (Panday *et al.*, 2009; Panday & Prinn, 2009) resulting in lower Mixing Layer Height (Mues *et al.*, 2017) that suppresses buoyant vertical transport of air pollutants. Rain scarcely occurs in the valley during winter—making precipitation scavenging a rare seasonal phenomenon. All of the above factors—air pollution emissions and meteorological—contribute to the intensification of winter haze.

Table 1. Trend results of occurrence frequency of haze, fog, and dense fog days in winter (DJF) at Tribhuvan International Airport (TIA) in Kathmandu from 1976 to 2022 using Mann-Kendall and Sen's slope estimator. CI denotes the confidence interval

	Period	Mann-Kendall		Sen's slope	
		Z_{MK}	*p*–value	Trend Q (%yr^{-1})	CI %
Occurrence frequency of haze days (%)	1976–2000	4.79	< 0.001	2.36*	[1.00, 3.69]
	2001–2022	2.01	0.044	0.36†	[-0.12,1.75]
	1976–2022	7.34	< 0.001	2.34*	[1.79,3.00]
Occurrence frequency of fog days (%)	1976–2000	1.92	0.055	0.46†	[-0.45, 1.25]
	2001–2022	-0.91	0.364	-0.56^{ns}	[-2.78, 3.83]
	1976–2022	2.52	0.012	0.46†	[-0.06, 1.04]
Occurrence frequency of dense-fog-days (%)	1976–2000	-0.89	0.374	-0.25^{ns}	[-0.75, 0.25]
	2001–2022	-3.23	0.001	-1.28**	[-1.84, 0.13]
	1976–2022	-4.07	< 0.001	-0.53*	[-0.79, 0.00]

*- 0.001, ** - 0.01, and † – 0 .05 level of significance ; ns – non significant

Through the analysis of Copernicus Atmosphere Monitoring Services (CAMS)-PM2.5 reanalysis data of Kathmandu for 2003–2019, Becker *et al.* (2021) revealed that the winter season witnessed the highest increase in PM2.5 levels (~ $2\ \mu g\ m^{-3}$) annually. Considering visibility as a proxy of air pollution, our present study using multi-decadal data, also suggests similar deteriorating winter air quality in the valley. Possible reasons could be either an increase in wintertime-air-pollution-activities—local and/or transboundary—or a meteorological impact. We could see a slight upward trend (0.28% /year at a = 0.05) of RH in regime-I (supplementary material, Table S.2), which might have played a contributory role in haze enhancement. In regime II, RH reversed the trend (−0.46 %/year at a = 0.01); already a higher level of air pollution should have outplayed the role of RH in this period. Though little, slowing down of the wind since 2000 (-0.02 m/s/year at a = 0.05) might have contributed to the intensification of winter haze in Kathmandu in regime II. Detailed analysis of the increase in air pollution emission is beyond the framework of the current study. However, it is reasonable to mainly link the seen intensification of winter haze to the significant increase in anthropogenic air pollution sources in KTM ranging from road/air traffic, and industrial activities, to refuse burnings—commensurate with the rapid increase in population (~ 4% per annum) (Timsina *et al.*, 2020) of the valley. Intensification of haze in the IGP region during the same period has been reported in tens of papers (e.g., De & Dandekar, 2001; Kathayat *et al.*, 2023; Saikawa *et al.*, 2019; Sarkar *et al.*, 2006). Thus, the observed haze uptrend in KTM can also be attributed to the transboundary transport of IGP haze into the valley.

Tens of papers have reported increasing frequency of both fog types (fog and dense-fog) elsewhere in the IGP region (e.g., Ghude *et al.*, 2017; Jenamani, 2007; Kathayat *et al.*, 2023; Shrestha *et al.*, 2018; Syed *et al.*, 2012) as well as central and eastern China (Niu *et al.*, 2010). Many (e.g., Kathayat *et al.*, 2023; Niu *et al.*, 2010; Sarkar *et al.*, 2006; Syed *et al.*, 2012) have attributed this to the increase in air pollution and thus abundance of CCN, resulting in more water droplets with higher optical depth (Syed *et al.*, 2012). Yan *et al.* (2020) suggested that aerosols promote fog by increasing Liquid Water Content (LWC) and droplet concentration while decreasing effective droplet size. Some works of literature have also pointed out the possible change in land cover use and irrigation area (Kathayat *et al.*, 2023; Shrestha *et al.*, 2018) and regional meteorological change (Niu *et al.*, 2010).

In addition to the looking at trend of plausible parameters (e.g., RH and WS), we also estimated the trend in Dew-point Depression (T_{dep})—the difference between ambient temperature (T) and dew-point temperature (T_d)—similar to the work of Kutty *et al.* (2020). If dew point depression is low, the saturation of air is more likely, and hence the fog formation, provided other conditions be met. In addition to elevated air pollution, declining nighttime T_{dep} (−0.03 ℃/year at a = 0.05) (Supplementary material, Table S.3) might have contributed to the observed increased trend of fog during 1976–2000. Whereas the decreased RH (−0.70 %/year at a = 0.001) and increase in T_{dep} (0.13 ℃ /year at a = 0.001) should have contributed to the decline in dense fog occurrence since 2000. We also observed an increase in average nighttime temperature (0.14 ℃ /year at a = 0.01) in the later period (2001–2022).

Kathmandu Valley is one of the fastest-growing metro cities in South Asia (Timsina *et al.*, 2020). Because of the increased population, agricultural land and other vegetation land coverage have shrunk considerably in

later periods. This can be visible in satellite imagery of Kathmandu taken 60 years apart (Supplementary material, Figure S.2). This vast change in land cover use led to a diminished source of moisture—one of the most important ingredients for the genesis of fog—as evidenced by a decrement in RH. Decreased moisture content in the atmosphere results in decreased dew point temperature and increased dew point depression as seen above. This may explain the reduced occurrence of dense fog in the later period.

CONCLUSIONS

In the present study, we considered over four and half decades of climatological data measured at the TIA in Kathmandu focusing on the occurrence of haze and fog in winter that usually impair winter visibility at the airport making it difficult for flight operations. We studied the two important properties of fog, namely, consecutive duration and onset/dispersal timing of winter fog at the airport. We found that ~ 86% (~95%) of fog (dense fog) days witnessed fog lasting not more than one hour. Dense fog exceedingly more than two hours is rare in TIA while some fog events lasted up to 6 hours. The onset of fog occurs in the early morning—usually between 05:00 to 09:45 am—in all three winter months and disperses before noon. The most favorable onset times for fog are 05:15 am in December and 06:45 am in January and February while the dense fog onset window is between 05:00 and 09:00 am. The highest percentage of dense fog onset occurs at 05:15 and 08:15 am and dissipates at 06:15 and 09:15 am.

Haze intensifies during winter in the TIA owing to the intensified air pollution, weaker air-pollution-dispersion-mechanism (colder air, slower wind, shallow boundary layer, and no rain), and unique topography of the valley. This has increased exceedingly over the study period mainly because of increased local air pollution. Increased RH in the winter season in regime and slowing down of wind in regime II could have partly contributed to the intensification of winter haze over the years.

Fog events have increased in the TIA, though little, due to the effect of enhanced aerosols (more Cloud Condensation Nuclei (CCN)) in the air. However, it appears that dense fog may have disappeared largely in the recent period (regime II) because of a reduction in agricultural land and vegetation cover and increased dew point depression in Kathmandu.

Increased haze and fog adversely affect aviation at TIA because of the reduced visibility they cause. It shall be a serious concern to aviation service at the country's major international airport. Effective measures are imminent to control air pollution emissions in winter and urbanization of the valley. We require further investigation into the mechanism of winter fog in Kathmandu Valley by using models and the effect of Urban Heat Island (UHI) on fog.

ACKNOWLEDGMENTS

We are highly thankful to the Department of Hydrology and Meteorology (DHM), Nepal, for the historic primary data record and equally grateful to the National Climatic Data Center (NCDC), which archives and publicly distributes the global climatological data used for this study as a part of World Meteorological Organization (WMO) data exchange protocol.

AUTHOR CONTRIBUTIONS

B. Kathayat: Conceptualization, methodology, software, formal analysis, investigation, data curation, writing original draft, and visualization; A.K. Panday: Conceptualization, validation, supervision, writing, review, and editing; B. Pokharel: Validation, supervision, writing, review, and editing; N.P. Chapagain: Supervision, writing, review, and editing.

CONFLICT OF INTEREST

The authors declare no conflict of interest.

DATA AVAILABILITY STATEMENT

Data used in this study are publicly available at https://www.ncei.noaa.gov/maps/hourly/.

REFERENCES

AIC. (2015). Final Report on the Investigation of the Accident of TC-JOC, A330-303, at TIA, KTM on 4 March. *Accident Investigation Commission (AIC), Government of Nepal.* https://reports.aviation-safety.net/2015/20150304-0_A333_TC-JOC.pdf

Aryal, R.K., Lee, B.K., Karki, R., Gurung, A., Kandasamy, J., Pathak, B.K., Sharma, S., & Giri, N. (2008). Seasonal PM_{10} dynamics in Kathmandu valley. *Atmospheric Environment*, *42*(37), 8623–8633. https://doi.org/10.1016/j.atmosenv.2008.08.016

Becker, S., Sapkota, R.P., Pokharel, B., Adhikari, L., Pokhrel, R.P., Khanal, S., & Giri, B. (2021). Particulate matter variability in Kathmandu based on in-situ measurements, remote sensing, and reanalysis data. *Atmospheric Research*, *258*, 105623. https://doi.org/10.1016/j.atmosres.2021.105623

Bhushan, B., Trivedi, H.K.N., Bhatia, R.C., Dube, R.K., Giri, R.K., & Negi, R.S. (2003). On the persistence of fog over northern parts of India. *MAUSAM*, *54*(4), 851–860. https://doi.org/10.54302/mausam.v54i4.1585

Chang, D., Song, Y., & Liu, B. (2009). Visibility trends in six megacities in China 1973–2007. *Atmospheric Research*, *94*(2), 161–167. https://doi.org/10.1016/j.atmosres.2009.05.006

Chen, J., Zhao, C.S., Ma, N., Liu, P.F., Göbel, T., Hallbauer, E., Deng, Z.Z., Ran, L., Xu, W.Y., & Liang, Z. (2012). A parameterization of low visibilities for hazy days in the North China Plain. *Atmospheric Chemistry and Physics*, *12*(11), 4935–4950. https://doi.org/10.5194/acp-12-4935-2012

Chen, Y., & Xie, S. (2013). Long-term trends and characteristics of visibility in two megacities in southwest China: Chengdu and Chongqing. *Journal of the Air & Waste Management Association*, *63*(9), 1058–1069. https://doi.org/10.1080/10962247.2013.791

348

De, U.S., & Dandekar, M.M. (2001). Natural disasters in urban areas. *Deccan Geographer*, *39*(2), 1–12.

Du, K., Mu, C., Deng, J., & Yuan, F. (2013). Study on atmospheric visibility variations and the impacts of meteorological parameters using high temporal resolution data: An application of Environmental Internet of Things in China. *International Journal of Sustainable Development & World Ecology*, *20*(3), 238–247. https://doi.org/10.1080/13504509.2013.783886

Fu, X., Wang, X., Hu, Q., Li, G., Ding, X., Zhang, Y., He, Q., Liu, T., Zhang, Z., & Yu, Q. (2016). Changes in visibility with PM2.5 composition and relative humidity at a background site in the Pearl River Delta region. *Journal of Environmental Sciences*, *40*, 10–19. https://doi.org/10.1016/j.jes.2015.12.001

Ghude, S.D., Bhat, G.S., Prabhakaran, T., Jenamani, R.K., Chate, D.M., Safai, P.D., Karipot, A.K., *et al.* (2017). Winter fog experiment over the Indo-Gangetic plains of India. *Current Science*, *12*(4), 767–784. https://doi.org/10.18520/cs/v112/i04/767-784

Gultepe, I., Tardif, R., Michaelides, S.C., Cermak, J., Bott, A., Bendix, J., Müller, M.D., Pagowski, M., Hansen, B., Ellrod, G., Jacobs, W., Toth, G., & Cober, S.G. (2007). Fog research: A review of past achievements and future perspectives. *Pure and Applied Geophysics*, *164*(6–7), 1121–1159. https://doi.org/10.1007/s00024-007-0211-x

Hameed, S., Mirza, M.I., Ghauri, B.M., Siddiqui, Z.R., Javed, R., Khan, A.R., Rattigan, O.V., Qureshi, S., & Husain, L. (2000). On the widespread winter fog in northeastern Pakistan and India. *Geophysical Research Letters*, *27*(13), 1891–1894. https://doi.org/10.1029/1999GL011020

Hanesiak, J.M., & Wang, X.L. (2005). Adverse-weather trends in the Canadian Arctic. *Journal of Climate*, *18*(16), 3140–3156. https://doi.org/10.1175/JCLI3505.1

Hu, Y., Yao, L., Cheng, Z., & Wang, Y. (2017). Long-term atmospheric visibility trends in megacities of China, India and the United States. *Environmental Research*, *159*, 466–473. https://doi.org/10.1016/j.envres.2017.08.018

Hunova, I., Brabec, M., Malý, M., Dumitrescu, A., & Geletič, J. (2021). Terrain and its effects on fog occurrence. *Science of the Total Environment*, *768*, 144359. https://doi.org/10.1016/j.scitotenv.2020.144359

Hunova, I., Brabec, M., Malỳ, M., & Valeriánová, A. (2020). Long-term trends in fog occurrence in the Czech Republic, Central Europe. *Science of the Total Environment*, *711*, 135018. https://doi.org/10.1016/j.scitotenv.2019.135018

Inhaber, H. (1976). Changes in Canadian national visibility. *Nature*, *260*(5547), 129–130. https://doi.org/10.1038/260129a0

Jaswal, A.K., Kumar, N., Prasad, A.K., & Kafatos, M. (2013). Decline in horizontal surface visibility over India (1961–2008) and its association with meteorological variables. *Natural Hazards*, *68*(2), 929–954. https://doi.org/10.1007/s11069-013-0666-2

Jenamani, R.K. (2007). Alarming rise in fog and pollution causing a fall in maximum temperature over Delhi. *Current Science*, 314–322.

Jenamani, R.K. (2012). Micro-climatic study and trend analysis of fog characteristics at IGI airport New Delhi using hourly data (1981-2005). *Mausam*, *63*(2), 203–218. https://doi.org/10.54302/mausam.v63i2.1391

Jenamani, R.K., & Kumar, A. (2013). Bad weather and aircraft accidents – global vis-à-vis Indian scenario. *Current Science*, *104*(3).

Kathayat, B., Panday, A.K., Pokharel, B., Kumar, V., & Chapagain, N.P. (2023). Four decades of aviation visibility at Bhairahawa airport, gateway to Buddha's birthplace Lumbini, Nepal. *Atmospheric Research*, *288*, 106746. https://doi.org/10.1016/j.atmosres.2023.106746

Kim, C.K., Yum, S.S., Kim, H.G., & Kang, Y.H. (2019). A WRF Modeling study on the effects of land use changes on fog off the west coast of the Korean peninsula. *Pure and Applied Geophysics*, *176*(10), 4623–4640. https://doi.org/10.1007/s00024-019-02242-z

Kulkarni, R., Jenamani, R.K., Pithani, P., Konwar, M., Nigam, N., & Ghude, S.D. (2019). Loss to Aviation Economy Due to Winter Fog in New Delhi during the Winter of 2011–2016. *Atmosphere*, *10*(4), 198. https://doi.org/10.3390/atmos10040198

Kutty, S.G., Dimri, A.P., & Gultepe, I. (2020). Climatic trends in fog occurrence over the Indo-Gangetic plains. *International Journal of Climatology*, *40*(4), 2048–2061. https://doi.org/10.1002/joc.6317

Larssen, S., Gram, F., Haugsbakk, I., Jansen, H., Olsthoorn, X., Giri, A.S., Shah, R., Shrestha, M.L., Shrestha, B., Shah, J.J. [editor, & Nagpal, T. [editor. (1997). *Urban air quality management strategy in Asia-Kathmandu Valley report*. World Bank.

Liu, D.Y., Niu, S.J., Yang, J., Zhao, L.J., Lü, J.J., & Lu, C.S. (2012). Summary of a 4-Year Fog Field Study in Northern Nanjing, Part 1: Fog Boundary Layer. *Pure and Applied Geophysics*, *169*(5–6), 809–819. https://doi.org/10.1007/s00024-011-0343-x

Malm, W.C. (1999). *Introduction to visibility*. Colorado State University, USA.

Manandhar, K.B. (2006). The fog episode in southern Terai plains of Nepal: Some observations and concepts. *Journal of Hydrology and Meteorology*, *3*(1). http://soham.org.np/wp-content/uploads/2006/03/v3-95-100.pdf

Mool, E., Bhave, P.V., Khanal, N., Byanju, R.M., Adhikari, S., Das, B., & Puppala, S.P. (2020). Traffic condition and emission factor from diesel vehicles within the Kathmandu valley. *Aerosol and Air Quality Research*, *20*(3), 395–409. https://doi.org/10.4209/aaqr.2019.03.0159

Morisset, T., & Odoni, A. (2011). Capacity, Delay, and Schedule Reliability at Major Airports in Europe and the United States. *Transportation Research Record: Journal*

of the Transportation Research Board, *2214*(1), 85–93. https://doi.org/10.3141/2214-11

Mues, A., Rupakheti, M., Münkel, C., Lauer, A., Bozem, H., Hoor, P., Butler, T., & Lawrence, M.G. (2017). Investigation of the mixing layer height derived from ceilometer measurements in the Kathmandu Valley and implications for local air quality. *Atmospheric Chemistry and Physics*, *17*(13), 8157–8176. https://doi.org/10.5194/acp-17-8157-2017

Munn, R.E. (1973). Secular increases in summer haziness in the Atlantic provinces. *Atmosphere*, *11*(4), 156–161. https://doi.org/10.1080/00046973.1973.9648357

Nakajima, C., Chalise, S.R., & Shrestha, M.L. (1980). On the fog in Kathmandu Valley. *Journal of the Japanese Society of Snow and Ice*, *41*(Special), 90–99. https://doi.org/10.5331/seppyo.41.Special_90

Niu, F., Li, Z., Li, C., Lee, K., & Wang, M. (2010). Increase of wintertime fog in China: Potential impacts of weakening of the Eastern Asian monsoon circulation and increasing aerosol loading. *Journal of Geophysical Research: Atmospheres*, *115*(D7), 2009JD013484. https://doi.org/10.1029/2009JD013484

Panday, A.K., & Prinn, R.G. (2009). Diurnal cycle of air pollution in the Kathmandu Valley, Nepal: Observations. *Journal of Geophysical Research: Atmospheres*, *114*(D9), 2008JD009777. https://doi.org/10.1029/2008JD009777

Panday, A.K., Prinn, R.G., & Schär, C. (2009). Diurnal cycle of air pollution in the Kathmandu Valley, Nepal: 2. Modeling results. *Journal of Geophysical Research: Atmospheres*, *114*(D21), 2008JD009808. https://doi.org/10.1029/2008JD009808

Putero, D., Cristofanelli, P., Marinoni, A., Adhikary, B., Duchi, R., Shrestha, S.D., Verza, G.P., Landi, T.C., Calzolari, F., & Busetto, M. (2015). Seasonal variation of ozone and black carbon observed at Paknajol, an urban site in the Kathmandu Valley, Nepal. *Atmospheric Chemistry and Physics*, *15*(24), 13957–13971. https://doi.org/10.5194/acp-15-13957-2015

Regmi, G., Shrestha, S., Maharjan, S., Khadka, A.K., Regmi, R.P., & Kaphle, G.C. (2020). The weather hazards associated with the US-Bangla aircraft accident at the Tribhuvan international airport, Nepal. *Weather and Forecasting*, *35*(5), 1891–1912. https://doi.org/10.1175/WAF-D-19-0183.1

Safai, P.D., Ghude, S., Pithani, P., Varpe, S., Kulkarni, R., Todekar, K., Tiwari, S., Chate, D.M., Prabhakaran, T., Jenamani, R.K., & Rajeevan, M.N. (2019). Two-way relationship between aerosols and fog: A case study at IGI airport, New Delhi. *Aerosol and Air Quality Research*, *19*(1), 71–79. https://doi.org/10.4209/aaqr.2017.11.0542

Saikawa, E., Panday, A., Kang, S., Gautam, R., Zusman, E., Cong, Z., Somanathan, E., & Adhikary, B. (2019). Air Pollution in the Hindu Kush Himalaya. In P. Wester, A. Mishra, A. Mukherji, & A. B. Shrestha (Eds.), *The Hindu Kush Himalaya Assessment* (pp. 339–387). Springer International Publishing. https://doi.org/10.1007/978-3-319-92288-1_10

Sapkota, B. (2002). *Suspended Matter in the Urban Air of Kathmandu Valley*.

Sapkota, B.K. (1996). Study of visibility and particulate pollution over Kathmandu Valley. *Project Report, Institute of Engineering, Pulchowk Campus*.

Sarkar, S., Chokngamwong, R., Cervone, G., Singh, R. P., & Kafatos, M. (2006). Variability of aerosol optical depth and aerosol forcing over India. *Advances in Space Research*, *37*(12), 2153–2159. https://doi.org/10.1016/j.asr.2005.09.043

Sen, P.K. (1968). Estimates of the Regression Coefficient Based on Kendall's Tau. *Journal of the American Statistical Association*, *63*(324), 1379–1389. https://doi.org/10.1080/01621459.1968.10480934

Sharma, C.K. (1997). Urban air quality of Kathmandu valley "Kingdom of Nepal." *Atmospheric Environment*, *31*(17), 2877–2883. https://doi.org/10.1016/S1352-2310(96)00346-9

Shrestha, S., Moore, G.A., & Peel, M.C. (2018). Trends in winter fog events in the Terai region of Nepal. *Agricultural and Forest Meteorology*, *259*, 118–130. https://doi.org/10.1016/j.agrformet.2018.04.018

Shrestha, S., Peel, M.C., & Moore, G.A. (2023). Cold waves in Terai region of Nepal and farmer's perception of the effect of fog events and cold waves on agriculture. *Theoretical and Applied Climatology*, *151*(1–2), 29–45. https://doi.org/10.1007/s00704-022-04262-7

Singh, A., & Dey, S. (2012). Influence of aerosol composition on visibility in megacity Delhi. *Atmospheric Environment*, *62*, 367–373. https://doi.org/10.1016/j.atmosenv.2012.08.048

Singh, J., Giri, R.K., & Kant, S. (2007). Radiation fog viewed by INSAT–1 D and Kalpana Geo-Stationary satellite. *Mausam*, *58*(2), 251–260. https://doi.org/10.54302/mausam.v58i2.1228

Srivastava, S.K., Sharma, A.R., & Sachdeva, K. (2016). A ground observation based climatology of winter fog: Study over the Indo-Gangetic Plains, India. *International Journal of Environmental and Ecological Engineering*, *10*(7), 742–753.

Stjern, C.W., Stohl, A., & Kristjánsson, J.E. (2011). Have aerosols affected trends in visibility and precipitation in Europe? *Journal of Geophysical Research*, *116*(D2), D02212. https://doi.org/10.1029/2010JD014603

Streets, D.G., Wu, Y., & Chin, M. (2006). Two-decadal aerosol trends as a likely explanation of the global dimming/brightening transition. *Geophysical Research Letters*, *33*(15), 2006GL026471. https://doi.org/10.1029/2006GL026471

Syed, F.S., Körnich, H., & Tjernström, M. (2012). On the fog variability over south Asia. *Climate Dynamics*, *39*(12), 2993–3005. https://doi.org/10.1007/s00382-012-1414-0

Timsina, N.P., Shrestha, A., Poudel, D.P., & Upadhyaya, R. (2020). *Trend of urban growth in Nepal with a focus in Kathmandu Valley: A review of processes and drivers of change*. https://doi.org/10.7488/ERA/722

Vautard, R., Yiou, P., & Van Oldenborgh, G.J. (2009). Decline of fog, mist and haze in Europe over the past 30 years. *Nature Geoscience*, *2*(2), 115–119. https://doi.org/10.1038/ngeo414

Wang, K., Dickinson, R.E., & Liang, S. (2009). Clear Sky Visibility Has Decreased over Land Globally from 1973 to 2007. *Science*, *323*(5920), 1468–1470. https://doi.org/10.1126/science.1167549

WMO. (1992). *International meteorological vocabulary, WMO-182*. World Meteorological Organization. https://library.wmo.int/records/item/35809-international-meteorological-vocabulary

Wu, D. (2006). More discussions on the differences between haze and fog in city. *Guangdong Meteorology*, *32*, 9–15.

Yan, S., Zhu, B., Huang, Y., Zhu, J., Kang, H., Lu, C., & Zhu, T. (2020). To what extents do urbanization and air pollution affect fog? *Atmospheric Chemistry and Physics*, *20*(9), 5559–5572. https://doi.org/10.5194/acp-20-5559-2020

Yue, S., & Wang, C. (2004). The Mann-Kendall Test Modified by Effective Sample Size to Detect Trend in Serially Correlated Hydrological Series. *Water Resources Management*, *18*(3), 201–218. https://doi.org/10.1023/B:WARM.0000043140.61082.60

Zhang, Q.H., Zhang, J.P., & Xue, H.W. (2010). The challenge of improving visibility in Beijing. *Atmospheric Chemistry and Physics*, *10*(16), 7821–7827. https://doi.org/10.5194/acp-10-7821-2010

Supplementary Materials:

Intensifying Haze and Disappearing Dense Fog in Winter at Tribhuvan International Airport, Kathmandu: Impacts in Aviation

Bhogendra Kathayat[1,2*], Arnico Kumar Panday[3], Binod Pokharel[4, 5], Narayan Prasad Chapagain[6]

[1]*Central Department of Physics, Institute of Science and Technology, Tribhuvan University, Kathmandu, Nepal*

[2]*Nepal Airlines Corporation, Kathmandu, Nepal*

[3]*National Planning Commission, Government of Nepal*

[4]*Central Department of Hydrology and Meteorology, Institute of Science and Technology, Tribhuvan University, Kathmandu, Nepal*

[5]*Department of Plants, Soils, and Climate, Utah State University, Logan, UT, USA*

[6]*Department of Physics, Amrit Campus, Tribhuvan University, Kathmandu, Nepal*

**Correspondence:* bhogendra.735711@cdp.tu.edu.np

Table S.1: Seasonal average values of different meteorological parameters namely, visibility, temperature, dew-point temperature, relative humidity, and wind speed at Tribhuvan international airport (TIA) in Kathmandu from Nov 1976 to 2023. The bold-faced numeric values are the highest and lowest monthly averages

Parameter	Jan	Feb	Mar	Apr	May	Jun	Jul	Aug	Sep	Oct	Nov	Dec
Visibility (km)	**5.83** ± **0.06**	6.41 ± 0.07	6.85 ± 0.07	7.13 ± 0.07	8.35 ± 0.07	8.69 ± 0.07	8.50 ± 0.06	**8.70** ± **0.06**	8.57 ± 0.06	8.44 ± 0.07	7.41 ± 0.07	6.24 ± 0.06
Temperature (°C)	**10.51** ± **0.07**	13.39 ± 0.08	17.29 ± 0.08	20.81 ± 0.0.08	22.38 ± 0.06	24.10 ± 0.05	23.82 ± 0.04	**23.94** ± **0.04**	22.93 ± 0.04	20.23 ± 0.06	15.47 ± 0.07	11.59 ± 0.07
Dew point Temperature (°C)	**5.00** ± **0.03**	6.85 ± 0.03	9.05 ± 0.05	11.62 ± 0.06	16.05 ± 0.04	19.67 ± 0.03	20.95 ± 0.02	**20.93** ± **0.02**	19.76 ± 0.02	15.33 ± 0.05	10.12 ± 0.04	6.25 ± 0.04
Relative Humidity (%)	73.6 ± 0.3	70.1 ± 0.3	64.1 ± 0.3	**62.4** ± **0.4**	72.0 ± 0.3	79.1 ± 0.2	**85.8** ± **0.2**	84.9 ± 0.2	84.1 ± 0.2	76.8 ± 0.3	74.9 ± 0.3	74.4 ± 0.3
Wind Speed (m/s)	**2.3** ± **0.3**	2.8 ± 0.3	3.6 ± 0.5	**3.9** ± **0.5**	2.9 ± 0.2	2.7 ± 0.3	2.7 ± 0.4	3.0 ± 0.4	2.4 ± 0.2	2.7 ± 0.4	2.5 ± 0.4	2.5 ± 0.5

Table S.2: Trend results of meteorological parameters: Relative Humidity (RH), temperature (T), and Wind Speed (WS) in winter (DJF) at Tribhuvan international airport (TIA) in Kathmandu from 1976 to 2022 using Mann-Kendall and Sen's slope estimator. CI denotes the confidence interval

		Mann-Kendall		**Sen's slope**	
	Period	Z_{MK}	p –value	Trend Q ($\%yr^{-1}$)	CI %
(a) Relative Humidity (RH) (%)	1976–2000	2.55	0.011	0.28†	[−0.10, 0.65]
	2001–2022	−2.87	0.004	−0.46**	[−0.94,0.64]
	1976–2022	−1.24	0.215	-0.06^{ns}	[−0.20, 0.18]
(b) Temperature (T) (℃)	1976–2000	0	1.0	0.00^{ns}	[−0.13, 0.13]
	2001–2022	−1.48	0.14	-0.06^{ns}	[−016, 0.12]
	1976–2022	3.06	0.002	0.04**	[0.01, 0.09]
(c) Wind Speed (WS) (m/s**)**	1976–2000	0.37	0.708	0.01^{ns}	[−0.06, 0.47]
	2001–2022	−1.96	0.049	−0.02†	[−0.03,0.01]
	1976–2022	−3.37	<0.001	−0.02*	[−0.03,0.00]*

*- 0.001, ** - 0.01, and † – 0 .05 level of significance ; ns – non significant

Table S.3: Trend results of winter season average values of nighttime meteorological parameters, namely, Relative Humidity (RH), Temperature (T), Dew-point Depression (Tdep), and Wind Speed (WS) in winter (DJF) at Tribhuvan international airport (TIA) in Kathmandu from 1976 to 2022 using Mann-Kendall and Sen's slope estimator. CI denotes the confidence interval

	Period	Mann-Kendall		Sen's slope	
		Z_{MK}	p –value	Trend Q (%yr^{-1})	CI %
(a) Relative Humidity (RH) (%)	1976-2000	1.89	0.059	0.18 ns	[−0.17,0.43]
	2001-2022	−3.44	<0.001	−0.70*	[−1.13, 0.18]
	1976-2022	−1.93	0.05	−0.11ns	[−0.29, 0.10]
(b) Temperature (T) (℃)	1976-2000	0.58	0.559	0.01ns	[−0.05,0.10]
	2001-2022	2.68	0.007	0.14**	[0.06, 0.34]
	1976-2022	3.75	<0.001	0.07*	[0.01, 0.11]
(c) Dew point Depression (T_{dep}) (℃)	1976-2000	−2.19	0.028	−0.03†	[−0.05, 0.00]
	2001-2022	3.29	<0.001	0.13*	[0.03, 0.25]
	1976-2022	1.67	0.10	0.02ns	[−0.01, 0.06]
(d) Wind Speed (WS) **(**m/s**)**	1976-2000	0.53	0.597	0.01ns	[−0.03, 3.43]
	2001-2022	−1.43	0.153	−0.01ns	[−0.09, 0.03]
	1976-2022	0.47	0.64	0.00ns	[0.00,0.00]

*- 0.001, ** - 0.01, and † – 0 .05 level of significance ; ns – non significant

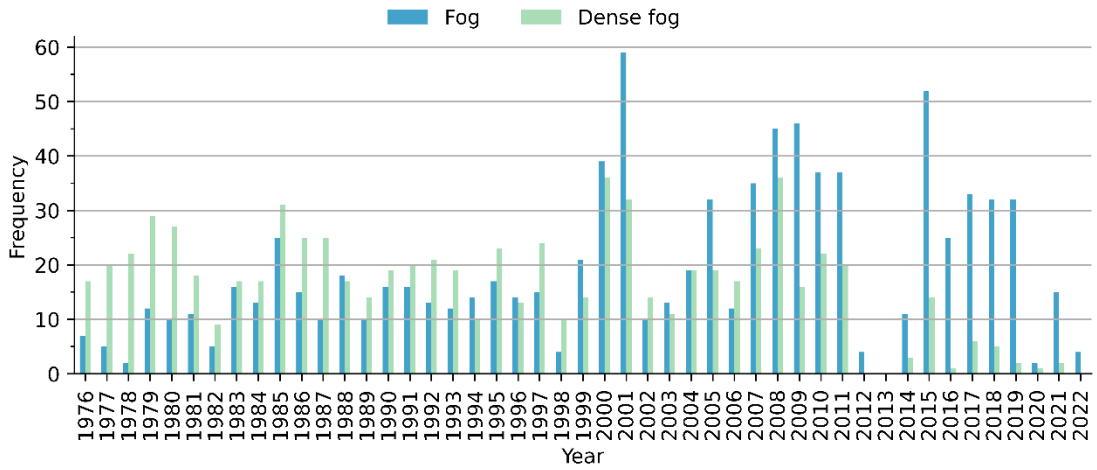

Figure S.2: Annual frequency of fog and dense fog days over TIA (1976–2022)

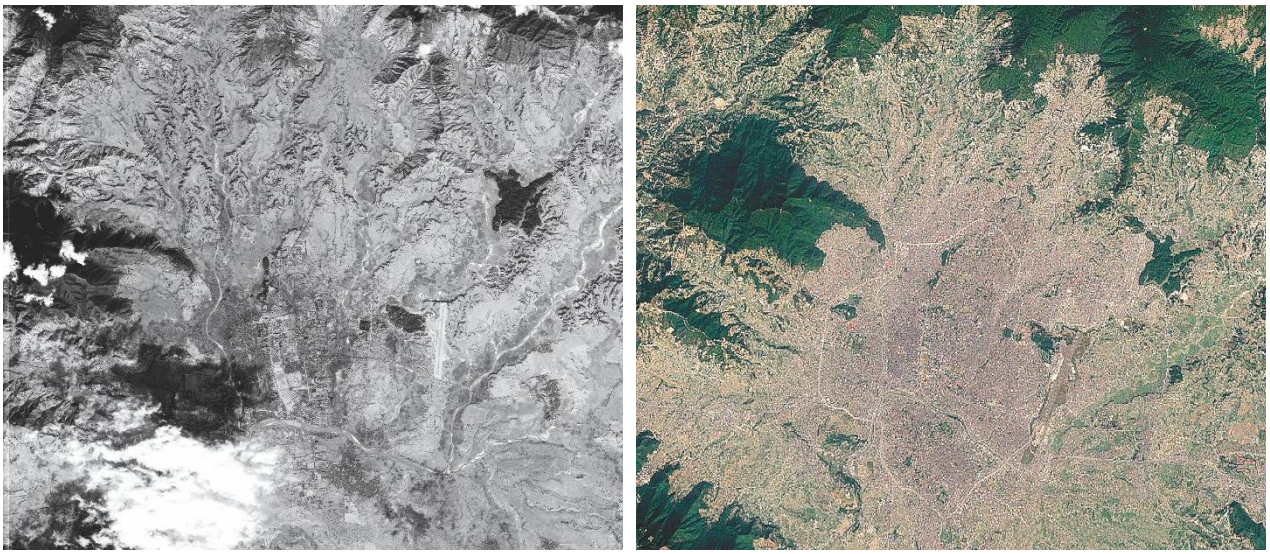

Figure S.2: Satellite image taken on 5 February 1967 (left) showing the broad floodplains of rivers flowing through the Valley floor and open areas and agricultural lands in and around TIA and Google Earth map taken on 20 April 2022 (right) showing urbanization of the Valley (Dixit, 2022)

REFERENCE

Dixit, K. (2022). Kathmandu from space 60 years apart. Nepali Times. Retrieved November 27, 2022 from https://www.nepalitimes.com/here-now/kathmandu-from-space-60-years-apart

ELSEVIER

Atmospheric Research

Certificate of publication for the article titled:

"Four decades of aviation visibility at Bhairahawa airport, gateway to Buddha's birthplace Lumbini, Nepal"

Authored by:

Bhogendra Kathayat, Arnico Kumar Panday, Binod Pokharel
Vinod Kumar, Narayan Prasad Chapagain

Published in:

Pages 106746

Serial number: PR-406472-1FE148C6760A

Certificate of Appreciation

THIS CERTIFICATE IS PRESENTED TO

MR. BHOGENDRA KATHAYAT

Tribhuvan University, Nepal

FOR YOUR PRESENTATION DURING THE ANPA CONFERENCE 2020

DR. CHET R. BHATT
CHAIR, ANPA CONFERENCE 2020

DR. SHREE K. BHATTARAI
PRESIDENT, ANPA

Nepal Physical Society

Ghantaghar, Kathmandu, Nepal

International Conference on Frontiers of Physics -2022
(ICFP-2022)

This Certificate of appreciation is awarded to

Bhogendra Kathayat

from IOST, Tribhuvan University, Nepal for his oral presentation on the **"Four decades of aviation visibility at Bhairahawa airport, gateway to Buddha's birthplace Lumbini"** in the

International Conference on Frontiers of Physics -2022

held on January 22-24, 2022 via virtual platform.

Prof. Dr. Narayan P. Chapagain
Conference Chair, ICFP-2022
President, Nepal Physical Society

February 1, 2022

AMERICAN EMBASSY

ICIMOD

Certificate of Participation

Presented to

Bhogendra Kathayat

for participating in the poster presentation session at the international workshop and science policy dialogue on

Air Pollution, Climate and Health in Southern Asia and the Hindu Kush Himalaya

27–28 November 2017, Kathmandu, Nepal

David Molden
Director General
ICIMOD

Arnico Panday
Regional Programme Manager (Interim)
Atmosphere Initiative

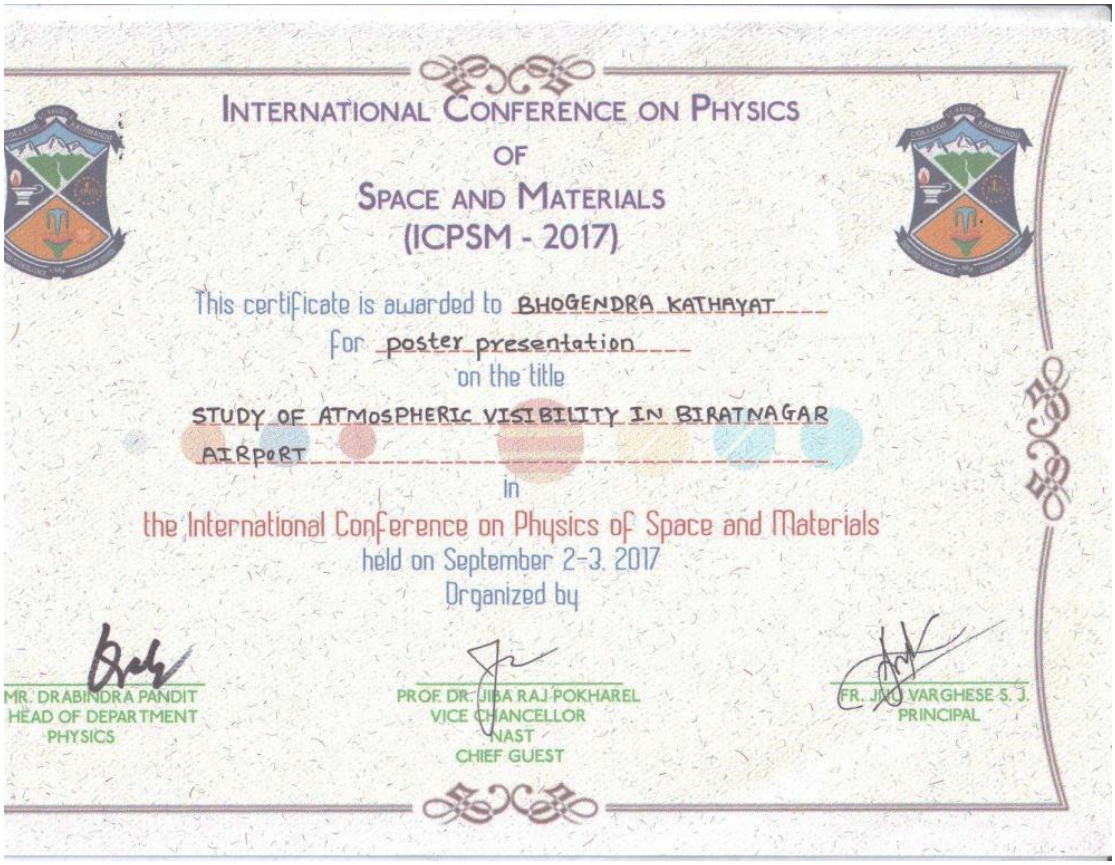

INTERNATIONAL CONFERENCE ON PHYSICS
OF
SPACE AND MATERIALS
(ICPSM - 2017)

This certificate is awarded to BHOGENDRA KATHAYAT
For poster presentation
on the title
STUDY OF ATMOSPHERIC VISIBILITY IN BIRATNAGAR AIRPORT
in
the International Conference on Physics of Space and Materials
held on September 2-3, 2017
Organized by

MR. DRABINDRA PANDIT
HEAD OF DEPARTMENT
PHYSICS

PROF. DR. JIBA RAJ POKHAREL
VICE CHANCELLOR
NAST
CHIEF GUEST

FR. JOJO VARGHESE S. J.
PRINCIPAL

This is to certify the participation of

Bhogendra Kathayat

in the 2nd ACAM Training School on
"Observations and Modeling of Atmospheric Chemistry and Aerosols in the Asian Monsoon region"

Jinan University, Guangzhou, China
10-12 June 2017

Mary C. Barth, Ritesh Gautam, Federico Fierli
Training School Organizers

ICIMOD

Certificate of Participation

Presented to

Bhogendra Kathayat

for participating in the poster presentation session at the international workshop and science policy dialogue on

Air Pollution, Climate and Health in Southern Asia and the Hindu Kush Himalaya

27–28 November 2017, Kathmandu, Nepal

David Molden
Director General
ICIMOD

Arnico Panday
Regional Programme Manager (Interim)
Atmosphere Initiative

Ref no:AG06 PAN NO:615991302 Reg NO:10314-77/78

Skill CORNER & CONSULTATION NEPAL

CERTIFICATE

awarded to

Mr. Bhogendra Kathayat

for successful completion of training on ArcGIS organized by Skill Corner and Consultation Nepal, from September 04, 2021 to September 28, 2021 (15 days)

MR. SAUDEN BADAL
Director
Skill Corner and Consultation,Nepal

MR UTSAV ADHIKARI
Course Trainer

Certificate
of
Participation

presented to

Mr. Bhogendra Kathayat

for participating on an online program on
How to Write an Impressive Research Proposal & ISP Promoting Equal Opportunity in Science
held on June 09, 2021, organized by
Atmospheric and Material Research Center, Department of Physics, Amrit Campus, Tribhuvan University
with the support of International Science Programme (ISP), Uppsala University, Sweden.

Prof. Chandima Gomes
High Voltage Engineering
University of the Witwatersrand

Prof. Carla Puglia
Director of the Physics Program (IPPS)
International Science Program (ISP)
Uppsala University, Sweden

Prof. Leela Pradhan Joshi
Head, Department of Physics
Amrit Campus

Atmospheric and Material Science Research Center
Department of Physics
Amrit Campus
Tribhuvan University

ISP
International Science Programme,
Uppsala University,
Sweden

UNIVERSITY OF MICHIGAN

COURSE CERTIFICATE

06/18/2020

Bhogendra Kathayat

has successfully completed

Understanding and Visualizing Data with Python

an online non-credit course authorized by University of Michigan and offered through Coursera

Brenda Gunderson, Ph.D., Lecturer IV

Kerby Shedden, Ph.D., Professor

Brady T. West, Ph.D., Research Associate Professor

Verify at coursera.org/verify/H3DECJ26VH8G

Coursera has confirmed the identity of this individual and their participation in the course.

UNIVERSITY OF MICHIGAN

COURSE CERTIFICATE

Aug 9, 2020

Bhogendra Kathayat

has successfully completed

Inferential Statistical Analysis with Python

an online non-credit course authorized by University of Michigan and offered through Coursera

Brenda Gunderson, Ph.D., Lecturer IV

Kerby Shedden, Ph.D., Professor

Brady T. West, Ph.D., Research Associate Professor

Verify at coursera.org/verify/AZJAYQT5NXNP

Coursera has confirmed the identity of this individual and their participation in the course.

UNIVERSITY OF MICHIGAN

COURSE CERTIFICATE

Jul 19, 2021

Bhogendra Kathayat

has successfully completed

Fitting Statistical Models to Data with Python

an online non-credit course authorized by University of Michigan and offered through Coursera

Brenda Gunderson, Ph.D., Lecturer IV

Kerby Shedden, Ph.D., Professor

Brady T. West, Ph.D., Research Associate Professor

Verify at coursera.org/verify/8SUBH4J7B3PQ

Coursera has confirmed the identity of this individual and their participation in the course.

---

3 Courses

- Understanding and Visualizing Data with Python
- Inferential Statistical Analysis with Python
- Fitting Statistical Models to Data with Python

UNIVERSITY OF MICHIGAN

Jul 19, 2021

Bhogendra Kathayat

has successfully completed the online, non-credit Specialization

Statistics with Python

This specialization is designed to teach learners beginning and intermediate concepts of statistical analysis, and use of the Python programming language to conduct data analyses. Learners will learn where data come from, what types of data can be collected, how to effectively summarize and visualize data, how to utilize data for estimation and assessing theories, proper interpretations of inferential results, and how to apply more advanced statistical modeling procedures.

Brenda Gunderson, Ph.D., Lecturer IV

Kerby Shedden, Ph.D., Professor

Brady T. West, Ph.D., Research Associate Professor

The online specialization named in this certificate may draw on material from courses taught on-campus, but the included courses are not equivalent to on-campus courses. Participation in this online specialization does not constitute enrollment at this university. This certificate does not confer a University grade, course credit or degree, and it does not verify the identity of the learner.

Verify this certificate at: coursera.org/verify/specialization/JK82SVLASNDL

SN: 021-02-023

LOCUS 2021
18th National Technological Festival

Tribhuvan University
Institute of Engineering

CERTIFICATE OF PARTICIPATION

24th - 30th July, 2021

This is to certify that

Bhogendra Kathayat

has successfully participated in

Quantum Computing

Organised by LOCUS at IOE, Pulchowk.

Adarsha Bohara	Dr. Dibakar Sigdel	Prof. Dr. Shashidar Ram Joshi	Assoc. Prof. Dr. Indra Prasad Acharya
Coordinator LOCUS 2021	Mentor ANPA	Dean Institute of Engineering	Campus Chief Pulchowk Campus

Nepal Physical Society
Ghantaghar, Kathmandu

Certificate of Participation

This certificate is awarded to

Mr. Bhogendra Kathayat from

Nepal Airlines, Kathmandu for his successful participation in

NPS School of Computing - 2020

Conducted from July 4, 2020 to January 31, 2021.

Prof. Dr. Narayan Prasad Chapagain	Dr. Sunil Babu Shrestha	Dr. Dibakar Sigdel
President Nepal Physical Society	Chief Guest Vice – Chancellor, NAST	Instructor Data Scientist, UCLA, USA

February 6, 2021